# Towards Seismic Metamaterials : From Forests to Wind Farms to Cities

Shoaib Ayjaz Mohammed

THÈSE

Pour obtenir le grade de

**DOCTEUR DE L'UNIVERSITÉ GRENOBLE ALPES**

École doctorale : STEP - Sciences de la Terre de l'Environnement et des Planètes
Spécialité : Sciences de la Terre et de l'Environnement
Unité de recherche : Institut des Sciences de la Terre

# Vers des métamatériaux sismiques : des forêts aux parcs éoliens en passant par les villes

# Towards Seismic Metamaterials: From Forests to Wind Farms to Cities

Présentée par :

**Shoaib Ayjaz MOHAMMED**

Direction de thèse :

| | |
|---|---|
| **Philippe ROUX**<br>DIRECTEUR DE RECHERCHE, CNRS | Directeur de thèse |
| **Stefano PAROLAI**<br>Università degli Studi di Trieste | Co-encadrant de thèse |

Rapporteurs :

**Julien DE ROSNY**
DIRECTEUR DE RECHERCHE, CNRS délégation Paris Centre
**Agnès MAUREL**
DIRECTRICE DE RECHERCHE, CNRS délégation Paris Centre

Thèse soutenue publiquement le **26 septembre 2024**, devant le jury composé de :

| | |
|---|---|
| **Olivier COUTANT,**<br>PHYSICIEN, Université Grenoble Alpes | Président |
| **Philippe ROUX,**<br>DIRECTEUR DE RECHERCHE, CNRS délégation Alpes | Directeur de thèse |
| **Stefano PAROLAI,**<br>FULL PROFESSOR, Università degli Studi di Trieste | Co-directeur de thèse |
| **Julien DE ROSNY,**<br>DIRECTEUR DE RECHERCHE, CNRS délégation Paris Centre | Rapporteur |
| **Agnès MAUREL,**<br>DIRECTRICE DE RECHERCHE, CNRS délégation Paris Centre | Rapporteure |
| **Marco PILZ,**<br>SENIOR SCIENTIST, German Research Centre for Geosciences | Examinateur |
| **Eleni CHATZI,**<br>FULL PROFESSOR, Ecole polytechnique fédérale de Zurich | Examinatrice |
| **Malgorzata CHMIEL,**<br>CHARGEE DE RECHERCHE, Université Côte d'Azur | Examinatrice |

# Abstract

It is well established that the presence of the urban agglomerate significantly modifies the free-field ground motion at the city scale. Each building can behave as a resonator, trapping a small fraction of seismic surface waves that is reradiated into the ground. But when tall buildings are densely clustered, like in a city, can we anticipate surface waves to interact with them in unusual ways? Perhaps yes. Evidence suggests resonance coupling between vibrating structures, like trees, can lead to anomalous dispersion of surface waves causing them to become evanescent in certain frequency bands. Such media are called *'locally-resonant' seismic metamaterials*, and the collective behavior when several structures are present inside one seismic wavelength corresponds to the physics observed at the lab-scale for elastic waves in a plate with a set of rods attached to it.

This doctoral thesis focuses on metamaterial physics at the geophysics scale (a few meters to a few kilometers) in the urban seismology context. Starting with a relatively well understood problem of elastic wave scattering due to buried inclusions, we explain how buried columns called 'piles' can resonate when clamped to a stiffer half-space. We demonstrate with 2D simulations a methodology to preferentially excite the dominant fundamental Rayleigh wave mode using time-reversal and a phased source array. This allows us to numerically quantify the scattering due to a clamped pile, which shows resonance peaks in the Mie regime.

We then analyze ambient noise recordings from (a) a forest of pine trees and (b) wind farms, which act as proxies for a city with tall buildings. First, we revisit the dataset acquired from dense arrays deployed in the Landes forest characterized by a dense pine tree configuration. We observe an evanescent field radiated by the longitudinal resonances of trees, as expected in an elastic metasurface. On the contrary, flexural resonances of trees in the 1-10 Hz regime, appear to be weakly coupled. Plane-wave beamforming analysis of a 9-day ambient noise recording reveals a strong cos $2\theta$ Rayleigh wave azimuthal anisotropy ($> 10\%$) in the forest. However, identifying the precise source of the anisotropy with the available field data proves challenging and numerical simulations seem necessary.

We then extend the hypothesis of coupled resonators to a forest of wind turbines. We initially acquire data from a relatively sparse array cutting across the San Gorgonio Pass wind farm in California. However, the spectral ratio analysis and noise correlation of geophone pairs do not suggest any metamaterial effect, which could be due to the spatial configuration of the turbines. We perform a field experiment in the Nauen wind farm in Brandenburg, which hosts much larger turbines. The dense spatial sampling from the DAS fiber-optic sensors gives us interesting insights

into the near-field radiation of the turbines. The surface field strongly attenuates in distinct frequency bands, suggesting a metamaterial-like effect inside the wind farm.

Finally, we conduct a field experiment that aims to understand the interaction between the ground and a simple resonator. Both active and passive data is acquired by designing three suitable array configurations for the different phases of the experiment, which we use to evaluate the dynamic response of the structure and the soil. Through this effort, we generate a quality dataset in a controlled environment for future investigation of soil-structure interaction.

The experimental and numerical studies in this thesis directly contribute to the understanding of how seismic surface waves interact with specific features of an urban-like landscape from the novel perspective of metamaterial physics. The results might have important implications for seismic hazard in urban areas.

# Acknowledgments

I am grateful to many people who made this thesis possible. Philippe was not only my research supervisor, but also a mentor and a friend. Learning from his approach to thinking, discussing ideas and doing science, transformed me from a student into an earth scientist. Stefano kept me grounded, constantly challenging the claims I made. His insights helped me refine my vocabulary and brought balance to my work. He kindly invited me to Trieste and hosted me at OGS for a couple of months.

I thank the thesis jury, especially the reviewers, for accepting to spend their summer reading my manuscript. Their comments and criticism were essential in maintaining the scientific quality of this thesis.

Andrea Colombi, Jean Virieux, Dino Bindi along with my supervisors regularly checked my progress. Beyond the scientific discussions, their advice helped me keep my goals realistic so that they remained feasible. Andrea's well-organized scripts for Trelis to run SPECFEM simulations, made my life easier and gave me a head start in this PhD. Moreover, he informally supervised the first half of my PhD.

Philippe Gueguen, along with Florence Cataye and Na'Omi Chapalain, excellently managed the URBASIS project before, during and after the pandemic. They ensured that there were no issues with the funding and addressed every concern I had. Fabrice Cotton kindly funded my extension for a couple of months, allowing me to stay at ISTerre a little longer. I thank all my fellow URBASIS ESRs and the entire consortium for making this PhD a collaborative experience.

At ISTerre, I benefited from the rich discussions with quite a lot of researchers in the Ondes team. Discussions with Martin Lott significantly enhanced my understanding of locally resonant metamaterials. Pierre Boué showed me how to use his `pycorr` package to retrieve waveforms from FDSN-webservices. Chloé Gradon helped me fix a small but frustrating bug (' vs .' for MATLAB complex matrix multiplication) in the beamforming code, over which I had spent a month breaking my head. Jian and Mus always came to my rescue whenever I needed help on the cluster. Sharing an office with SEISCOPE PhD students and postdocs has been a pleasant experience, and they were kind enough to treat me as one of their own.

I would also like to acknowledge Martijn van den Ende of Géoazur for his patience in clarifying all my questions about beamforming with DAS. Despite not being directly involved in my project, he generously gave his time for both in-person and virtual discussions.

I left my hometown in India, thousands of miles away from my family, to pursue my PhD research. I did not see them for the first two years due to travel restrictions, yet their prayers and encouragement kept me going. I was fortunate to meet my wife midway through my PhD. Her care and support by taking up my responsibilities, especially during the writing phase, were instrumental in helping me complete this manuscript.

Above all, I am deeply grateful to my Creator, The All-Knowing, The All-Powerful, for showing me His signs, guiding me on this path and blessing me with the people I have encountered along the way.

# Contents

# List of Figures

# List of Tables

# Chapter 0

# Introduction

## 0.1 Motivation for studying complex wave phenomena

Have you ever wondered why some buildings collapse after a strong earthquake while neighboring identical buildings stand upright? These buildings might have the same design, be constructed using the same materials and practices and even be founded on the same type of soil. This phenomenon observed in past earthquakes (Fig. 1) has intrigued the engineering seismology community. Ground motion at a specific location is influenced by the earthquake's source, the path the seismic waves travel, and the local site conditions. Since these factors should be the same for neighboring buildings, one would expect identical buildings to have the same response to a given ground motion. This would only hold true in the context of "free-field" conditions i.e., in the absence of the building stock. In urban areas, however, the presence of the urban fabric may lead to significant interactions between the buildings and the soil, thereby modifying the ground motion itself. Various terminology has been used in the literature to describe these interactions, such as 'soil-structure interaction' (SSI) in the case of a single structure coupled to the soil, 'structure-soil-structure interaction' (SSSI) in case of multiple structures coupled through the soil, and 'site-city interaction' (SCI) on the city scale.

The term 'Site-city interaction' originally put forward by Guéguen et al. [2002] refers to the global interactions between building clusters and the subsurface. The interactions can be either (a) kinematic i.e., the foundation heterogenities diffracting the incident wavefield (e.g. Kausel [2010]); or (b) inertial i.e., each building can behave as a resonator, trapping a small fraction of seismic waves that is reradiated into the ground (e.g. Jennings [1970], Kanamori et al. [1991], Gueguen et al. [2000], GUÉGUEN and BARD [2005], Kham et al. [2006], Laurenzano et al. [2010]). The total wavefield reradiated into the ground is the superposition of the contribution from each individual building considered simultaneously. Thus, a city with buildings is a fully coupled dynamic system that should be treated as a whole. However, the classical ground motion prediction equations neglect the city contribution. If we have to write the modified Fourier spectra of the ground motion, we can incorporate the site-city coupling by convolution of an extra term related to the urban environment to the existing site term (Fig. 2).

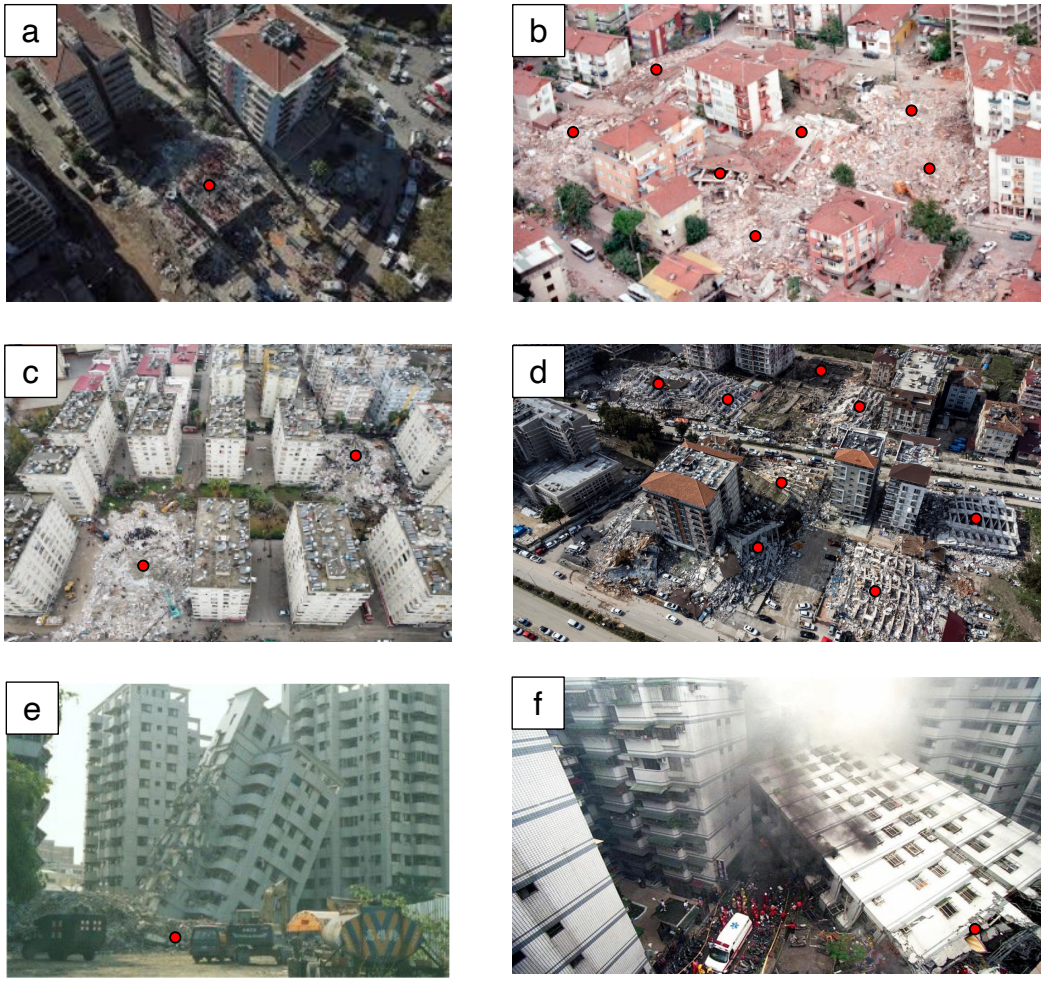


Figure 1: Photos taken after earthquake events highlighting the spatial variability of collapse (marked by red circles) within identical building typology. This can be attributed to the variability in ground motion itself, presumably due to multiple interactions between buildings and the wavefield. The pictures clearly show that this is not a one-off phenomena, but rather observed in several instances when a strong earthquake effects an urban area. (a) 2020 Aegean Sea earthquake, Turkey (Photo: Getty Images) (b) Izmit earthquake, Turkey 1999 (Photo: Getty Images), (c, d) The $6^{\text{th}}$ and $7^{\text{th}}$ February 2023 Turkey earthquake (Photo: Getty Images/EPA-EFE/ERDEM SAHI), and (e,f) 1999 Chi Chi earthquake, Taiwan (Photos: The New Taipei City Public Works Department)

The interactions between the soil and the structures and between the structures can strongly modify the lateral variability of the observed ground motion. This is also intriguing because the observations in connection to earthquake damage, even at short distances less than a wavelength (subwavelength) of similarly designed and constructed buildings is drastically different (see the photographs in the Fig. 1). These can be hints that the wavelength of surface waves inside urban areas is very different from what is usually expected. Waves radiated from buildings to the surrounding soil medium are uneasy to detect when looking only at the signal amplitude. Identification of the phase of the signals that are radiated is equally important. This was shown recently by Skłodowska et al. [2023] using innovative processing combining deconvolution and polarization analysis for the wavefield ra-

diated by a single building to its surroundings.

For better characterizing the seismic hazard and therefore the seismic risk in urban areas, we need to better understand the origin of the ground motion variability in cities, when we are inside a cluster of buildings. The physics of coupled resonances which can lead to complex wave propagation could be one way to explain this variability and forms the context of the investigations made in this thesis. In the following, I first introduce the different types of seismic waves, and argue why I am interested in only the seismic waves that propagate along surface of the earth.

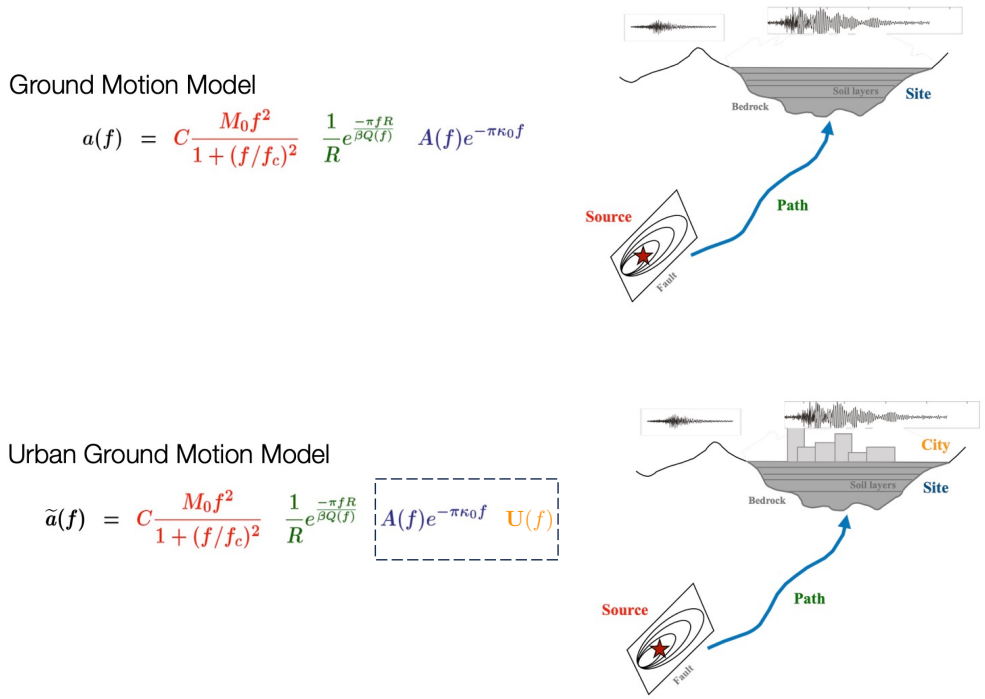


Figure 2: Modification of the earthquake ground motion in urban areas. In the classical ground motion model we have the source, path and site effect convolved to obtain the ground motion any location. An additional term corresponding to the presence of the 'urban layer' would be necessary to accurately describe the ground motion model for urban areas. The modified term shown in the dashed box of urban ground motion Fourier spectra is due to the site-city effect, wherein the two terms are non-independent. (Adapted from P. Gueguen, ISTerre)

## 0.2 Seismic waves: Body and surface waves

Mechanical waves produced by a disturbance in an elastic medium can propagate in the medium as body waves and surface waves. As the names suggest, the former is a class of waves which can travel in the bulk of the corresponding medium, whereas the latter require a surface to propagate as guided waves. When these waves travel in the earth or on the earth's surface, they are usually referred to as seismic waves. The body waves can be further classified into two, namely, Primary or P-waves and Secondary or S-waves, based on the way they deform the medium. When the disturbance in the medium causes the particles to move parallel to the direction

of the propagation, they are called P-waves and are thus longitudinal or compressional in nature. On the other hand, if the disturbance causes the particles to move perpendicular to the direction of propagation they are termed S-waves, and they have a shearing nature. These two body waves can be produced simultaneously but travel at different speeds depending on the elastic medium through which they are propagating. Of the two, the P-waves travel faster because of the manner in which they cause the medium to deform and the restoring forces of the medium (Fig. 3).

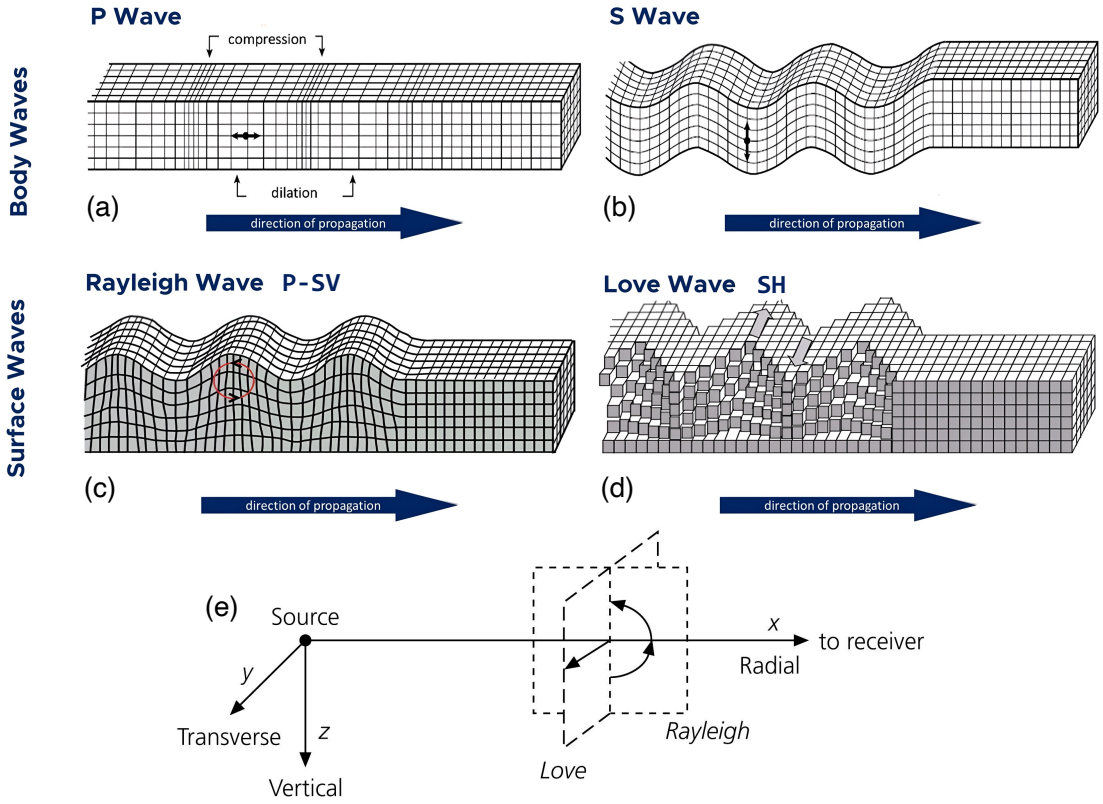


Figure 3: A seismic wave is an elastic wave generated by a disturbance in the earth, for example an impulse such as an earthquake or an explosion. They may travel either through the earth's interior as P and S waves (a,b) or along or near the earth's surface as Rayleigh and Love waves (c,d). (e) Geometry for surface waves propagating in a vertical plane containing the source and receiver. Rayleigh (P–SV) waves appear on the vertical and radial components, whereas, Love (SH) waves appear on the transverse component. ( a-d are adapted from LukeTriton, Steven Earle, Mario Bačić, Lovorka Librić, Danijela Jurić Kaćunić, Meho Saša Kovačević, CC BY-SA 4.0 https://creativecommons.org/licenses/by-sa/4.0, via Wikimedia Commons), whereas (e) is borrowed, as it is, from Stein and Wysession [2009]

All waves satisfy the same elastodynamic equation, albeit with unique set of boundary conditions. The free surface of the Earth acts like a waveguide which is mathematically defined by the vanishing of surface tractions. Body wave energy, incident on to the free surface of an elastic medium, is guided along this interface of soil and air. Thus, surface acoustic waves (SAWs) belong to the broader category of guided waves. The two main types of surface acoustic waves are Rayleigh and Love waves. When the P waves are coupled with the vertically polarized shear (SV)

waves by the vertical gradient of the material properties, the interaction of their energy effectively propagates as a Rayleigh wave. This interference wave exhibits properties that are different from those of P and S waves and the resulting particle motion is elliptical. Love waves, on the other hand, are a result of the total reflection of horizontally polarized shear (SH) waves at the free surface when the layer(s) of the earth trap these reverberations near the surface. It can be better visualized from the Fig. 3(c-e) how Rayleigh waves travel in the vertical and radial planes (having both horizontal and vertical motion), whereas Love waves travel in the transverse plane (having purely horizontal motion).

Although P and S waves are the basic wave types, as we discussed above they can however couple with each other when they hit an interface. The surface waves resulting from their coupling travel longer distances and usually carry the highest energy. Having said that, the peak ground acceleration (PGA), which is a common ground motion parameter for seismic hazard, can be produced due to any type of seismic wave. Surface waves can be the dominant wave type based on the relative source location, path and site effects. For example, if an earthquake source is shallow or if the faulting mechanism is predominantly strike-slip, the observed wavefield is dominated by the surface waves. Similarly if the site is located in a sedimentary basin, the amplification of surface waves in some cases can be higher than the body waves and in a different frequency regime (Bowden and Tsai [2017]). How drastically the surface waves effect a structure, depends on the frequency content of the surface waves and the resonance frequency of that individual structure.

#### Scope of this thesis

All seismic waves travel with different speeds and the physics can become quite complicated when they are considered simultaneously in a medium with dense resonator configurations, like in a city. Surface waves can be more interesting in the study of the interactions with multiple resonators that are attached to the surface. Moreover, controlling the impact of seismic surface waves on the built environment is a key challenge in seismology and earthquake engineering. My objective in this thesis is neither to study surface waves produced by earthquakes, nor to consider an actual urban environment. But rather, my goal is to use ambient seismic noise, which I assume is predominantly surface (Rayleigh) wave energy excited by shallow sources, to explain the physics of wave propagation in dense city-like environments on the geophysics scale. This brings me to the introduction of the concept of 'metamaterials', mainly in the context of seismic waves.

## 0.3 What are (seismic) metamaterials?

The idea of manipulation of electromagnetic waves using structured materials has been popular with the photonics community. A photonic crystal is one having a nanoscale periodic structure which can produce prohibited frequency bands in which light cannot pass or only a narrow band of wavelengths get reflected. Such structured materials that have exceptional properties due to the collective behavior of their unitary structures, came in the focus of attention at the turn of this century and were termed as 'metamaterials'. The idea of such a material, although predicted for electromagnetic waves by the seminal work of Veselago [1968] was reintroduced

by Pendry et al. [1999]. The very first demonstration was made using a periodic array of split ring resonators by Smith et al. [2000], which was achieved by creating an effective medium for scattering electromagnetic waves when the wavelength is significantly greater than both the size of the elements and the spacing between them. *But one may ask, why as seismologists should we be interested in metamaterials?*

The physics of metamaterials soon found corollaries in other fields for example, in manipulating sound waves and elastic vibrations. Structured bandgap materials like a phononic crystal are engineered in such a way that sound waves can be attenuated or stopped completely or they can be diverted from their expected path. Based on the developments in other fields, researchers were curious to find if elastic surface waves could also show similar behavior in spatially ordered and/or subwavelength[†] locally-resonant media. These can posses dispersion properties that are not observed in usual materials and are characterized by frequency bandgaps[‡]. Thus, sometimes also referred to as bandgap media. Here, the constituent materials themselves do not possess any exceptional dispersion properties but are acquired by virtue of their structure. The first such demonstration of bandgaps for Rayleigh waves was made by Meseguer et al. [1999] by a periodic distribution of cylindrical holes in a marble quarry. However, this was in the kHz regime and not relevant to seismology. In 2012, an experiment by Brûlé et al. [2014] for the first time demonstrated at much larger scale that a mesh of vertical empty inclusions could dampen seismic waves at 50 Hz (Fig. 4).

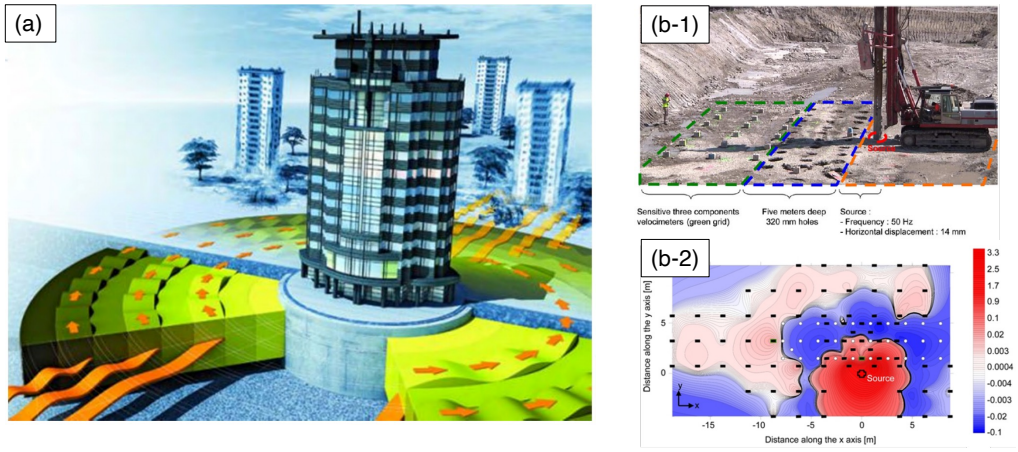


Figure 4: (a) Cartoon fantasizing the idea of a seismic metamaterial cloak (in green) as an analogy to a metamaterial cloak for electromagnetic waves, Popular Science (Credits: Sébastien Guenneau, Institut Fresnel, Marseille). (b-1) Realization of a seismic metamaterial: First full-scale experiment conducted by Ménard Company near Lyon with empty boreholes in the soil mimicking a phononic crystal. (b-2) The boreholes' effect on the energy field - the difference of the measured energy field with and without the boreholes (Brûlé et al. [2014]).

In elastodynamics, one can find two interesting mechanisms in the literature that explain the formation of frequency bandgaps: (a) Bragg scattering, and (b) lo-

[†]length scale smaller than the wavelength propagating in the medium
[‡]frequency bands of prohibited propagation

cally resonant sub-wavelength media. Different physics drives these bandgap mechanisms. Waves propagating in periodic media, similar to phononic crystals rely on the destructive interference of incident and reflected waves based on the lattice pitch (distance between neighboring scatterers). The important physical parameter, especially for band-gap characterization in such materials, is the dimension of the elementary cell, $l$. Depending on the arrangement, if the size of the cell is comparable to the wavelength (say, $l \approx \lambda/3$ or $\lambda/2$), there can be a total reflection of waves (Bragg scattering) and a completely different behavior when the cells have a sub-wavelength arrangement ($l \ll \lambda$).

The physics of Bragg interferences can be distinguished from metamaterials where the resonance of the unit cell is the driving factor. Their properties are governed by the interference between the incident and the scattered waves that results in the manipulation of the surface impedance. Such interaction leads to the hybridization of the guided waves (Lemoult et al. [2012]). Here, it is not necessary for cells to be periodic, but rather that several resonators should be within one wavelength, so that they couple with each other to produce frequency bandgaps. Lab-scale and meter-scale experiments (e.g. Rupin et al. [2014], Roux et al. [2018]) and simulations of elastic waves in plates and half-spaces Colombi et al. [2014, 2016c], Palermo et al. [2016], Colombi et al. [2016a]) support the hypothesis of sub-wavelength local resonances. Some studies have also combined the two mechanisms of Bragg scattering and sub-wavelength local resonances to obtain very efficient and broad bandgaps (Krushynska et al. [2017]), which is inspired by previous results in electromagnetic waves (Kaina et al. [2013a]).

Another idea that can be borrowed from electromagnetism, where lenses are naturally used, is to direct or channel the wave energy in a particular fashion. This works by devising an effective refractive index, which changes spatially, done using homogenization theory. These 'gradient refractive-index lenses' can be mimicked for seismic waves by ground mediation, so that the properties of the soil gradually change in a certain way, to eventually steer and sharply focus wave energy as required (Colombi et al. [2016b]). Finally, the acoustic analogue or the polarized electromagnetic analogue of Dirichlet inclusions (Antonakakis et al. [2013, 2014a]) have found an interesting application in shielding very long-wavelength seismic waves (Achaoui et al. [2017], Antonakakis et al. [2023]). The concept is to completely reflect low-frequency waves using a regular arrangement of inclusions that are 'clamped' or having zero Dirichlet boundary conditions, through multiple scattering of waves (different from Bragg scattering). In the literature, these are called 'zero-frequency' bandgap media.

The concept of a seismic metamaterial has found interesting applications in wave manipulation and control to protect critical or sensitive infrastructure. Many studies that make use of the above mentioned physics of creating bandgap media, propose 'seismic barriers' or 'metasurfaces'* that can entirely or partially dampen surface waves in certain frequency bands, modify the direction of the wavefront or convert surface waves into bulk waves. These are all interesting from the perspective of metamaterials on the geophysics scale.

*A 2D counterpart of a metamaterial often at or near the surface of a medium

## 0.4 Thesis placement within the state of the art

Although the idea of a seismic metamaterial is relatively new, research efforts in the recent years show that it is of topical interest, especially in the seismology and the earthquake engineering communities (Figure 5) . Despite the many studies that have taken interest in seismic metamaterials in the last decade, several fundamental questions still remain. This is mainly because a large fraction of the studies that are published, focus on applied research i.e., design of specific metasurfaces to cancel out or divert surface waves for undesired frequency bands. Unlike many studies in the literature that design specific metasurfaces, my aim in this thesis is to understand the physics governing the behavior of subwavelength configurations of dense resonators, that may couple to each other to modify the surface wave dispersion at the geophysics scale.

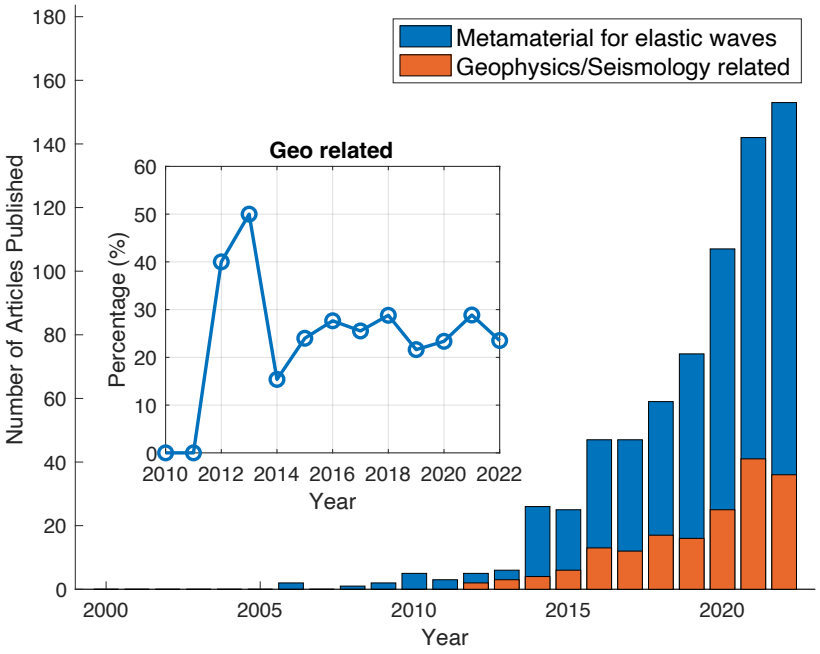


Figure 5: Trend of publications related to metamaterials concerning elastic wave propagation, according to the Dimensions® (data accessed in July 2023). While the counts are likely incomplete (e.g., not including conference proceedings, book chapters or recent preprints), there is a growing interest in metamaterials for the control of elastic waves. In the meanwhile, the application to seismology and earthquake engineering fields started around 2012–2013, and on average, make up a quarter of the publication share in this domain.

Studies that have investigated the propagation of seismic waves through metamaterials use diverse methodological approaches. Interestingly, there are no reported full scale experiments other than the 2012 periodic borehole experiment by Brûlé et al. [2014] and the 2016 forest experiment by Roux et al. [2018]. These two field experiments for investigating surface Rayleigh waves in a half-space and laboratory

experiments, particularly for flexural waves in the plate (Rupin et al. [2014, 2015], Rupin and Roux [2017], Lott et al. [2017], Lott and Roux [2019a], Lott et al. [2020b]), coupled with the initial theoretical framework were effective in providing the proof of concept. Full time-domain simulations have also been extensively employed for studying realistic cases that have finite arrays of metastructures (e.g. Colombi et al. [2016c, 2019], Zaccherini et al. [2020]). The existence of frequency bandgaps is also well predicted by the Floquet–Bloch theory (e.g. Palermo et al. [2018]), which can be applied to any type of waves propagating within infinitely periodic media. Using periodic boundaries, the bandgap properties of metamaterials can be directly inferred from the complex dispersion relation for both plates and half-spaces (e.g. Lott and Roux [2019a]).

My approach in this thesis will mainly rely on using passive seismic data from field experiments to study metamaterial physics. The ambient noise recorded over a relatively long time period (how long is long enough depends on the frequency) should allow me to compare the spectral properties in the free-field to the field inside the metamaterial, and additionally to measure the surface wave dispersion. Besides data analysis this work also relies on numerical simulations in both time domain and frequency domain.

### Scalability of seismic metamaterials

Metamaterials possess a strong scalability characteristic, allowing them to be used in various wave realms and at different length scales. Buildings in a city can be well idealized at the lab scale by a set of beams/rods attached to a substrate. The lab-scale experiment provides interesting conclusions that can be used as a reference for large scale experiments e.g. with a subwavelength arrangement of trees in a forest. The collective behavior when several trees are present inside one seismic wavelength corresponds to the physics observed at the lab-scale for elastic waves in a plate with a set of rods attached to it. As one would expect, the resonances occur at relatively lower frequencies as the size of the resonator increases, but the physics of subwavelength coupled resonances remains the same (Fig. 6). Similarly based on the results of the forest experiment, one can explore further large-scale resonator configurations like wind turbines or buildings which can resonate at even lower frequencies (a few Hz) that are relevant to urban seismology. Thus, we exploit this scalability property of metamaterials to study both forests and wind farms that are ideal proxies to a city with tall buildings, and still on the geophysics scale.

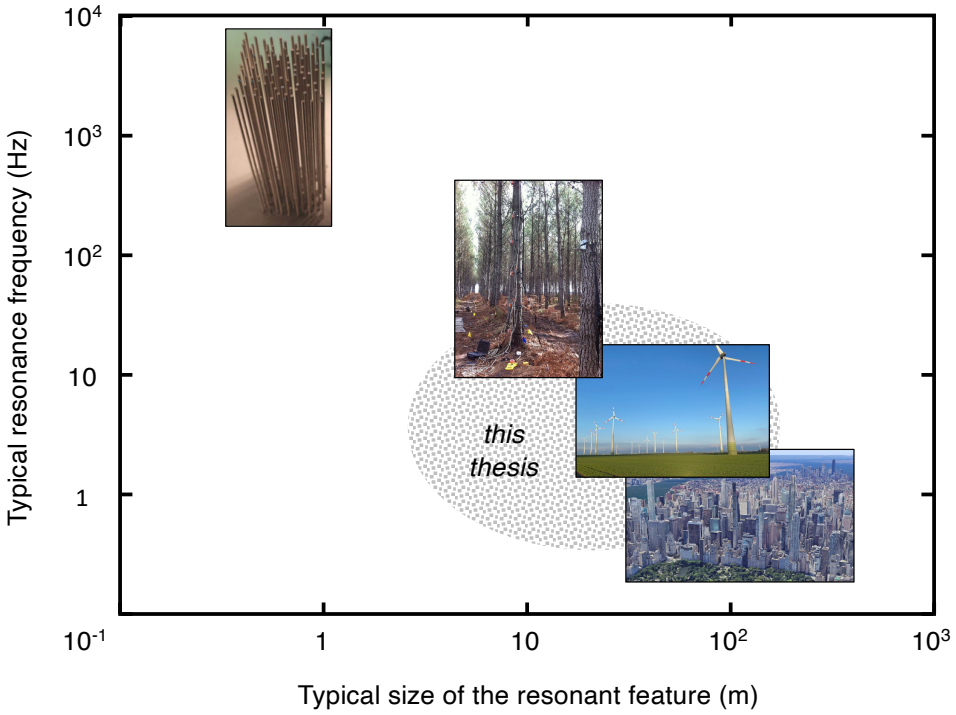


Figure 6: Scalability of elastic metamaterials. Schematic plot showing locally-resonant features like rods on a plate, trees in a forest, wind turbines in a wind farm and buildings in a city that fall several orders apart on the length scale and resonate with frequencies that vary from several kHz down to sub-Hz. The wave propagation in each of these settings can be driven by subwavelength coupled resonances. In this work, focused is placed on the frequencies relevant to seismology.

## 0.5 Thesis organization

This thesis revolves around four main themes or questions that are organized in chapters, connected through the broad idea of seismic metamaterials on the geophysics scale. The first question deals with the theoretical aspect of Rayleigh wave propagation and scattering. The next two questions are related to the experimental investigation of seismic metamaterials. The common approach is based on ambient noise data analysis from dense seismic arrays which also forms the core of this thesis. The forth and final question indirectly contributes to our overarching goal of understanding coupled surface resonators and is tackled by an experimental design to capture soil-structure interaction. Below I synopsize the chapters that follow.

1. Rayleigh wave scattering by shallow buried structures
   We begin in Chapter 1 with a relatively well-studied problem of Rayleigh waves in periodic media. We first recall the vast literature available on this topic before discussing a few theoretical aspects of Rayleigh wave propagation in a layer over half-space medium. This sets the stage not only for this chapter, but also for the whole thesis as we mainly deal with Rayleigh waves. We demonstrate a methodology that can preferentially excite the dominant surface modes in order to study the modal sensitivity to buried inclusion(s). We then verify and execute the proposed approach through direct time-domain

numerical simulations. Using the simulations, we also investigate our hypothesis that clamping a pile inclusion to the half-space can introduce resonances. We conclude Chapter 1 by weighing up the limitations of our methodology and the scattering study.

2. Surface wave propagation in a dense forest of trees
   In Chapter 2, we begin to analyze passive data. We first summarize the literature on locally-resonant subwavelength metamaterials, focusing on the relevant previous studies. We also highlight the benefits of using ambient noise to study azimuthal anisotropy of surface waves. We then describe the pioneering METAFORET experiment and the data acquired during this experiment which we analyze in the remainder of the chapter. Building upon the previous results from this dataset, the first part concerns the spectral properties of the noise recordings. In the second part we describe and implement array processing techniques, applying them to the two dense arrays and show the results of plane-wave beamforming. A discussion on the observed anisotropy concludes the chapter.

3. Surface wave propagation in a dense wind farm
   We extend the results from the forest study to a cluster of wind turbines, which is another setting that more closely resembles a dense urban area. A description of the wind turbine structure and their dynamics is presented with an emphasis on the effect they have on the ground motion. Studies that have analyzed wind turbine emissions are reviewed thoroughly. In Chapter 3 we verify the metamaterial behavior of two different wind turbine configurations, and thus the chapter is organized around these two datasets. Each dataset is analyzed by following a similar systematic approach - a first-order spectral analysis of the noise inside and outside the wind farm is made, followed by an empirical technique to extract information from time-average cross-correlation of noise. The results shown from the second experiment (META-WT project) are based on the Distributed Acoustic Sensing (DAS) data and therefore providing a separate introduction to this acquisition technique is deemed necessary. The overall first results of the META-WT experiment, that have been published are appended to this chapter. A few aspects of this study are ongoing research.

4. Experimental evaluation of Soil-Structure Interaction
   In 2022, I had the opportunity to participate in a field campaign to study the coupling of a simple hybrid steel-concrete structure with the ground. Chapter 4 focuses on the experimental design and data acquisition with 3 different setups of sensors that were deployed in separate stages of the experiment. Such an experiment is interesting for this thesis since metamaterial effects are primarily driven by the efficiency of the coupling between the resonators and the substrate. A brief motivation is presented at the beginning that follows the manuscript of the data article.

The thesis closes with the main conclusions from each study summarized. The outstanding questions from each chapter and the perspectives are presented following the conclusions.

# Chapter 1

# Rayleigh wave scattering by shallow buried structures

**Summary**

We explain the nature of wave propagation in a medium hosting stiff and slender heterogeneity(-ies) buried near the surface using a scattering approach. We interpret the scattering phenomenon of Rayleigh waves when such heterogeneities, called "piles", are clamped at their base, like in geotechnical engineering applications. To achieve this objective, it is argued that in a layered medium, wherein the phenomenon of surface wave propagation is multi-modal, it becomes essential to first decouple the Rayleigh wave modes from themselves, but also from other body waves. Progressively, a methodology is devised to preferentially and effectively excite the two dominant Rayleigh modes observed in a layer over half-space medium. Finally, the modal scattering is numerically quantified directly in the time domain using the spectral element method (SEM) for the single-scatterer and multiple-scatterer cases. The investigation is made for both (i) a half-space (non-dispersive medium), and a (ii) layer over half-space (dispersive medium). Based on this, we see the signature of the pile scatterer, which indicates Mie-like resonances when the pile is clamped to the half-space. At the end of the chapter, we also introduce the scattering matrix (S-matrix) formulation, which relates the incident and scattered Rayleigh modes.

## 1.1 Background

When seismic waves propagating in a homogeneous elastic medium interact with heterogeneities, they can "scatter" in multiple directions with varying amplitudes and phases. The scattering can be strong or weak depending on the impedance mismatch that is introduced and often depending on the size of the heterogeneities they encounter in their path, thus making it frequency dependent. However, it is usually assumed that the inclusion only contributes to the kinematic soil-structure interaction, but it is possible to have a resonant behavior of the inclusion(s). Understanding this involves considering how propagating incident energy is reflected, refracted, or transmitted as it interacts with heterogeneities or subsurface structures. The study of wave scattering in elastic media has found broad applications in the domains of structural health monitoring for the identification of defects, especially in the field of ultrasonics. In geophysics, it has played an important role

because the heterogeneities present in the soils and rocks filter the seismic waves, thus useful in various seismological investigations. In the broad domain of metamaterial physics, research has taken an enormous leap, and now it is possible to tune the characteristics of a medium by engineering structured materials that can scatter electromagnetic, acoustic, and elastic waves in specific and often unusual ways. The manifestations of these phenomena have been harnessed across a spectrum of applications, with particular significance in the realm of elasticity, notably within the field of seismology. In principle, seismic waves can be strongly reflected (shielding) , mode converted (hybridization), or steered (lensing) in particular directions. Seismic risk in cities is connected to seismic waves impacting anthropic constructions. We recall that the overarching objective of this thesis is to understand how seismic surface waves propagate when entering the rather complex near-surface structure modified by urbanism.

### 1.1.1 Wave propagation in media with periodic inclusions

Over the past two decades, researchers have aimed to extend the concepts of metamaterials from the nano-scale to the macro-scale. Photonic crystals have paved the way for the transition of this new physics from electromagnetic to acoustic ('phononic crystals') and seismic waves ('seismic crystals'). These crystals are usually artificial and can vary in size, ranging from a few meters to hundreds of nanometers or even smaller. Bragg scattering is exploited to obtain bandgaps by constructing such periodic structures (usually non-resonant). These concepts have also appealed to the engineering community, where it is particularly important to understand the dynamic behavior of composite materials or obtain shielding from unwanted vibrations. In this thesis, we work in the context of the seismic waves on the geophysics scale. Woods [1968] experimented open trenches for shielding surface waves emitted from a foundation. The same idea of boreholes was later implemented by Meseguer et al. [1999] demonstrating the existence of band gaps for Rayleigh waves for two different hole configurations. The first practical implementation of the concept of a 'seismic crystal' on the geophysics scale was realized by Brûlé et al. [2014] in a soft silty clay soil site near Grenoble, France. The crystal was in the form of a 2D grid of empty boreholes (Fig. 1.1) which strong reflected surface elastic waves around 50 Hz ($\lambda/a = 0.9$, which was not far from the Bragg regime). However, a seismic barrier does not necessarily consist of boreholes or a material softer than soil. Seismic wave cancellation can also be achieved by having heterogenities which are relatively dense and/or stiff compared to the host material. A small part of the transmitting energy is reflected at these heterogenities. Regardless of the inclusion material, the wavelengths scattered would still depend on the spacing between the scatterers. Therefore, the use of construction materials from civil engineering, such as concrete and steel, to structure the soil can be a good way to control seismic surface waves.

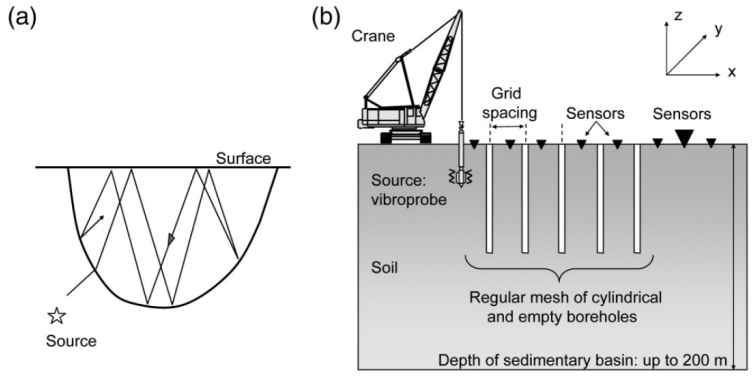


Figure 1.1: (a) Schematics of seismic waves trapped in a basin and (b) the cross section of the experiment done by Brûlé et al. [2014] with a regular mesh of boreholes in the soil, excited by a vibro probe source near the surface. The sensors are distributed within and behind the 2D grid of boreholes.

Pile columns are traditionally employed in geotechnical engineering practices for deep foundations and soil reinforcement. But some early theoretical and numerical studies (Avilés and Sánchez-Sesma [1983, 1988], Xia et al. [2011]) realized that piles can be considered for attenuation of seismic waves by reinforcing softer soil with stiffer columns. Based on the multiple scattering of seismic body and surface waves, these studies explained the effect of various geometrical parameters (pile radius, spacing, length, filling fraction, etc.) with practical recommendations. Various other efforts were made towards developing a seismic barrier design for low-frequency Rayleigh waves in the 5-10 Hz range by seismic trenches or columns of different cross-sections and materials (for example Diatta et al. [2016], Miniaci et al. [2016]). Cylindrical concrete columns embedded in soil (modeled as a thick plate), when arranged in certain configurations can be efficient not only for seismic protection but also cause less disturbance of the wavefield giving good invisibility characteristics. Although most of these studies were based on multiple scattering, a different but a rather common approach to use homogenization was also employed to study such periodic structures.

Homogenization (effective medium) theory is the conventional approach to substitute a micro-structured medium with an effective continuum representation. When dealing with long wavelengths in elastic composite media such as a stiff inclusion embedded in a softer matrix, one can expect varied macroscopic behavior, depending on the contrast of the fiber and the matrix (Auriault and Bonnet [1985], Boutin and Auriault [1993], Boutin and Soubestre [2011], Auriault and Boutin [2012], Soubestre and Boutin [2012], Boutin et al. [2013]). In their pioneering work, Auriault and Bonnet [1985] showed evidence that when contrast is high (two orders of stiffness) with the stiff component connected, the dynamic macroscopic behavior can deviate from classical behavior. For strong contrast, it was demonstrated that the propagation of long wavelengths may match the resonant frequencies of the composite system. Moreover, they use the term “inner resonance” (axial behavior), which can open bandgaps, distinct from those seen due to diffraction in periodic lattices (Auriault and Boutin [2012], Soubestre and Boutin [2012]). This ‘inner

resonance' is synonymous with the more widely used term 'local resonance'. The 'stiff inclusions problem' was also studied experimentally by testing the dynamics of a foam-matrix/steel-beam system (Boutin et al. [2013]). They showed that there exist both homogeneous and inhomogeneous modes of the system when the beam has clamped-free boundary conditions. Another set to recent studies have similarly looked into the effective behavior of an array of elastic inclusions embedded in an elastic matrix using the homogenization process that leads to effective jump conditions, in both cases of non-resonant inclusions ( Marigo et al. [2017]) and resonant inclusions (Pham et al. [2017], Touboul et al. [2020]). By using this approach for a single row of inclusions that have a two order stiffness contrast with the matrix , Pham et al. [2017] found Mie (monopolar) resonances of inclusions, but for quite high frequencies when the wavelength is of the order of the inclusion thickness.

For the specific case of a pile-soil system, researchers have also dealt with such problems in the context of metamaterial physics in a geophysical setting (e.g. Achaoui et al. [2017]). The system considered by Achaoui et al. [2017] has piles embedded in the soft soil and clamped into the bedrock (bottom panel of Fig. 1.2). However, they only consider the Rayleigh-Lamb mode which has no interaction with the bedrock and do not investigate other modes, which can potentially have inhomogeneous kinematics i.e., pile and soil behaving differently. A discussion on possible coupling of resonances of the pile-soil periodic system and the local resonances of the pile has also been made by Brûlé et al. [2017b], **?**. They hint towards the possible effective resonance of the system having a two orders stiffness ratio between the pile and the soil.

### 1.1.2 Motivation and Hypothesis

This work is mainly motivated by the results of the work done during my master's thesis, which was partly on the subject of shielding Rayleigh waves by a pile barrier for gravitational wave observatories (Mohammed and Somala [2019]). Based on the results of full 3D time-domain numerical simulations (Fig. 1.3), it was observed that the presence of a finite 2D array of cylindrical concrete columns anchored in a half-space and buried within a soft shallow soil layer strongly reflects the Rayleigh waves in the layer. This idea was first proposed by Achaoui et al. [2017], showing the emergence of zero-frequency bandgap for clamped piles infinitely periodic in one and two directions. In the master's thesis, the clamped pile problem was not dealt with as rigorously as for the piles buried in a homogeneous half-space; nevertheless, it was quite intriguing. This shielding effect was more pronounced for the vertical component than for the horizontal component. An explanation for this is that the clamping restrains the vertical motion of the pile column more than its horizontal motion.

It is quite clear from the literature that the problem of dynamics of such composite media with buried inclusions has received a lot of attention. While most studies on pile-soil structures have only highlighted the effects of multiple scattering of seismic waves, there are other studies which demonstrate the presence of inner/local resonances in such composite structures when certain conditions are met. Given these findings, we seek to understand the presence of such resonance effects, if any, when a stiff pile is buried in the soil layer and clamped at the base. Since surface waves are guided along the free surface and have the highest sensitivity near to the

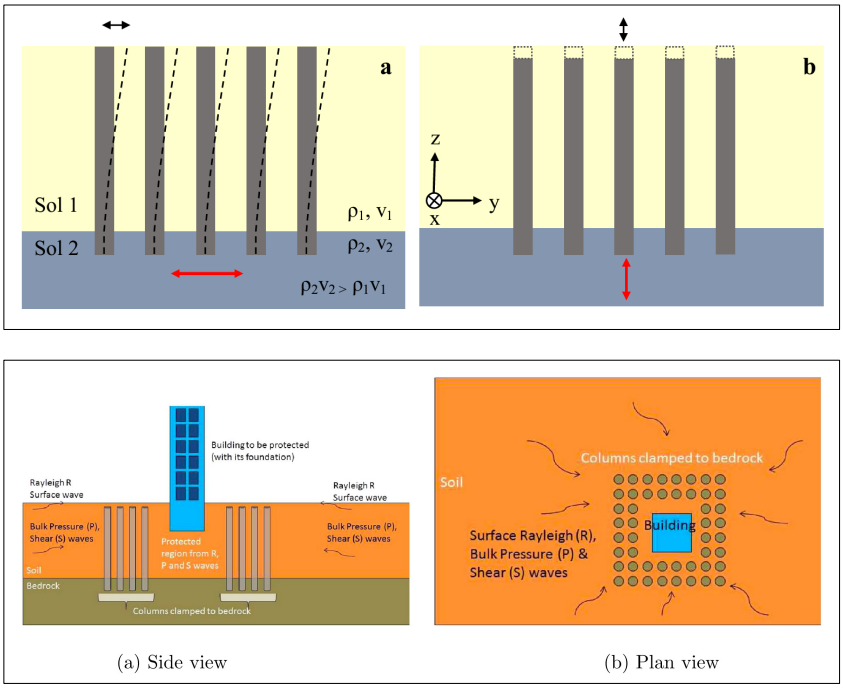


(a) Side view (b) Plan view

Figure 1.2: (Top panel) Schematic view of principle (side view) of vertical columns buried with in a soft soil (soil 1) and clamped within a bedrock (soil 2). These columns can undergo bending (a) and longitudinal (b) motions. The local resonances can create elastic stop bands at low frequencies (i.e., long wavelengths get reflected by arrays of columns with a deeply subwavelength cross section (from Brûlé et al. [2017a]). (Bottom panel) Schematic of a seismic barrier consisting of columns clamped to the bedrock surrounding the building to be protected (from Achaoui et al. [2017]).

surface, they are interesting to perform such an investigation. Thus, building on the results in the literature, we propose investigating the scattering of Rayleigh waves as a result of the periodic pile-soil metamaterial. Measuring the scattering of the Rayleigh waves should give the signature of the metamaterial. If there exist any "local resonances", we should be able to observe them with this approach.

## 1.2 Data-based Mode-selective focusing of Rayleigh waves

Studying the scattering properties of Rayleigh waves due to the metamaterial with piles clamped to the half-space, first requires a good understanding of wave dynamics in the free layer over a half-space (LOH) medium without the pile. Unlike a homogeneous half-space (HHS), a LOH model will have a more complex surface wave propagation. In this section, the importance of considering the higher modes when we have a multi-modal Rayleigh wave propagation is first introduced. Then, to understand the sensitivity of the scatterer or the scattering medium to a particular mode, it is important to effectively and preferentially excite a desired surface

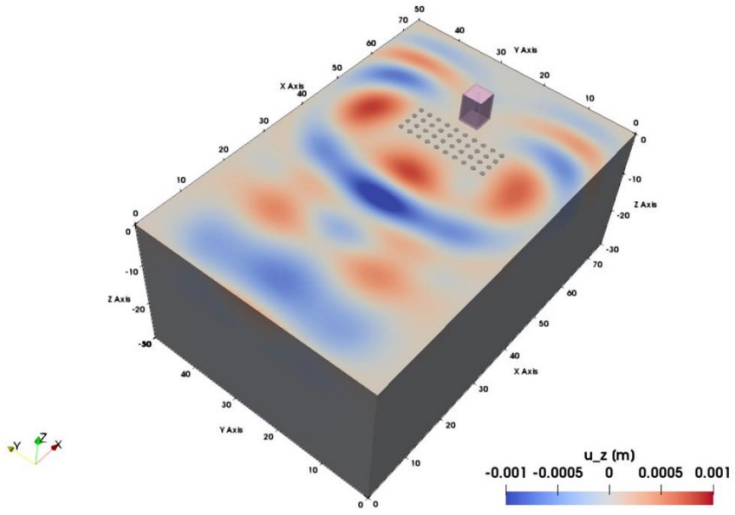


Figure 1.3: Clamped Pile barrier: Snapshot of the surface wavefield for the vertical displacement field from a SPECFEM3D simulation. Surface waves are detoured around the barrier and also strongly reflected off of it (from Mohammed and Somala [2019]).

wave mode. To achieve this objective, we propose a methodology for the filtering and focusing of Rayleigh wave modes using a spatial-temporal time-reversal mirror (Fink [1997]) and phased array excitation in this section.

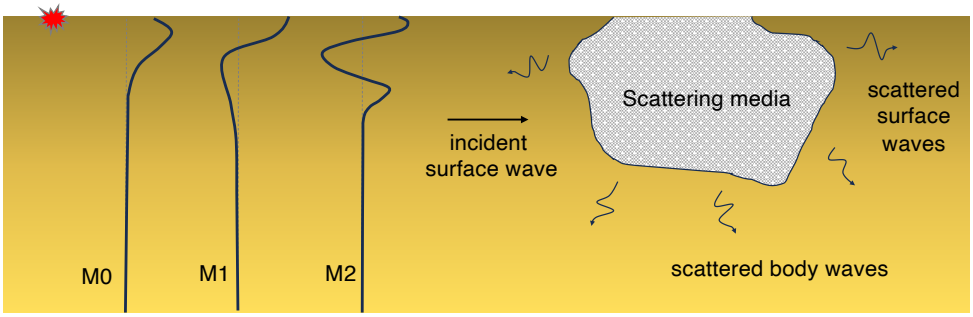


Figure 1.4: Schematic depicting a medium that supports multiple surface modes when excited by a source at the surface. The frequency-dependent modes can scatter in distinct ways, as the modes are depth dependent and can have varying particle motion in the different regimes. In order to understand the sensitivity of the scattering medium to each of the surface modes, it is important to excite them preferentially.

### 1.2.1 Fundamental and Higher order Rayleigh modes in a Layer over Half-space

For our study, we choose an LOH model as shown in Table 1.1. The depth of the layer is 10m, which is considered shallow, yet realistic. In a medium with a shallow

soft layer overlying a bedrock-like stiffer half-space like this, the wave propagation of Rayleigh waves is a multi-modal phenomenon. Surface wave dispersion occurs in vertically stratified media and the dispersion leads to higher-order modes. The propagation behavior of the modes of Rayleigh waves in layered half-spaces is thus frequency-dependent. The shear velocity of the layer and the half-space are the most important parameters. We plot the theoretical dispersion using Herrmann codes (Herrmann [2013]) for the LOH model. At low frequencies, only the fundamental mode exists. The first higher mode has a cut-off at around 9Hz that depends on the depth of the layer and the contrast. Phase velocity approaches shear wave velocity in the half-space for long wavelengths which is evident. The higher modes are faster because they are sensitive to the deeper structure and thus sample more of the half-space. We use another routine from Herrmann [2013] to plot depth-dependent mode shapes for the first two modes (M0 and M1) for the vertical component $u_z$ of Rayleigh waves (Fig. 1.6). At frequency $f = 23Hz$, there exist three modes, but only the first two are shown.

| $i$ | $z_i$ (m) | $\rho_i$ (kg m$^{-3}$) | $V_{p_i}$ (m s$^{-1}$) | $V_{s_i}$ (m s$^{-1}$) | $\nu_i$ | $Q_{\kappa_i}$ | $Q_{\mu_i}$ |
|---|---|---|---|---|---|---|---|
| 1 | 10 | 1800 | 1000 | 350 | 0.43 | 160 | 160 |
| 2 | $\infty$ | 2500 | 3000 | 1800 | 0.219 | 80 | 80 |

Table 1.1: Model LOH (layer over half-space). Properties are chosen such that they are realistic for shallow soil layers. $i$: layer index, $z_i$: depth to bottom of layer, $\rho_i$: mass density, $V_{p_i}$, $V_{s_i}$: velocity of compressional and shear waves, $\nu_i$: Poisson's ratio. $i = 2$ for the elastic half-space. To provide anelastic dissipation in the both the layer and the half-space, quality factors $Q_{\kappa_i}$ & $Q_{\mu_i}$are chosen such that the fundamental and higher modes have the same order of amplitudes.

The impedance of the layers, given by $Z_i = V_{s_i} * \rho_i$, becomes important in a LOH medium for the energy distribution between the fundamental and higher modes. Boaga et al. [2014] quantified the mode contamination as a function of increasing impedance contrast between the layer and the half-space. They found that as the impedance contrast increases, the energy maxima shifts from the fundamental mode to the first higher mode at the osculation point. For our model (Table 1.1), the impedance of the half-space is almost 7 times that of the layer. This can cause a potential mode osculation or "mode kissing", as it was observed in their study for a high impedance contrast between the layer and half-space. Most of the Rayleigh wave dispersion signal is contained in the fundamental mode in such a velocity model. Apart from the impedance contrast, the depth of the source is also a factor in determining the excited surface modes. The deeper the source, the more energy is injected into the higher modes. Although in the study of Achaoui et al. [2017] they use a surface excitation in their model, the underlying bedrock is fixed without any consideration of the higher Rayleigh modes, i.e, the Rayleigh waves do not interact with the bedrock. But in reality low-frequency surface waves do interact with the half-space and propagate dispersively, as can be seen here. Whether these higher modes, which travel close to the speeds of the bedrock, can be shielded by finite number of clamped piles is not known.

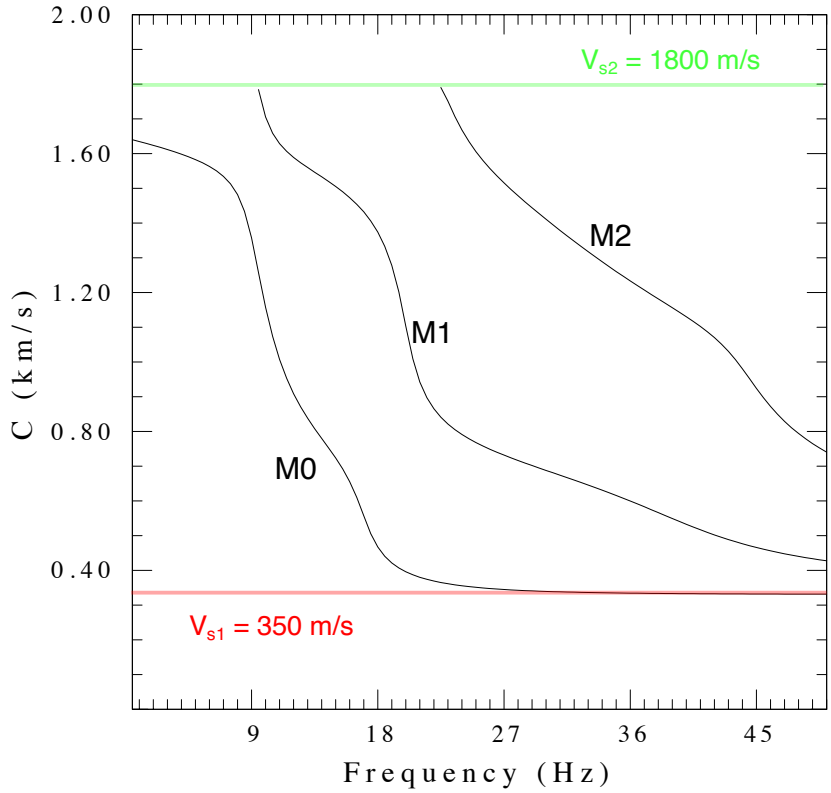


Figure 1.5: Theoretical dispersion curves for the LOH model in Table 1.1 showing the fundamental and first two higher modes. The modes 0 and 1 coexist in the frequency regime 9-22.5 Hz. The dispersion curves are computed by the routine `sdisp96` and plotted using the routine `sdpsrf96`, both provided by Robert B. Hermann available for public download (Herrmann [2013]).

### Peculiarity of the selected velocity model

The dispersion phenomenon in elastic media that has a shallow layer on a substrate extending to infinity has recently been revisited by some researchers (Maznev and Every [2011], Malischewsky et al. [2017], Forbriger et al. [2020]). It has been found that when the layer P-wave velocity approaches three times the S-wave velocity corresponding to a Poisson ratio around 0.44, there is a special effect observed. The dispersion curves for the higher mode become multivalued and can lead to incorrect estimation of the velocity. This special effect is generally seen due to the high contrast between the layer and the underlying substrate. In the demonstration of this effect, the models used in the literature have shear-wave velocity ratios between layer and half-space of different orders, for example, 0.0256, 0.12, 0.07, 0.52. In the model we considered, although the Poisson ratio of the layer is 0.43, which is close to that where this effect is observed, the contrast we have for the layer and the half-space is $\frac{V_{s,layer}}{V_{s,HS}} = 0.19$. In the theoretical dispersion curve from the Herrmann code (Fig. 1.5), the higher-mode curve does not seem to show multivaluedness. However, according to Forbriger et al. [2020], such algorithms miss the phenomenon due to the implicit requirement of single-valuedness of the dispersion relation. We do not perform any further investigation to find if there is indeed any phenomenon that modifies the dispersion relation, because in our method, which is discussed in the

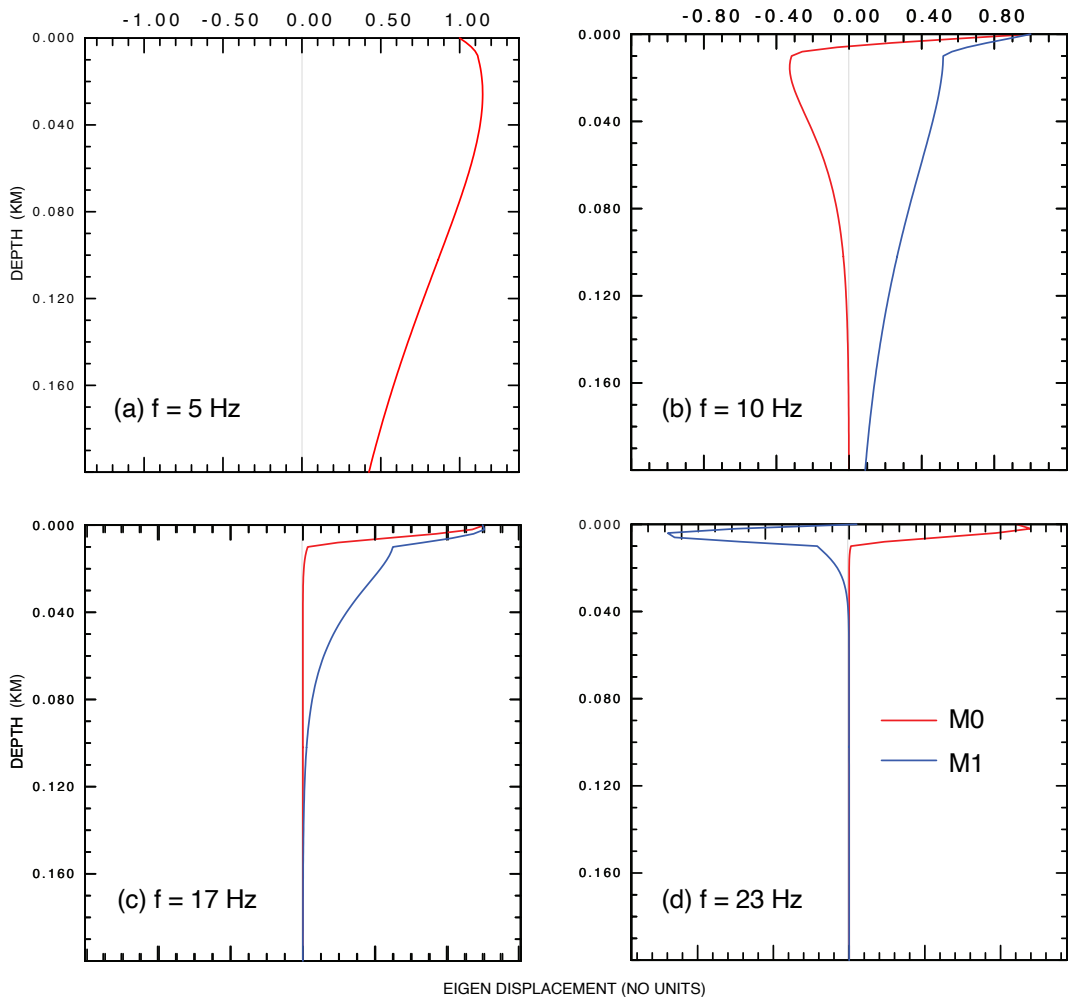


Figure 1.6: Normalized mode shapes at frequencies f = 5, 10, 17 and 23 Hz (a through d), for the fundamental and first higher modes for the LOH medium with properties given in Table 1.1. Note that the first higher mode only exists after the cut-off frequency of ∼9 Hz. The mode shapes are generated by the routines `sdisp96` and `sregn96`, and plotted using the routine `sdpder96`, all provided by Robert B. Hermann available for public download (Herrmann [2013]).

following sections, we deal in the frequency wavenumber $f-k$ space rather than the $C-f$ space. However, this is something that can be looked into if required.

### Remark on the ellipticity of Rayleigh wave modes

The elliptical particle motion of Rayleigh waves can either be retrograde or prograde depending on both the depth in question, the Poisson ratio, or the layering of the materials. A fundamental mode Rayleigh wave cannot have purely horizontal or vertical particle motion in a homogeneous half-space. But when a substrate is added on the top of the half-space we can observe the polarization becoming purely horizontal or vertical at some critical frequencies where the particle motion changes from retrograde to prograde. For a HHS, the ellipticity goes from retrograde to prograde with increasing depth and weakly depends on the frequency. The change in sense is approximately at a depth of $\lambda/5$. However, the dynamics of Rayleigh

wave propagation completely changes when a layer is added on top of the half-space. In terms of ellipticity, Poggi and Fäh [2010], define the frequency-dependent Rayleigh wave particle motion. Similarly, Brule and Erbeja [2022] also shows the same phenomenon for the bilayer medium. The layer depth controls the cutoff period of the first higher mode, which coincides with a rapid increase (over period) in the particle-motion ellipticity or H/V ratio of the fundamental mode. Therefore, particle motions potentially provide a good test to distinguish and separate the fundamental mode from the first higher mode, with the fundamental mode retrograde and the first higher mode having prograde motion in the 1–10 s period of interest. However, because of its strong dependence on numerous parameters, we refrain from employing ellipticity as a means of distinguishing Rayleigh modes.

The synthetics for the individual modes can easily be obtained from the theoretical dispersion curves and depth-dependent eigen functions based on the source and receiver depths. However, in this approach to excite the modes, we use a numerical tool for exciting individual modes and to compute the corresponding scattering. This way we learn how the waves are propagating in the layer and half-space and excite what we want to excite and suppress the rest. Also, the possible peculiar behavior of such a velocity model is another good reason for performing numerical simulations as a check instead of relying on the synthetics from the theoretical dispersion which can sometimes fail in giving the true roots as discussed above.

### 1.2.2 Spectral Element Method

For simulations in the time domain, we choose the open source spectral element code called SPECFEM2D. This code uses the spectral element method (SEM) (Komatitsch and Tromp [1999]) which uses higher-order basis functions ($\mathcal{O} > 4$). It can simulate wave propagation in acoustic, elastic, and poroelastic media with the flexibility of FEM and accuracy of a pseudospectral method. It uses the Gauss-Lobatto-Legendre (GLL) quadrature, which has the beneficial property that the mass matrix obtained is diagonal. SPECFEM uses Newmark's explicit time integration as the time marching scheme. For generating the unstructured conformal quadrilateral or hexahedral meshes for the domains, we use an advanced 2D and 3D mesh generation tool Trelis, now Cubit. It has a powerful Python scripting interface that eventually helped automate the meshing process. The CUBIT generated meshes are exported in a SPECFEM readable format. All simulations are run on a parallel cluster (the Froggy platform of GRICAD Infrastructure at Université Grenoble Alpes). SPECFEM is a heavily parallelized code - all simulations are run in parallel using MPI on 64 CPUs.

The propagation of Rayleigh waves may be satisfactorily treated by a two-dimensional plane strain approximation. Previous numerical studies with different metamaterial configurations have successfully used SEM for example, Colombi et al. [2014, 2015, 2016c], Colquitt et al. [2017], Zaccherini et al. [2020, 2021]. Thus, we reduce the complexity to a 2D half-space and consider a linear, isotropic, and homogeneous viscoelastic medium shown in 1.7. To simulate unbounded media in three directions, we impose Stacey's absorbing boundary conditions on the left, right, and bottom edges whereas the top edge is traction-free. However, from our experience with SPECFEM, these absorbing boundaries are not perfect, and we see reverbera-

tion from the boundaries. Thus, we extend the width of our computational domain on either side to avoid as much as possible the spuriously reflected waves in the physical domain during the simulation. Although SPECFEM2D also has an option to implement CPML absorbing boundary, we do not use this due to instability of the simulations (Martin and Komatitsch [2009]). The material and geometric properties of the system are specified in Table 1.1. The soil-bedrock interface is at a constant depth of 10 m. The mesh consisting of quadrilateral elements is generated by a commercial tool called Trelis, now Cubit. Both the soil and bedrock are modeled as homogeneous viscoelastic layers.

For the simulation, the mesh needs to be set up in such a way that it can spatially resolve the shortest wavelength of interest. The S-wave is the slower body wave and has the shorter wavelength. The Rayleigh wave propagates with a wavelength similar to that of the S wave due to similar speeds. The mesh size is thus defined by this length scale. The other important simulation parameters required to be set are defined in the "Par file" which is an input file for the SPECFEM2D solver. A time step of $10^{-5}s$ is chosen, which is smaller than that suggested by the program, in order to guarantee the stability of the time marching scheme. The time step is dictated by the smallest mesh element size and the fastest wave speed. This is based on the CFL stability condition, $\Delta t < C\min_{\Omega}(h/v)$, where $C$ is the Courant number and $\Omega$ denotes the model space. The variable $h$ depends on the size of the mesh and the number of Gauss-Lobatto-Legendre (GLL) points (in this case, the number of GLL points = 5). The wave speed $v$ is determined based on the P wave speed of the model (the fastest wave speed). For the Newmark's time marching scheme, the CFL bound $C = 0.697$ for elastic media (when $Vp/Vs = \sqrt{2}$). For a viscoelastic simulation as in this case, the CFL bound remains the same because SPECFEM2D employs a rational approximation of $Q(f) =$ constant, which means that there is no effect of attenuation on zero-frequency waves (Blanc et al. [2016]). To simplify the model, we chose the same attenuation values for the P and S waves i.e., $Q_p = Q_s = 160$ for the shallow layer and $Q_p = Q_s = 80$ for the half-space. Since $Q_p$ and $Q_s$ are the same, which implies $Q_\kappa = Q_p = Q_\mu = Q_s$. These quality factors are related by the P and S wave speeds, and for a plane-strain assumption, they are simplified to $Q_p^{-1} = (1 - \frac{V_s^2}{V_p^2})Q_\kappa^{-1} + (\frac{V_s^2}{V_p^2})Q_\mu^{-1}$ and $Q_s^{-1} = Q_\mu^{-1}$. Although it may seem unrealistic, we assign a lower quality factor for the half-space, because it helps in better demonstrating the methodology.

### 1.2.3 Proposed Methodology

In this section, we propose a mode-selective focusing algorithm to filter the modes and excite them separately with the help of numerical simulations. Selective focusing techniques Tanter et al. [2000, 2001], Aubry et al. [2001]) using time-reversal mirrors (TRM) have been well demonstrated for ultrasonic waves in acoustics (Prada et al. [1996], Mordant et al. [1999]. In principle, a source placed at the surface generates seismic waves which are recorded by a surface array (acting as the 'mirror'). Subsequently, traces are time-reversed and back propagated from their original receiver positions to be recorded, not only at the at the original source location, but also on the nearby positions. This is interesting to study, for example, the modal insulation capabilities of a metamaterial. In a sandbox experiment with periodic rigid mass scatterers, Mora et al. [2021] used line sources at different depths with a chosen

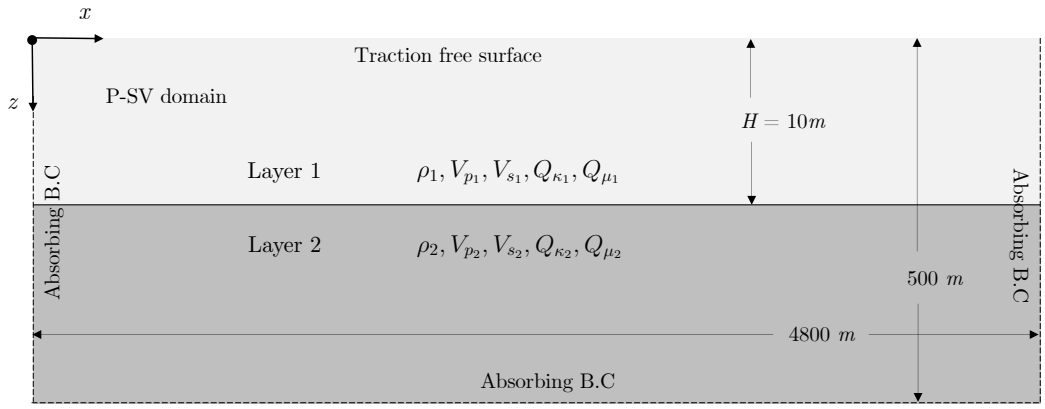


Figure 1.7: The 2D computational domain (P-SV) of the layer over half-space (LOH) model in Table 1.1. Stacey absorbing boundary conditions are applied on the left, right and bottom of the domain, whereas the top surface is traction free.

in-plane polarization, to selectively excite the first three modes to match the mode shapes.

**Remark on initial unsuccessful attempts to focus Rayleigh wave modes**

Exploiting the non-identical depth dependence of Rayleigh wave modes, we initially attempted to focus the modes in a LOH medium by two different approaches, (a) amplitude modulation, and (b) both amplitude and phase modulation. We try to separate the modes with a vertical line array (VLA) of sources placed in the depth direction and a horizontal receiver array on the surface as explained by Walker et al. [2005] for mode focusing in a shallow ocean waveguide (acoustic data). Eventually, these initial attempts brought us to two important conclusions:

1. The Rayleigh modes are more sensitive to the time delay (phase) compared to the depth-dependent eigen function (amplitude), and

2. Separation of modes in wavenumber space achieved with this source-receiver array configuration is not satisfactory.

We now describe the methodology that works better than the above two approaches - configuration of evenly distributed sources and receivers placed on the surface of an LOH medium, as in Fig. 1.8. We consider $\mathbf{N}$ uniformly-spaced sources and an equal number of uniformly-spaced receivers, symmetrically placed over the surface of a LOH medium (Fig. 1.8). We choose, $\mathbf{N} = 201$, with an inter-source and inter-receiver spacing of $\Delta\mathbf{x} = 4$m. The array aperture of 800 meters should be sufficient to accurately measure long wavelengths, which are related to the transmission of low frequency components, and provides an excellent resolution in the wavenumber domain ($\Delta k \approx 2.45 * 10^{-4}\mathrm{m}^{-1}$). The spacing between adjacent sources and adjacent receivers, $\Delta\mathbf{x}$, is adequate to reliably sample shorter wavelengths (up to 8m), which is associated with the propagation of higher frequencies (up to ∼43.5 Hz). According to the Shannon–Nyquist sampling theorem, signals with wavelength $\lambda < 2\Delta\mathbf{x}$ or $\lambda < 8$m will be spatially aliased. The upper limit for the longest wavelength $\lambda_{max}$ that can be resolved by the receiver array is approximately equal to the aperture $R$. The array behaves like a single station for signals with $\lambda \gg R$. The

source and receiver arrays (i.e., the last source and the first receiver) are separated by a lateral distance of 800 m ($D = R$) which we consider to be in the far-field regime for the lowest frequency of interest ($D \gg \lambda$).

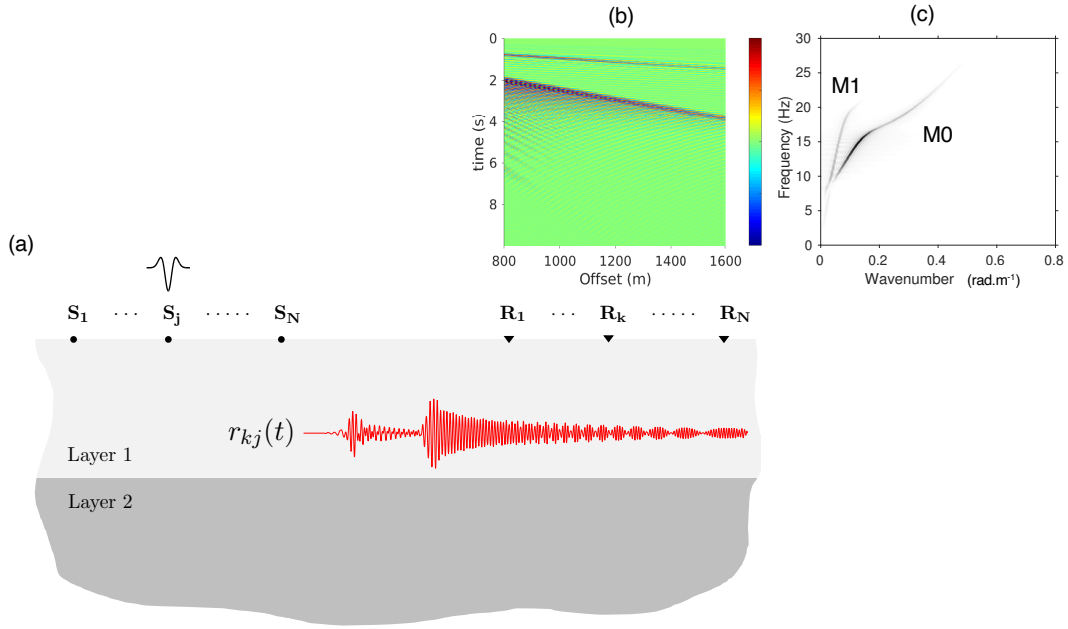


Figure 1.8: (a) The sagittal plane (P-SV domain) comprising the symmetric source-receiver array configuration over the surface of the layer overlying a half-space model. The Green's function $r_{kj}(t)$ for a Ricker source $\mathbf{S_j}$ and receiver $\mathbf{R_k}$. (b) $x$–$t$ representation of the vertical displacement field $u_z$ for the source excited at position $x = x_j$ (linear color bar, normalized amplitude). (c) f-k transform of the vertical displacement field gives the dispersion plot in which the Rayleigh wave fundamental and first higher mode branches are clearly seen as distinct and localized dark curves.

The proposed method involves a combination of masking the individual modes in the frequency-wavenumber representation of the excited full wavefield and a subsequent backpropagation of the modes to excite it with a phased array. Therefore we break down this method into a four-step process, between excitation of the overlapping modes and the obtaining the final focused modes: (1) Pulse excitation, (2) Mode selection, (3) Back propagation of the selected mode, and (4) Phased array excitation for mode focusing.

### 1. Excitation of Rayleigh waves: Forward propagation step

In this first step, the aim is to excite all sources $\mathbf{S_j}$ where $j \in 1$ to $\mathbf{N}$ and receive the signals at each of the receivers $\mathbf{R_k}$ where $k \in 1$ to $\mathbf{N}$. The reason for choosing a symmetric source-receiver array will be evident in the following steps of the methodology. Taking advantage of the range independent medium, we only run a single simulation with one source and $2\mathbf{N}-1$ receivers, as if the sources and receivers span a range aperture of 800 m each at the surface. Thus, when the layer is excited by a single source, one can efficiently obtain the $\mathbf{N}^2$ number of required Green's functions-$\mathbf{r}_{kj}(t)$.

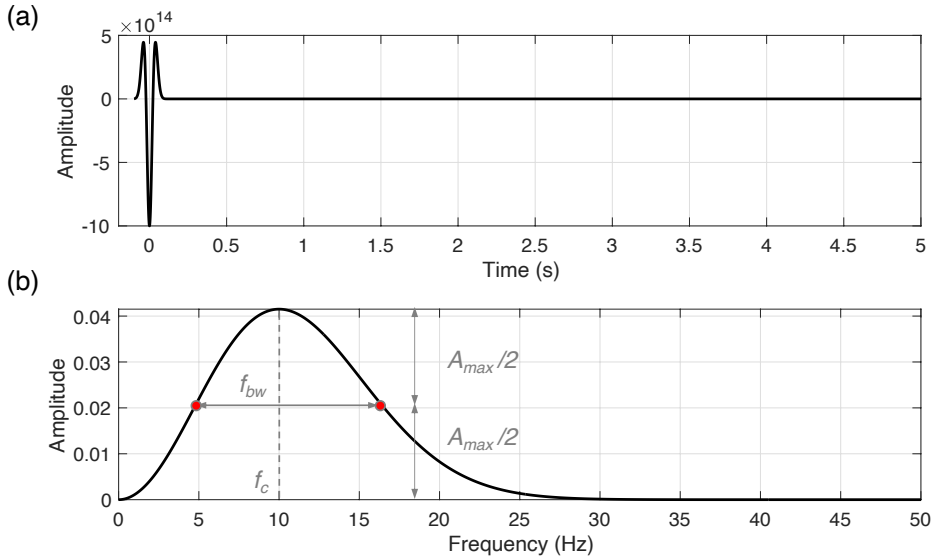


Figure 1.9: (a) Source-time function for the point force to excite Rayleigh waves in SPECFEM2D: Ricker wavelet centered around $f_c = 10$Hz in time domain given by the function, $Ricker(t) = (1 - 2\pi^2 f_c^2 t^2)e^{-\pi^2 f_c^2 t^2}$ (b) The bandwidth of the source is defined by the width of the spectrum at the half amplitude point for the frequency $f_c$. The Fourier transform is thus $\frac{1}{2}\frac{\sqrt{\pi}\omega^2}{(\pi^2 f_c^2)^{3/2}} e^{-\frac{\omega^2}{4\pi^2 f_c^2}}$ .

Once the viscoelastic material properties and simulation parameters are set, we illuminate the LOH medium with a vertical point source on the surface. We use a broadband Ricker pulse (Komatitsch and Tromp [1999]) centered at 10 Hz, applied vertically on the free surface (Fig 1.9) to excite the LOH medium. We expect the P-waves, SV waves and Rayleigh waves, to be radiated from the point source, in that order of arrival at the receiver array (Fig. 1.11(a)). The body wave energy, as expected, is much lower compared to the Rayleigh waves and have first arrivals. The Rayleigh wavetrain has superimposed fundamental and higher mode which are separated due to the different speed of propagation. Thus, more is the lateral separation of the source and receiver arrays, the more easily it is to distinguish between Rayleigh modes are separated in time due to their different speeds. We observe beating of the fundamental mode due to multiple reflections at the interface of the layers, thereby trapping most of the energy in the shallow layer. The higher mode Rayleigh waves sample the half-space deeper than the fundamental mode, and by adjusting the quality factors the Rayleigh waves excited by a surface source we ensure that both modes have the same order of amplitudes to aid in the demonstration of this methodology. Thus, in this way, by exciting the medium by a single source we have obtained the Green's function $r_{kj}(t)$ for all the source-receiver pairs. The 2D-FFT of the vertical displacement field collected at the receiver array i.e., $\hat{r}_{kp}(k, f)$ reveals the two dominant Rayleigh wave mode branches in the frequency-wavenumber domain as expected (Fig. 1.8(b)). Since here, we are interested in the propagation of the Ricker wavelet centered around 10Hz, and having a bandwidth of ∼11.48 Hz (Fig. 1.9(b)), we can expect that only the first two modes will be excited. Moreover, since the peak energy is below cutoff for the second higher mode (≈ 23Hz), this mode will only be weakly excited. Thus, in the remainder of this chapter, we refer to the first

higher mode as the higher mode.

### 2. Mode Separation

For a frequency–wavenumber ($f$–$k$) transform of the time-range ($x-t$) data, the wavenumber resolution is determined by the array length: the longer the array, the better the resolution in $k-$space and the lower the minimum observable wavenumber. For the LOH earth model chosen in our numerical experiments, the modes are dispersed and localized in the frequency-wavenumber ($f-k$) domain (Fig. 1.10). Thus, it becomes possible to isolate the modes and work with them individually (Walker et al. [2005]). For the isolation of modes, we define a primary source $\mathbf{S_p}$ acting at source position, $p$. In our case, we choose the source closest to the receiver array i.e., $\mathbf{S_N}$, as our primary source. The aim of this primary source is to act like the reference for the selection of mode, and the backpropagation of the selected mode, which is explained in the following step. The f-k dispersion plot of the vertical displacement field for this source excitation has two dominant mode branches: the fundamental and the first higher mode (Fig. 1.10(a)). The modes are relatively well separated, although there remains some interference between different mode branches, particularly around the fundamental resonance frequency of the layer $f^0_{SH} = V_{s,layer}/4H = 8.75$ Hz. Around this frequency, the fundamental mode Rayleigh wave motion will be predominantly horizontal (Poggi and Fäh [2010]), thus disappears in the vertical displacement component. Even below this frequency, there seems to be quite low energy of the fundamental mode branch. From the theoretical dispersion (Fig. 1.5), we know that the first mode has a cut-off around 9 Hz. The second higher mode exists only after 23 Hz, but is weakly excited because of the source being at the surface and the source frequency bandwidth. In the example here, we manually apply a mask to filter the first higher mode and only retain the fundamental mode (Fig. 1.10(b)). Note that the mask is traversed around the distinct, localized curvilinear region of the fundamental mode between 9Hz and 28Hz, since the two modes overlap in this frequency range. The mask is a boxcar filter in both f and k dimensions of the 2D transform, thus we have the weight 1 inside and 0 outside the mask region. Indeed, a better choice would have been to use a Hanning window, or a Butterworth filter to have even smoother filtering. The 2D Inverse Fourier Transform gives the virtual trace $r^{(m)}_{kp}(t)$ where m=0, corresponding to the clean fundamental mode at each receiver. The signals for the clean higher mode can be obtained in a similar manner.

$$r_{kp}(x,t) \overset{\mathcal{F}}{\leftrightarrow} \hat{r}_{kp}(f,k) \xrightarrow[(m)]{mask} \hat{r}^{(m)}_{kp}(f,k) \overset{\mathcal{F}^{-1}}{\leftrightarrow} r^{(m)}_{kp}(x,t) \tag{1.1}$$

### 3. Back Propagation of the isolated mode

The clean mode signals can be time-reversed and back propagated to the source positions by performing a convolution with the Green's functions obtained in the first step. Due to reciprocity, the Green's functions from the receiver to the source array remain unchanged i.e., $r_{kj}(t) = r_{jk}(t)$. The roles of the source and receiver arrays are swapped i.e., the receiver array acts like a source array and vice versa. Equation (1.2) describes the process of back propagation which is focusing on the source array. The effect of this back propagation of an isolated mode is such that its

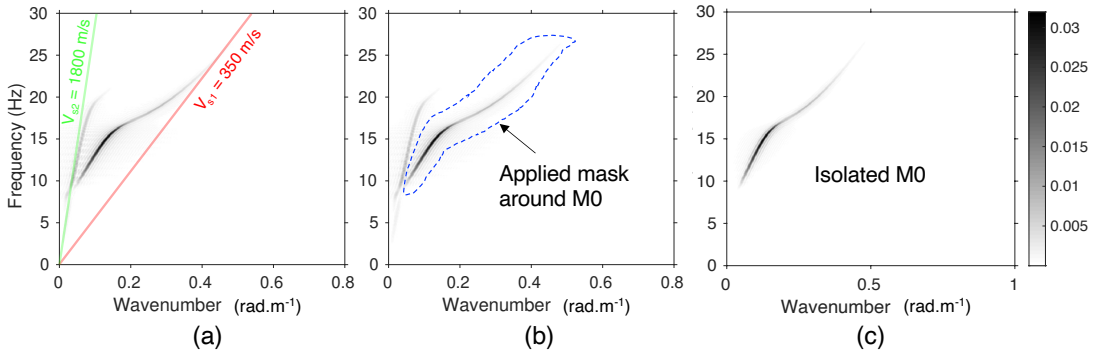


Figure 1.10: Mode Isolation: (a) Propagating modes appear as localized dark curves in the frequency-wavenumber (f-k) domain, (b) the bounding curve in blue shows the mask applied to the fundamental mode, and (c) the retained fundamental mode, respectively. The filter is a boxcar function with weight 1 inside and 0 outside the mask. The 2D inverse Fourier transform of panel (c) gives the signals corresponding to the clean fundamental mode.

effective excitation at the source array is much greater than the effective excitation of the other mode.

$$F^{(m)}_{j,x=x_p}(t) = \sum_k r^{(m)}_{kp}(-t) * r_{kj}(t) \quad \text{where, } (j,k) \in \ [1 \text{ N}] \tag{1.2}$$

### 4. Phased Array Excitation

The back propagated signals obtained in the previous step can now be used to excite the medium with a phased array antenna from the source positions $\mathbf{S_1}$ to $\mathbf{S_N}$ as shown in Figure 1.11. The waves superimpose and effectively result in a single mode excitation at the receiver array. For the fundamental mode, this works well as seen in the frequency-wavenumber domain in Figure 1.11(c). However, the higher frequencies are highly attenuated and only the lower frequency components are retained. This could be due to the fact that we use a boxcar function in the mode filtering step. If we filter a signal in the frequency domain using a boxcar function, whose impulse response in the time domain would be a sinc-like function, is a low-pass filter. In addition to this, the superimposed surface waves from the N sources is producing waves that are trapped in the layer having energy in a narrow frequency band. As the phased wave propagates, the amplitude of a the seismic wave decays, the peak frequency shifts towards the lower frequencies, and the width of the wavelet broadens. On the other hand, the phased array excitation of the first higher mode at the source array has resulted in a relatively strong first mode accompanied by a weaker fundamental mode, which pollutes the pure higher mode signals at the receiver array (Figure 1.11(e,f)). This can be attributed to the cleaning process with the manual application of the mask, which is never perfect close to the 10 Hz frequency where the mode branches are not well separated in the k-space. Iteratively exciting the higher mode does not change the energy partition of modes in the $f - k$ domain.

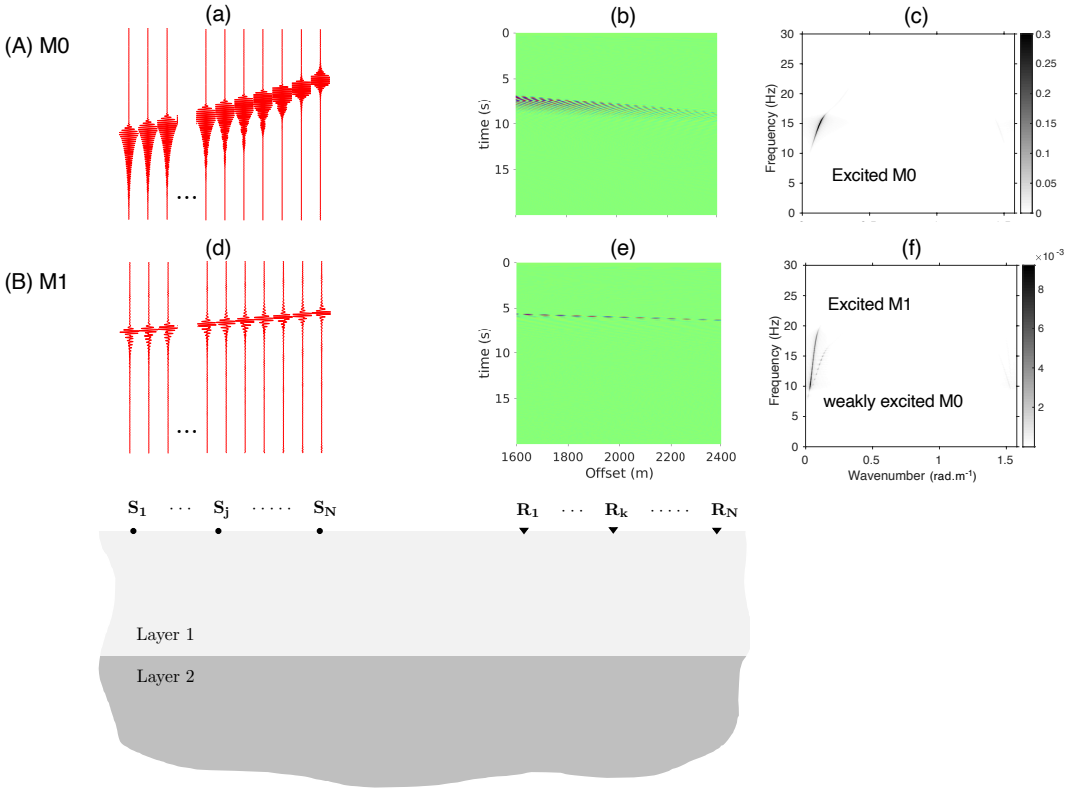


Figure 1.11: Phased source array for mode focusing: Input signals corresponding to the back propagated fundamental mode (panel. a) and first higher mode (panel d) applied at source positions $S_1$ to $S_N$ resulting in the vertical displacement field $u_z$ (panels b and e). The $f$–$k$ dispersion plots show that the fundamental mode is retrieved without any pollution of higher mode (panel c) whereas the higher mode is accompanied by a weakly excited fundamental mode (panel f).

## 1.3 Deducing Single-Pile and Multiple-Pile Scattering from Rayleigh Modal Excitation

In this section, we apply the methodology described in 1.2.3 to a medium with buried stiff and slender heterogeneity(-ies). A perturbation of the medium, for example, by such buried finite heterogeneity that act as secondary sources, generates scattered waves. The heterogeneity in our case is a stiff vertical pile that has been buried in the soil near the surface. Such rigid pile columns are commonly employed in geotechnical engineering for reinforcing compressible soils, or as deep foundations of civil engineering structures. The pile has a regular shape in 2D, having the dimensions $a$ x $h$. The notation used for the lateral dimension of the pile, $a$, should not be confused with that generally used for denoting Bloch periodicity in metamaterial physics, also referred to as the lattice constant in solid state physics. The spacing between adjacent piles is denoted as, $l$ for the multiple pile case, whereas the pile vertical dimension is denoted by $h$. All of these quantities are constant throughout our analysis and are given in Table 1.3. The pile is assumed to be perfectly bonded to its surrounding soil.

| Pile dimension | Value (m) |
|---|---|
| Width, $a$ | 1 |
| Depth, $h$ | 11 |
| Spacing, $l$ | 2 |

Table 1.2: Geometrical properties of the pile scatterer

### Scattering cross-section

At this point, we define a fundamental quantity of interest in scattering experiments, called the scattering cross-section ($\sigma$). It quantifies the strength of the scatterer, or the ability of a scatterer to modify the incident wave. In 3D it's a surface, but in 2D, the cross-section is a distance. The greater the SCS, the stronger the scatterer.

The classical scattering theory introduces the concept of scattering cross-section ($\sigma$) which is mathematically defined as the differential scattering cross-section of the object or volume, integrated over all solid angles. At any pulsation $\omega$ and solid angle $\phi$,

$$\frac{d\sigma}{d\phi} = \left|f(\omega,\phi)\right|^2 \tag{1.3}$$

$$\sigma(\phi) = \int_0^{2\pi} \left|f(\omega,\phi)\right|^2 d\phi \tag{1.4}$$

The differential scattering cross-section in eq. 1.3 is essentially the ratio of the free-field scattered power of the waves per unit solid angle in a specified direction to the intensity of the incident propagating plane wave. The complex function $f(\omega,\phi)$, called the scattering amplitude, describes how the waves are scattered in different directions for various frequencies. The units are that of area.

### Remark on scattering in 2D vs 3D

The right hand term in the equation 1.4 for the scattering cross sections in 2D is different from the corresponding term in 3D, since the solid angle $\phi$ is only limited to two discrete values. In a P-SV domain, this reduces to the discrete sum of the two possible directions, forward ($\phi = 0$) and backward ($\phi = \pi$) and the units would have the dimension of length. This will lead to an overestimation of the scattering cross-section, in the sense that the scattering is restricted to the plane. In this study, we are more interested in the differential scattering cross-section for the **forward scattered Rayleigh wave** or commonly referred to as the diffracted field in acoustics. Scattering hereon refers to forward scattering, since we are more interested in the scattered wave after the pile(s). However, the scattering cross sections for scatterers that are analogous in 2D and 3D can show some differences. In the remainder of the chapter we sometimes loosely use the term 'scattering cross-section' for the differential scattering cross-section and not for the total cross-section.

The key parameter in the physical description of scattering is the normalized quantity $ka$, wave number $k$ multiplied by the characteristic dimension $a$ of heterogeneities. Classically we can demarcate the scattering phenomenon into three distinct regimes: (1) the Rayleigh regime ($ka \ll 1$), the intermediary or stochastic

regime ($ka \approx$ or $< 1$)and the high frequency regime ($ka \gg 1$). The scattering cross-section. In the scenario where the the waves encounter small size heterogeneities (compared to the wavelength), the scattering behavior can be described by Rayleigh scattering. The limiting value of the scattering cross-section scales as $k^4$ for the classical Rayleigh scattering limit, which has been observed in various domains of wave physics. The intermediate regime is where the most interesting physics is expected for the pile scatterer(s) when the size of the scatterer is still sub-wavelength. We limit ourselves to these two regimes and the regime beyond the Bragg limit is not in the scope of this work. The purpose of the present study is not to offer an extensive characterization of scattering cross-sections for various pile configurations, but rather to examine the general behavior of a cross-section by treating a few important scenarios which can help explain the fundamental physics.

### 1.3.1 Scattering in a Homogeneous Half-space

A key question is to understand what information can be retrieved from the observation of a single scatterer, and before studying a group of scatterers with effective properties. In order to explain scattering, it is necessary to first identify a reference medium in which an unperturbed wave propagates. Moreover, a reference medium also helps in distinguishing the attenuation of the Rayleigh wave from the pile barrier from the intrinsic attenuation of the material itself. We consider a homogeneous half-space having the material properties used for the shallow layer in the previous sections (Table 1.1). A homogeneous half-space is a non-dispersive medium and can only support the fundamental Rayleigh mode apart from the body waves. We should be able to separate this fundamental Rayleigh mode from the body waves using the same methodology described in the 1.2.3. This may seem an overkill and unnecessary, but is done for the reason of consistency. The non-dispersive branch of the Rayleigh wave is isolated in the $f - k$ domain and backpropagated using a time-reversal mirror. The excitation of the fundamental mode Rayleigh wave is achieved by a phased array as shown in Fig. 1.12(a,c).

We start by considering the scattering properties of one scatterer, $n = 1$. The pile is placed mid-way between the two symmetric arrays. We insonify the pile with incident waves over a broad frequency range in order to cover different scattering regimes. This requires broadband sources, in order to construct the scattering cross-section up to the highest frequency of interest. We find that using three Ricker sources centered at 5 Hz, 20 Hz and 50 Hz separately, sufficiently illuminates the pile with a broad range of frequencies (up to $\lambda/a = 5$).

From the simulations in time-domain, we obtained on the receiver array to the right,

- the reference field: $u_{z,0}(t, \phi = 0°)$ for the case without the pile, and
- the transmitted field: $u_{z,p}(t, \phi = 0°)$ for the case with the pile.

By subtracting the reference field from the transmitted field, we can obtain the exact scattered field, which is essentially the (fictive) wave re-radiated by the pile $u_{z,sc}(t, \phi = 0°)$. The nearest receiver was always greater than 380m away from the pile scatterer. Thus, the scattered signals can be considered as "far-field" signatures of the scatterer, traveling at least 5 to 10 wavelengths after the pile (for all frequencies having a wavenumber $k > 0.013$ to $0.026$).

For computing the scattering cross-section of the pile, the angular intensity of the re-emitted wave in the forward direction is normalized by the angular intensity of the reference wave (Larose [2006]) as shown in Eq. 1.5.

$$\frac{d\sigma}{d\phi}(\omega, \phi = 0^{\circ}) = \frac{\left|U_{sc}(\omega, \phi = 0^{\circ})\right|^2}{\left|U_0(\omega, \phi = 0^{\circ}\right|^2} = \frac{\left|\mathcal{F}\{u_{z,p}(t, \phi = 0^{\circ}) - u_{z,0}(t, \phi = 0^{\circ})\}\right|^2}{\left|\mathcal{F}\{u_{z,0}(t, \phi = 0^{\circ})\}\right|^2} \quad (1.5)$$

It is important to remark that for the denominator in the equation, we chose the reference field instead of the incident field before impinging on the pile, so that the effect of intrinsic attenuation of the medium is canceled out. That means that the attenuation effect is compensated for by measuring both the reference and scattered fields at the same receiver array. In this study, we only consider the vertical component of the Rayleigh wave $u_z(t)$, but similar results are expected for the horizontal component $u_x(t)$ because in a homogeneous half-space, the Rayleigh wave motion is always elliptical.

We repeat the same exercise for the case where $n = 11$. The scattering cross section is plotted in Fig. 1.12 (b) for a single pile and for a group of 11 piles in Fig. 1.12 (d). The x-axis of the plot is the normalized quantity $ka$, where $k$ is the wavenumber and $a$ is the pile width. For the case of a single pile, the scattering cross-section shows an exponential increase with no peaks in the Mie regime. This was expected since the pile behaves more or less like a rigid heterogeneity in the whole regime, although it is elastic. However, we expect that the scattering behavior of the pile should be different in a higher frequency regime. When considering an ensemble of piles ($n = 11$), the strongest forward scattering of the fundamental Rayleigh mode occurs when $ka = 0.09$ or $\lambda/a \approx 11$ for this particular configuration of the pile group. The subsequent drop in differential SCS indicates that more and more energy is being backscattered as the wavelength becomes smaller. Eventually, for a frequency at which the pile spacing is whole factor of the wavelength, i.e., $l \approx \lambda/2$ or at $ka = 0.25$ in our pile arrangement, we expect a complete reflection of the waves. This is because, for the multiple-pile case, the combined result of a large number of scattering events (secondary and higher order scattering effects) produces a standing wave that does not propagate through the medium owing to the destructive interference of incident and reflected waves. This is typical of Bragg scattering, a well known phenomenon. Beyond the Bragg limit, we expect the scattering cross-section to increase again. However, in our experiment, we do not excite this frequency, which is also not the primary interest of this study.

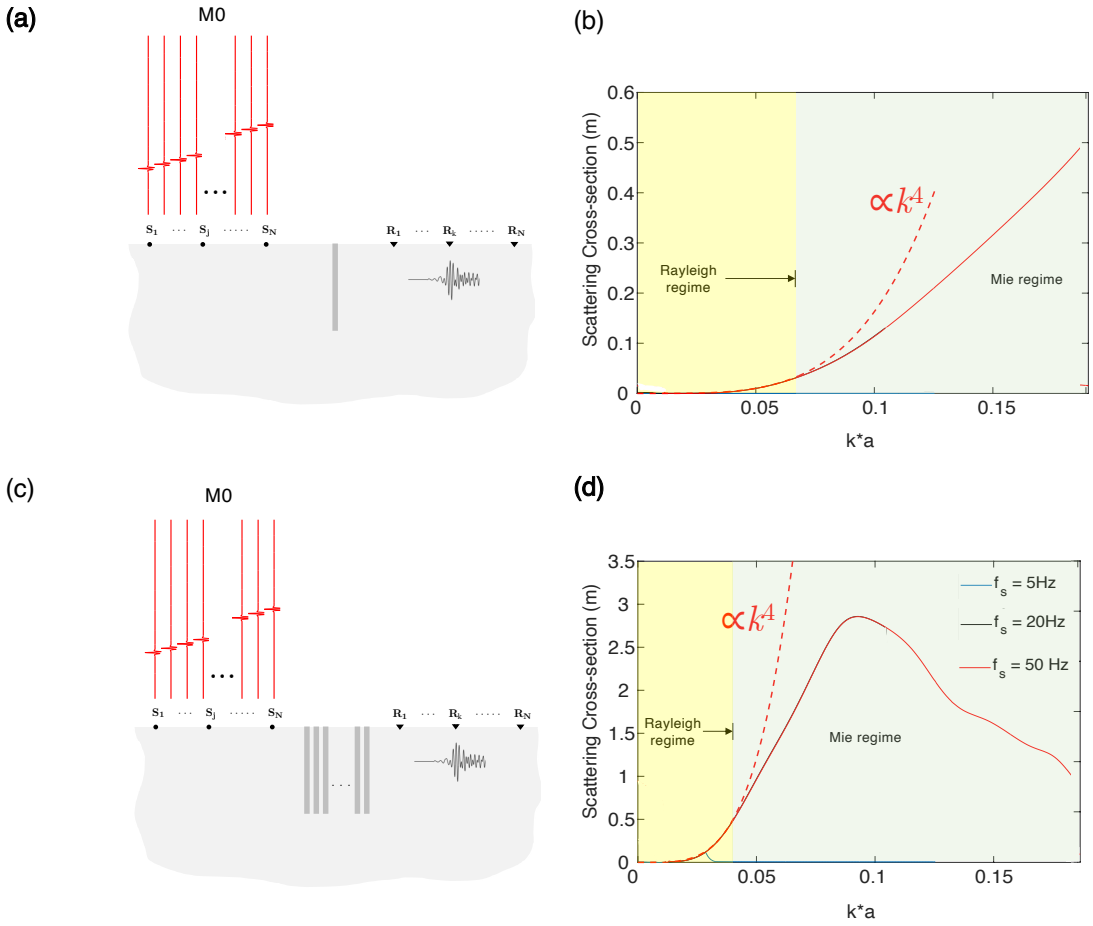


Figure 1.12: (a,c) Setup of the numerical experiment to insonify the fundamental Rayleigh wave mode in single-pile and multiple-pile configurations. (b,d) The differential scattering cross-sections $\frac{d\sigma}{d\phi}(\omega, \phi = 0°)$ for the vertical component fundamental mode Rayleigh wave versus the normalized parameter $ka$, where $k$ is the wavenumber and $a$ is the pile width. The cross-section has units of length in 2D. The dashed red curve shows the fourth power scaling of the wave number $k$, indicating the limit of Rayleigh regime of scattering to its left, indicated by the (yellow shaded region) and the Mie regime to the right (green shaded region).

We would now like to see the relative scattering amplitudes for the cases when $n = 1$ (single-pile) and $n = 11$ (multiple-pile). To do that, we take a ratio of the scattering coefficients, which is simply the ratio of the Fourier amplitudes of the scattered fields for $n = 11$ and $n = 1$ . Interestingly, in the long wavelength limit (quasi-static) $\lambda/a > 90$ and in the Mie regime $\lambda/a < 23$, the ratio of the scattering coefficient drops below the 'pile factor' i.e., ratio of the number of piles in the multiple-pile case to the single-pile case (i.e., $Ratio < 11$) - seen in Fig. 1.13. Between these two limits, i.e., in the majority of the Rayleigh regime, when $23 < \lambda/a < 90$, the $Ratio > 11$ and it peaks when $\lambda/a = 50$. It is interesting to note that the ratio crosses the pile factor (which is equal to 11 in this case) exactly near the boundary of Rayleigh and Mie scattering regimes. There is a need to perform a parametric study to conclude if this hold good for varying pile spacing in a homogeneous half-space.

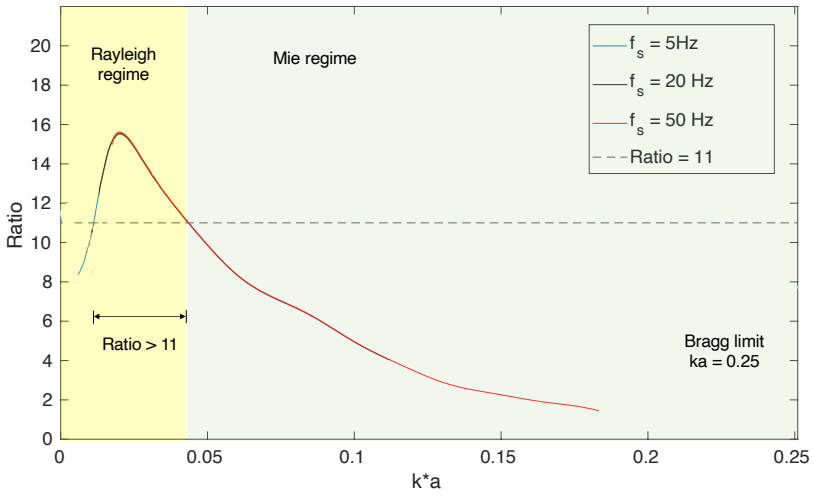


Figure 1.13: Variation of the ratio of scattering coefficients in the multiple-pile to the single-pile configuration with the normalized parameter $ka$. Note that the ratio drops below the pile factor (11 in this case), exactly at the boundary of the Rayleigh and Mie scattering regimes.

### 1.3.2 Scattering in a Layer over Half-space

An important question to be answered is how would the signature of the buried pile change when it is clamped at its base. To do that we have to introduce the pile in a layer over Half-space (LOH) medium with the same model geometry as shown in Fig. 1.7. This allows us to anchor the base of the pile to the half-space. In order to have an efficient exchange of energy between the buried piles and the supporting medium i.e., the half-space, we provide a perfect impedance match by assigning the same material properties for the half-space as those of the pile. While having a layer itself adds an unavoidable complexity to the problem, having to deal with parameters of two different material instead of three, seems a favorable choice. Moreover, eliminating any biases and second order effects of having an impedance mismatch between the potential resonator and substrate, makes it easier to interpret the resonance effects, if any.

The methodology followed in 1.2.3 has resulted in the excitation of a clean fundamental Rayleigh mode (Fig. 1.11(c)). However, the bandwidth of the excited waves was restricted to the 11-16 Hz band. On the other hand, in the process of retrieving the higher mode, we obtain a signal polluted by the fundamental mode (Fig. 1.11(f)). This complicates the process of the modal excitation and can give an incorrect estimate of the scattering cross-section. Thus we simply use a single Ricker source on the surface to insonify the clamped pile. The layer and half-space are modeled as perfectly elastic, i.e., without attenuation. This allows maximum energy to propagate as a fundamental mode Rayleigh wave. However, the pile can still scatter the energy spreading onto several modes. This mode cross-coupling needs to be taken into account. In a P-SV domain, we are restricted to only P-waves, S-waves, and Rayleigh waves, but in a full 3D case, we can also have conversion to the out-of-plane Love waves (not in the scope of this work). In this thesis, we limit our calculation to the differential cross-section of scattered fundamental Rayleigh

mode due to itself, $\left(\frac{d\sigma}{d\phi}\right)_{R0-R0}$.

To perform the numerical experiment, we insonify the pile with a Ricker sources having a center frequency of 10 Hz (Fig. 1.14(a)). The scattered field received at the array on the right is treated by spatially averaging the spectral amplitudes. This corresponds to the full Rayleigh wave which we approximate as the fundamental mode. Depending on the dispersion of the fundamental mode in the reference medium, we extract all wavenumbers by mapping them to each individual frequency. We then use this wavenumber (corresponding to the fundamental mode) in the computation of the frequency-dependent scattering cross section, just like in the case of a homogeneous half-space. As seen in Fig. 1.14(b), after the low-frequency Rayleigh regime ($\propto$ k$^4$), the curve shows rapid fluctuations. Ignoring the initial instabilities in scattering cross-section caused by the highly fluctuating intensity of the scattered field in the layer, we observe a strong peak at around $ka = 0.032$. This is analogous to the classical Mie-like resonances as seen in particle physics or acoustics. Beyond the strong resonance peak, the scattering cross-section appears to become more stable.

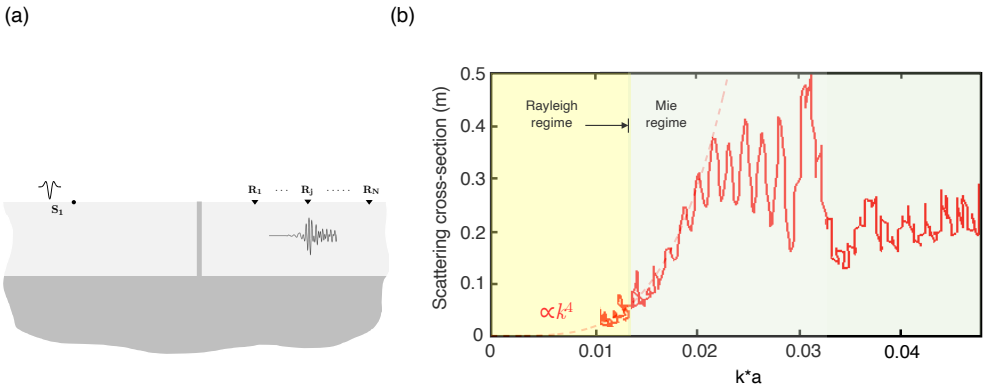


Figure 1.14: (a) Setup for the scattering numerical experiment for the single pile that is clamped to the half-space and insonified with a Ricker pulse centered at 10 Hz. (b) The differential scattering cross-section $\frac{d\sigma}{d\phi}(\omega, \phi = 0°)$ for the fundamental Rayleigh wave mode versus the normalized parameter $ka$, where $k$ is the wavenumber and $a$ is the pile width. The x-axis is irregularly spaced as a result of the mapping of frequency to wavenumber using the actual dispersion curve of the fundamental mode. The dashed red curve shows the fourth power scaling of the wave number $k$, indicating the limit of Rayleigh regime of scattering to its left, indicated by the yellow shaded region, and the Mie regime to the right, green shaded region. The strong peak in the Mie scattering regime at $ka = 0.032$ denotes the pile signature indicating a resonance.

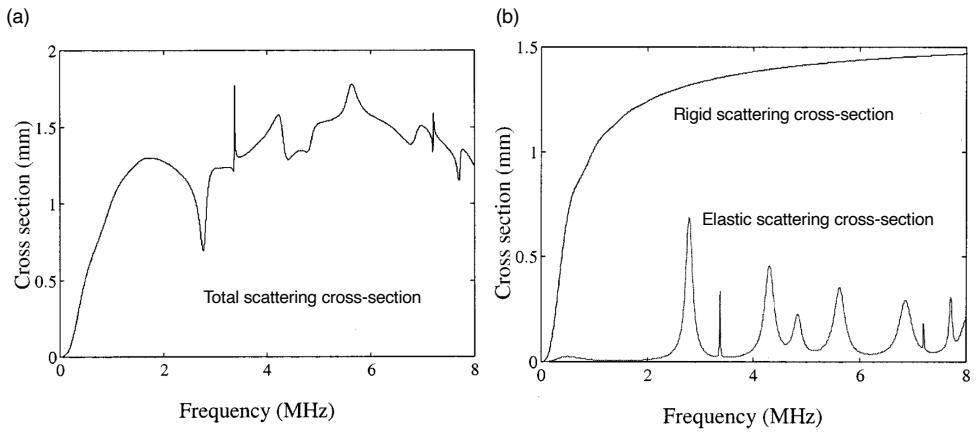


Figure 1.15: (a) Total scattering cross-section and, (b) Rigid and elastic scattering cross-sections versus frequency, for a single cylindrical steel rod with diameter 0.8 mm, $V_p = 5.7km/s, V_s = 3km/s, \rho = 7.8$ immersed in water (adapted from Derode et al. [2001])

### 1.3.3 Discussion

#### Resonance of a single clamped pile

One should be careful while interpreting the resonances because these can manifest as dips in the total scattering cross-section, instead of peaks, due to the interference between the contribution from rigid body motion of the pile and the discrete resonances (see, for example, the theoretical study of Derode et al. [2001]). The plotted curve in Fig. 1.14 is the total scattering cross-section which is essentially be received as the sum of the rigid and the elastic scattering cross sections, but with a phase shift between the two. In the acoustics analogue, for a single rod-like scatterer immersed in water studied by Derode et al. [2001], shows a dip in the total scattering cross-section at the resonance frequency of the steel rod (Fig. 1.15). This can happen when the scattered waves re-radiated by the steel cylinder in water (or by the pile in the soil layer) are out-of-phase with the rigid scattering cross-section term. Similarly, if the pile is a resonator, the phase of the field in the pile shifts abruptly from 0 to $\pi$ near the resonance frequency. The pile can be imagined as a secondary source emitting dipole radiation at the connection with the half-space when in flexion and monopole radiation when in compression. This can potentially interfere more efficiently with the higher mode(s) which is relatively more sensitive to the half-space at the higher frequencies and can give another picture by interacting with the scatters in a different way as compared to the fundamental mode, for example, see mode shape at 23 Hz in Fig. 1.6. At a given frequency, if these scattered modes can contribute simultaneously and either constructively or destructively to the scattering process, one could drastically change the scattering cross-section of a sub-wavelength resonant scatterer, which can be verified in a future study.

#### What prediction can be made in the case of multiple clamped piles?

The scattering from one pile resonator has allowed us to understand the individual response of the clamped pile under the excitation of the Rayleigh wave fundamental

mode. This can then be easily extended to multiple-pile scattering. One can predict the macroscopic behavior of the transverse motion of such a periodic pile-soil system (statics) using the theory developed in Boutin and Soubestre [2011] based on dimensional analysis and the asymptotic homogenization method. The behavior is mainly driven by the contrast of shear moduli between the matrix $\mu_m$ and the inclusion $\mu_p$ as compared to the order of the period slenderness for the unit cell, $\varepsilon = l/L$, i.e., ratio of the period $l$ and the characteristic dimension along the beam axis $L$. For the periodic pile-soil system considered in this study, $\frac{\mu_m}{\mu_p} = \frac{0.22*10^9 \text{ Pa}}{8.1*10^9 \text{ Pa}} = 0.027$ and $\varepsilon = l/L = 2/10 = 0.04$. Thus, $\mu_m/\mu_p = \mathcal{O}(\varepsilon^2)$ and therefore should behave as a fully coupled system between the beam behavior of the pile and the shear behavior of the soil in a static (and quasi-static) consideration. In a dynamic consideration (Soubestre and Boutin [2012]), the behavior of such a pile-soil system can be again predicted based on the same two-order stiffness contrast. Using the same relation, $\mu_m/\mu_p = \mathcal{O}(\varepsilon^2)$, the two modes - transverse (horizontal) and axial (vertical) deformations - can show different dynamics from the usual composites. Moreover, the frequency ranges associated with, what they call, "inner resonance" (axial compression mode) is predicted to one order higher than the one at "inner bending" (transverse mode). Hence, the order of magnitude of scattering frequencies should eventually depend on the propagation mode. These ideas were a perspective of the work done by Achaoui et al. [2017] and the corresponding patent Antonakakis et al. [2023], which is quite interesting in the context of seismic metamaterials. At the edge of the zero frequency bandgap in that study, the shear-dominated mode means that the pile-soil medium effectively has inner bending at these low frequencies, but should have other interesting dynamics, like inner resonance at higher frequencies.

It is crucial to note that we cannot conclusively characterize the bandgaps associated with this metamaterial unless we perform scattering measurements for the multiple-clamped pile system, which shall be looked into in a later study. However, it is evident that the frequencies at which we detect the Mie-like resonances of an individual pile are distinct from (i) the low frequencies associated with Rayleigh scattering, where local dynamic effects are absent, and (ii) the high frequencies associated with Bragg interference, which occur when the wavelengths are similar to the period size $l$.

### Scattering Matrix

To provide a complete description of the scatterer, one needs to consider all possible wave types, modal order, and azimuthal order. However, since our aim is to study the Rayleigh wave scattering, we have restricted ourselves to the P-SV plane for convenience. The full description of the scatterer thus reduces to Rayleigh wave modes and two scattering directions (forward and backward). Assuming that there are only two dominant Rayleigh modes as in this study, we can imagine a scattering matrix, also called the S matrix (Williams et al. [2015]) that can relate the incident and the scattered field. Although in the theoretical study of plates and rods, this is more straightforward to compute, in the case of a half-space performing numerical simulations is more convenient. It is important to note that we are more interested in evaluating the scattered field rather than the transmitted field as in the literature. We first want to evaluate the scattering amplitudes of the two dominant scattering modes in a layer over a half-space by insonifying the scatterer with each

mode separately by applying the methodology explained in 1.2.3. The scatterer, for example, can be a buried column or a resonator attached to the surface, or any other heterogeneity.

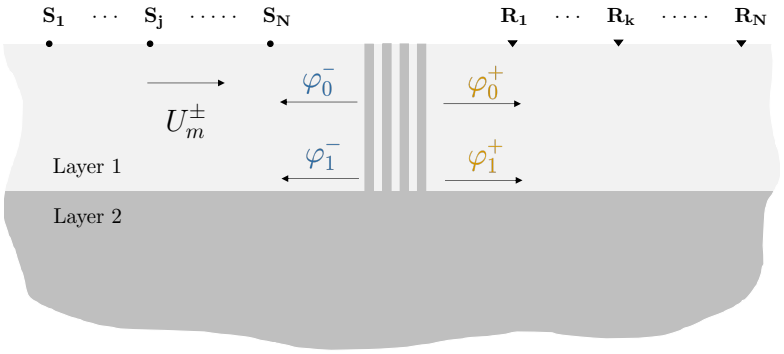


Figure 1.16: Scattering Matrix formulation: A layer over half-space (LOH) medium with a set of scatterers. The modal excitation can be performed by a phased source array on the left and the incoming and outgoing fields can be measured by an array of receivers on the two sides of the scatterers in the far-field. The four modal fields, either mode-preserving or mode-converting, $\varphi_{0,1}^{\pm}$ can be obtained by taking a 2D $f-k$ transform of the wavefield.

Consider a 2D medium where it is possible to measure the incoming and outgoing fields for the reference and the scattering medium. Fig. 1.16 shows the four scattered fields for the two dominant modes that can result from the modal excitation of a scattering medium. For example, a scattering medium insonified by a fundamental mode amplitude $U_0^+$ can produce: (1) a forward scattered fundamental mode of amplitude $\varphi_0^+ = \mathrm{S}_{00}^+\ \mathrm{U}_0^+$ (where $\mathrm{S}_{00}^+$ is the scattering coefficient), (2) a forward scattered first higher mode of amplitude $\varphi_1^+ = \mathrm{S}_{10}^+\ \mathrm{U}_0^+$ (where $\mathrm{S}_{10}^+$ is the fundamental to first higher mode coupling scattering coefficient), (3) a back scattered fundamental mode of amplitude $\varphi_0^- = \mathrm{S}_{00}^-\ \mathrm{U}_0^+$, and (4) a back scattered first higher mode of amplitude $\varphi_1^- = \mathrm{S}_{10}^-\ \mathrm{U}_0^+$.

Furthermore, the incident first higher mode also produces similarly four junction events, that are either mode-preserving or mode-converting, but with different forward and back scattering coefficients. There will be a linear dependence of the scattered mode amplitude and the amplitude of the incident mode. Thus we can populate the S-matrix as in Eq. 1.6 with scattering coefficients, based on the various possible mode conversions in the two directions. We impose a symmetrical system i.e., the scattering coefficients are determined by the direction of the incident wave field in relation to the scatterer(s), but remain the same irrespective of which direction they are entering from.

$$\begin{bmatrix} \varphi_0^+ \\ \varphi_0^- \\ \varphi_1^+ \\ \varphi_1^- \end{bmatrix} = \begin{bmatrix} S_{00}^+ & S_{00}^- & S_{01}^+ & S_{01}^- \\ S_{00}^- & S_{00}^+ & S_{01}^- & S_{01}^+ \\ S_{10}^+ & S_{10}^- & S_{11}^+ & S_{11}^- \\ S_{10}^- & S_{10}^+ & S_{11}^- & S_{11}^+ \end{bmatrix} \begin{bmatrix} U_0^+ \\ U_0^- \\ U_1^+ \\ U_1^- \end{bmatrix} \tag{1.6}$$

$$\varphi(\omega) = \mathbf{S}(\omega)\ U(\omega)$$

The order of the scattering depends on the dominant modes in the LOH medium and can be scaled with the number of modes $N$. For two dominant modes, we have the S-matrix of size 2Nx2N.

## 1.4 Limitations of this study

To describe the limitations of the study, it is appropriate to first describe the limitations of the proposed methodology for the Rayleigh wave mode focusing.

**Limitations of the method used**

1. The mode isolation works well when the modes are well-localized in the $f-k$ domain. However, when there is mode crossing or when the modes are too close to each other in $f-k$ space, it becomes difficult to apply a mask to perfectly isolate the modes. This is strongly dependent on the layer depth and material contrast, but also depends on how well the array is able to resolve the signals in the wavenumber domain. Thus, the range aperture of the receiver array becomes important to be able to properly apply a mask.

2. Choice of the filter function: The $f-k$ mask itself should be a smooth filter instead of the boxcar function we use in our study. We suggest a Hanning filter to obtain better results. The smoother filter function should definitely improve the quality of the back propagated signals, and thus the excited modes.

3. The source bandwidth of the Ricker source is limited for a single central frequency. Instead, a sharp pulse in time that will have a broad frequency response can be used. Also, a flat chirp can be used for the excitation of the medium so that the bandwidth is sufficient to excite all desired modes. This will also ensure that the frequencies are all equally excited without any bias. This will not change the scattering coefficients or the scattering cross-sections, but will simply prevent from re-running the simulations with multiple Ricker sources.

4. Although the obtained k-resolution with 201 sources and receivers with 4m spacing was excellent, the number of sources (and receivers) was not optimized. That is to say that the least number of array points for sources (and receivers) with the given spacing, needed for satisfactory focusing the modes in the LOH medium were not explicitly computed.

Now, the main drawbacks of the scattering study are enumerated here,

**Drawbacks of the scattering study**

1. The contact between the pile and the surrounding soil layer is perfect i.e., no sliding allowed. In reality, this is far from true, and composites whose inclusions are not in perfect contact with the surrounding 'matrix' can exist. This

imperfect contact condition should be accounted for; by introducing elastic or visco-elastic interface laws using a suitable modeling technique - for example, via Kelvin–Voigt contact condition (also recommended by Boutin et al. [2013], Achaoui et al. [2017]). The 'weakly bonded' imperfect interfaces will have an effect on the resonances of both the inclusions and the matrix.

2. In an LOH medium, surface wave mode conversion can occur and different cross-sections must be considered. In the case of incident Rayleigh fundamental mode, they can be denoted as $\sigma_{R0\rightarrow R0}, \sigma_{R0\rightarrow R1}$, respectively for the fundamental to itself, and fundamental to first higher mode. In this study, we only calculated the $\sigma_{R0\rightarrow R0}$, which is not the full scattering description of this pile scatterer.

3. A parametric study is mandatory to comprehensively understand the scattering behavior of a clamped pile system. However, this study employs full time-domain Spectral element simulations for every single case which requires at least $\sim$ 768 CPU hours when taken together with the dense 2D mesh necessary in the upper layer and the pile region. If we consider changing the parameters of the pile geometry: width, height (depth of layer), and spacing, along with the perturbation of the material parameters like velocity and impedance of the pile, each with say 5 variations, we would end up requiring at least 768 ${}^5P_5$ or 92160 CPU hours on a well optimized machine. Thus, this time requirement makes the simulations computationally expensive. A study that can dedicate such required time and resources, should be able to fully link the chosen parameters to the effective scattering properties of the clamped pile system.

4. In a medium with 1D arrangement of scatterers, i.e, for $D = 1$, the wave can only be scattered in the forward or backward directions $\phi = 0$ and $\phi = \pi$, but for $D > 1$ the Rayleigh waves can be scattered in a much more unrestrained way (Bostock [1991]). This increase in dimensionality will also give rise to SH waves. However, to study the incidence of the Love and Rayleigh waves separately, it will not be required to use the methodology proposed here, because they will not be recorded on the same component i.e., P-SV (in-plane) and SH (out-of-plane). Nevertheless, we can now expect the conversion of incident Rayleigh modes not only to other Rayleigh modes but also Love modes. Even though we only considered the simplest case of a 1D scattering, the concepts in our approach and the main results should still be valid in a 2D array of piles. In fact, the physics associated should be even more interesting since for those dimensionalities and not only the scattering cross-section of the resonators, but also the unit cell symmetry of the medium will play an important role in the dispersive properties of the effective medium. Finally, it is necessary to study the limitations of this 2-D approach and to see if they are excluding any significant scattering mechanisms compared to 3D. This will make it necessary to run some fully 3D models.

## 1.5 Concluding remarks

In this chapter, we ask an important question: Does a soil medium containing clamped pile inclusions behave as a resonant metamaterial distinct from the well-understood Bragg scattering observed at higher frequencies? We proposed a methodology to demonstrate the focusing of the Rayleigh wave modes in a layer over half-space medium using a combination of mode masking, time-reversal mirror and phased array excitation. Using this proposed method, the scattering of the fundamental mode Rayleigh wave in a homogeneous half-space with single and multiple buried piles was analyzed. The scattering cross-section has provided a more nuanced understanding of the scattering behavior, indicating that the scattering is mostly of rigid nature. We found that the ratio of scattering coefficients of multiple-pile and single-pile cases, can also be helpful in distinguishing between the Rayleigh and Mie scattering regimes of classical physics. When we introduce a half-space to clamp the pile, Mie-like resonances were identified in the lower frequencies. Whether a series of such resonant clamped piles can create stop bands is yet to be explored.

**Acknowledgment**

*All (or most of) the computations presented in this chapter were performed using the Froggy platform of the GRICAD infrastructure (https://gricad.univ-grenoble-alpes.fr), which is supported by the Rhône-Alpes region (GRANT CPER07_13 CIRA), the OSUG@2020 labex (reference ANR10 LABX56) and the Equip@Meso project (reference ANR-10-EQPX-29-01) of the programme Investissements d'Avenir supervised by the Agence Nationale pour la Recherche.*

# Chapter 2

# Surface wave propagation in a dense forest of trees

**Summary**

This chapter focuses on the ability of an array of trees to modify surface wave propagation in a forest. We analyze passive data from two dense array deployments of (i) ∼1000 vertical component geophones and (ii) 100 three-component geophones, which partially cover the forest and extend into a canola field. Initially, we look at the dynamics of the tree resonators. Specifically, we link the tree resonances with the spectral properties of the passive recordings in the forest and the field. We build on previous studies to further improve our understanding of the frequency bandgaps corresponding to flexural and longitudinal tree resonances. The surface waves radiated by the trees through their longitudinal resonances are found to be evanescent. We then shift our focus to array processing, specifically plane wave beamforming (related to wave phase), to quantify the azimuthal anisotropy of surface waves. We analyze continuous ambient noise recordings for 9 days and nights. A strong Rayleigh wave azimuthal anisotropy was observed inside the forest, showing a cos $2\theta$ variation with a fast axis oriented in the 45° direction with the array. This result is consistent over a broad frequency range and stable over the entire period. The Love wave anisotropy is not well constrained due to a smaller 3C array and inadequate illumination from the ambient noise. When trying to interpret the combined results obtained from the two dense arrays, we present various possible physical origins for the observed anisotropy.

## 2.1 Background

The concept of *locally-resonant* metamaterials have attracted a lot of attention in recent years, due to their ability to manipulate seismic waves and, more specifically, surface waves. The advantage of the locally-resonant mechanism of achieving wave control is in its deep sub-wavelength character, i.e. the spacing between the resonant features can be much smaller than the wavelength $a \ll \lambda$ (at least an order less than the wavelength). The effective properties of such a medium, which was initially conceptualized by Veselago [1968], arise from the resonant characteristics of its sub-wavelength unit cell. The formation of such bandgaps at much lower frequencies compared to Bragg mirrors, was demonstrated in the GHz frequency regime with

resonant pillars of micrometer scale unit cells by Khelif et al. [2010], Achaoui et al. [2011]. Experimental realization at the lab scale with a set of rods attached to a plate has explained the physics coupling Lamb waves with multi-resonators. Formation of wide band gaps and other interesting physics has been observed when $A_0$ Lamb waves in the kHz regime interact with the flexural and compression resonances of the centimeter scale rods/beams (Rupin et al. [2014, 2015], Lott et al. [2020b], Lott and Roux [2021]). Colquitt et al. [2017] analytically constructed the dispersion curves for a 1D array of resonators on a plate, using a scalar approach and a full-wave approach. The latter makes the dispersion curve more complicated because the flexural resonances are considered along with the compressional resonances. They see the bending and anti-bending branches for the dispersion around the rod resonances, which was also seen in the experiments. The three main conclusions from the lab experiments were that (1) the beams acting as coupled resonators for the beam-plate system strongly degenerate the free plate response, (2) the two resonance modes of the beam differently affect the system - the compression is monopolar having a low Q-factor while the flexural is dipolar having a high Q-factor, and (3) in the bandgap, the two resonances couple, resulting in leakage and a strong coupling of the beams.

For the case of a half-space to which resonators are attached, there is a similar slowdown of the waves near the rod resonance frequency $\omega_0$ as shown in the schematic of Fig.2.1 (a). The hybridization mechanism that creates bandgaps for elastic waves propagating in both a plate and a half-space is analogous, but the waves are constrained in the plate, whereas there can be leakage into the half-space (conversion of surface waves to bulk waves). In principle, these waves are distinct from the usual Rayleigh waves that exist on free surfaces and are referred to as the Rayleigh-Bloch waves in the literature (Porter and Evans [1999], Colquitt et al. [2015, 2017]), because they arise as a consequence of the periodicity of the array present on the surface. The dispersion characteristics can be further modified by having a graded resonator design (array of rods with decreasing or increasing height) for both the plate (Colombi et al. [2015]) and half-space (Colombi et al. [2016a]). In case of seismic waves, in order to modify the incoming Rayleigh waves, the individual units of the seismic metamaterial can contain resonating structures coupled to the ground. This is called a *'metasurface'*, because the resonators are either attached over the ground surface (Colombi et al. [2016c]) or buried in the soil close to the surface (Palermo et al. [2016]) so that a strong interaction with the surface waves is achieved. This collective interaction can result in the waves being attenuated either by diverting them into the bulk or by locally trapping them inside the metamaterial, by creating a 'seismic wedge' (Colombi et al. [2016a]). However, the arrangement of these individual resonant units does not necessarily need to be spatially periodic, since resonances drive the bandgaps, unlike periodic composite materials, where the bandgap is driven by an interference effect only as seen in the Bragg effect (Kaina et al. [2013a], Colombi et al. [2014]). This was demonstrated by Kaina et al. [2013b] in the context of electromagnetic metamaterials and by Rupin et al. [2014], Colombi et al. [2014], Lott and Roux [2021] for elastic metamaterials with a random arrangement of beam attached to the plate. It is the impedance ratio between the resonators and the substrate, the spatial density of resonators and the quality factor of the resonators that decide the efficiency of the bandgap. The extent of the bandgap is driven by the distance between the resonance and anti-resonance frequencies. The physics of locally-resonant metasurfaces have not

only been demonstrated experimentally at the lab scale (Colombi et al. [2017a]) but also at the geophysical scale (Colombi et al. [2016c], Roux et al. [2018], Lott et al. [2020a]), which is discussed in the following section.

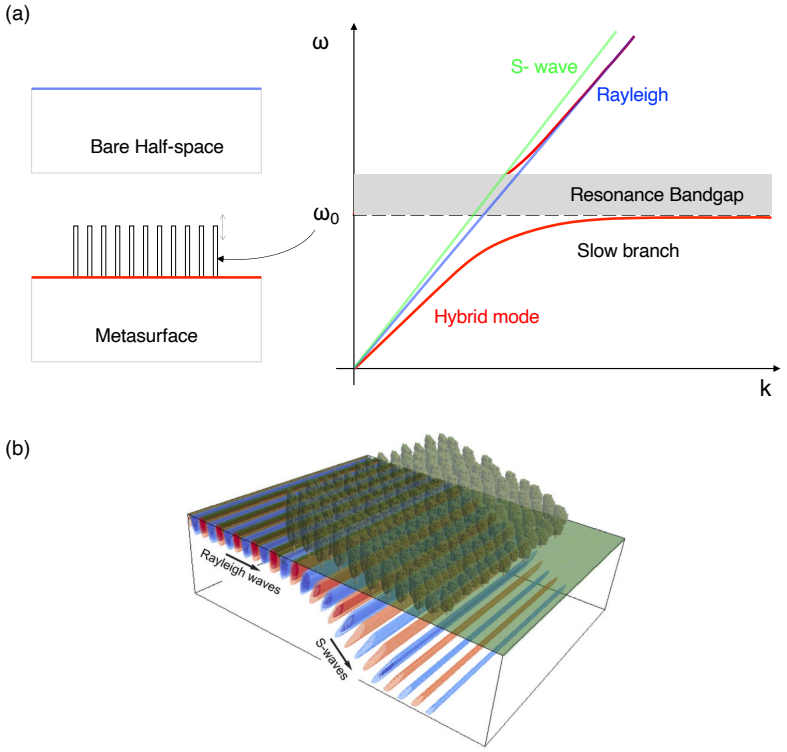


Figure 2.1: (a) Schematic showing the dispersion features for a bare half-space and a metasurface. The Rayleigh wave sound line (in blue) is slightly slower than the shear wave sound line (in green). The Rayleigh wave hybrib mode slows down near the resonance frequency. (b) An extruded view of the 2D simulation results of the phenomena where surface waves covert to shear body waves by the tree metawedge (from Colombi et al. [2016a]).

### 2.1.1 Forest of trees - a locally-resonant 'natural' metamaterial

On the geophysical scale, a cluster of densely spaced trees can be thought of as a dense configuration of beam-like features attached to the ground. This idea was first investigated by Colombi et al. [2016c] by installing two seismic stations, one inside and one outside a forest of trees, on the campus of the Université Grenoble Alpes. From ambient recordings, they observed a drop in the energy close to the first and second compressional resonances of the trees. The confirmation of this phenomenon is provided by 2D numerical simulations, which clearly show the hybridization of Rayleigh waves as a result of their interaction with trees within the frequency range of the bandgap (Fig. 2.1 (b)). Following this interesting result, an ambitious seismic experiment, called the METAFORET experiment, was planned in a pine forest with dense tree arrangement in the southwest of France in 2016 by the same team of researchers (Roux). A dense array of geophones made it possible to detect a

sharp bending of the dispersion curve inside the forest around the tree longitudinal resonance. This anomaly in the dispersion was a result of the collective longitudinal resonances of the trees, which couple well with the Rayleigh waves. Not only the dispersion properties, but also the ellipticity and the mean free path are dynamically modified near the bandgap (Lott et al. [2020a]). The METAFORET project had for the first time proven experimentally on the geophysics scale that locally-resonant structures can couple to each other and create wide frequency bandgaps. All previous studies on the METAFORET dataset have focused mainly on compressional resonances. However, we also consider the effect of the flexural resonances of the trees and their coupling with the surface waves in the first part of this chapter.

### 2.1.2 Array Processing of ambient noise for evaluating medium anisotropy

There is a special interest in understanding the directional properties of the effective medium in the context of locally-resonant sub-wavelength metamaterials. Anisotropy is that property of a medium, wherein one or more physical properties of that medium has a directional dependence. In seismology, anisotropy can be observed by measuring the speed of the seismic waves propagating through the medium in different directions. In the context of array processing, it is often assumed that the noise field exhibits isotropy. This assumption means that the noise comprises random waves propagating uniformly towards the array from all directions. Dense arrays have unprecedented azimuthal resolution because of the sensor distribution. Surface-wave measurements from seismic noise, especially with such dense arrays, offer advantages for capturing different paths and directions inaccessible to ballistic waves. One of the limitations of using ballistic waves from impulsive sources, like active shots, is that they can only sample the source-to-array direction, leaving other propagation directions unsampled.

An alternative approach involves retrieving information about the Green's function of the Earth's elastic impulse response from passive noise recordings which that are diffuse or random wavefield (Campillo and Paul [2003], Shapiro and Campillo [2004], Weaver and Lobkis [2005]). Fully diffuse wavefield is characterized by waves with random amplitudes and phases propagating in all directions, and store information about all possible paths. This information can be deduced by cross-correlating pairs of receivers. In ambient noise correlations, surface wave phases are most easily retrieved (Shapiro and Campillo [2004]), as they are inherently more prominent due to the prevalent occurrence of seismic noise sources at the Earth's surface. The waves that sample the medium between these two points are affected by the physical properties of the medium and thus can change with both depth (frequency) and direction (azimuth). The azimuthal variations of the seismic wave speed can be extracted by array processing techniques such as beamforming in either the time domain (ex. Gerstoft et al. [2006]) or the frequency domain (ex. Gerstoft and Tanimoto [2007]). Ruigrok et al. [2017] compared the conventional beamforming results with those obtained from beamforming of cross-correlations of station pairs. They found several advantages of cross-correlation BF including slightly better resolution, weaker artifacts and suppression of incoherent noise. In the second part of this chapter, we take advantage of the above stated benefits of noise correlations to investigate the presence of azimuthal anisotropy of surface waves inside the forest using plane wave

beamforming. Although there may be different motivations to study the directional properties of the seismic waves, we explore this property in the context of the forest metamaterial that could potentially lead to new physics.

### 2.1.3 Objectives and Chapter organization

In this study our aim is to explain the nature of surface wave propagation inside a forest of trees using ambinet seismic noise. We utilize the dense geophone array configurations to

1. Explain the tree dynamics and identify the contribution of the tree resonances to the nature of the surface wavefield inside and outside the forest, especially in the low frequency band ($< 20$ Hz), and
2. Quantify the azimuthal anisotropy of surface waves propagating in the forest by performing plane wave beamforming on the noise data and discuss its possible origin.

This chapter is organized as follows. First, the METAFORET experiment, including the various array configurations and the characteristics of ambient noise, is introduced in Section 2.2. This is followed by a discussion on the contribution of tree dynamics to the spectral characteristics of the surface wavefield inside and outside the forest. This contribution is evaluated for both longitudinal and flexural resonances of the trees with the help of numerical modeling in Section 2.3. Shifting our focus to array processing, specifically plane wave beamforming, we outline the related theory and demonstrate the method for continuous ambient noise data, detailed in Section 2.4. Thereafter, in the subsequent section 2.5 our aim is to quantify the observed azimuthal anisotropy and discuss its potential origins.

## 2.2 The METAFORET Experiment

### 2.2.1 Natural Setting

The METAFORET experiment (Roux et al. [2018]) is a passive cum active seismic experiment that was performed at the edge of a forest. Tree planting in the forest was done semi-regularly, in rows of 4m spacing in one direction (Fig. 2.2). Although there are numerous benefits to planting trees in such a fashion in silvicultural practices, this kind of dense tree arrangement is ideal for studying the metamaterial behavior of the forest. Instrument deployment and experimentation were carried out for two weeks (15-31 October 2016) in the southwest of France, in the Landes forest range, where Maritime pine (scientific name: *Pinus pinaster*) is the main tree cropping species (Danjon et al. [2005], Bakker et al. [2006]). The Landes de Gascogne massif is the largest artificial forest in western Europe, where maritime pines are grown on more than a million hectares. The average properties of 50 of these pine trees were measured. The trees had a diameter of $\sim$ 20 cm and were measured on average about $\sim$ 12 m tall and weighed $\sim$ 250 kg. The tree density in the forest was 900 trees/ha. Trees are well coupled to the ground by a complex root system extending into the upper layers of the soil, both in the depth direction as

well as laterally. Just below the uppermost soil layer of the forest there is a discontinuous layer of "alios", which is an impermeable, compacted sand and gravel layer, typical of the Landes de Gascogne. This kind of subsurface structure can permit the trapping (or guiding) of the surface waves in the topmost layer, which in turn facilitates the efficient interaction of surface waves with the trees. However, there will be attenuation of the field as waves can still scatter and propagate in the bulk, unlike plates. The upper layers of the subsurface were clearly revealed when the soil was dug invasively at the edge of the forest during the experiment, as shown in Fig. 2.3.

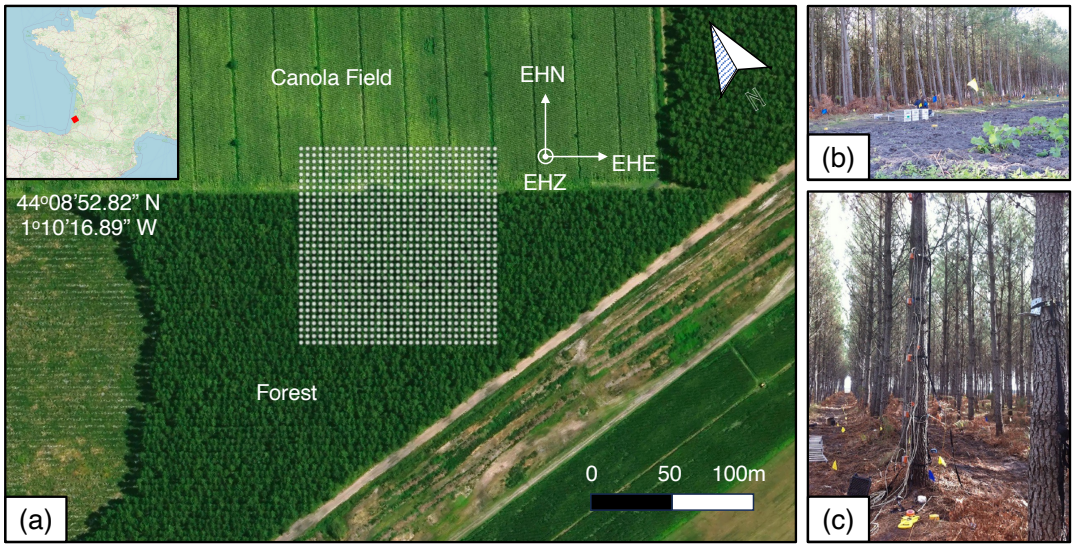


Figure 2.2: (a) Satellite view of the METAFORET array deployment at the interface of a pine forest and a canola field in the Landes region of south-west France (inset). The experimental site is just next to the municipal airfield of Mimizan town (beyond the extent of the image, to the right). The passive cum active seismic experiment took place during two weeks in October 2016. The Z-component array layout is a regular grid shown in white circles, oriented parallel to the forest-field interface. The horizontal components of the three-component geophones EHE, EHN are also oriented along the principal directions of the array, instead of the true north. Ambient noise was continuously recorded for two weeks and active source experiments were also performed simultaneously. (b,c) Images show the forest-field interface and the pine trees within the forest, respectively (accessed from `metaforet.osug.fr`).

### 2.2.2 Experimental Configuration

The experiment was designed such that the surface wave propagation can be captured, not only inside the forest where trees are present, but also outside the forest, so that wave propagation can be distinguished. A set of 995, 5-Hz vertical component geophones were installed on the ground partially covering the forest and the canola field. This array spans 120×120m with a regular interstation distance of 4m in both directions (black circles in Fig. 2.4). We refer to this array as the


Figure 2.3: (a) Soil pit locally excavated down to 2.5m at the edge of the forest reveals a highly compacted sand interface called "alios" (see inset). (b) This compacted sand layer is located approximately from $\sim$ 0.5m to 1.5m below the surface and is ploughed before plantation, particularly to allow water percolation into the ground. The ground water table was approximately 1.7m from the surface during the experiment. The same subsurface structure has been observed both in the forest and the field, except for the parallel row structure and presence of tree roots in the forest. (Images are accessed from metaforet.osug.fr)

"Z-land array" or the "Geokinetics array" in the remainder of the chapter. As seen in Fig. 2.2 (a), this matrix was deployed at the interface of the forest and the canola field and aligned with the structure of the forest itself. A large part of the array $\sim 3/4^{th}$ is inside the forest and a smaller fraction $\sim 1/4^{th}$ is deployed outside the forest. Another set of 100 three-component 4.5 Hz geophones were also installed as a square array on the forest edge covering an area of 36 x 36 m, interleaved within the Z-component array, also with a 4m spacing (red '+' symbols in Fig. 2.4). The same three-component geophones were reconfigured in a linear fashion during a partial period of the experiment with an even denser arrangement of 1 m spacing cutting across the forest-field interface. These arrays are respectively referred to as the "GFZ square array" and the "GFZ line array" in the remainder of the chapter.

The $x$-coordinate of the array is oriented parallel to the edge of the forest (Fig. 2.4). The trees are planted in parallel rows of 4m spacing along the $y$-direction, whereas the intra-tree distance along the $x$-direction is not quite regular (2.5). Inside the area covered by the Geokinetics array, on average, there are 0.33 trees/m in the $x$-direction and 0.25 trees/m in the $y$-direction. The three-component instruments of the GFZ square and line arrays were aligned parallel to the array - which means the EHN component of the geophones was pointing towards the field (in the

$y$-direction) instead of the true north and the EHE component of the geophones was parallel to the edge of the forest ($x$-direction).

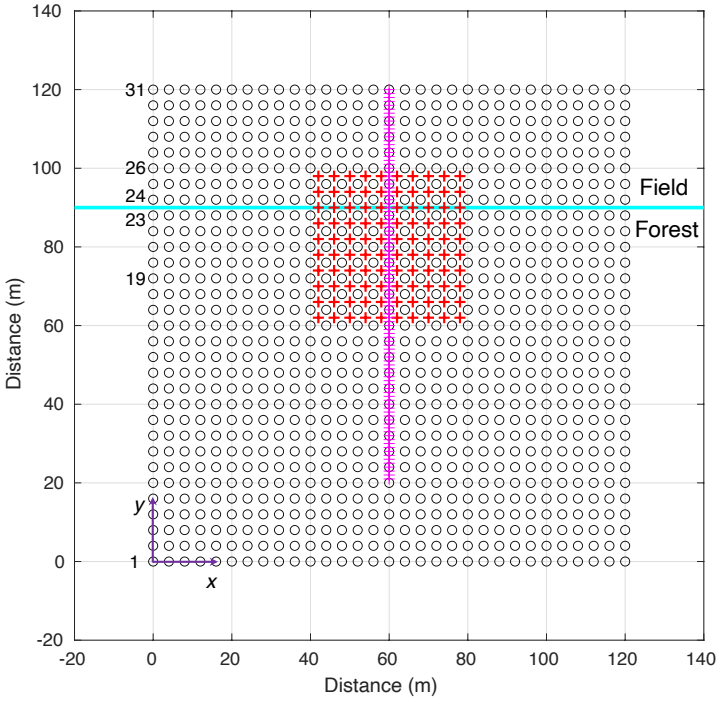


Figure 2.4: METAFORET experimental configuration: The Z-land sensors 31x31 square array (black circles) with an intergeophone spacing of 4m spans 120m in both directions. The cyan line marks the forest-field interface. Another 10x10 square array of three-component geophones (red '+' symbols) with a 4m spacing is installed near the forest-field interface. The same three-component geophones are also reconfigured and installed perpenticular to the forest-field boundary as a line array (magenta '+' symbols) with a denser 1m spacing for a partial period of the experiment.

In addition to the regular geophone arrays, some extra geophones were installed at the bases of selected trees. These are shown in Fig. 2.5 with black circles in 2 parallel rows - T1 to T14 and T16 to T30. Of the total geophones installed at the tree bases, only a few were found to have recorded data, while an even lesser number of them recorded good data. Furthermore, the experiment involved measuring tree resonances by instrumenting a set of ten trees in the forest with velocimeters (encircled in red in Fig. 2.5). To image the near-surface (top 2m) of the forest, a ground-penetrating radar (GPR) survey was performed along the 120m long lines in between the tree rows.

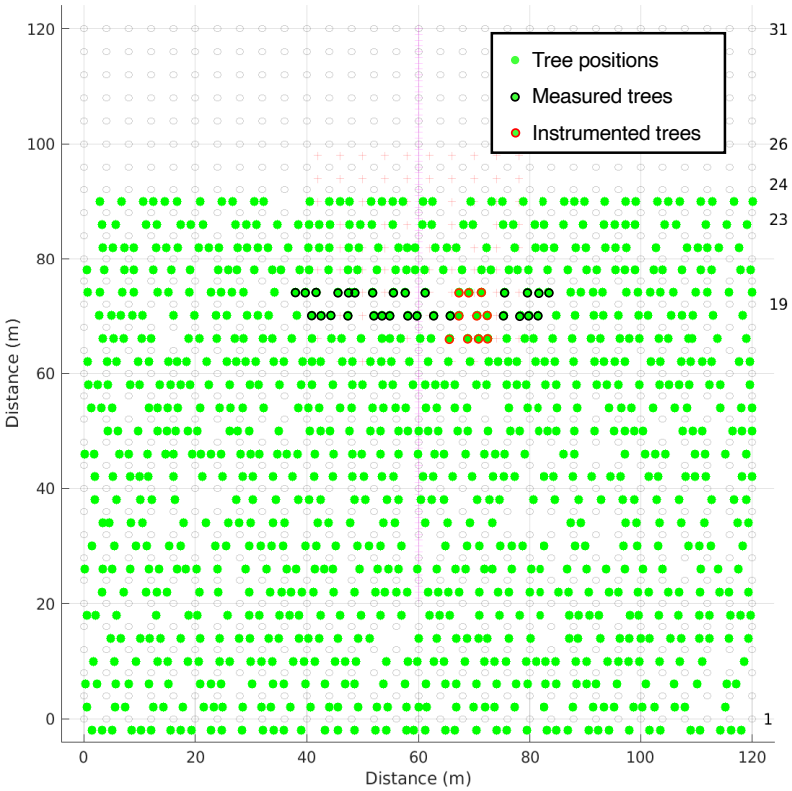


Figure 2.5: Layout of the tree positions shown as filled green circles within the array in the foreground. The trees that have an extra Z-land sensor, each installed at their base are encircled in black, whereas the trees which are instrumented by three-component velocimeters are encircled in red. The transparent background shows the geopheone positions relative to the tree positions. Note that the forest contigueously extends in the other three directions except towards the canola field.

### 2.2.3 Ambient Noise

Ambient seismic noise recorded by a seismometer is the sum of a large number of wavetrains that can originate from different sources. In the frequency band, 0.1 to 10 Hz, the significant noise sources have their origin in the ocean and from anthropogenic activities. Ocean microseisms dominate below 1 Hz and are linked to characteristic ocean swell periods. Above 1 Hz, anthropogenic noise, such as industrial or traffic-generated noise, may predominate. In addition to these sources, the action of wind, either directly on the ground or when it excites resonant features on the ground, can have an effect of seismic noise in a broad frequency band of $10^{-3} - 10^{2}$ Hz (Lott et al. [2017]). In a forest, trees themselves can be sources of seismic noise. When trees are excited by wind, they can vibrate and couple this energy to the ground, which contributes to the seismic wavefield. These can be observed from the spectra of the geophones installed on the ground. A seismometer installed on the surface picks up both body and surface seismic waves. Body waves that are produced by distant sources undergo a high attenuation. The same sources can produce surface waves that travel greater distances before losing energy. Surface waves attenuate with a $1/r$ factor, unlike body waves which attenuate with distance as $1/r^2$. Thus, a large part of ambient noise is composed of surface waves, especially at lower frequencies because surface waves contain a longer period energy than body

waves (Stein and Wysession [2009]). Thus, we can reliably assume for our analyses that the most of the energy contained in the vertical component of the geophone comes from Rayleigh waves.

The passive part of the METAFORET experiment involved 9 days and nights of continuous recording during 18th October 2016 through 26th October 2016. Simultaneously, the active part of the experiment consisted of shots from a vibrometer source placed both inside and outside the forest, which excite a high-frequency transient wavefield ($> 15$ Hz). For our study, we only used ambient seismic noise data to determine the various properties of surface waves that could not be excited by active shots. Such low frequencies can be excited by ambient noise sources, albeit weakly, but can sustain over the entire recording period. Fig. 2.6 shows spectrograms for one hour of recording from a set of geophones inside and outside the forest. The frequency window shown only goes up to 20 Hz, which is mainly dominated by anthropogenic noise.

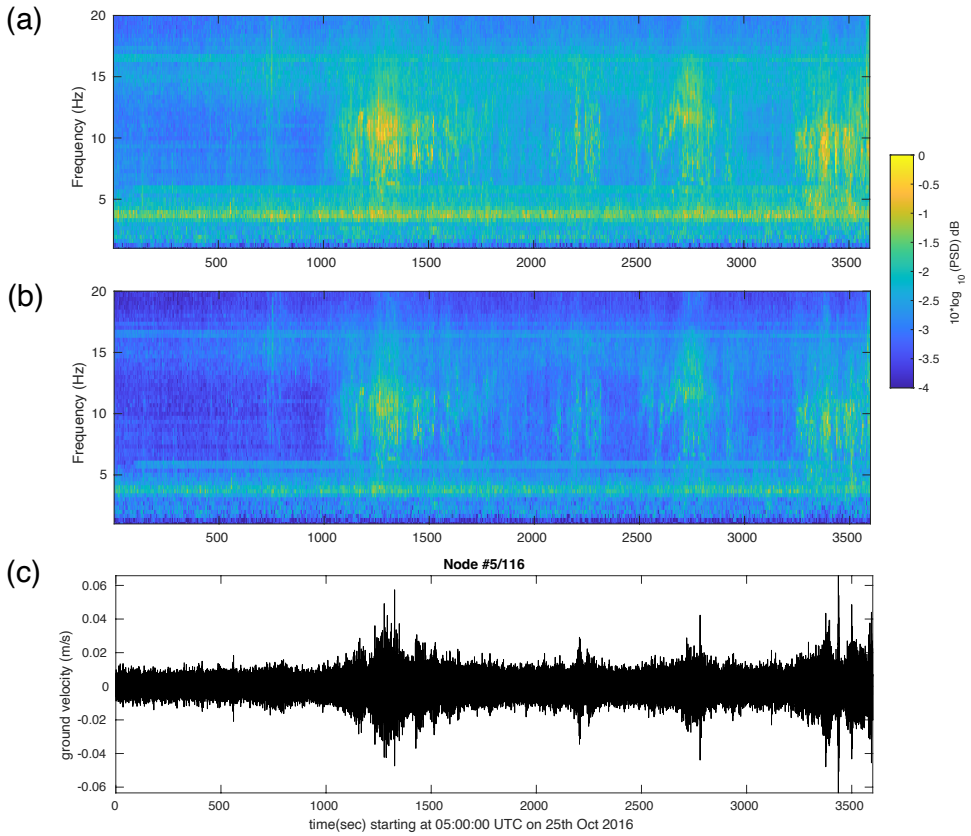


Figure 2.6: Mean spectrogram of a sample Z-component recording from Geokinetics array 5-Hz sensors inside the forest (a) and, from the canola field (b). (c) Data are lowpass filtered below 20Hz for the station 5/116 located at the position (x,y) = (44,16)m in the forest. All the panels (a), (b) and (c), show the data starting at 05:00:00 UTC on 25th Oct 2016 for a period of one hour.

## 2.3 Spectral Analyses

The goal of spectral analyses is to establish any potential link between the tree dynamics and surface wave properties inside and outside the forest. There will be a complex interaction between the flexural and longitudinal resonances and the associated geophone spectra. Previous studies that analyzed data from the METAFORET experiment (Roux et al. [2018], Lott et al. [2020a]), focused on the higher frequency regime ($\sim 50 - 60$ Hz). The tree longitudinal resonance mode opens a bandgap and is primarily responsible for the drop in energy propagating inside the forest. This is explained by the fact that there is a sudden change in phase velocity as we approach the longitudinal resonance of the trees (see Fig. 2.7). From the same figure, we notice that in the low-frequency range, there is also an abrupt change in phase velocity, where the trees exhibit flexural resonances. This anomaly in dispersion was observed below 10 Hz from the ambient noise data and has to be related to the flexural resonances (Fig. 9 from Roux et al. [2018]). We know that the vertical motion of trees is efficiently coupled with the vertical component of the Rayleigh wave, and thus the drop in energy is more significant around tree longitudinal resonance (Colombi et al. [2016c], Roux et al. [2018]). On the other hand, it is possible that the vertical component will be less interesting in case of the flexural resonances as compared to the horizontal component. An interesting analogy from the laboratory-scale plate and rod experiment and the corresponding numerical simulations (Colombi et al. [2014]), is that the flexural motion is weakly coupled with the A0 lamb mode. Keeping this in mind, we revisit tree resonance identification by complementing the existing experimental results with some frequency domain numerical analysis. We then analyze the spectra from the geophones inside and outside the forest and comment on the origin of the observed low-frequency peaks.

### 2.3.1 Dynamic response of the trees

Trees can exhibit mechanical resonances similar to a slender cantilever beam, anchored at one end and free at the other end. These resonances can primarily be flexural or compressional in nature. The vibration analysis of the tree motion in the METAFORET experiment was captured in the field using velocimeters (Lennartz 3C 1s) directly attached to the trees. The analysis has been shown in previous studies using both ambient vibrations (Roux et al. [2018]) and active source excitation (Lott et al. [2020a]), as in Figs. 2.8 (a) and (b), respectively. The Fourier analysis of both ambient vibrations as well as the active shot windows reveal distinct resonances near frequencies 0.3, 0.9, 2 Hz and around 45 Hz. These correspond to the first three flexion modes and the compressional resonance of the trees, respectively, determined by the modal analysis. The flexural motion of the trees is mainly excited in the low-frequency regime, whereas the longitudinal resonances are seen at the higher frequencies. Lott et al. [2020a] reported that all the instrumented trees have about the same frequency behavior. Specific details of these trees, including tree dimensions and weight, are not available. For this reason and the fact that they are co-located in the forest, we assume there must have been no significant differences in their geometry and mass.

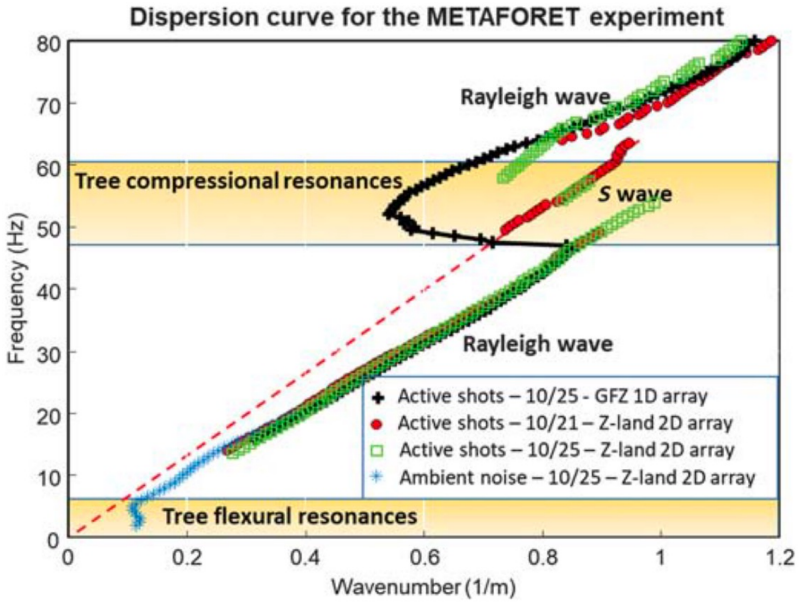


Figure 2.7: Surface wave dispersion measured inside the forest from ambient noise (blue) and active shots (black, red, and green) is represented in the frequency–wavenumber (f-k) space. Frequency intervals linked to the tree flexural and compressional resonances are shown as shaded bands. Between $\sim 50 - 60$ Hz, the main inflexion point in the dispersion curve corresponds to a frequency bandgap in agreement with the locally-resonant metamaterial behavior of the forest. Another less significant, but visible bending of the dispersion curve is seen in the band below 10 Hz where the flexural resonances dominate (from Roux et al. [2018]).

### Frequency domain numerical analysis

To better understand how the tree resonator behaves to various input excitation frequencies, we set up a frequency-response analysis in COMSOL Multiphysics. The 2D numerical model of a single tree coupled to the ground with the root is shown in Fig. 2.9(a). The tree is modeled as a 2D solid beam of height $h$ and diameter $d$, attached to the soil half-space via a root region. The mechanical parameters of the tree are taken from Roux et al. [2018], which are the mean values of tree wood as determined by Colombi et al. [2016c]. The half-space is modeled as a homogeneous layer with average properties of the first 20m depth from the velocity inversion performed by Lott et al. [2020a]. The coupling element, i.e., the root, is limited to a 3 m wide and 0.5 m deep region, as typical for maritime pine species in Landes forest (Danjon et al. [2005]). The root is assigned with the mechanical properties referenced in the Supplementary Information of Colombi et al. [2016c] that also correspond approximately to the mean values of the tree and the soil medium. The properties of different domains are shown in Table 2.1 below. It should be noted that the tree and the ground are characterized by sharply contrasting material properties.

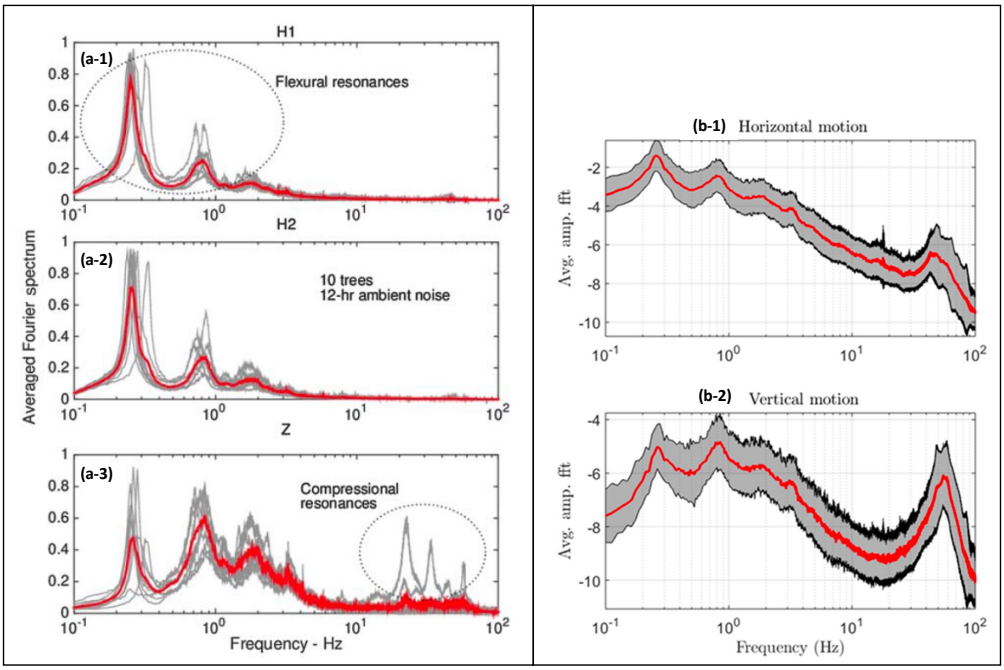


Figure 2.8: Tree response (Left panel) Normalized Fourier spectra of the ambient vibrations recorded in 10 instrumented trees during a night along (a-1) H1 or north, (a-2) H2 or east, and (a-3) Z or vertical directions. Gray curves are the averaged Fourier spectra of a 12-hr-long recording window and the red curves are the average response of the trees. The spectra were normalized by the global maximum of the three-component spectra (H1, H2, and Z). (from Roux et al. [2018]). (Right panel) Normalized Fourier spectra averaged for 10 instrumented trees and all active sources, for the horizontal (b-1) and vertical (b-2) components in red with a confidence interval depicted as a shaded area in grey. The horizontal component is the average of the two radial and tangential components (from Lott et al. [2020a]).

| Domain | $\rho$ (kg.m$^{-3}$) | V$_p$(m.s$^{-1}$) | V$_s$(m.s$^{-1}$) |
|---|---|---|---|
| Tree | 500 | 2500 | 1300 |
| Soil | 1700 | 900 | 500 |
| Root | 1100 | 1600 | 900 |

Table 2.1: Material properties used for the tree, root and soil for the frequncy domain numerical simulations of a single tree fixed to the ground via a root link. The tree properties are taken from Roux et al. [2018], and the soil shear speed is averaged of the first 20m from the inversion obtained in Lott et al. [2020a]. The root region is assigned mean values of those from the tree and soil.

A harmonic sweep reveals peaks in the response of the top free end of the tree by monitoring the horizontal and vertical displacement amplitudes, seen in Figs. 2.9 (b) and (c), respectively. As expected, the dominant flexural motion of the trees can be seen in the low frequencies (below 10 Hz), whereas the compressional resonance is observed at the higher frequencies (above 30 Hz). It is worth noting that higher-order flexural modes can be coupled with the longitudinal mode. In our analysis,

the mode coupling is seen for the 6th flexural mode and the compressional mode. We performed a sensitivity analysis by varying tree heights $h \in [9 \,..\, 15]m$, which is the natural variation in the forest. The diameter of the tree is taken as a constant value of $d = 0.2m$ due to the low variation. The results of the sensitivity test are shown in Table 2.2. The resonance frequencies of the first three flexural modes and the first longitudinal mode are approximated to the first decimal.

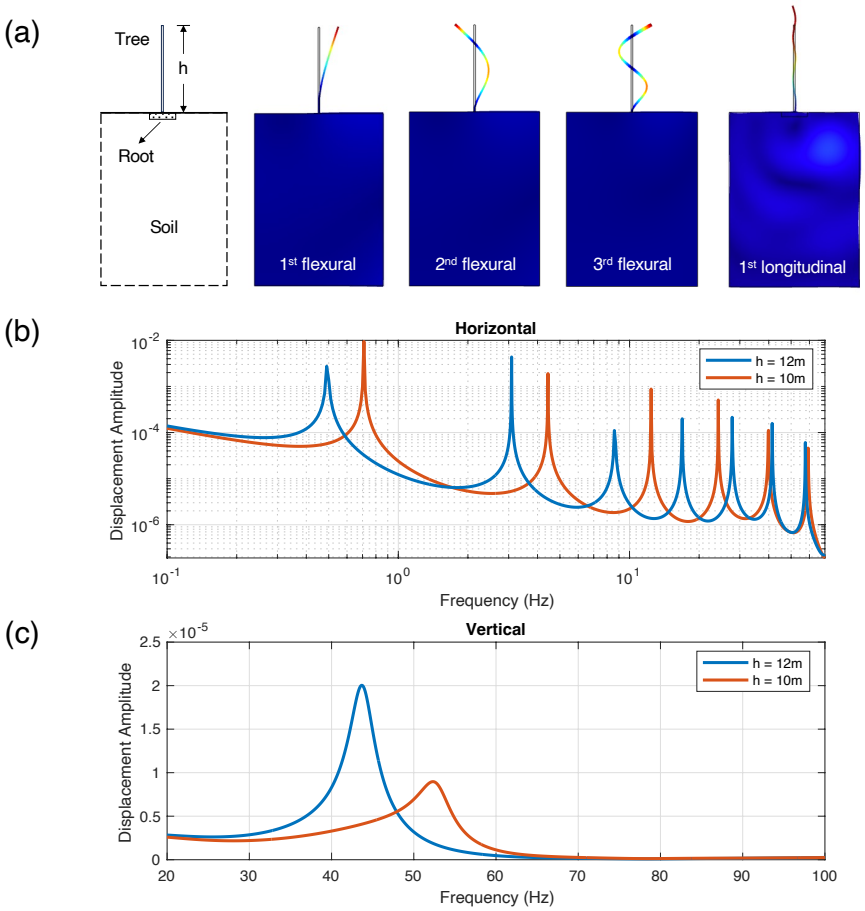


Figure 2.9: (a) Frequency domain analysis of the motion of a single tree modeled as a uniform 2D beam of height $h$ and diameter $d$, coupled to the ground by the root. The various material properties are shown in Table 2.1. (a) The model schematic and the series of figures showing the total displacement at various resonance peaks. (b,c) The horizontal and vertical displacement amplitudes are respectively shown for the response at the free end of the tree, for the tree heights $h = 10m$ and $12m$, having a constant diameter $0.2m$ and root region $3m$ wide and $0.5m$ deep. The horizontal motion is characterized by high $Q$ factor flexural resonances, while the vertical response shows the associated longitudinal resonance having a low $Q$ factor.

| | Resonance frequency (Hz) | | | |
|---|---|---|---|---|
| Tree height, $h$ (m) | 1st flexural | 2nd flexural | 3rd flexural | 1st longitudinal |
| 9 | 0.9 | 5.5 | 15.3 | 58.6 |
| 10 | 0.7 | 4.5 | 12.4 | 53.1 |
| 11 | 0.6 | 3.7 | 10.3 | 47.6 |
| 12 | 0.5 | 3.1 | 8.7 | 42.9 |
| 13 | 0.4 | 2.6 | 7.4 | 40.4 |
| 14 | 0.4 | 2.2 | 6.3 | 37.5 |
| 15 | 0.3 | 2.0 | 5.5 | 35.3 |

Table 2.2: Resonance frequency peaks corresponding to the first three flexural and the first longitudinal resonances for varying tree heights. The model shown in Fig. 2.9 and material properties in Table 2.1 are used for the frequency domain analysis.

From the above table, both the flexural and longitudinal resonances are quite sensitive to the height of the tree. A small increase in tree height significantly shifts the position of the low-quality factor compressional peak in the spectrum. For the multiple flexural peaks, we also see them gradually shift towards the lower frequencies as the tree height increases. The flexural resonances of a 15m tree are more closer to the observations, whereas a 10-12 m tree is more representative of the longitudinal resonances. However, trees have different mass distributions along their heights, according to their branching and foliage, significantly affecting the resonance frequencies (Maurel et al. [2018]). This could be an important factor in understanding why we do not see a decent match of the peaks from the velocimeter and the simulations for any specific case. The sensitivity analysis for the other parameter, the tree diameter, is not shown here because of the low variation in tree diameter in the forest. Another important parameter in the model is the dimension of the base of the root. However, the resonance peaks were not significantly affected by the variation in root size in a reasonable range (not shown here).

### 2.3.2 Spectral characteristics of noise inside and outside the forest

The surface waves propagating on the ground interact with the trees, and around the tree resonances it has been observed that the surface wave propagation shows anomalous behavior (Colombi et al. [2016c], Roux et al. [2018]). Looking at the response of the geophones inside and outside the forest, we can point out differences in the spectra. If the forest plays a role in shaping the way surface waves propagate, then we should be able to see a clear difference in the amplitude and the phase. Here, we focus on the amplitude information of the waves. We select a set of geophones from the Geokinetics array that well represent the forest and field. Rows 10 and 11 (y = 36 and y = 40m, respectively) that are well inside the forest, and rows 30 and 31 (y = 116 and y = 120m, respectively) outside the forest are chosen (see Fig. 2.4). We consider recordings only during the calm periods between 7pm and 7am. The spectra are spatially averaged for each sliding time window 100 s long with 20 s overlap, and also averaged over all time windows of these synchronous records. In the same way, the geophone data from all stations at the tree bases are also analyzed

(see circles with black outline in Fig. 2.5). The amplitude spectra for the geophones inside the forest (i.e., between the tree rows), in the canola field and those placed right at the base of the trees, are shown in Fig. 2.10 (a). We note that the peak around 50 Hz, which is seen in the spectra from stations at the tree bases (black) and those outside the forest (blue), is completely missing from the spectra of stations between the tree rows (red). This suppression of the longitudinal resonance peak means that the energy radiated by the trees is evanescent inside the forest, but leaks outside the forest. This energy drop is also evident from the spectral ratio plot in Fig. 2.10 (b), where the black curve indicates the spectral ratio for the Geokinetics array. The spectral ratio increases just before the tree resonance frequency, similar to that observed by Colombi et al. [2016c]. Interpreting the spectral ratio becomes more challenging when frequencies above 60 Hz are considered, because surface waves are scattered by local heterogeneities and the contribution of body waves becomes more prominent (Lott et al. [2020a]). On the other side of the spectrum, frequencies below 5 Hz will be damped because of the sensor cut-off. Thus, the ability to accurately capture low-frequency signals near tree flexural resonances (observed at 0.3, 0.9 and 2 Hz from velocimeter data) is limited depending on the signal-to-noise ratio. We nonetheless observe the 2 Hz peak in all the three sets of stations (tree bases, between rows, canola field), which is also seen in the velocimeter data and has to be from the tree flexural resonance. Further below in frequency, the amplitude spectra cannot be reliable, especially in the subhertz range due to a damped response. However, in ideal conditions (temperature stable vault) and low noise environments, recordings can be deemed reliable up to 0.25 Hz (Ringler et al. [2018]).

There is another peak that is suppressed inside the forest, or, in other words, a drop in the spectral ratio around 13 Hz, also observed by Lott et al. [2020a] from the active data (which they did not discuss). The reason for this peak in the spectra outside the forest is unclear, since we did not see any tree resonance at this frequency from the velocimeter data or geophones at tree bases. However, the frequency response of a 10m tall numerical tree shows a higher flexural mode around 12-13 Hz (Fig. 2.9 (b)). Thus, the 13 Hz peak has to be from a source external to the forest, for example, from train-induced noise. The fundamental frequency of the harmonic signal resulting from a moving train is controlled by the speed of the train and the distance between the axles, $f_1 = V_{train}/\Delta_a$ (Lavoué et al. [2020]). Studies by Lopes et al. [2014] and López-Mendoza et al. [2017] both report a peak around 13 Hz in ground recordings near a railway track. In the former, it is generated when the train with axle length $\Delta_a = 2.9m$ is traveling at 144 kmph, and in the case of the latter, when a train with $\Delta_a = 3m$ is traveling at 150 kmph. This is consistent with the ground-borne spectral peaks at 13 Hz observed in these two studies. The closest railway line to the METAFORET experiment site is 20 km to the east. The signals generated by the train could be recurrent and can travel several tens of kilometers from the tracks (Inbal et al. [2018], Brenguier et al. [2019]). The beamforming result at this frequency (shown later in Section 2.4.2) does not explicitly hint at an isolated source from the direction of the railway line. However, we do not have any conclusive argument to prove this hypothesis and, moreover, observing the drop in the spectral ratio for active source data itself contradicts it.

A possible reason for a peak outside that is missing inside the forest could also imply reflection due to Bragg scattering. Given the fact that the forest has trees arranged in regular rows in the N-S direction, similar to lattice planes, an incoming

plane wave incident normal to the forest can constructively interfere and reflect the waves – a 'Bragg mirror'. However, the wavelengths at those frequencies do not agree with the Bragg condition at normal incidence i.e., $n\lambda = 2d$, where $d$ is the distance between the tree rows. We discard this theory too.

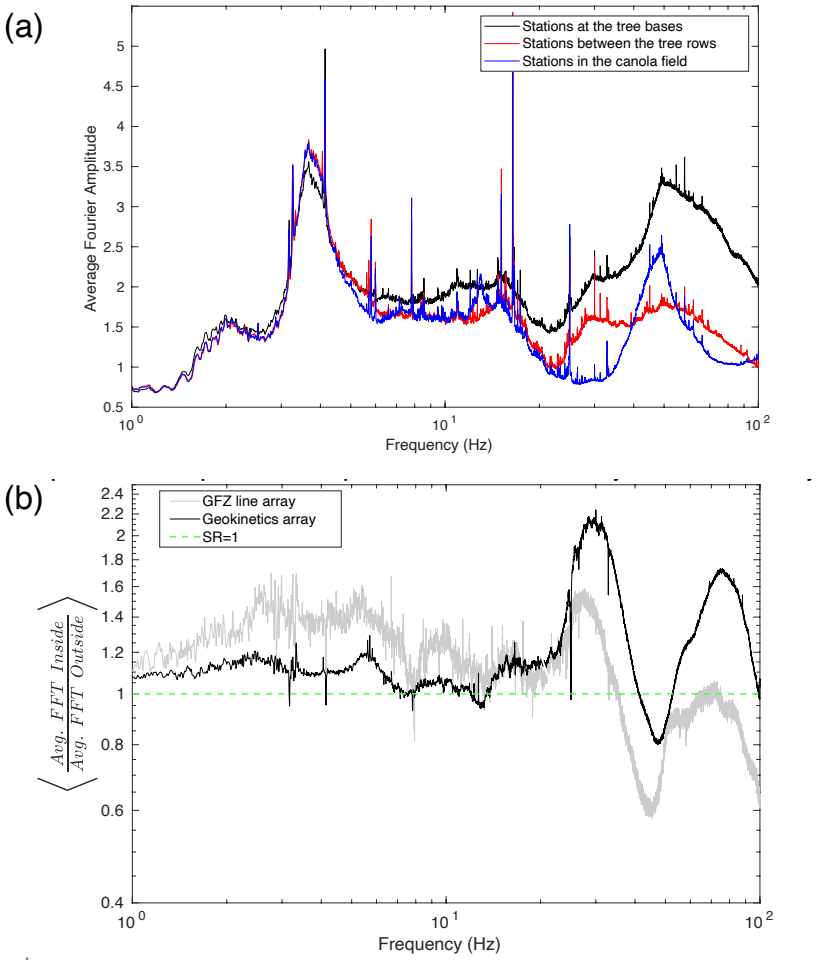


Figure 2.10: The spectral amplitudes and spectral ratio of the Z-component recordings for different sub arrays. (a) The spectra are shown for selected station sets inside (red) and outside the forest (blue), along with the stations installed at the tree bases (black). All spectra are for the recordings only during the calm periods between 7pm and 7am. Note that the instrument response has not been removed for plotting the spectra. (b) The black and gray curves correspond to the spectral ratio measured from the Z-land sensor array and the vertical component of the GFZ line array, respectively. Both the spectra and the spectral ratio are spatially averaged for each sliding time window 100s long with 20s overlap and also averaged over all time windows. The drop in spectral ratio around 50 Hz is due to the longitudinal resonance coupling of the trees. There are other relatively less significant drops, noticeably around $\sim 8$ Hz and $\sim 13$ Hz.

We perform a similar spectral analysis of ambient noise recorded by the 3C GFZ line array (magenta crosses in Fig. 2.4) which was deployed from 23rd October 20106 for a period of three days. For the spectra inside and outside the forest, we

chose 20 stations in the range $20 < y < 40$m (inside) and $100 < y < 120$m (outside). Similarly to the Geokinetics array, we choose only the calm periods and spatially and temporally average the spectra. We did not notice any difference between the spectra below 20 Hz for the vertical component. The 2 Hz flexural resonance is not very evidently seen in the horizontal components. However, a missing peak is observed for the two horizontal components around $7.5 - 8$ Hz. This is also seen in the spectral ratio in Fig. 2.10 (b), shown in gray. Again, the tree velocimeters do not capture any peaks at this frequency, but a numerical tree of height 12-13m has higher flexural resonances around 3 and 8 Hz (Table 2.2). These seem to roughly align with the observed amplitude spectra for the horizontal components EHN and EHE, which should be most sensitive to flexural resonances.

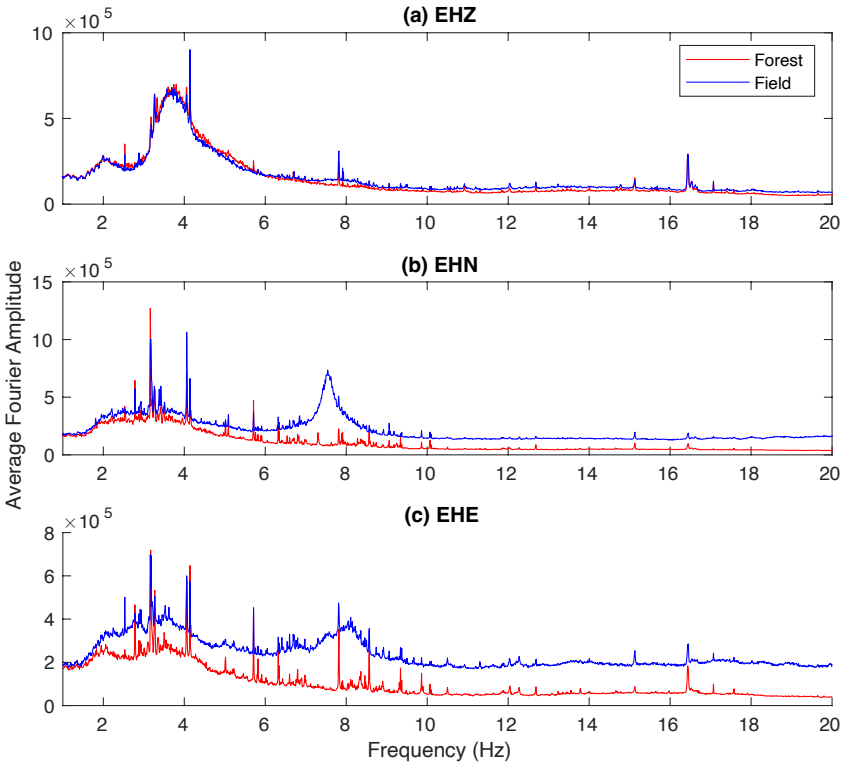


Figure 2.11: The spectral amplitudes of the three component recordings from (a) EHZ and (b) EHN and (c) EHE channels of the GFZ line array. The spectra are shown for the station sets both inside ($20 < y < 40m$) and outside ($100 < y < 120m$) the forest. All spectra are for the recordings only during the calm periods between 7pm and 7am. Note that the instrument response has not been removed for plotting the spectra. Spatial and temporal averaging was done similar to Fig. 2.10(a). There is a missing peak inside the forest around $7.5 - 8$ Hz for both the horizontal components. However, there was no tree resonance observed at this frequency.

### Discussion

We observe both inside and outside the forest, one low-frequency peak at 2 Hz corresponding to the tree flexural resonance This suggests that the bending of the Rayleigh wave dispersion curve observed by Roux et al. [2018] at this low frequency

does not conform to the hypothesis of interference effect associated with trees behaving as coupled resonators at the subwavelength scale. Uncorrelated peaks that appear in the geophone spectra (forest) but are not seen in the velocimeter spectra (trees), for example the prominent peak in the vertical direction just below 4 Hz, should be external to the forest. The extremely complex propagation path between the more flexible trees and the stations installed in the vicinity of the trees, can give rise to observable spatial frequencies. In addition to this, the impedance mismatch between trees and the ground is critical to identifying the overall efficiency of the ground-tree coupling. Indeed, a significant impedance mismatch will prohibit efficient exchange of energy over the interface (root), therefore also limiting the metamaterial behavior of the forest. The root region, as also modeled in the simulations with the average properties of wood and soil, provides an impedance matching layer between the tree and the ground which can improve the coupling. The other peaks which are seen only outside the forest but missing inside the forest are interesting for our study. However, not all of them correspond to a resonance bandgaps, since we do not observe tree resonances around some of those missing peaks. As for such peaks at 8 Hz and 13 Hz, regardless of their source, the filtering of these frequencies by the forest is difficult to explain with the available data. Finally, the coupling between the instruments (velocimeters and geophones) and the medium (trees or ground) can further influence the peaks in the spectra.

## 2.4 Plane wave Beamforming

### 2.4.1 Theory

As discussed previously, the vertical component in the ambient noise recordings is primarily due to the propagating Rayleigh waves, at least in the frequency regime where body waves do not dominate. By measuring phase speed associated with the Z-component geophone array for the different incident directions, we can obtain the azimuthal anisotropy of the Rayleigh waves. Similarly, Love wave anisotropy can be deduced from the measurement of phase speed associated to the horizontal component of the geophone that is perpendicular to the direction of propagation. One way to access the azimuthal dependence of surface wave phase velocities is to use array processing methods such as plane wave beamforming, which access the coherence of the wave field across an array (Rost and Thomas [2002]). The method we use here is a special case of the more generalized *Matched Field Processing (MFP)*, a technique developed in ocean acoustics for localizing point sources in acoustic wave guides (Baggeroer et al. [1988]). The difference between the MFP and Plane wave beamforming, is that the former can be used for curved wavefronts, whereas the latter can be only applied to plane waves, as the name suggests. Thus, the main limitation of plane wave beamforming is that sources have to be far away. The conventional plane wave beamformer can be used in any complex environment, as long as it is possible to obtain spatially coherent phase information between nearby sensors (Jensen et al. [2011]). In this section, we discuss the theory of the plane wave beamforming technique applied to noise recordings in the context of dense nodal arrays.

### Cross Spectral Density Matrix (CSDM)

We process the continuous noise data for each geophone to accumulate a coherent phase signal in the form of a cross-spectral density matrix which is the spatial covariance matrix of the data in the Fourier domain. This CSDM or covariance matrix has previously been applied to microseismic noise (Gerstoft and Tanimoto [2007]), teleseismic earthquakes (Seydoux et al. [2016b]), to classify seismovolcanic tremors (Soubestre et al. [2018], to analyze the wavefield of ambient noise (Roux [2009], Seydoux et al. [2016a, 2017]) and also in the context of the lab-scale metamaterial (Lott and Roux [2021]). The continuous ambient noise time series is divided into several time windows (Fig. 2.12(a)) to compute the Fourier transforms for the $N$ geophones in the array. Thus, the array data vector at a particular frequency $f$ is defined as

$$\mathbf{d} = \begin{bmatrix} d_1(f) \\ d_2(f) \\ \vdots \\ d_N(f) \end{bmatrix} \tag{2.1}$$

where, $d_i(f)$ is the Fourier transform (keeping the phase only) of the component measured from the geophone at $\vec{r_i}$ ,$i = \{1, ...., N\}$, for a finite-duration recording window. We then build a cross-spectral density matrix (CSDM) by performing correlations between all the station pairs of the array over this time segment. The CSDM is a N x N square matrix that captures the relative spatial phase difference between all sensor pairs and is defined as

$$\mathbf{K}_{ij}(f) = \left\langle \mathbf{d}_i(f)\ \mathbf{d}_j^*(f) \right\rangle \tag{2.2}$$

where * indicates the complex transpose operation and $\langle\cdot\rangle$ denotes the temporal average of the ensemble over all time windows. Throughout this chapter, vectors are denoted by boldface lowercase letters and matrices by boldface uppercase letters. For the temporal averaging, we choose two time windows, one for the CSDM averaging (W1, shown in blue) and another for the averaging of the beamforming output (W2, shown in red), as shown in Fig. 2.12(a). The CSDM averaging window is a subwindow of the BF averaging window. To construct the CSDM shown in Fig. 2.12(b), the noise data are processed into 15 min segments. CSDM averaging is done using a 30 s long sliding window with 50% overlap, over $M = 58$ consecutive windows for each 15 min segment. It should be noted that here $M < N$, which implies that the CSDM is not full-rank, which is not mandatory. However, this implies that if we have many plane wave directions in the same noise segment, they cannot be decoupled from each other. As $M \to \infty$, the CSDM matrix converges towards the theoretical array covariance matrix $\mathcal{K}$ (Seydoux et al. [2017]). Fig. 2.12(b) shows an example CSDM for a 15min trace of noise data at frequency $f = 21Hz$. The CSDM is complex and symmetric with the autocorrelations of all stations on the diagonal elements and the cross-correlations on the off-diagonal elements. For the sake of clarity, fifty randomly selected geophones from the Z-component array inside the forest are shown in this figure. The $i^{th}$ row and the $j^{th}$ column of the matrix $\mathbf{K}$ contain the mean phase delay between the $i^{th}$ and $j^{th}$ geophones at frequency $f$. In the time domain, this corresponds to the cross-correlation between the geophones at

positions $\mathbf{r}_i$ and $\mathbf{r}_j$. The possible range of the cross-spectral value is between 1 and -1, where 1 indicates perfect positive correlation and -1 indicates perfect negative correlation. Note that the CSDM is symmetric and complex and only the real part is shown. The imaginary part is small compared to the real part and close to zero, as one would expect from the noise correlation theorem. Following Löer et al. [2018], we omit the CSDM frequency averaging, because the effects of aliasing in the frequency range under consideration are minor due to the large number of stations in the array.

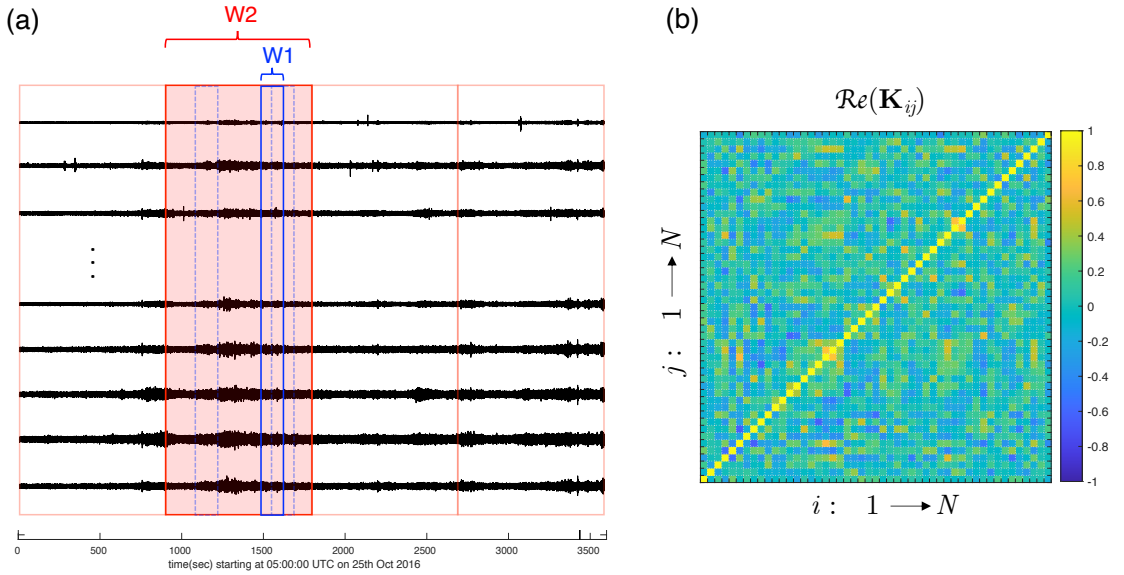


Figure 2.12: CSDM construction based on time averaging of noise correlations. (a) Windowing of the ambient noise traces using a half-overlapping 30s long sliding window W1 (in blue) for FFT computation, that is averaged inside a longer window W2 (in red) that samples every 15min of noise data with no overlap. (b) Real part of the CSDM for 50 randomly selected geophones of the array inside the forest at frequency $f = 21Hz$ for one such 15min window. The color indicates phase correlation at all station pairs with the autocorrelations lying along the diagonal axis.

### Replica/Steering Vector

In plane wave beamforming, the data that are received across the array is phase-matched with the replica, i.e., a synthetic plane wavefield of varying wavevector amplitude and direction. Thus, a set of plane waves need to be "steered" in various directions $\theta_s$ to probe the direction of the noise source (Fig. 2.13). The model-based plane wave field, called the replica / steering vector, $\mathbf{w} = e^{i\mathbf{k}\cdot\mathbf{r}}$ can be constructed for each given frequency $f$, phase speed $C$ and steering angle $\theta_s$ as

$$\mathbf{w}(f, C, \theta_s) = e^{-i\frac{2\pi f}{C}(\mathbf{x}cos\theta_s + \mathbf{y}sin\theta_s)} \tag{2.3}$$

where, $\mathbf{k}$ is defined as the wave vector having directional cosines $(\cos\theta, \sin\theta)$ , and $\mathbf{x}$ and $\mathbf{y}$ are the relative spatial positions of the geophones with respect to a selected reference geophone.

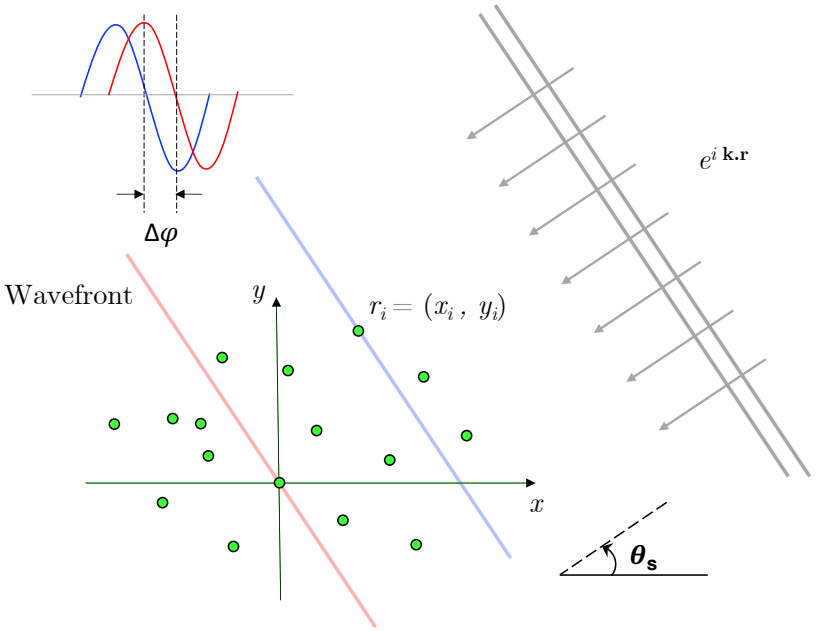


Figure 2.13: Convention used for the replica vector. Plane wave of frequency $f$ and a phase speed $C$, impinging on the array from a direction $\theta_s$. The azimuth is measured in a counterclockwise sense from east of array. The convention is chosen such that azimuth gives the direction of arrival of the plane wave and not the direction of it's propagation.

Finally, the azimuth-dependent phase velocity is recovered for the array by matching the CSDM matrix $\mathbf{K}(f)$ against the plane wave steering/replica vector (Jensen et al. [2011]). The beamforming output at a given frequency $f$ is defined for each wave vector amplitude and direction as

$$B(f, C, \theta_s) = \frac{1}{N}\Big\langle \left|\mathbf{w}^*(f, C, \theta_s)\ \mathbf{K}(f)\ \mathbf{w}(f, C, \theta_s)\right| \Big\rangle \tag{2.4}$$

where the angle brackets $\langle\rangle$ denote the ensemble average of the beamforming output for all windows W2. The normalization factor $1/N$ means that the beampower must be 1 for a signal that is perfectly coherent across the array. For each frequency, by searching for a combination of phase velocity and azimuth, we construct an image with beampower. The beampower is maximized when $\mathbf{k}$ matches the actual plane wave arriving at the array.

### Plane wave Beamforming for horizontally polarized waves

A one-component array does not capture the full nature of a wavefield and entirely omits the pure SH waves. With a three-component seismic array, the enhanced spatial information enables the isolation and estimation of the propagation direction and apparent velocity of coherent signals prior to polarization analysis (Rost and Thomas [2002]). Similar to the beamforming of the vertical component, we apply the same method to beamform the horizontal components of a 3C array. However, to correctly estimate phase velocity for a plane wave direction, we need to rotate

the horizontal orthogonal components in the look direction itself. This is because the rotation of the components ensures that the wave polarization is either in the direction of **k**, the plane wave vector (as in the case of a Rayleigh wave) or perpendicular to the wave vector (for pure SH waves). However, this is not always true, for example, in an anisotropic medium, the plane of polarization is no longer transverse (Tanimoto [2004]). Quasi-Rayleigh (qR) and quasi-Love (qL) waves can be slightly tilted with respect to the direction of propagation. In any case, if qR and qL waves exist, it will be evident from the beamforming output.

When the components EHE and EHN are rotated by $\phi$ , the new components are given by

$$\begin{aligned} \text{EHE}_\phi &= \text{EHE}\ cos\phi - \text{EHN}\ sin\phi \\ \text{EHN}_\phi &= \text{EHE}\ sin\phi + \text{EHN}\ cos\phi \end{aligned} \tag{2.5}$$

The rotation angle $\phi$ is varied with the look direction $\theta_s$ itself. Fig. 2.14 shows the rotation of the horizontal component of the array in the look direction. Now, the CSDM $\mathbf{K}(f)$ needs to be constructed from the rotated data of the horizontal components. The replica vector remains unchanged, as it does not depend only on the look direction and the geophone positions. The beamforming can be repeated in different look directions and for all required frequencies.

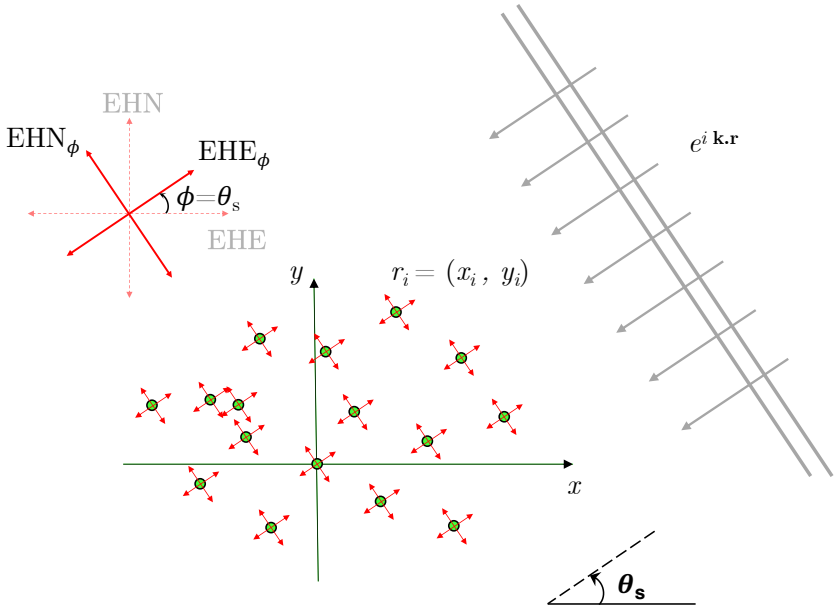


Figure 2.14: Plane wave Beamforming with horizontal components. The array looking in the direction of the plane wave arrival direction to beamform the pure SH component of the wavefield. For this, the rotation of the horizontal components of the data has to match as the steering direction, $\phi = \theta_s$. In this figure, the beamforming of component EHN$_\phi$ with the replica vector of a plane wave arriving from azimuth $\theta_s$ gives an estimate of the pure SH wave phase speed. The CSDM matrix contains the correlation of the rotated horizontal components whereas the replica vector remains same as that for the vertical component beamforming.

Some other formulations are proposed in the literature to optimally beamform

three component array data. In addition to velocity and azimuth, the polarization is another parameter that describes seismic waves. Riahi et al. [2013] based their 3C beamforming algorithm on that of Esmersoy et al. [1985] to simultaneously estimate the particle motion (wave type) and propagation direction (azimuth). Distinguishing between wave types is performed by estimates of wave polarization from the energy distribution among the vertical and horizontal components of the sensors. Although this is interesting, we did not use this approach since there is only one SH polarization state, and thus no parameterization was necessary in our case.

### 2.4.2 Beamformer Output: 1C Array

Using the approach explained in the previous section, we first perform beamforming in a broad frequency range (4-40 Hz) for the vertical component noise data recorded by the Z-land sensor subarrays inside and outside the forest. Phase velocity interval is selected based on the expected value between $250 - 450 m/s$ and in all possible azimuth directions 0° to 360°. The beamforming results are normalized for 15-min windows for continuous recordings of 9 days and nights starting from 18th October 2016. Average beamforming plots are shown for some selected frequencies in Fig. 2.15 for both subarrays. Although we did not manage to have a full-rank CSDM, i.e., $M < N$, the projection on the replica vector gives an interpretable result which is not polluted by the fact that the plane waves from different directions can be coupled. An important observation is the sinusoidal variation of phase speed inside the forest for almost all the quasi-harmonic frequencies for which the beamforming was performed. After frequency $\sim 37 Hz$, the array response starts to interfere with the plot of the azimuthal variation of phase velocity. On the other hand, for the subarray in the canola field, it is difficult to see the continuous azimuthal variation. The observed patterns can be explained by the aperture of the subarray outside the forest, which badly resolves the noise in the NS direction of the forest (Fig. 2.15 a-2 through e-2). The azimuthal variations of the group velocity should, in theory, behave in the same way as phase velocity. However, we did not measure group velocities in this study.

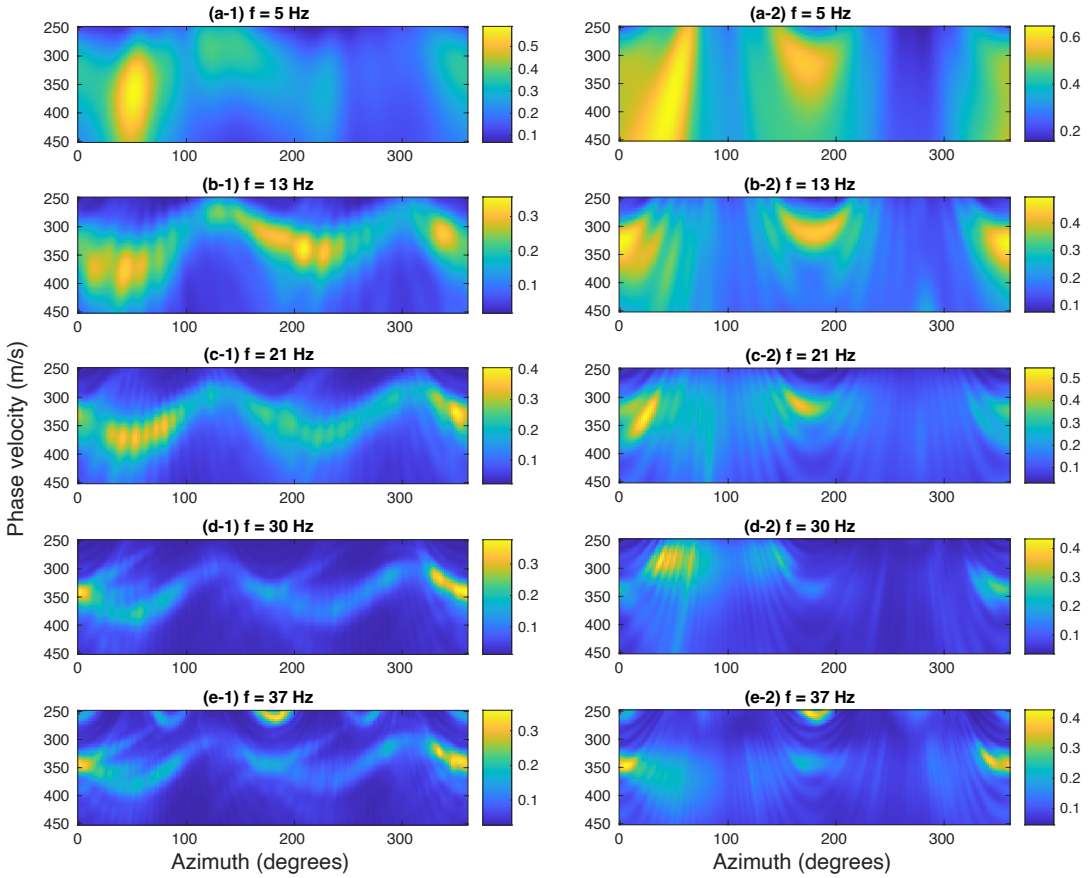


Figure 2.15: Plane wave beamforming of ambient noise data from 9 days and 9 nights of continuous recordings shown for five selected frequencies. Beamforming for the subarray inside the forest (a-1 through e-1), and for the subarray outside the forest (a-2 through e-2). Note the sinusoidal pattern in the beamformer output of the subarray inside the forest for all the frequencies shown. The subarray in the field is evidently not able to sufficiently resolve the noise along the direction perpendicular to the forest-field boundary (around 90 degrees and 270 degrees) because of the smaller array aperture. Note that the $y$ axis representing phase velocity is reversed in all the plots. The color scale denotes the beampower which is always less than 1. This is because incoherent noise that approaches the array from different directions prevents it from being ideally tuned to a specific noise source.

### Influence of array geometry

There is smearing out of the peaks in the beamformer output due to inhomogeneous velocity structure and a finite array, i.e. energy reception will extend beyond the intended look direction for each steered or beamformed angle. The degradation of the plane-wave beamformer can also occur due to a curved wavefront, resulting in high beamformer output across a broader range of azimuths. This ambiguity arises from the matching of the curved wavefront with plane waves at multiple angles. Surface waves generated by sources close to the array, characterized by a curved wavefront, contribute to this degradation.

### Array Response

The impact of the array geometry on the beamforming estimates is primarily governed by the array response, which represents the beam response to an ideal plane wave signal. The array response varies for each frequency and azimuth considered, and can be plotted separately in the $C - \theta$ domain by summing the response for each azimuth bin for a given frequency. The response of an array is, of course, independent of the data and only a property of the array geometry. Thus, we construct the CSDM based on the replica itself, which will be an ideal plane wave. For the subarray inside the forest, in Fig. 2.16 the array response for a chosen frequency $f = 40Hz$ and phase velocity $C = 330m/s$ by summing the result over all azimuths. The regular lobes and the side lobes correspond to the response of the array. The position of the lobes and their resolution depend on the frequency.

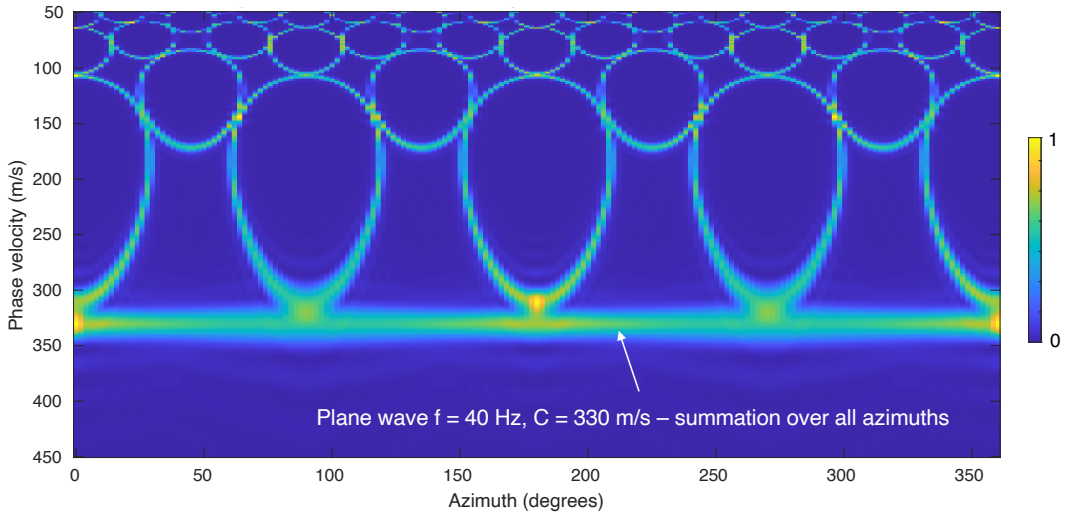


Figure 2.16: Array response at frequency $f = 40Hz$ and wave speed $C = 330m/s$, for the Z-land geophone subarray inside the forest. The response is obtained by summation done over all azimuths from 0° to 360° in steps of 2°. Here, the CSDM is not constructed from the actual data but rather from a model similar to the replica vector with a selected frequency $f$ and phase velocity $C$.

### Array aperture

The array aperture governs the velocity resolution in the beamforming output. The term "array aperture" refers to the size of an array. This is to say that the larger the array size, the more constrained is the beamforming output in the velocity space. This is demonstrated by a simple example using three subarrays A, B and C of increasing aperture for the vertical component Geokinetics array shown in Fig. 2.17. For the subarray A, at a frequency of 21 Hz, it becomes difficult to focus the surface waves projected with wavelength of $\sim 17m$, which is comparable to the aperture of the array of $36m$ for a given direction of the incoming wave (here, roughly from azimuth $\theta = 200°$). For a smaller aperture, it becomes more difficult to measure phase shift between the station pairs, which results in a bigger spot in the beamforming plot. The size of a geophone array must extend many wavelengths to

achieve high gain. As the size of the array increases for subarray B and eventually to subarray C, not only are phase velocity estimates more stable, but also the arrivals are better distributed across azimuths. The simultaneous increase of the number of stations with size permits more azimuthally distributed paths (station pairs) used in the CSDM computation and thus improves the beamforming output. The effect of the array aperture is also clearly observed in the subarray outside the forest, where we have a 120m aperture in the $x$-direction and a 30m aperture in the $y$-direction. This results in a poor resolution of the Rayleigh wave phase velocity for the azimuths $\theta = 90°$ and $\theta = 270°$ and good estimates for $\theta = 0°$ and $\theta = 180°$ (Fig. 2.15 a-2 through e-2).

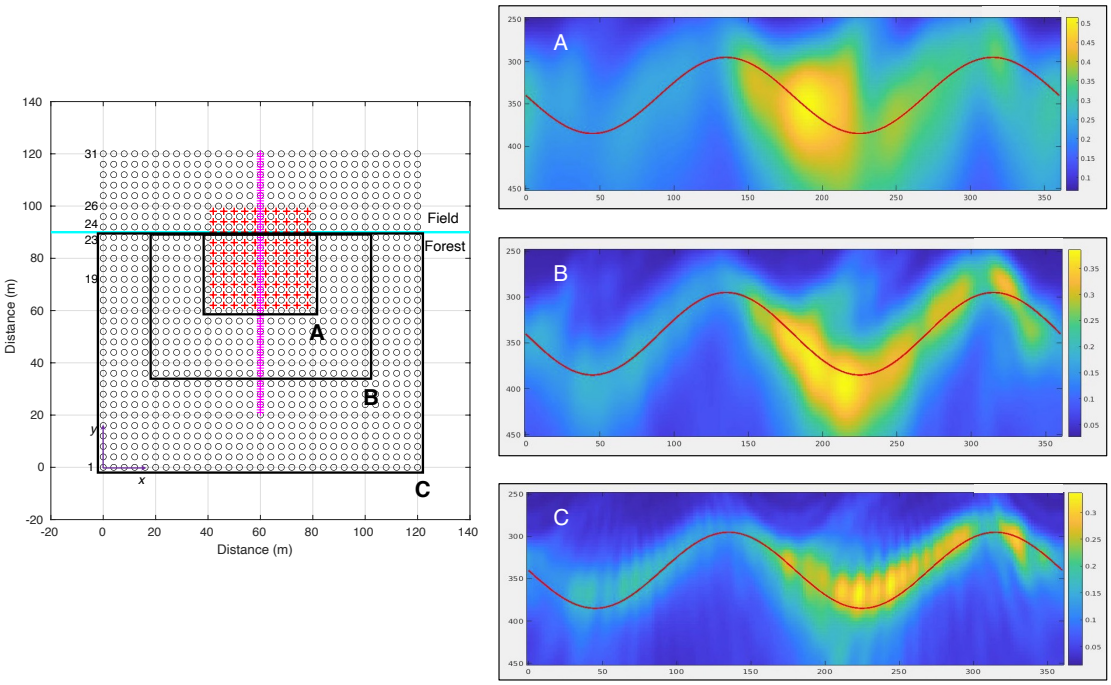


Figure 2.17: Effect of array size on the beamforming at frequency $f = 21Hz$ for three different subarrays A, B and C, for the same noise recording of five hours starting at 05:00:00 UTC on 20th Oct 2016. The red curve is not a fit, but rather serves as a fixed reference to see the variation of the beamformer output with increasing array size.

### 2.4.3 Beamformer Output: 3C Array

The beamforming of the rotated horizontal components from the 3C GFZ square array employs a similar approach as that used for the vertical component array. The array layout is regular with a 10 x 10 configuration and a 4m intergeophone spacing. We used the full array, both inside and outside the forest, due to the small aperture of 36m in both the $x$ and $y$ directions. We process 46 hours of data from the 20th, 21st and 22nd October 2016. The selected data correspond to the hourly recordings that had at least 99 nodes, i.e., ($N \geq 99$). Other hourly recordings that contained lesser nodes ($N < 99$) were not considered due to ambiguity in geophone ordering.

We take 1 min long time segments with 30s overlap to construct the CSDM for every such window. For each 1 min recording, we take 10s long half-overlapping windows for the CSDM averaging. Finally, for each frequency, the CSDM of the rotated data is matched against a replica, and the beamforming output is obtained. Due to the polarization of the waves, we always see maxima in two azimuth directions in every beamformer output (Fig. 2.18). Phase velocity pairs from these two directions of wave incidence can thus be considered as that corresponding to the pure SH wave polarization state and thus corresponds to Love wave propagation.

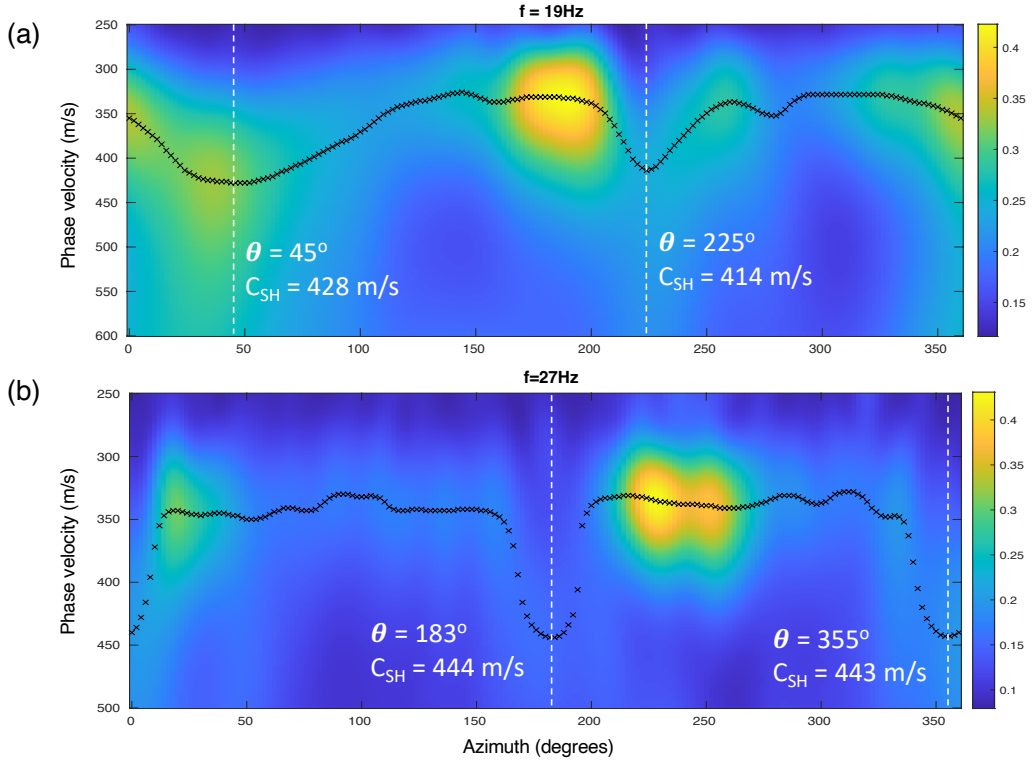


Figure 2.18: Plane wave beamforming of the horizontal component $EHN_{\phi}$ at two frequencies $f = 19Hz$ and $f = 27Hz$ usuing the GFZ square array. The black crosses here are simply the maxima for each azimuth. (a) When the horizontal components are rotated by $\phi = 45°$, the plane wave arriving from the direction $\theta = 45°$, will show a maximum phase velocity along this axis, i.e., for directions $\theta = 45°$ and $225°$ corresponding to the pure SH wave. (b) When the horizontal components are not rotated, i.e. $\phi = 0°$, the plane wave arriving from directions $\theta = 355°$ and $183°$, shows a maximum velocity for the EHN component due to the pure SH-wave propagation. The slight tilt, which is a discrepancy from the expected fast directions of $0°$ and $180°$ is due to the anisotropy of the medium.

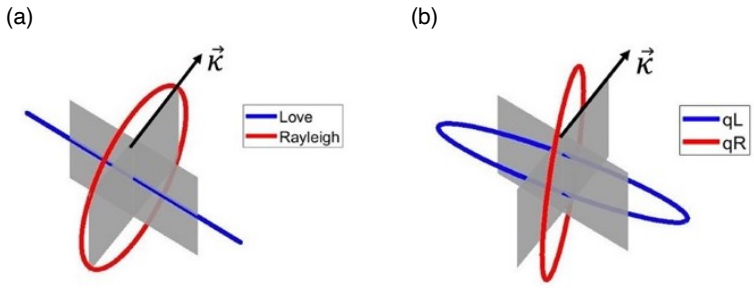


Figure 2.19: Illustration of polarization of Rayleigh and Love wave w.r.t the direction of propagation in isotropic media (a), and quasi-Love (qL) and quasi-Rayliegh (qL) wave in ansiotropic media (b) as proposed by Tanimoto [2004]. The qR wave and Rayleigh wave are both elliptically polarized except that that the qR wave is tilted w.r.t the vertical plane. The qL wave polarization and is no longer linear and has a tilt. (adapted from Tang et al. [2023]).

The maximum phase velocity for frequency $f = 27Hz$ is obtained for a plane wave incidence at 355° and 183° when the particle motion is in the plane of the EHN component. Thus, there is a tilt of $3° - 5°$ for the Love waves propagating in this direction. This was described by Tanimoto [2004] for an anisotropic medium that the particle motion is neither orthogonal nor linear due to the small vertical component with phase lag (Fig. 2.19). He pointed out that although the particle motion of the "quasi-Love" waves is not transverse in an anisotropic medium, when the anisotropy is weak, it is expected that the angle between the direction of propagation and the horizontal plane remains close to 90°. Hence, we consider the assumption of orthogonal particle motion to be rational for the analysis of Love wave beamforming. In the following section, we quantify the Rayleigh and Love wave anisotropy using the beamforming results.

## 2.5 Azimuthal Anisotropy of surface waves

In this section, we discuss the dependence of surface wave phase velocity on the azimuth as observed from the results of the array processing in the previous section. According to the classical anisotropy for surface waves, first proposed by Smith and Dahlen [1973], the azimuthally dependent phase velocity for laterally homogeneous media can be written as

$$C(\omega, \theta) = A_1(\omega) + A_2(\omega)cos2\theta + A_3(\omega)sin2\theta + A_4(\omega)cos4\theta + A_5(\omega)sin4\theta \quad (2.6)$$

where $\omega$ is the angular frequency and $\theta$ is the azimuth of the wave-number vector. The coefficients $A_n(\omega)$ are functions of frequency $\omega$ since the surface waves are dispersive. This equation describes a general anisotropy model with the coefficients $A_n(\omega)$ depending on 13 depth functions that are linear combinations of the elastic coefficients of the material (see Montagner and Nataf [1986] for a detailed description of these functions).

### 2.5.1 Rayleigh wave Azimuthal Anisotropy

From the beamforming output of the vertical component shown in Fig. 2.15 (a-1 through e-1), it is clear that the forest shows strong anisotropy in phase velocity with respect to azimuth for all observable frequencies. In this section, we quantify the Rayleigh wave (RW) azimuthal anisotropy. Surface waves mainly sample the crust and the upper mantle. Theoretical computations by Montagner and Nataf [1986] and Montagner and Anderson [1989] for the upper mantle and direct observations for the crust (3C array in Southern California) by Alvizuri and Tanimoto [2011] and Riahi and Saenger [2014] have shown that the $2\theta$ term is the dominant feature of the RW anisotropy compared to the $4\theta$ term. The dominant $2\theta$ term is due to the elastic coefficients that are related to the speed of P waves and SV waves (Montagner and Nataf [1986]). Thus, we reduce the anisotropy model for surface waves in Eq. 2.6 to just the first two terms, while the other terms are assumed to be negligible. Rewriting and simplifying, the azimuthally dependent phase velocity for a given frequency $f$ becomes

$$C(f,\theta) = C_0(f) + \Delta C(f) * cos(2(\theta - \theta_{fast})) \tag{2.7}$$

where, $C_0$ is the mean velocity of the medium, the coefficient $\Delta C$ gives the deviation of the velocity from the mean value and $\theta_{fast}$ is the direction of the fast axis. For $f = 21Hz$ as shown in Fig. 2.20(a), the mean velocity is 340 m/s and the variation is 45 m/s from the mean, with a fast axis oriented in the 45° direction. We define the degree of anisotropy as $(\Delta C/C_0) * 100$, which is 13% at $f = 21Hz$. By averaging phase velocity over all azimuths for each frequency, we estimate the dispersion of Rayleigh waves, as shown in Fig. 2.20 (b). The dispersion trend is the opposite of what is typically expected, i.e., phase velocity increases with frequency, evident between 7-20 Hz. This is explained by the velocity structure beneath the forest, with the presence of a hard pan having high velocity. Lott et al. [2020a] obtained dispersion curves for Rayleigh waves from active source excitations using two methods (1) double beamforming (DBF) of the GFZ line array and (2) using two-point correlation for the Geokinetics Z-comp array inside the forest. There is a good match after 25 Hz between the dispersion obtained in this study and that of the previous study. There is, however, a slight discrepancy in the results from the DBF, since it only measures phase velocities in one direction (GFZ line aray, oriented at $\theta = 90°$) whereas the 2-point correlation is averaged over different azimuths and thus better matches our result. The strength of anisotropy (Fig. 2.20 (c)) varies with frequency and has a maximum of 17% at 10 Hz, which is considered significant in a local seismology context.

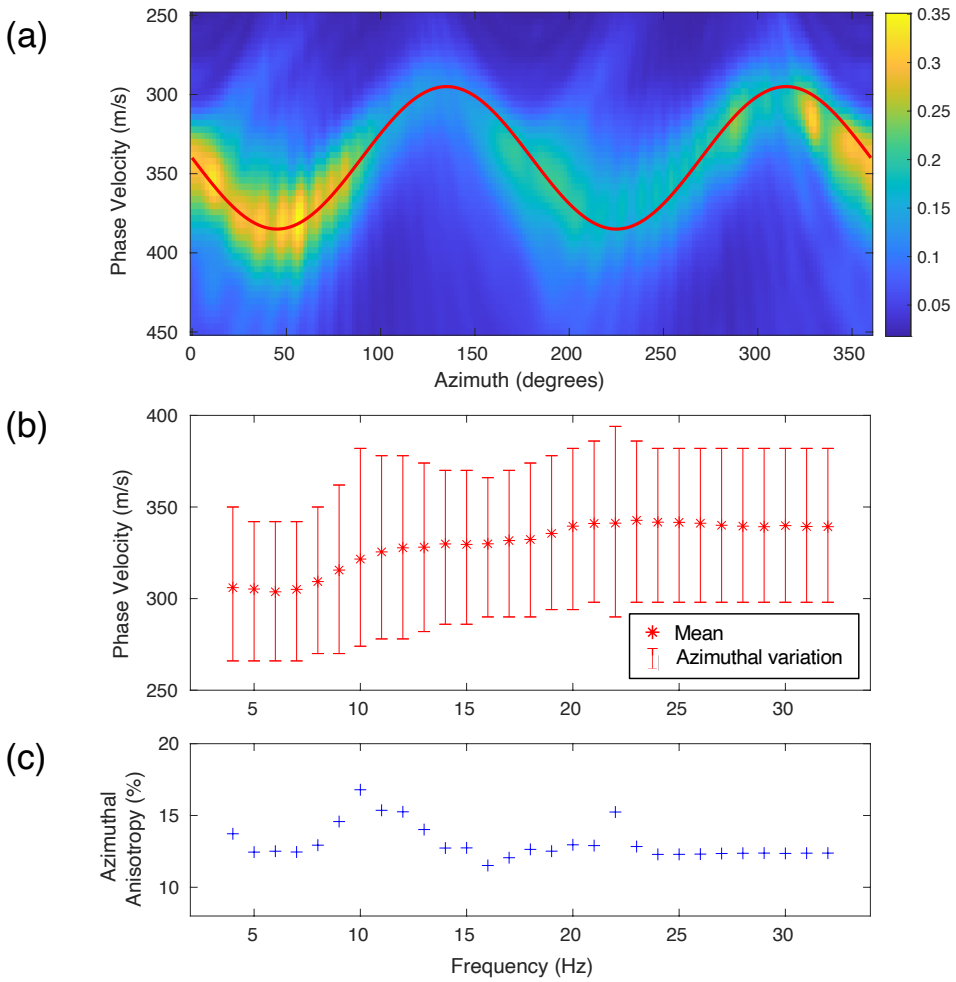


Figure 2.20: (a) Anisotropy model (shown in red) with only the cos2$\theta$ term is overlaid on the plane wave beamforming result for frequency f = 21 Hz. A high degree of anisotropy ($\sim$ 13%) with a fast axis oriented in the 45° direction is observed. The red curve is an "eye ball" fit. (b) Rayleigh wave dispersion from the azimuthal averaging of the beamforming results. For frequencies above 32 Hz the array response starts interfering with the beamforming result. (c) The degree of anisotropy $\Delta C/C_0 * 100$ is observed to be high across the observed frequencies, varying from $11 - 17\%$ inside the forest.

The azimuthal anisotropy of Rayleigh waves can also be confirmed by wavefield dispersion in the reciprocal space $(k_x, k_y)$. Fig. **??** shows a series of plots for selected frequencies. The plots are obtained from active source data, taking a spatial Fourier transform for every $(k_x, k_y)$ value possible, and stacking over small temporal windows of the diffuse coda, similar to the method followed in Lott and Roux [2021]. The radiation ellipse shows a clear anisotropy with a fast axis oriented at 45°. Beyond the frequency of $\sim$ 40 Hz there is aliasing. The bright dots close to the center of the plots are from the body wave branch of the dispersion.

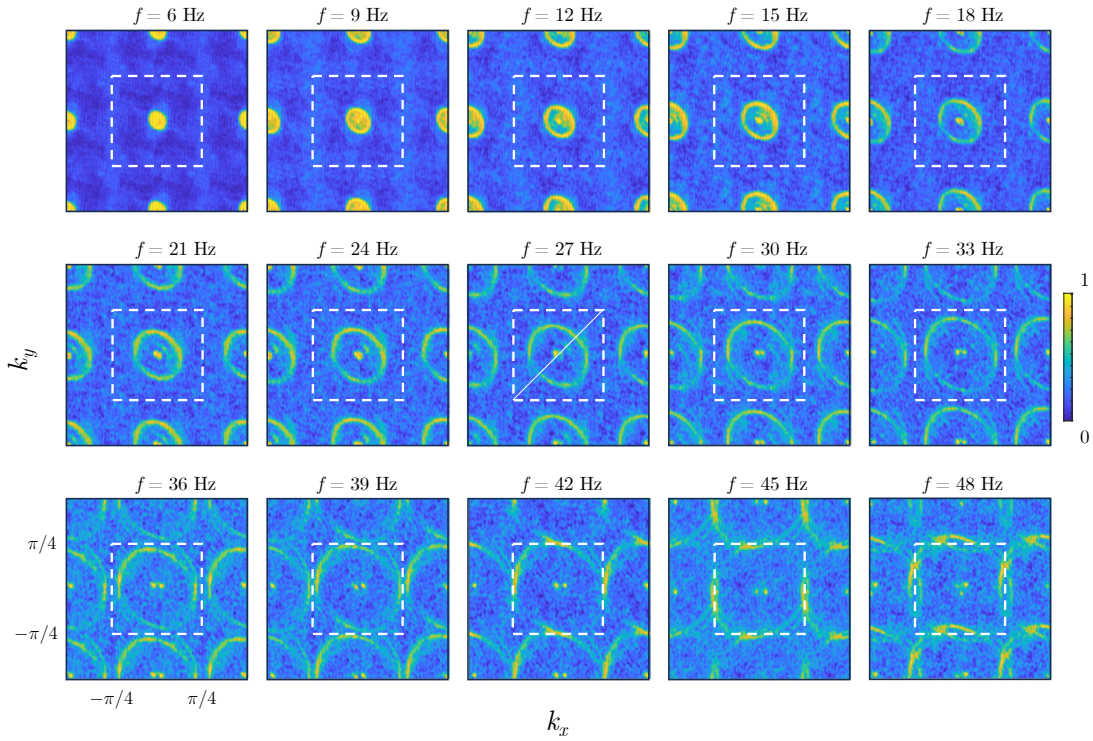


Figure 2.21: Wavefield pattern at selected frequencies in reciprocal space by computing the spatial Fourier transform for every $k_x, k_y$ possible value, stacking over small temporal windows of diffuse coda of active sources. The white dashed square is the Nyquist-Shannon limit. One can clearly observe the radiation ellipse for the surface waves inclined at 45° over the entire frequency range. The bright spots near the centre of the images correspond to the P wave which travels much faster than the surface waves. (Snapshots of the movie used with permission from Martin Lott)

### 2.5.2 Love wave Azimuthal Anisotropy

We use phase velocity pairs obtained for the fast directions corresponding to the pure SH wave polarization, as shown in Section 2.4.3. We use these values from various rotation scenarios of horizontal components to populate the azimuthal distribution of phase velocity of Love waves in Fig. 2.22. Contrary to Rayleigh waves, for Love waves, it was observed in the literature that the anisotropy is contributed by both $2\theta$ and $4\theta$ terms, and mainly by $4\theta$ because the elastic coefficients are related to the speed of SH waves (Montagner and Nataf [1986]). However, we did not quantify this anisotropy as a result of gaps in the azimuth domain. A rough estimate at two frequncy points of $f = 19Hz$ and $f = 27Hz$, gives an idea of the anisotropy, although from partial azimuthal trend. This seems to be on the same order of the Rayleigh waves (about 13%).

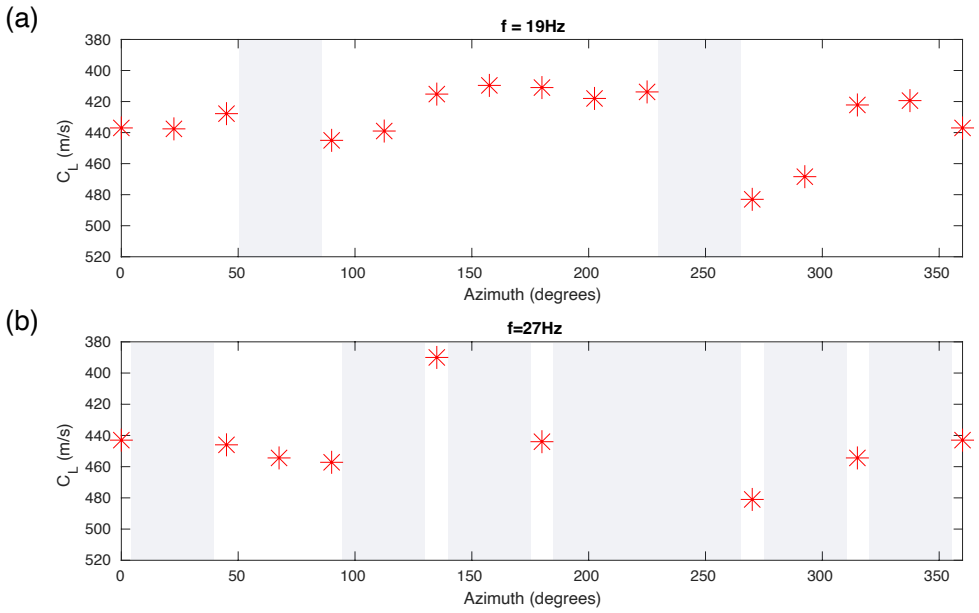


Figure 2.22: Love wave phase velocity distribution with azimuth, at two frequencies (a) f= 19Hz and (b) f = 27Hz. The plots are populated by discrete values of phase speed (red asterisks) obtained from the rotation of the horizontal components. The gray regions are the azimuths for which the Love wave illumination is not sufficient to perform a good quality beamforming.

### 2.5.3 Discussion: Origin of the anisotropy

Identifying the cause of the observed anisotropy is important to understand the propagation of surface waves in the forest metamaterial. It is challenging to track the origin of anisotropy, especially in the near-surface region, where the soil is layered and heterogeneities are present. An important advantage of using noise correlations is that the sensitivity zone of the measurements is localized in a narrow region connecting the sets of station pairs. This means that the anisotropy for the subarrays we choose is well localized inside and outside the forest, respectively. For the case of Rayeigh waves, comparing the beamforming plots for the vertical component inside and outside the forest (Fig. 2.15), we cannot immediately conclude if the observed Rayleigh wave anisotropy is caused by the trees or the forest structure itself. This can be attributed to the insufficient resolution provided by the subarray outside the forest in the N-S direction. But comparing the results from the two arrays only in the direction of the same aperture for different frequencies, there seems to be little to no difference in phase velocities inside and outside the forest. However, to have a conclusive argument, we would require more evidence for a clear difference between the two cases. Another possibility is that the forest can have a strong anisotropy and in the canola field there could be a weaker anisotropy.

There are two distinct characteristics that define the Rayleigh wave anisotropy inside the forest, irrespective of the frequency;

- a $2\theta$ variation, and

- a 45° fast axis,

In our case, focusing on qualitative aspects of anisotropy may be more useful. he reason why we omit the other characteristic, which is a high degree of anisotropy $\sim 11 - 17\%$, weakly dependent on frequency. Although there could be many elements that could influence the anisotropy, the intrinsic anisotropy of the materials is the most basic form of azimuthal anisotropy. This is a commonly encountered phenomenon for the deeper crust and upper mantle, for example, in olivine crystals, where the intrinsic anisotropy is present at all scales. The single biggest clue for intrinsic anisotropic properties that are responsible for our observations is that the qualitative aspects of the azimuthal anisotropy remain the same irrespective of the observed wavelength, i.e., sensitivity depths from 3m (40 Hz) to 30m (4 Hz).

On the other hand, we also have extrinsic anisotropy, which are anisotropic effects caused, for example, by the presence of fluid in the medium or due to the crack distribution. Another example of this is when we have a layered medium in which each layer itself is an isotropic material, but the effective properties of the medium are anisotropic. Unlike intrinsic anisotropy, extrinsic anisotropy depends on the wavelength and spatial scale of the various processes. It is possible that the origin of the anisotropy is non-unique, but the challenge would be to separate the effects. There are several fundamental ambiguities that prevent us from finding the origin of the anisotropy. We break down our discussion into the possible role of (1) trees and (2) the subsurface structure.

### 1. Role of trees as resonators

Trees themselves can be assumed to be discrete masses, which increase the local density of the medium near the surface. We know that surface waves are quite sensitive to perturbations of the free surface. This can, in principle, be a reason for the surface waves to have anisotropic properties. However, we can immediately discard this hypothesis because had it been so, the Rayleigh wave anisotropy would show a $4\theta$ dependency instead of $2\theta$. Also, if it were the case that the tree resonances were causing the anisotropy, it would have been limited to finite frequency bands, but we observe similar results for all the observed frequencies.

### 2. Role of forest and subsurface structure

*Forest structure*

Soils in a forest often have a heterogeneous structure, with surface layers that are more or less penetrable by roots, stones, and buried plant debris. Soil analysis (Fig. 2.3) and GPR survey have confirmed the presence of the hard pan layer. The soft sediment layer can guide the surface waves, similar to plates, but there will be attenuation of the field as waves are free to scatter in the bulk. Before planting the trees, the farmer breaks the ground in parallel rows to increase the effectiveness of top soil cultivation by ripping and improving the impermeable or heavy subsoil, resulting in better survival and growth of the trees. The tree plantation is then done roughly in equally spaced parallel rows. Thus, this bilayer forest structure could be a possible origin for the observed azimuthal anisotropy.

The root system consists of a deep taproot with a well-developed secondary root system commonly seen in pine. Danjon et al. [1999b] use three-dimensional (3D) digitization methods to measure cross-sectional areas and root volume distribution

as a function of depth, azimuth, and radial distance, as shown in Fig. 2.23. The root distribution in the depth direction is mostly confined to the first layer above the fractured hard pan that has a decent lateral spread. The plan shows that the tree volume is not perfectly distributed along all radial directions and is least in the direction of the tree rows. Although trees are planted uniformly in rows, the non-uniform distribution of nutrients can influence root distribution and development at the full maturity of the forest. Furthermore, from the tomography results (personal communication), there seems to be a tilted reflector under the forest, at a depth of roughly 20-25m. However, surface waves become sensitive to this reflector at frequencies lower than 5-6 Hz. But we observe the anisotropy at much higher frequencies. Therefore, we also discard this hypothesis.

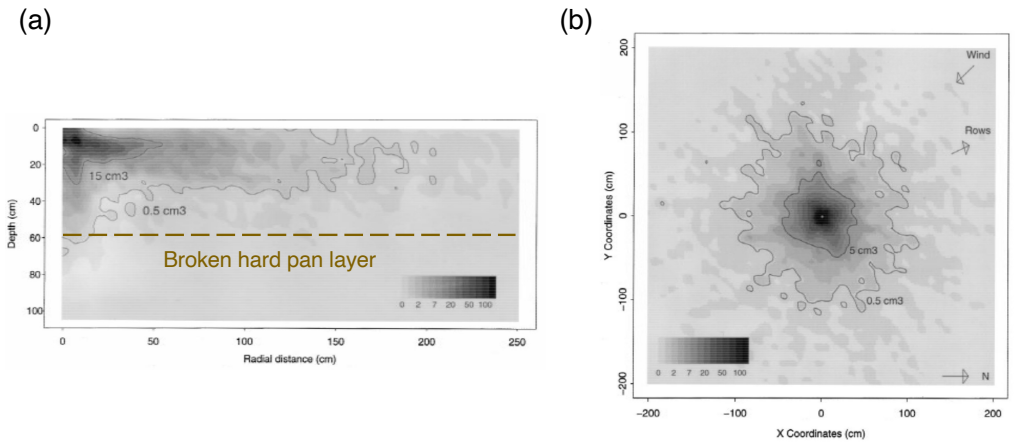


Figure 2.23: Spatial distribution of roots of pinus pinaster. (a) Cumulative 2D spatial distribution of root volume ($cm^3$ within a surface area of $25cm^2$) as a function of depth and radial distance: tree mean, and (b) Cumulative 2D spatial distribution of surface (depth $<$ 30cm) root volume ($cm^3$ within a surface area of $100cm^2$) in the horizontal plane (i.e. integrated over depth): tree mean (from Danjon et al. [1999a]).

*Aligned fractures*

This leaves us with the explanation that the anisotropy could be due to regular fracturing of the upper soil layers that can cause HTI anisotropy (Fig.2.24). A medium having vertical fractures which are preferentially aligned, as in the forest, the symmetry is horizontal transverse isotropy and, therefore, can exhibit azimuthal anisotropy. Tanimoto [2004] showed plots of analytic and exact solutions for both Rayleigh and Love waves in a layer of HTI media overlying an isotropic half-space (Fig.2.24). According to Montagner and Nataf [1986], Rayleigh waves travel faster in a direction that is the same as that of faster P waves, due to the particle motion. If aligned fractures are responsible for the azimuthal anisotropy, then the fractures in the forest should be oriented N45°E with respect to the array, which may be unlikely.

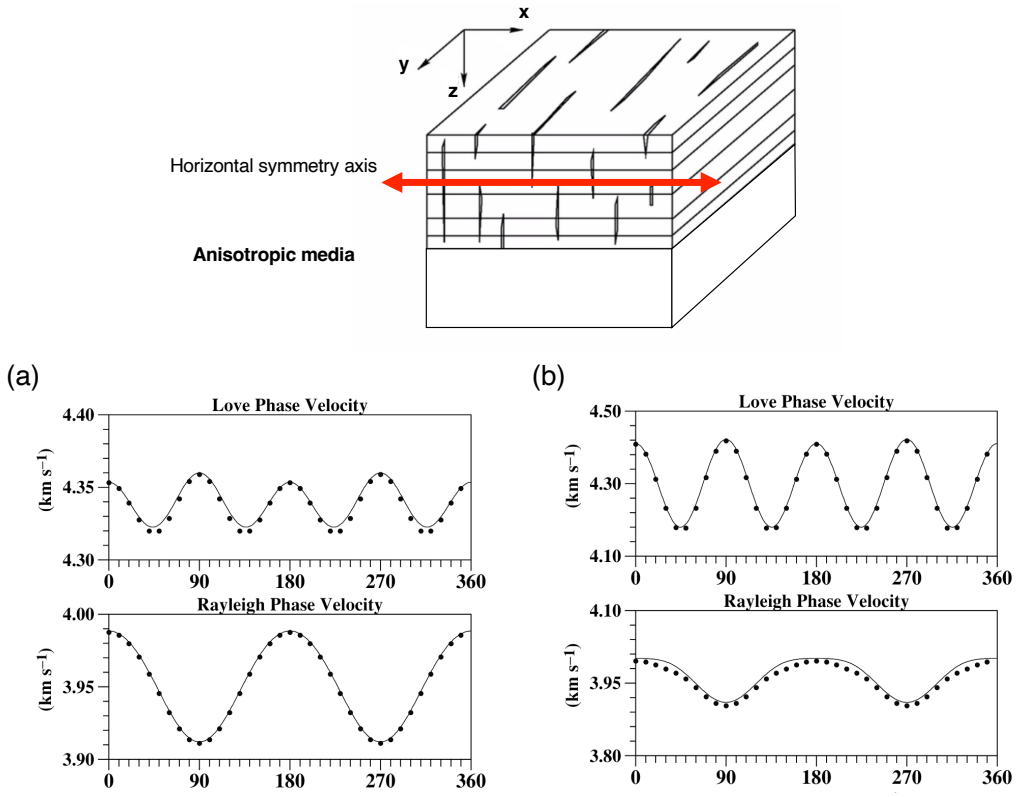


Figure 2.24: Azimuthal anistropy of HTI media. Results from a study by Tanimoto [2004] showing a comparison of analytic and exact (numerical) solutions. The medium has a simple one-layer over a half-space model and transversely isotropic symmetry with the symmetry axis pointing in the $x$-direction whereas the lower half-space is isotropic. (a) Both P and S wave velocities are assigned 5% anisotropy in the two orthogonal directions, and (b) isotropic P-wave velocity and 10% anisotropy for S-wave velocity in the upper layer. This kind of medium produces a cos $2\theta$ anisotropy.

### Numerical simulations for diagnosing the observed anisotropy

We ask the question: if the anisptropy is derived from the forest or subsurface structure, how can the effect of the trees be isolated from the effect of the subsurface structure on the anisotropy? The key differences between the forest subsurface and the field would be (a) the absence of roots and (b) the absence of a damaged hard pan in the field. Running simulations with different models that account for both soil structure and tree roots will be more conducive to identifying their respective contribution.

Anisotropy in the case of elastic metamaterials is not unusual. For example, Antonakakis et al. [2014b] through simple analytical and numerical studies, observed strong anisotropy for the effective medium of a plate with periodic clamped holes. In a laboratory experiment with a forest of regularly glued aluminum rods to an aluminum plate, Lott and Roux [2021] observed that after the inflection point, the energy leakage from the source inside the metasurface is anisotropic. A similar dynamic anisotropy was also observed by Colombi et al. [2017b] from numerical simulations in the time domain of both a plate and a half-space with rods attached to

the free surface. All these studies report a cross-shaped anisotropic profile that starts to be visible at the inflection point of the dispersion curve (see the bottom panel of Fig. 2.25). However, those observations are different from the METAFORET results in two ways: first, we see a radiation ellipse ($2\theta$ variation) instead of a cross-shape ($4\theta$ variation), and second, we see the same shape of the ellipse for all observed frequencies which is more of a quasi-static anisotropy. These frequencies are below the longitudinal resonance of the trees, and thus we cannot comment on the anisotropy in that regime.

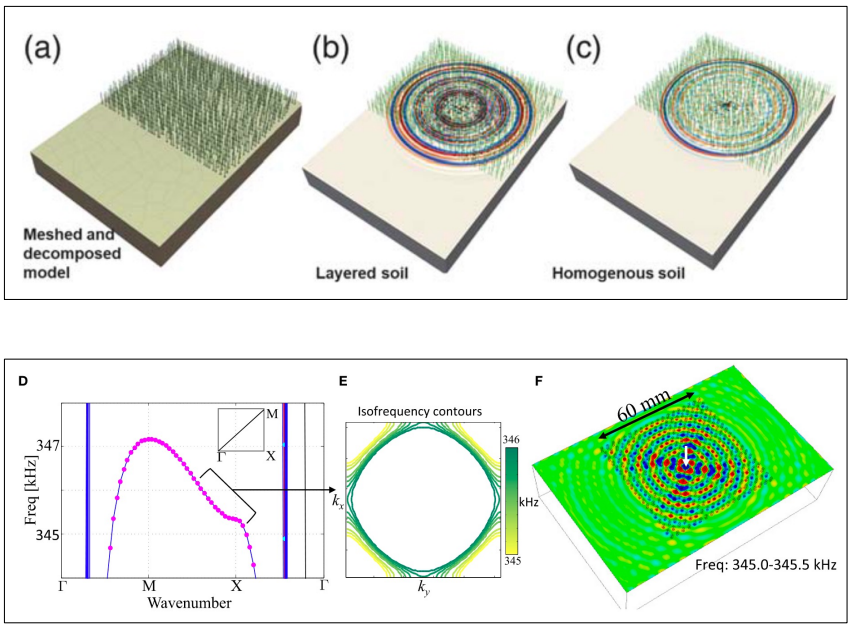


Figure 2.25: Anisotropy in locally-resonant metamaterials. (Top panel) 3D numerical simulations reported by Roux et al. [2018] for trees over an elastic half-space. The figures show the model meshing (a) and the vertical component wavefield snapshots for a broadband source inside the forest for the cases of layered (b) and homogeneous (c) soil media, respectively. (Bottom Panel) Similar numerical simulations from Colombi et al. [2017b], but for 2D array of rods showing a zoomed section of the dispersion curve around the first longitudinal resonance (D). The plots in reciprocal space show the isofrequency contours with a hyperbolic pattern around the inflection point (E). Wavefield snapshot with the source located at the center of a cluster of rods (F), when filtered in the band shown by the bracket in the dispersion curve plot. The tree simulation shows a relatively circular spreading of the broadband wavefront inside the forest. On the other hand, the beam metasurface reveals a strong dynamic anisotropy in the regime of the inflection point of the dispersion curve.

In Roux et al. [2018], spectral-element time domain simulations are discussed briefly without discussing about the anisotropy aspect of the wavefield. For example, see snapshots of the wavefield excited by a Ricker source centered at 50 Hz for a domain having a realistic forest tree pattern and vertical soil layering (top panel of Fig. 2.25 (b)). Apparently, the wavefield after a few milliseconds of the zero time of

the source, for both the layered and the homogeneous soil cases, seems to be quite isotropic (circular wavefront instead of elliptical) for such broadband excitation. We nevertheless ask ourselves the question: *Could the observed anisotropy be reproduced with numerical simulations considering (a) the tree arrangement, and (b) subsurface that is more accurate than a 1D stratified soil profile?*

For a future study, we suggest a simulation using a heterogeneity model to evaluate the anisotropy effects. We propose one such model schematic shown in Fig. 2.26 based on the literature and some of the findings of this study. The top layer of soil overlying the hard pan can be idealized as an HTI medium with a symmetry axis that points in the $y$-direction. Alternating rows of soil and root-soil composite can be assumed for this top layer. Intuitively, the surface wave speed should be faster along the direction of the fracture ($x$-axis) and slowest in the perpendicular direction ($y$-axis), but this should be verified. In the second step, a checkerboard model can be used, but with the root-soil composite staggered in the $x$ and regular in the $y$-direction that matches the actual tree distributions.

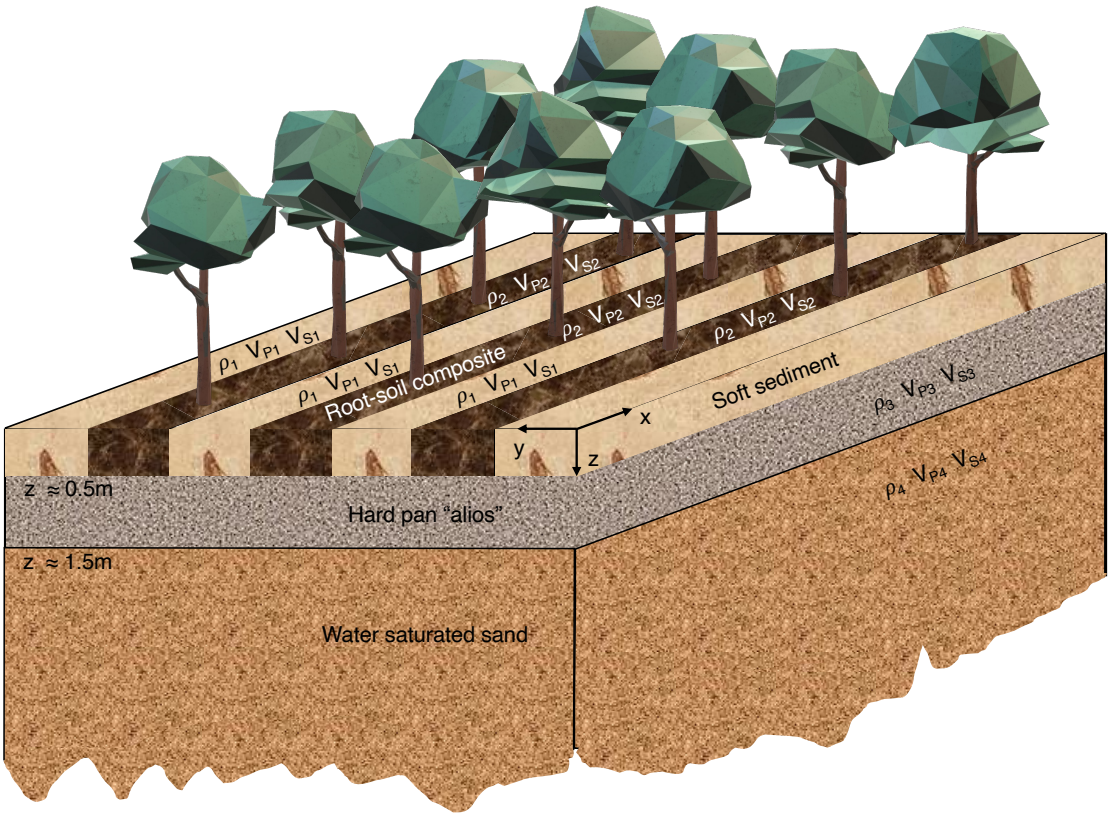


Figure 2.26: The proposed simplified METAFORET velocity model that can be reasonable for performing numerical simulations to further understand the role of the layering and the tree root structure in the observed azimuthal anisotropy.

A more realistic model can be further analyzed to take into account (only for a second-order analysis):

1. trees as slender beams that exhibit flexural modes at low frequencies and compressional resonances at higher frequencies,

2. more realistic effects in the mechanical parameters of the soil, for example, using a viscoelastic model instead of an elastic one and vertical gradients for density and shear stiffness/velocity, and

3. the shape of the heterogeneities, e.g., accounting for the conical shape for the root-soil composite (example, see Ding et al. [2022]), for the tap root system of pine trees.

## 2.6 Concluding remarks

It was found that around the tree longitudinal resonance frequency, the energy radiated by the trees is evanescent inside the forest. However, for tree flexural resonances, we observe a weak coupling of the tree dynamics and the surface waves in the frequency band of 1-10 Hz. Strong surface wave azimuthal anisotropy exists in the forest. Rayleigh wave anisotropy exhibits a $\cos 2\theta$ variation with a fast axis oriented in the 45° direction with respect to the array over a broad observable frequency range. Results for the Love wave anisotropy are less conclusive, because of the small aperture of the 3C array and due to the inadequate illumination of the SH waves. Nevertheless, the degree of anisotropy for both Rayleigh and Love waves seems to be high, on the order of $11-17\%$. The origin of the strong anisotropy could not be determined. However, the total anisotropy we observe could be either due to: (1) intrinsic anisotropy of the shallow soil layer, (2) near-surface heterogenities introduced by roots, and (3) preferential fracturing of the layers, or a combination of these factors.

# Chapter 3

# Surface wave propagation in a dense wind farm

The META-WT experiment piece of this chapter with the initial comprehensive results was published in Pilz M, Roux P, Mohammed SA, Garcia RF, Steinmann R, Aubert C, Bernauer F, Guéguen P, Ohrnberger M and Cotton F (2024), Wind turbines as a metamaterial-like urban layer: an experimental investigation using a dense seismic array and complementary sensing technologies. *Front. Earth Sci.* 12:1352027. doi: 10.3389/feart.2024.1352027

**Summary**

The core of this chapter lies in the experimental investigation of the possible metasurface created by arrays of wind turbines at the geophysics scale. We identified two wind farm sites that house densely arranged wind turbines - one with smaller but identical turbines and another with much bigger but heterogeneous turbines. We analyzed ambient noise data from arrays deployed at these locations using a similar approach. This is effectuated by (1) analyzing spectral amplitudes both inside and outside the wind farm, and (2) performing a coherent analysis involving spatial correlations to extract the effective properties of surface waves like phase velocity and scattering. In the first wind farm with a sparse geophone array, we observed no drop in spectral intensity inside the farm, nor any anomalous surface wave dispersion or strong scattering associated with wind turbine fundamental resonance. At the site of the second wind farm, we deployed a DAS fiber optic cable as part of the seismic near-field assessment alongside other sensors. The dense sampling allowed a detailed study of the near-field radiation and propagation of surface waves. Here, we observed unusually strong damping of surface waves in specific frequency bands, indicating evanescent propagation within the wind farm. We have experimentally demonstrated that a set of wind turbines in a wind farm - that are sufficiently close to each other in relation to the seismic wavelength (a few hundred meters), can in some respects exhibit a metasurface-like behavior for seismic surface waves.

## 3.1 Background

Classical approaches with seismic metamaterials aim at designing a set of spring-mass resonators coupled to the ground to cancel seismic surface waves on a specific

meta-surface. In this chapter, we investigate the role of the wind turbines (WTs) themselves as the set of coupled resonators that could potentially create a meta-surface. Based on the results of the METAFORET experiment, the purpose of this study is to transpose the previous results (both the experiment and the numerical simulations) to a larger scale (hundreds of meters to a few kilometers) and lower frequencies ($< 10Hz$), on the assumption that the cluster of WTs in a wind farm should behave as the pine trees did in the METAFORET experiment.

### 3.1.1 Motivation for this study

In the preceding chapter (Chapter 2), it was comprehensively described how trees, due to their local resonances, can modify the propagation of surface waves in the forest. It has been experimentally observed and confirmed through numerical simulations that the frequency bandgap is associated with the longitudinal tree resonance (Colombi et al. [2016c], Roux et al. [2018], Lott et al. [2020a]). Furthermore, within the bandgap, we have found the radiation of the tree resonances to be evanescent inside the forest. As far as earthquake ground motion in urban areas is concerned, which is also the motivation for this thesis, the target frequency band is one to two orders lower (∼0.5-5 Hz) for the longitudinal resonances of trees. In the context of seismic protection of civil engineering structures through a forest of trees, one would need trees that can resonate at much lower frequencies, i.e., trees that are extremely tall and heavy. Although flexural resonances of trees are present at low frequencies (below 10 Hz), we did not find any interesting bandgap-like behavior.

For the purpose of discussion, consider a tree 10 m tall with a uniform cross section, clamped at its lower end and free at the top, and assume the average material properties from the literature (Colombi et al. [2016c],Roux et al. [2018]): $\rho = 500$ kg m$^{-3}$, $V_p$= 2500 m s$^{-1}$ and $V_s = 1300$ ms$^{-1}$. We obtain the fundamental longitudinal mode of the tree around $f_l^{(1)} = 52$ Hz using the expression $f_l^{(n)} = \frac{(2n-1)}{4L}.\sqrt{\frac{E}{\rho}}$. Here, $L$ is the height of the resonator, which has a material density $\rho$ and a Young modulus $E$. The position of the bandgap is certainly driven by the resonator height. However, it is not just the height of the resonator that dictates the metamaterial effect. In the analytical expression derived by Colquitt et al. [2017], the bandgap width around the longitudinal resonance of beams attached to a half-space is inversely proportional to the length of the resonator. Intuitively, short resonators maximize the bandgap size, but there are other material parameters of the resonator that appear in that expression. The bandgap opened at the tree resonance frequency would still be too high considering practical applications in the seismic hazard context. As a hypothetical scenario, if we consider trees ten times taller (∼ 100m) , then the resonance should occur around 5 Hz, although resulting in a relatively narrow bandgap. In any case, this would be more interesting from an earthquake engineering perspective. Such tree species corresponding to these low frequencies, for example, the Giant Sequoia, which can reach heights of more than 100 meters, are not always feasible. Thus, we turn our attention to WTs, which are man-made structures that are relatively tall, heavy, and well-coupled to the ground, and are increasingly prevalent in today's landscape. A scaled version of the tree forest configuration could be a dense forest of WTs.

Interestingly, WTs are often clustered together in configurations labeled as 'wind farm' or sometimes as a 'park', 'plant' or an 'array'. Wind farms can typically vary

in size from a few turbines to several hundred WTs that cover an extensive area. By taking advantage of the grouping of WTs, we can potentially explore their locally-resonant subwavelength behavior. Here, the resonators are neighboring turbines, which are much taller and heavier. The resonance effects of these structures is much more pronounced in low frequencies, similar to those of tall buildings.

### 3.1.2 Structural Characteristics of a Wind Turbine

In recent decades, concerns over the global increase in temperatures have fueled the demand for alternate sources of energy, for example, sunlight, wind, or heat from the earth's interior. WTs are designed and built for the generation of electricity by using the kinetic energy of the wind. These are equipped with a set of blades (usually 3 blades) that are designed such that the aerodynamic forces due to the wind, i.e. the difference in air pressure across the two sides of the blade, make them rotate around their axis when the wind speed is above a certain threshold (cut-in wind speed). When the flow of the air stream is parallel to the axis of rotation, the turbines are called horizontal axis wind turbines (HAWT) (Fig. 3.1). The blades, which are coupled to a main shaft, then transfer this mechanical energy via the high-speed shaft to a generator housed in the nacelle, which converts it into electrical energy. The whole turbine assembly including the rotor blades, hub, and the nacelle is mounted on top of a tower, which is supported by a foundation. We limit our discussion to the horizontal axis WTs in this thesis, as they are the most prevalent WT configuration that is in use today.

Following this climate-driven energy transition, wind energy has seen an increasing share in the global electric power market. Consequently, with the progress in WT technology over the years, individual turbine capacities have consistently increased, resulting in larger and taller WTs (Fig's 3.2a & 3.2b). The power captured by the turbine increases with the swept area and the generation becomes more efficient, since the wind speeds increase with height and become less turbulent. Thus, the same turbine assembly can be mounted on towers of different heights (Fig. 3.2a) to optimally harvest energy according to the wind conditions at a given site. Land-based (onshore) WTs are relatively smaller, and thus have lower capacity compared to their offshore counterparts. However, the scope of this thesis is limited to land-based WTs. The global average hub heights for inland turbines have increased from 81 m in 2010 to 103 m in 2020 (IRENA [2022]). Greater hub heights naturally mean taller and heavier turbine towers.

The turbine tower is the primary load bearing structure of a WT. In addition to being responsible for raising the turbine to the design height, the tower is required to resist both static and different dynamic forces acting on the global structure. The gravity loads are from the assembly including the rotor hub and blades, the nacelle, and all the components that are housed within the nacelle, and the self-weight of the tower itself. In addition to static gravity loads, the forces from the rotation of the blades and aerodynamic loading from the wind are the important dynamic loads that the turbine structure experiences. Steel tubular towers that are tapered along their height are the most common. For larger turbines, the tower is a prestressed concrete-steel hybrid (PCSH), i.e., a major fraction (generally $\sim$ 2/3rd

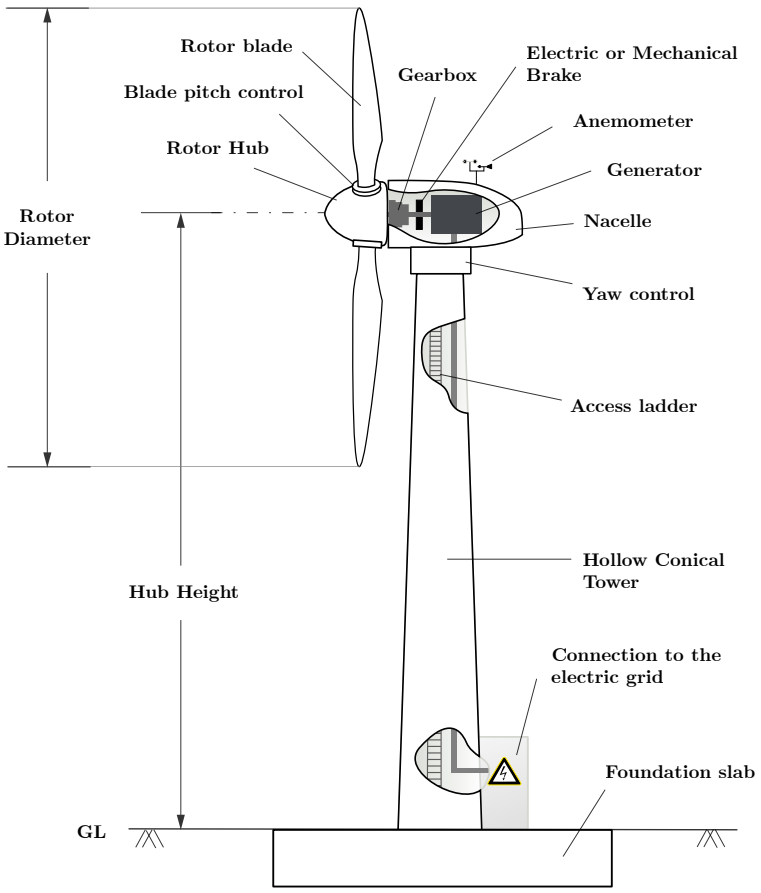


Figure 3.1: Components of a typical Land-based Horizontal Axis Wind Turbine. The various terms are explained in the Glossary section of the thesis. (adapted from Arne Nordmann (norro), CC BY-SA 3.0 http://creativecommons.org/licenses/by-sa/3.0/, via Wikimedia Commons)

of the tower height) is the prestressed concrete sections and towards the top are the steel sections. The dynamic behavior and both the overall and local stability of prestressed concrete towers are superior to those of conventional steel tubular towers. The WT tower safely transfers all the forces and moments at the base to the subsurface through the foundation, which is typically a reinforced concrete base with micro-piles, which is designed based on local soil conditions. The coupling between the WT and the ground is governed by the type and design of the foundation and the various subsurface properties. This coupling, called Soil-Structure Interaction (SSI) in the literature, contributes to the ground motion, which is discussed in the following chapter (Chapter 4).

### 3.1.3 Dynamics of a Wind Turbine and its influence on ground motion

WT structures are tall cylindrical towers that vibrate continuously even when the turbine is not operating, usually due to wind excitation. The spectrum of wind excitation is depicted in Fig. 3.3 (a) with a green curve and in (b) as a dashed curve. Under the excitation of the wind, the spectra of seismic noise indicate some

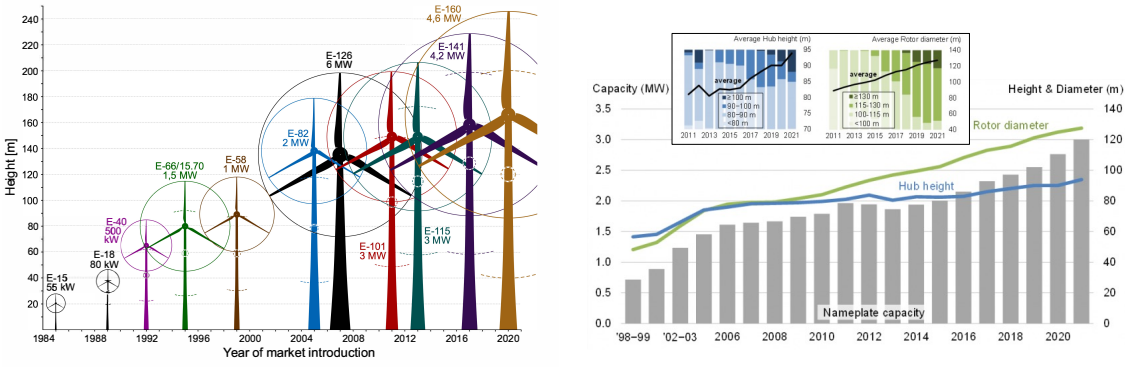


(a) (b)

Figure 3.2: Phenomenal growth of WT sizes over the last few decades. The figures show the increase in rated capacity of wind turbines (in megawatts) associated with the more recent taller and heavier WT structures. Trend shown for (a) WTs manufactured by ENERCON® from 1984-2020. The turbines can be mounted on towers of different heights. The highest variant is shown in the figure, the shortest variant is indicated with dashed lines (adapted from Jahobr, CC0, via Wikimedia Commons), and (b) WT nameplate capacity, hub height, and rotor diameter for land-based wind projects in the US from 1998-2021. The inset shows the trends in turbine hub height and rotor diameter over the last decade (Wiser et al. [2022]).

temporal variation i.e., wind speed affects the seismic noise observed. For calm conditions, the WTs serve as passive bodies under continuous low-frequency seismic noise excitation, mainly from the microseisms, scattering the seismic wave field. In the case of higher wind speeds, the turbine is in the operating state, and thus the active component of the WT, which is the rotor, generates low-frequency acoustic signals. Thus, the WTs are non-stationary active sources of seismic waves. The strong coupling of WTs to the ground through massive concrete foundations means that signals are efficiently transferred to the subsurface. A secondary path for these mechanical ground vibrations (for example, infrasound signals) is to travel through the air and couple to the ground.

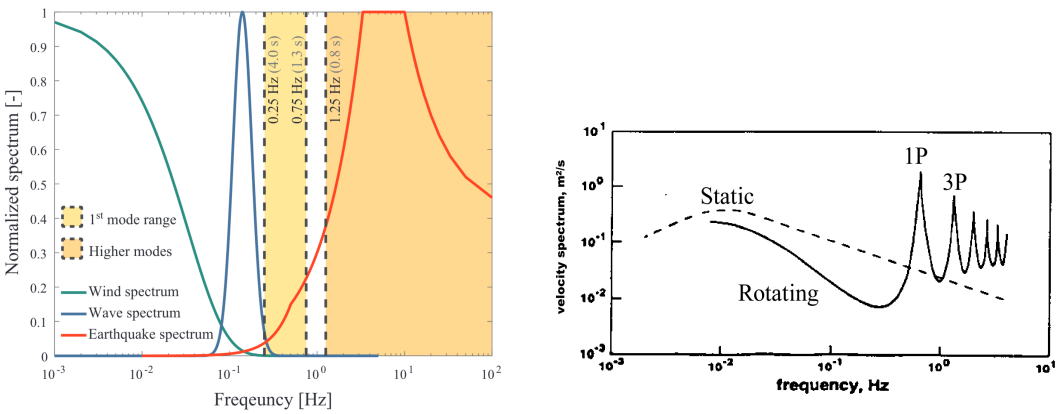


Figure 3.3: Excitation of the Wind Turbine structure (a) Typical normalized spectra from depicting the actions due to wind, sea waves, and earthquake ground motions (taken from De Risi et al. [2018]). The yellow and orange bands represent the ranges of vibration periods for steel monopile-supported offshore WTs corresponding to main and higher modes, respectively, and (b) The difference between a static wind load spectrum and the spectrum felt by the turbine due to the blade rotation. Here, 1P and 3P indicate the blade passing frequency (adapted from Van der Tempel and Molenaar [2002]).

Several recent studies have shown the influence of single or multiple WTs on seismic recordings, the increase in local noise levels, and the influence of local wind speed (for example, Saccorotti et al. [2011], Stammler and Ceranna [2016], Neuffer et al. [2019], Hu et al. [2019]). In Fig. 3.4 (a), one can see the diurnal variations of seismic noise, i.e., an alternation of high and low amplitudes during the day and night, respectively. From the various studies in the literature that recorded and analyzed seismic signals in the proximity of WTs, we can deduce that the seismic noise recordings show a complex spectrum, which includes:

1. time-varying frequency peaks directly related to the blade-passing frequency and their harmonics, and

2. stationary peaks associated with the various modes of oscillation of the WT.

The WTs are usually designed such that the two do not overlap and thus are distinct from each other in most cases. The latter are excited at the natural frequencies of the structure, which depend on the (a) stiffness of the tower, (b) mass of the WT components, including the tower assembly, and (c) foundation and soil rigidity. Therefore, external factors such as wind speed cause a variation in the peaks related to blade passing frequencies, whereas the eigenvalues do not change unless there is a change in the mass or stiffness of the system. For typical WT structures that are constructed today, both onshore and offshore, the fundamental resonance frequency is typically subhertz, starting from 0.1 Hz (Fig. 3.3 (a)). An important criterion in the design of the WT structure is to locate the natural frequencies away from the blade passing frequencies 1P and 3P, which can otherwise coincide and result in an unstable resonance condition.

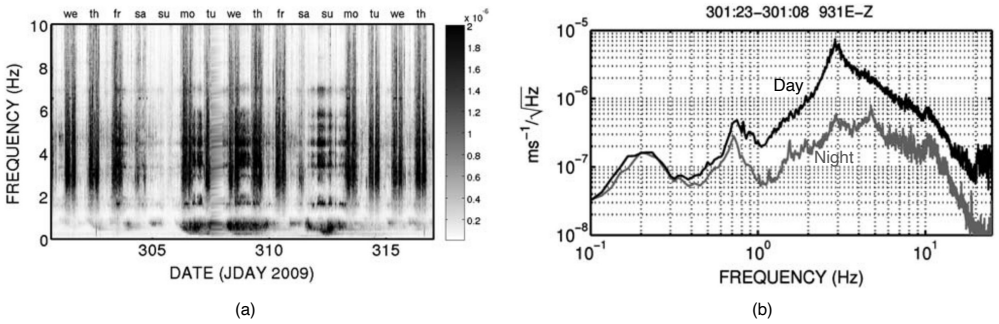


Figure 3.4: WT seismic noise from an onshore WT (modified from Saccorotti et al. [2011]) (a) Spectrogram for the vertical component of the ground velocity recorded in the vicinity of the WT showing the diurnal variation of amplitude spectral density (b) Amplitude spectral densities for the vertical component recording at the a reference site away from the WT during day-time and night-time periods (black and gray curves respectively).

The seismic noise generated by WT operation can be detected by seismic instruments installed several kilometers from the wind farm (Saccorotti et al. [2011], Stammler and Ceranna [2016], Estrella et al. [2017]). Saccorotti et al. [2011] observed two steady peaks at 0.45 Hz and 1.7 Hz, which is likely due to the different modes of oscillation of the WT. Signals at 1.7 Hz were detected as far as 11 km from the wind farm. The studies have comprehensively analyzed the attenuation characteristics of seismic waves away from wind farms. All the studies concluded that the WT signals reduce the seismic event detection abilities of the seismic stations, particularly in the frequency band of 1-10 Hz. In general, the amplitude of the seismic noise generated shows a good correlation with the wind speed. At the same time, the dynamic response of WTs and the corresponding wave field is diversely affected by their operational states (i.e. normal operating conditions, parked state and emergency shut-down due to excessive loads) and the related phenomena (i.e. aerodynamic damping due to the spinning rotor). Estrella et al. [2017] and Zieger et al. [2020] demonstrated that ground motion correlates well with the active component of the WT and identified the spectral peaks under different WT operating conditions, as well as how they propagate in the subsurface. The transfer of motion to the subsurface induced by different oscillating modes of a WT through the foundation is thoroughly discussed in the following section.

### 3.1.4 Wind turbine source characteristics and near-field radiation

For this study, it is quite important to understand how a WT, as a source, radiates in the near-field due to the tower oscillations. WTs are well anchored in the subsurface through their foundation. The transfer of WT tower oscillations to the subsurface was well captured by two experiments performed by Lerbs et al. [2020] and Neuffer et al. [2021]. Lerbs et al. [2020] in their experiment installed two ring arrays of different radii around the WT, to investigate the WT-induced seismic signals and the radiation pattern of a single WT using particle motions. Surprisingly, the direction of motion vary temporally over a short time period of 20 seconds.

However, they did not analyze the motions from each mode separately, which was then considered by Neuffer et al. [2021]. In their experiment, in addition to the ground stations, sensors were installed on the tower and foundation, which helps to understand the fully coupled system. At resonance frequencies, the tower, the foundation, and the adjacent soil exhibit complex particle motion which was found to have linear, elliptical, or circular traces similar to Lerbs et al. [2020]. In the vertical plane, the foundation showed a greater displacement of the vertical component than the two horizontal components at all frequencies considered. Further, both studies show radiation in the near-field with respect to the wind direction. The radiation corresponding to different eigen frequencies is shown in Fig. 3.5 (a through d). The dipolar radiation of the vertical displacement field is visible in the near field, at least for the first two modes (panels a and b), on either side of the WT, depending on the direction of the tower flexure. The motion of the turbine tower, similar to that of a fixed cantilever, predominantly oscillating in flexure, gives rise to a bending moment at the base. At the foundation-soil interface, this moment is equivalent to a force couple separated by a finite distance (dipole). However, a screw-type motion is observed for the higher modes (panels c and d), indicating a torsion effect that can be expected along with the flexure. The pitching moment, as explained by Lerbs et al. [2020] is induced by the change of angular momentum of the WT rotor and this also explains the elliptical motion seen in the near-field, which is induced by the tower to the subsurface through the foundation. From the experiments, it appears that wind direction plays a less significant role in understanding WT motion. However, it is not necessarily the case that the tower only oscillates in the direction of the wind, as seen in Fig. 3.5. The nacelle is usually oriented in the direction of the wind, but because of its geometry (nacelle inertia), the system can oscillate both in the fore-aft direction or in the side-side motion for a given mode (Thresher and Holley [1981], Westwood et al. [2015]). This decides the tower bending direction and thus the dipole orientation.

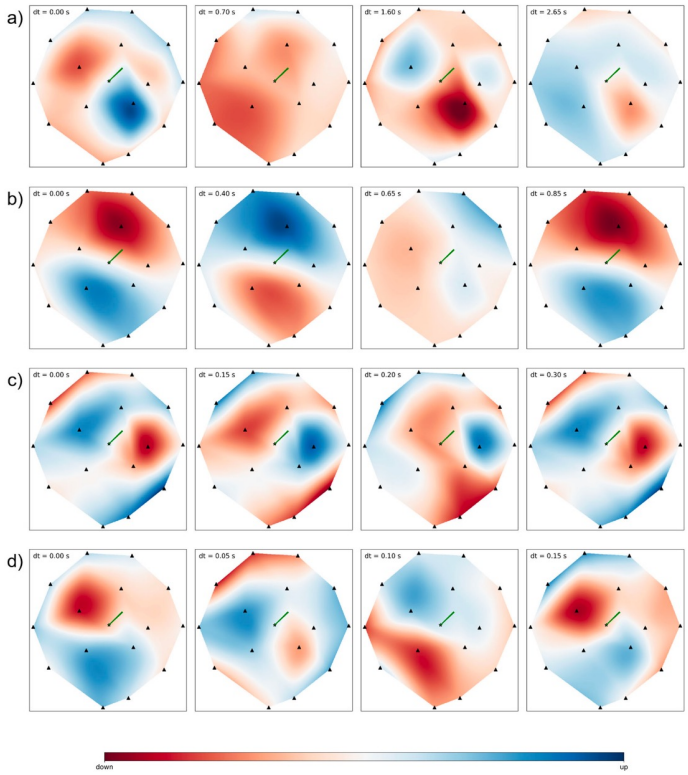


Figure 3.5: WT source radiation: (a to d) Patterns of vertical ground notion in the near-field of a WT (200m radius). Each row indicates the time progression for the four eigen frequencies. The sensor placements are indicated by the black triangles, and the wind direction throughout the measurement period is indicated by the green line pointing NW from the map's midpoint. Blue and red color correspond to upward and downward motion respectively. The data between the stations is bicubic interpolated and normalized to the highest amplitude for each frequency (from Neuffer et al. [2019]).

Different studies have come to the conclusion that Rayleigh waves are the main type of seismic waves excited by a WT. For example, Westwood and Styles [2017] used polarization analysis to identify surface waves that dominate the wave field radiated due to WT blade rotation and harmonics, which was also confirmed by numerical simulations (Gortsas et al. [2017]). Neuffer and Kremers [2017] found Rayleigh waves to dominate the surface wavefield when the turbines are operating and specifically in the band 3-4 Hz which correspond to tower eigen frequencies. However, in the literature, we do not find many studies that discuss the impact of the source mechanism on the wave field. Gortsas et al. [2017] and Gaßner et al. [2023] studied the effect of ground motion attenuation considering the two source types: monopolar vs dipolar. The latter implementing a 'tilt' source in their simulations, which is essentially a pair of vertical forces separated by a distance similar to the foundation diameter. Unlike the case of a monopolar source, they find a strong directivity effect shown by the attenuation of surface waves generated by the dipolar source, i.e. stronger damping in the direction perpendicular to the tilt compared to the other principal directions. Regardless, the local geology plays a crucial role in path effects and propagation of WT signals. In the studies, which used simulations

to study WT radiation, assume homogeneous subsoil which is not true. The turbine has been replaced by equivalent forces, either a tilt force (Gaßner et al. [2023]) or a single vertical force (Limberger et al. [2022, 2023]), or even by directly applying vertical force and moment forces on the foundation slab (Gortsas et al. [2017]). However, the tower itself is not included in the model, which we attempt to include in our study later in the chapter.

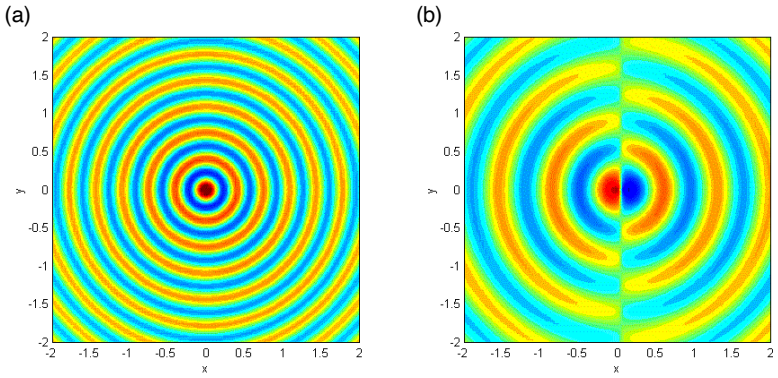


Figure 3.6: Monopolar (a) and dipolar (b) source radiation of waves in an acoustic medium. (adapted from Korchagova et al. [2017]). An ideal dipolar source is characterized by a pair of two monopoles of equal magnitude but opposite polarity, and separated by a distance $d$ that should be small compared to the wavelength ($kd \ll 1$). A WT source primarily behaves as a dipole due to the oscillations of the tower.

In terms of seismic radiation from a group of WTs i.e., in the scenario of a wind farm, some studies, for example, Limberger et al. [2021, 2022], analyze how a wind farm hosting three or seven WTs affects seismic propagation. They develop analytical and numerical models that simulate wave propagation from WT sources and conclude that the wavefield interferences of multiple WTs significantly affect the seismic radiation pattern of a wind farm. In their studies, the phase differences between WT excitation are varied, but the WTs are modeled as pure normal forces neglecting the other source effects. This would be true if the turbines vibrate only in the axial direction, as explained above. However, the authors acknowledge that source mechanisms with different polarizations can affect the wave propagation. Nevertheless, the superposition and propagation of the signals of a *dense* clusters of WTs is not yet fully understood in the literature, since most studies that considered multiple WTs had a rather linear turbine arrangement or a sparse scattered configuration.

## 3.2 Hypothesis and Objectives

### 3.2.1 Wind Turbines as coupled resonators

While recent work discussed in the previous section have confirmed that multiple WTs have a significant influence on the seismic wavefield due to their interferences, we extend these studies to dense WT clusters. We hypothesize that a set of

closely spaced WTs can be considered as sub-wavelength coupled resonators for low-frequency seismic surface waves (below 10 Hz). A crucial design factor in increasing wind farm efficiency is the arrangement and relative positioning of the turbines. Turbines are strategically arranged to optimize energy capture: they can be equally spaced, unequally spaced, or in a staggered grid arrangement, based on the optimization of the wind farm layout taking into account several factors. Interestingly, the physics of locally resonant metamaterials is independent of the spatial ordering of the resonators when they are organized at the subwavelength scale (Kaina et al. [2013a], Rupin et al. [2014], Colombi et al. [2014], Lott and Roux [2021]), which means that these effects should be observed whether the WTs are regularly arranged or not. If the wind farm acts as a metasurface, then the set of resonating WTs should slow down or delay the propagation of surface waves, resulting in unexpected dispersion as well as frequency bandgap(s). Fig. 3.7 shows a schematic that is based on Fano-like interference of the surface wave field with the discrete resonances of the WT. The turbine resonances that are out-of-phase with respect to the incoming surface waves should result in an evanescent surface field within the cluster. For wavelengths that span more than a few turbine spacings, should be in the sub-wavelength regime, enough to create a seismic metasurface.

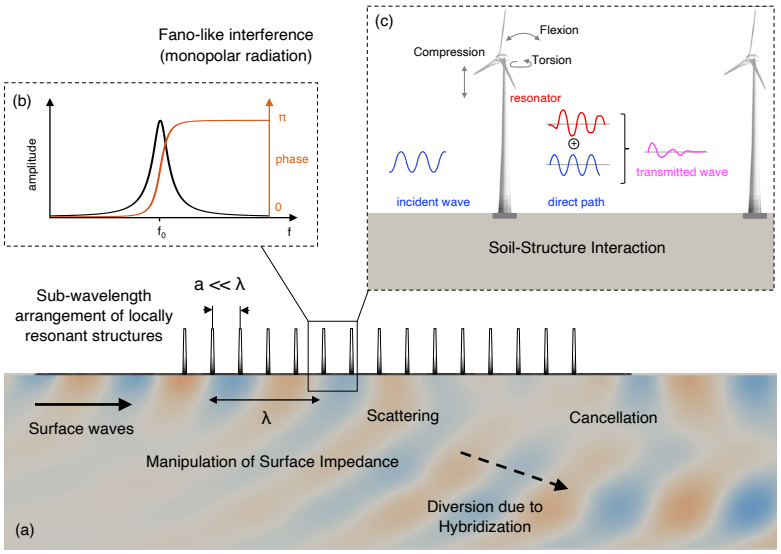


Figure 3.7: Schematic of the hypothesis proposed to explain how a wind turbine array can potentially behave as *locally-resonant metasurface*. Each resonator acts as a strong scatterer and deviates the surface waves for lengths shorter than the wavelength which causes them to mode convert into body waves, the so-called 'hybridization' phenomenon. Such metamaterial behavior results from Fano interference between the turbine resonances which are out-of-phase with respect to the incoming surface waves. Similar effect can be expected from having a spatially disordered array of wind turbines because the hybridization bandgap originates from the resonances only and not from the periodicity.

### 3.2.2 Objectives

To validate our hypothesis stated in the above section, we propose to experimentally study the ambient seismic wavefield inside dense wind farms, assuming it mainly consists of surface waves. We identify two potential wind farm sites with a dense arrangement of WTs;

1. San Gorgonio Pass Wind Farm in California, USA
2. Nauen Wind Farm in Brandenburg, Germany

The two wind farms host different WT builds and have different spatial density of turbines, allowing us to investigate two different scenarios to test our hypothesis. We aim to study surface wave propagation by analyzing ambient noise recorded by temporary seismic arrays in both wind farms, following a similar approach in each case. Our goal is to understand the differences in surface wave propagation inside and outside the wind farm by performing both (a) an "incoherent analysis" - average wavefield intensities, and (b) a "coherent analysis" - effective speed and scattering. For the former, we specifically choose to perform **spectral ratio analysis** of noise recordings from inside and outside the wind farm. Whereas, for the latter, we rely on **ambient noise correlations** to verify if there is a difference in the effective properties in the two media and how the WT can potentially scatter the wavefield when we are inside the wind farm. Since we are dealing with seismic arrays, the correlation technique can be useful in the identification of a potential metasurface. More generally, our goal is the identification of the processes by which WT clusters can influence seismic recordings at both short and intermediate distances.

## 3.3 San Gorgonio Pass Wind Farm

To investigate the role played by the WTs described as a field of heavy-mass coupled resonators, we chose to first analyze data available from the 2011 Salton Sea Imaging Project - SSIP (Rose et al. [2013], Han et al. [2016]). The SSIP in general was designed with the aim of producing an approximate 3D image of the subsurface of the Coachella and Imperial Valleys. 'Line 6' of the array in this experiment cuts directly across the San Gorgonio Wind Farm (Fig. 3.8 (a)). We take advantage of this temporary array to investigate our hypothesis of coupled resonators on the geophysics scale.

### 3.3.1 Wind farm configuration

San Gorgonio wind farm has thousands of WTs of varying size and is located north-west of Palm Springs, California (see the inset of Fig. 3.8). In January 2008, the farm consisted of 3,218 units that delivered 615 MW (Source: U.S. Wind Energy Projects – California Archives). The location where it cuts through the wind farm, the WT units are identical and arranged in a periodic manner, with a uniform 130m spacing between WT rows and an inter-turbine spacing of roughly 40m. The temporary array had stations not only inside the WT field but also just outside it, allowing us to study the amplitude and phase properties of the wavefield in both environments. The aerial image shows only a part of the wind farm which mainly

includes the turbines of the Micon M108 model, which are towards the south-east part of the wind farm (as seen in Fig. 3.8 (b,c)). This part of the wind farm is located within the Whitewater River floodplain between the I-10 highway and State Highway 111, and has nearly constant wind due to the venturi effect created by the San Bernardino Mountains to the north and the San Jacinto Mountains to the south. The stations installed on the wind farm are sitting between rows of Micon M108 turbines, but also NM 44/750 turbines a bit further away. The turbine models with a dense arrangement on either side of the array are the Micon M108 having a rated capacity of 108 kW. There are several hundreds of these turbines that were installed in 1985/86 and were only decommissioned in 2020 to be replaced by bigger turbines.

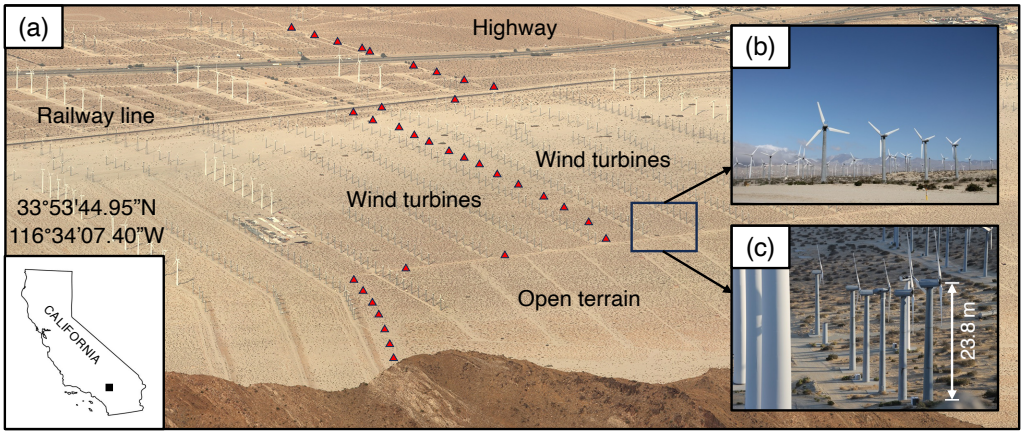


Figure 3.8: (a) Aerial view of the San Gorgonio Pass wind farm taken from over the San Jacinto mountains (seen in the image foreground) showing the positions of the 'Line 6' stations of the SSIP temporary array (red triangles) deployed in 2011 (photograph is from 2008 and adapted from Matthew Field, CC BY-SA 3.0 http://creativecommons.org/licenses/by-sa/3.0/, via Wikimedia Commons). Inset in the bottom left shows the position of the site which is located north-west of Palm Springs, California. (b,c) Densely spaced Micon M108 model wind turbines as seen from two vantage points (Images are accessed from wind-turbine-models.com)

### Predicted resonance frequency of Micon M108 wind turbine

One of the key ingredients in understanding the potential role of WTs in shaping the wavefield is identifying resonances of the individual turbine structures. Unlike trees, WTs are identical and therefore the masses and dimensions are not subject to variation or randomness. The specifications for the M108 Micon were partially retrieved via the database available at https://en.wind-turbine-models.com/turbines/562-micon-108 (last accessed January 2024). The missing dimensions of the turbine were approximated using field images and applying proportional estimates. The turbine is essentially a tubular steel tower made up of three segments of different shell thicknesses that support the generator assembly at the top. The various specifications of the Micon M108 turbine are listed in Table 3.1.

| Specification | Value |
|---|---|
| Tower height ($L$) | 23 m |
| Tower mean outer diameter ($D_o$)* | 1.83 m |
| Tower mean shell thickness ($t$)* | 7.33 mm |
| Tower mass ($M_t$) | 7.2 tons |
| Assembly mass ($M_a$) | 10.8 tons |

*estimated value

Table 3.1: Specifications of the Micon M108 turbine model.

The fundamental resonance frequency of such an elongated beam-like structure is in flexion is thus more easily excited. The approximate formula for the first natural frequency of a uniform cantilever beam of length $L$ having a distributed beam mass $M_t$ and a concentrated end mass $M_a$ is given as

$$f_r = \frac{1}{2\pi}\sqrt{\frac{K}{M_{eff}}} = \frac{1}{2\pi}\sqrt{\frac{3EI/L^3}{M_a + 0.23M_t}} \tag{3.1}$$

where $K = \frac{3EI}{L^3}$ is the bending stiffness of the Young Modulus beam $E$ and the moment of inertia $I$, while $M_{eff} = (M_a + 0.23M_t)$ is the effective mass (pae [2010]). For Micon M108, using the above formula, we obtain a fundamental resonance frequency of $\mathbf{f_r = 1.36Hz}$. In addition to flexural resonances, the structure also exhibits torsional and compressional resonances, albeit at higher frequencies. The vibrations induced by the passage of the blades can also exert a notable impact on the spectral peaks observed in the frequency range of 1-10 Hz, as presented in the literature in the previous section.

### 3.3.2 Array configuration

The positions of the stations, which can be seen in Fig. 3.9 as red triangles, were installed within the forest of several hundred WTs (shown as yellow circles). The interstation spacing is in the range of 80-110 m, which allows us to study the propagation of wavelengths ($\lambda > 200m$ - Nyquist limit) longer than the scale of WT spacing (40m and 130m in the N-S and E-W direction, respectively). We find this to be an interesting dataset to study metamaterial physics on a geophysics scale. The stations in and around the wind farm were installed only for a brief period between 05th March 2011 and 11th March 2011. We choose to analyze the data from different linear segments of the array running in the NS direction, starting from the edge of the San Jacinto mountain in the south extending up to the highway towards the north. The instruments are RefTek125a ("Texans") with OYO Geospace GS-11D seismometers with a cutoff frequency of 4.5 Hz, which records the velocity only in the vertical component. Data and metadata were downloaded from the Incorporated Research Institutions for Seismology Management Center (IRIS DMC), now the Seismological Facility for the Advancement of Geoscience (SAGE). For two days (Julian days 69 and 70), continuous recordings of 7 hours each day from 07:00:00 to 14:00:00 UTC or 11 p.m. to 6 a.m. Pacific Standard (local) Time (John Hole

[2011]) are available for the analysis. The station nomenclature is maintained as in the original dataset, thus we have 36 stations from YG 6023 to YG 6058.

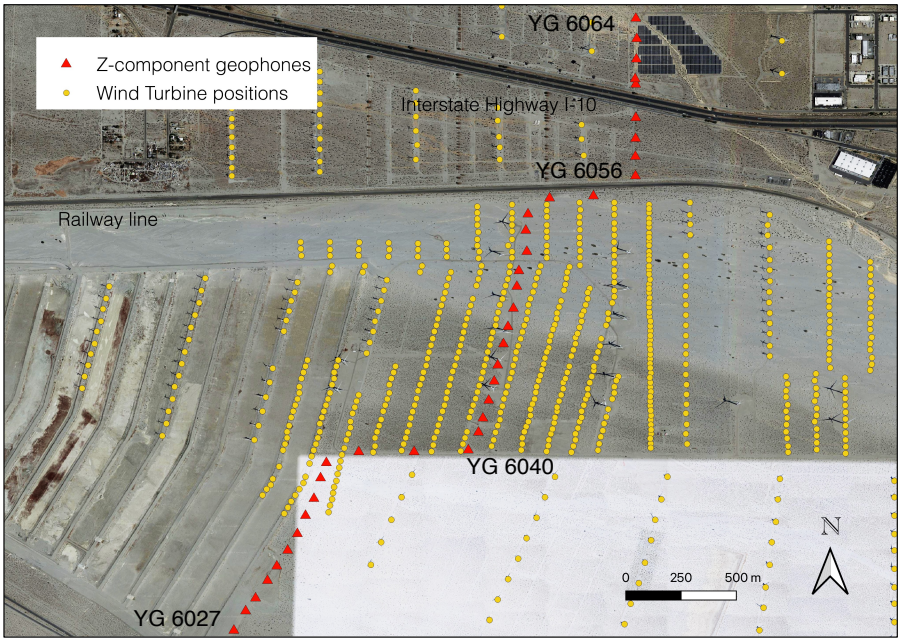


Figure 3.9: Satellite view of the part of San Gorgonio Wind Farm showing the location of wind turbines (yellow circles) that were in existence as of March 2011 during the SSIP experiment. The Z-component geophones (red triangles) inside the forest of wind turbines (yellow circles) extending into the open terrain towards the south. The wind turbines positions were obtained from the United States Wind Turbine Database (Hoen et al. [2018], Rand et al. [2020]).

### 3.3.3 Spectral Analyses

In this section, we use ambient noise recordings to find the spectral peaks and try to link them to the predicted WT resonances. The raw data are originally sampled at 250 Hz. We used the data without being treated for instrument response removal because the ratio of the spectra should not be affected by this operation. The response below 4.5 Hz is the damped response according to the slope of the instrument gain, which is the same for all chosen instruments. Below 1 Hz, the spectrum is dominated by Rayleigh waves that originate primarily from the secondary microseismic field (Juretzek and Hadziioannou [2016]), but not be considered for our study.

We plot the spectrograms for the two 7-hour recordings from March 10 and 11, 2011 (here referred to as JD 69 and 70, respectively) separately in Fig. 3.10. These are spatially averaged for all 33 selected stations, i.e., both inside and outside (YG 6026 through YG 6058). The columns of the spectrogram were computed by averaging the spectral estimates obtained over 40-s-long windows of the signal with an overlap of 20 seconds. The day 69 recordings have relatively much lower overall amplitudes, suggesting that the wind conditions must have been much calmer on this day. The publicly available wind data for 2011 are available from a station in Palm

Springs ("PALM SPRINGS ASOS") that is 10 km from the wind farm site (Data available from National Oceanic & Atmospheric Administration, U.S Department of Commerce). Since wind speeds change quite quickly both spatially and with altitude, these data cannot be used to interpret our results. The signals originating from the passing of trains can be clearly seen as strong vertical features in the spectrograms on both days. In addition to this, the Interstate 10 freeway crosses the wind farm just north of the railway track and State Highway 111 to the south, which adds to the noise in a broad frequency band. Both Julian days 69 and 70 are weekdays; thus, the noise levels would have no correlation with the vehicular traffic. Another defining feature of the spectrograms are the dominant peaks at 11.6 Hz and 20 Hz, which persist for most of the recording on day 69 (since 09:00:00 UTC) and for all the recording duration on day 70. The 'switch on' conditions can be seen in Fig. 3.10 (a) around 09:00:00 UTC, which means that the source of the 11.6 Hz peak could be related to the blade rotation harmonics. For the 20 Hz peak, it does exist before the switch on of the turbine, but we suspect it is from the Micon M108 turbine generators, which have a rating of 1200 rpm i.e., 20 Hz. The harmonics of this 20 Hz peak are also seen in the broadband spectra as peaks at 40, 60, 80 and 100 Hz (not shown here). We performed plane-wave and spherical beamforming for the ambient noise at those frequencies, but the results from the linear array were not decent enough to isolate the source. In the following sections, we separately analyze the recordings from Julian days 69 and 70 due to the large difference in their amplitudes.

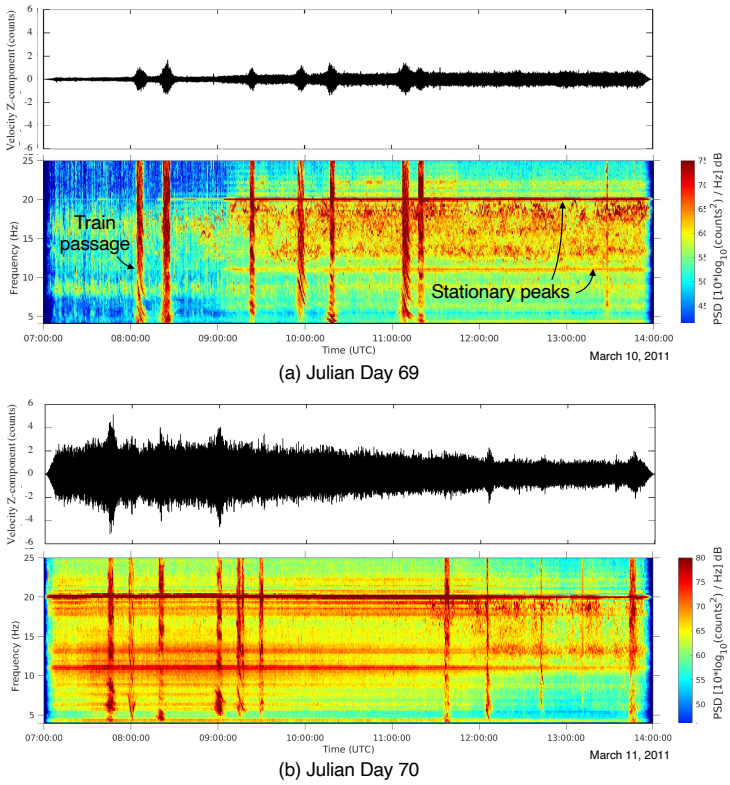


Figure 3.10: (a,b) Time domain signals for the vertical component of the ground velocity (in counts) for the station YG6040 for the 7-hour recordings on March 10 and 11, 2011 respectively. The signals are low pass filtered below 40 Hz. Mean Spectrograms spatially averaged over 33 stations located inside and outside the wind turbine area shown in Fig. 3.9 for the Julian day 69 and 70. Each spectrogram column results from the average of the spectral estimates obtained over 40-s-long windows of the signal with an overlap of 20 seconds. Units are power spectral density counts$^2$/Hz, according to the color scale on the right.

### Spectral Ratio

We select four sets of three stations (Sets 1 through 4) from the array, marked by green triangles in Fig. 3.11 (a). Sets 1 and 2 are fully inside the WT area, Set 3 is also within the WT field but close to its edge, and finally Set 4 stations are in the open terrain outside the WT field. The sets of stations were chosen to understand the amplitude characteristics of the wavefield at different positions within the wind farm. The analysis of spectral ratio was done separately for the two recordings of March 10 and March 11, 2011 (Julian days 69 and 70), so if there is an effect of the varying noise levels on the spectral ratios, it should be apparent. The total records have been windowed in 30-minute long spectrogram records with a 20-minute overlap between the consecutive windows. The spectral ratios between the two sets inside the WT field are plotted in Fig. 3.11 (b,c). The gray curves are the spectral ratios for each sliding time window, and the mean is plotted in black. We see a drop in the ratio around 1.5 Hz that roughly coincides with the fundamental resonance frequency of the Micon M108 turbine. This drop, although the stations sets are both inside the WT array, is due to the higher number of

WTs radiating the signals from close proximity in the case of station set 2. For stations in Set 1, there was not as much stacking of the peak amplitude from the resonances of individual turbines. In a similar way, the spectral ratio plots for the other stations sets inside with respect to those outside the wind farm display a peak at the resonance frequency of the turbines. This again means that the resonances are contributing to the higher spectral amplitudes inside the farm, which are 4 times higher as compared to the outside. The difference between the spectral ratios of the two days is not quite significant in most of the frequency bands, although there is a difference in the overall noise levels between the two recordings. There is deviation of 10% in the resonance frequency that we observe from the data and that which was estimated from the analytical formula in the previous section (Section 3.3.1). This can be attributed to the approximation of the uniform tower diameter and shell thickness, which must have directly contributed to the lower tower stiffness as compared to the actual structure. There is also no eccentricity provided for the assembly mass at the top of the tower.

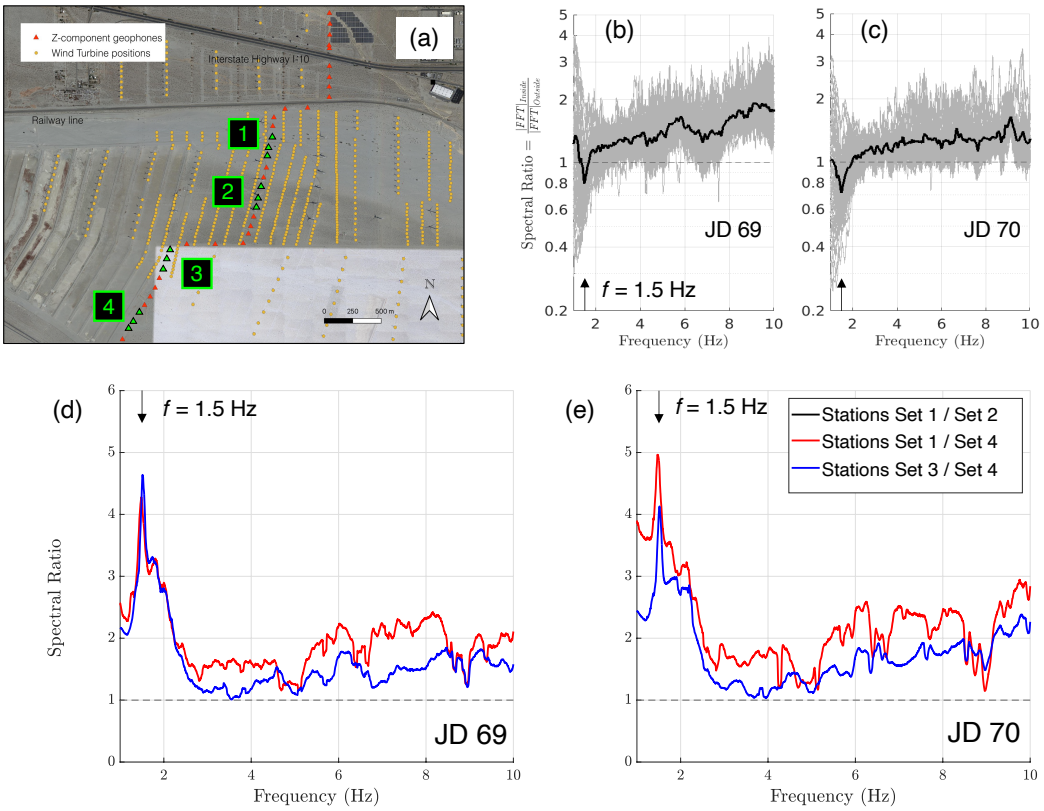


Figure 3.11: Spectral ratio plots for the Julian days 69 and 70 (a) Map showing the selected sets of stations for the analysis. The gray curves in (b,c) are the spectral ratios for the vertical displacement component for different 30-min-long windows with a 20 min overlap. The mean is shown as a bold curve in black. The panels (d,e) are the mean spectral ratios between the other sets inside and outside the wind turbine area. There is no drop observed near the resonance frequency of the Micon M108 turbines, but instead there is a peak showing that the amplitudes are higher inside the wind farm.

### 3.3.4 Surface wave dispersion and scattering

From the spectral ratio analysis, which is related to amplitude of the wavefield, we did not obtain a result that hints towards a metamaterial-like behavior of the WT cluster. To further understand the role of WTs, we need to look at the effective parameters which are related to the coherent part of the ambient wavefield, for example, phase velocity and scattering. One method of detecting potential frequency ranges in which attenuation effects might occur is to analyze the correlation between the geophones. As previously discussed in this thesis, in Section 2.1.2, noise correlations can be useful in extracting the deterministic information of wave propagation between any two receivers. For an isotropic distribution of sources, we can assume that the incident plane wave arrival is omnidirectional. For such an assumption, the correlation function between any two points in the field reduces to the zero-order Bessel function of the first kind (Campillo and Roux [2015]). This is the basis of the spatial correlation methods first proposed by Aki [1957], which have been used to estimate the phase velocity of microtremors and investigate shallow structures (for example, using methods such as SAC and ESAC). The correlation analysis also helps us in understanding whether the correlation of the wave field is much faster inside compared to the outside of the WT field.

#### Average two-point correlation function

In the context of elastic metamaterials, in a lab experiment with the setup of rods attached to the plate, Lott and Roux [2019a] used the correlation functions between receiver pairs to extract the effective impedance of such locally-resonant metasurface. The ensemble-averaged two-point correlation function $C(\omega, dr)$ at pulsation $\omega$, and for all possible receiving points separated by an absolute distance $dr$, is given by

$$C(\omega, dr) = \frac{\left\langle \Psi(\omega, \mathbf{r})\ \Psi^*(\omega, \mathbf{r} + \mathbf{dr}) \right\rangle}{\left\langle \left| \Psi(\omega, \mathbf{r}) \right|^2 \right\rangle} \tag{3.2}$$

where $\Psi(\omega, \mathbf{r})$ is the field measured in $\mathbf{r}$ for a finite duration recording window. $\langle \cdot \rangle$ denotes the ensemble average over all sources, time windows, and distance pairs. The numerator in the above equation essentially gives us the cross-spectral density matrix (CSDM) of the array. The denominator is the normalization coefficient that corresponds to the averaged intensity measured from all the receiving points. The plot of the real part of the correlation function $C(\omega, dr)$ for all frequencies, both inside and outside the metamaterial, is shown in Fig. 3.12(A). A clear difference between the frequency bands corresponding to the stopband and the passband of the metasurface is evident. Based on the data, they then model the average 2-point correlation at each frequency using the 2D Green's function for the infinite plate in the pass band, whereas in the stop band they use an effective wave number with equal real and imaginary parts, as in Williams et al. [2015]. This gives an estimate of the effective wavenumber (complex value) inside and outside the metamaterial. However, they did not take into account the scattering attenuation in their model, which becomes important at the edge of the passband where high scattering of the field is expected.

Similarly, for the forest metamaterial, Lott et al. [2020a] performed the two-point correlation analysis for the field recorded from all geophones inside the forest that were excited by active shots. These data come from the METAFORET experiment, which has been described in the preceding chapter (Chapter 2). As in the case of the plate, they compute the correlation coefficients using Eq. 3.2 between every pair of geophones at each frequency, and finally average it over all sources and then over all azimuths (Fig. 3.12(B)). The model used pertains to the 2D Green's function that is defined in the case of a surface wave propagating in a half-space. The real and imaginary parts of the effective wavenumber are obtained by fitting this model. The real part gives the phase velocity through the dispersion relation, and the inverse of the imaginary part accounts for the classical attenuation length (shown in the subplot (b) of Fig. 3.12(B)). This property of the effective wavenumber is discussed in more detail in the following paragraphs.

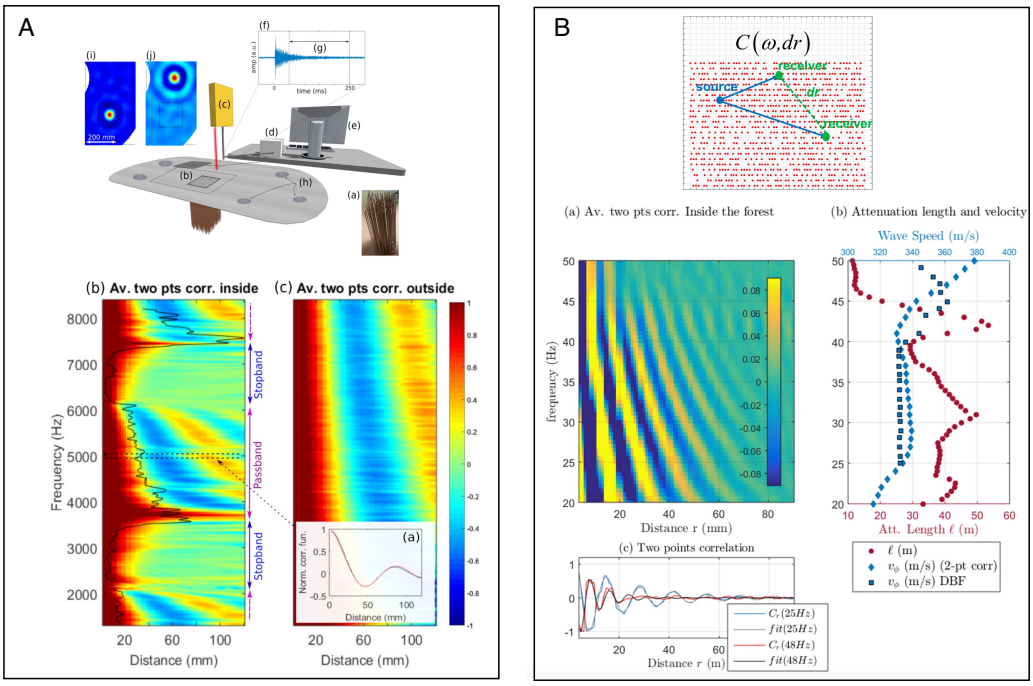


Figure 3.12: Two point correlation measured in two different media: (A) Plate and rods experiment (Lott and Roux [2019a]). Real part of the averaged two-point correlation function (normalized) measured at 5 kHz for all of the receiver pairs located inside the metamaterial region (blue). The modeled plate Green's function is in red. (b), (c) Averaged two-point correlation versus frequency measured inside the metamaterial (b) and outside the metamaterial (c). The black line in (b) corresponds to the averaged intensity versus frequency measured inside the metamaterial. (B) Forest of trees experiment (Lott et al. [2020a]). (a) Average two-point correlation as a function of the frequency measured within the forest. (b) Attenuation length (red circles) and phase velocity (blue diamonds and blue square for the 2-pts corr. and DBF measurements, respectively) inside the forest versus frequency. (c) Real part of the correlation function (blue, red) for two frequencies (25, 48 Hz), and the corresponding modeled Green's functions (gray, black).

### Two-point correlation inside and outside the wind farm

To compute the average two-point correlation function, we follow a similar approach to that used by Lott and Roux [2019a], Lott et al. [2020a], but instead of active source signals, we perform correlations for seven hours of ambient noise recording from March 10, 2011 (JD 69). We selected a set of 14 stations YG6038-YG6053 to represent the field inside the wind farm and another set of 11 stations YG6023-YG6033 for the outside (see Fig. 3.9). The outside subarray has an almost linear geometry, but the inside subarray has an L shape with a relatively shorter leg in the E-W direction. We first compute the Fourier transform at all the stations by dividing the recordings into short time intervals of 100 s each with a 50 s overlap. The ensemble averaged two-point correlation function $C(\omega, dr)$ is computed using Eq. 3.2 at each frequency for all the possible pairs of stations for each of the two subarrays. Due to the mostly linear and uniform spacing of the geophones in the subarrays ($\sim 100m$), we averaged $C(\omega, dr)$ for all interstation distances $dr$ within bins of 100 m. Similarly, we find that averaging the correlation function within frequency bins of 0.1 Hz gives the optimal resolution for the frequency vs distance representation. The real part of this correlation function is plotted in the frequency range of 1.5 and 3.5 Hz in Figs. 3.13 (a) and (b) for inside and outside the WT region, respectively. The horizontal axis denotes the distance between station pairs averaged for 100m bins. Below 1.5 Hz, the correlation function is quite noisy, and beyond 3.1 Hz, both subarrays fail to satisfy the Nyquist-Shannon condition (Nyquist [1928], Shannon [1949]) and thus have aliasing effects.

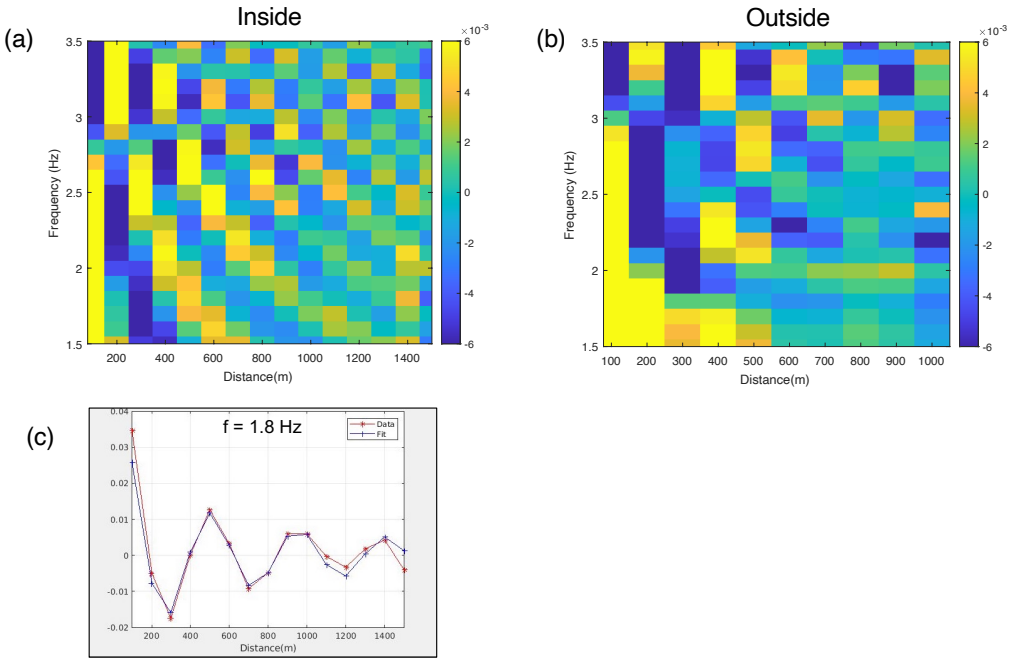


Figure 3.13: Real part of the averaged two-point correlation function for the receiver pairs inside(a) and outside(b) the wind turbine field. In panel (c), the model of 2D Rayleigh wave Green's function (blue curve) is fit to the correlation function (red curve) at a frequency of 1.8 Hz, and similarly for all frequencies.

For the case of a surface wave propagating in a half-space, in theory, $C(\omega, dr)$ should approach the 2D Green's function (Campillo and Roux [2015]). To fit the

data, we choose a function which can represent both (1) a propagative part related to the spatial spreading, for example, a Hankel function, and (2) an evanescent part that decays exponentially and is related to the attenuation due to scattering. Note that the normalization factor in the denominator of equation 3.2 cancels out intrinsic attenuation caused by viscous loss in the medium. Thus, scattering, if present, should be mainly due to the WTs. The model can be expressed as

$$C(\omega, dr) \approx A\ H_0^{(1)}(k_{eff}\ dr) \tag{3.3}$$

Here $A = A'e^{\frac{-dr}{2l_s}}$ is the amplitude of the function, $H_0^{(1)}$is the zero-order Hankel function of the first kind. The wavenumber $k_{eff}$ that controls the oscillations of the function gives the phase velocity, i.e., $k_{eff} = \frac{2\pi}{\lambda}$ and thus $C_{eff} = \frac{\omega}{k_{eff}}$. The term in the exponential, which is essentially the damping of the function, gives the attenuation length, $l_s$. This length corresponds to the average distance between the scatterers in the medium. Only the real part of the model is used for the fit. We extract the parameters frequency by frequency, first fitting the amplitude of the function $A$ and the wavenumber $k_{eff}$, without considering the damping. In the second step, we fit the wavenumber $k_{eff}$ and the attenuation length $l_s$ by fixing the amplitude $A$ obtained from the first step. In Fig. 3.13(c), we show an example of fitting the modeled Green's function to the experimental data. The results are plotted in Fig. 3.14(a) and (b), for the phase velocity and the attenuation length, respectively. The goodness of fit in terms of the sum of squares error (SSE) for all frequencies is shown in panel (c) of Fig. 3.13.

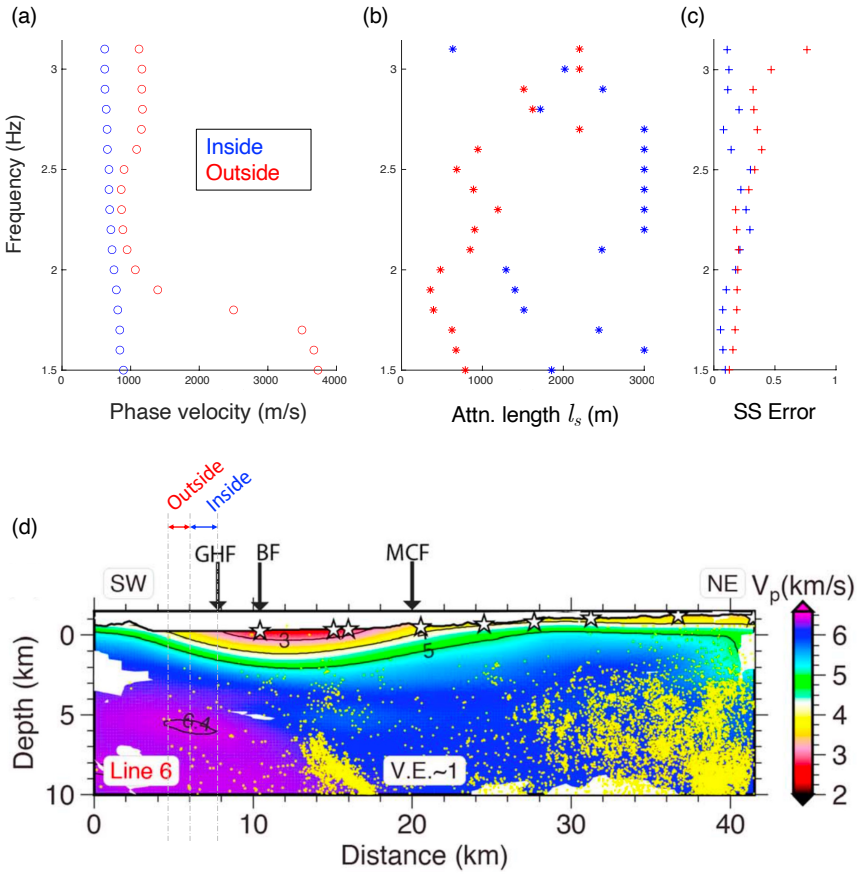


Figure 3.14: Frequency dependent phase velocity and attenuation length extracted from the model fit are shown in panels (a) and (b) respectively. The goodness of fit is shown in the panel (c) as the sum of squared errors (SSE). (d) Cross-sectional slices through the velocity model oriented along Salton Seismic Imaging Project (SSIP) Line 6, adapted from Ajala et al. [2019]. Contour intervals of 1 km/s are used to highlight the shape of the sedimentary basin. The increase in phase velocity for the subarray outside the WT region below frequency of 2 Hz is justified by the velocity model.

### 3.3.5 Discussion

In this section, we discuss the collective results from both the spectral ratio analysis and the coherent analysis of the ambient noise recordings.

1. The phase velocity between 1.5-2 Hz for the array outside the wind farm seems rather high for surface waves. This can be due to the dominance of continuous P-waves in the ambient noise recording which are excited by distant ocean winds up to a frequency of 2 Hz. The high P-wave energy has been well observed in the background noise recorded at remote sites in Parkfield and the Mojave desert in California (Zhang et al. [2009]). A phase speed of $\sim 3.7$ km.s$^{-1}$ at f=1.5 Hz with a contribution from both P-waves and Rayleigh waves can be expected for the outside array which is deployed at the edge of the sedimentary basin, with a quite shallow bedrock depth. Fig. 3.14 (d) shows the cross section of the velocity model that was obtained by Ajala et al.

[2019], using the data from the SSIP experiment. There are significant lateral variations in the section along the array as the depth of the sediments increases from south to north. As we approach 2Hz, we gradually retrieve lower phase speeds, due to the increased presence of Rayleigh waves in the ambient noise.

2. Conversely, for the array inside the wind farm, in the whole frequency band, we observe the phase velocity to be suggestive of Rayleigh waves. The bedrock is relatively deeper under this array, which is in the Whitewater river plain ($\sim 2km$ from the basin edge) where we can expect the signal to be dominated by basin-induced, locally generated surface waves (Pilz et al. [2018]). However, we do not see any abrupt slow down of the Rayleigh waves at the resonance frequency of the WTs (f=1.5 Hz). It is important to mention that despite the frequency range of our study being outside the nominal frequency range of the geophones (4.5 Hz corner frequency), we still detect strong Rayleigh wave signals up to 1.5 Hz in the correlations.

3. Due to the design of the subarrays and their orientation with respect to the predominant energy flux, the surface wave phase velocities anticipated from the correlation functions may not match the actual phase velocities (Hillers et al. [2012]). The plane-wave beamforming was of low quality which could be due to the linear geometry of the array, in which the backazimuth resolution is restricted (Rost and Thomas [2002]).

4. The spectral ratio around the resonance frequency of the WTs (f=1.5 Hz), shows a peak. This could imply that the wind farm does not act as locally-resonant metasurface for the surface waves inside the wind farm. However, since we have argued that at 1.5 Hz the P-waves seem to dominate the ambient noise outside the wind farm, the spectral ratio is not a good indicator of the metasurface behavior anymore.

5. It is more challenging to interpret the attenuation length $l_s$. Classically, this length represents the average distance a wave travels before encountering a scatterer in its path, often referred to as the mean free path. Just after the WT fundamental resonance frequency ($f = 1.5Hz$), there is a drop in the attenuation distance both inside and outside. But outside the wind farm, the scattering seems to be higher, since the attenuation length is less than or comparable to the wavelength ($l_s \approx \lambda$) up to 2.5 Hz. However, this scattering cannot be from the WTs, but rather has to be due to the presence of lateral heterogeneities, like in this case, where we expect high scattering at the edge of the basin.

6. Within the wind farm, $l_s \gg a$ and $l_s > 3\lambda$, suggesting that there is no interaction of the surface waves with the WTs and that there is weak attenuation of the coherent field at this frequency. For frequencies where $l_s$ reaches its upper bound ($l_s \gg \lambda$), it means that WTs do not have any role to play in the scattering. There is no clear drop indicating strong scattering as seen in the case of the forest metamaterial (Lott et al. [2020a]).

In conclusion, despite the presence of WT arrays, we found no indications of unusual dampening of surface waves or discernible deviation in dispersion characteristics of

surface waves within the wind farm, as we would have expected in the case of a locally-resonant metasurface.

## 3.4 The META-WT Experiment

In our effort to confirm the hypothesis that WTs act as coupled resonators, we selected a site near Nauen in Brandenburg, Germany, which hosts relatively taller and heavier turbines. Supported by a dense acquisition grid, we conduct a high-resolution geophysical experiment over three weeks in February 2023, called the 'META-WT' experiment (Pilz et al. [2024]). We opted to perform this experiment in the winter, when storm activity and wave energy are typically higher, in order to capitalize on the heightened microseism signals. The continuous ambient noise recordings with dense spatial sampling permit us to study in great detail the potential locally-resonant metamaterial behavior of this wind farm. Compared to the WTs in San Gorgonio, here the WT units are much more sparsely distributed in space ($\sim 200 - 300m$ apart) due to their size and other factors related to topography and wind. We anticipate to see metamaterial effects when wavelengths on the order of a kilometer or higher interact with such a wind farm configuration. Our approach is further complementary to recently completed research projects (e.g., MISS - Mitigation of the disturbance effect of WTs on seismological stations; TremAc - Objective Criteria for Vibration and Noise Emissions of Inland Wind Power Plants) which aimed at investigating vibration and infrasound emissions in the near-field of single WTs and mitigating disturbing effect on seismic stations.

**Contribution to the collaborative study**

This experimental study being a collaborative effort, a significant portion of the overall outcomes is from analyses performed by colleagues from GFZ and the University of Potsdam, Germany. The peer-reviewed article towards the end of the chapter describes the comprehensive first results from the META-WT experiment. Our primary contributions to this study include:

- active participation in the deployment of the various sensors in the wind farm
- wind turbine modeling, and
- (to some extent) the analysis of Distributed Acoustic Sensing (DAS) data.

In the remainder of this chapter, our focus mainly shifts to these contributions. We perform detailed analysis of the DAS data, offering insights that complement the results already presented in the article. However, before delving into the main analysis, we first provide an overview of the deployment and the array configuration, with a focus on the acquisition of the DAS data.

### 3.4.1 Wind farm configuration

The wind farm in located on the Nauen Plateau, a low plateau in the German state of Brandenburg. The wind park is composed of 198 WTs and is subdivided

into a number of smaller administrative sub-wind parks. We choose the sub-wind park which is to the west of Nauen town and has a collection of over seventy WTs that can potentially act as heavy-mass coupled resonators. WTs are of different builds from various manufacturers, have different power ratings, and a range of hub heights ranging from 65 to 115 m (identified in Fig. 3.15). The WT rows are slightly inclined $\sim 10^{\circ}$ with respect to the NS direction and are approximately 400 m apart with a typical inter-WT distance of 250 m. In this region of the wind farm, a dense nodal array is installed that covers about thirty of the WTs. The towers are either prestressed concrete-steel hybrid (PCSH) towers or tubular steel towers, depending on the WT model and its manufacturer. In this study, we do not compute the resonances of all the WTs, but rather just the one that has been well instrumented in its surroundings with geophones, broadband sensors, and a fiber optic cable.

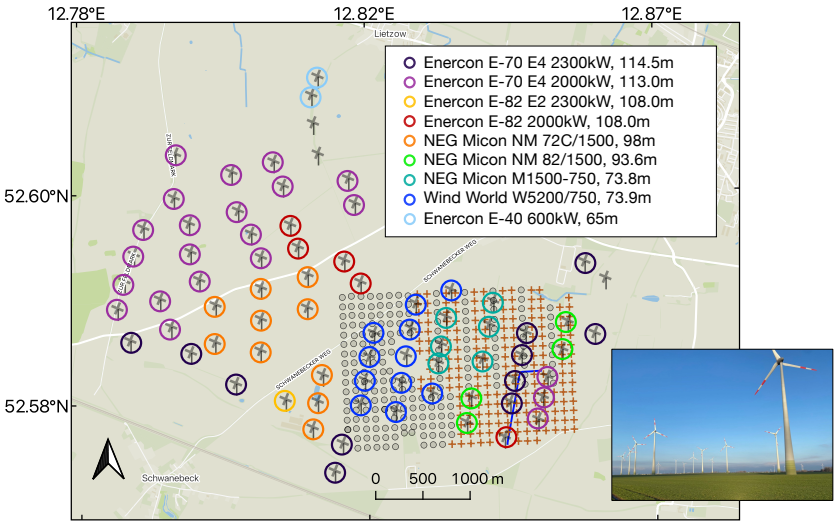


Figure 3.15: META-WT experiment setting in the Nauen wind farm in Brandenburg region, Germany. The dense nodal array of 1C and 3C geophones extends 2.5 km in the E-W direction and 1.5 km in the N-S direction. The array is located within a quasi-periodic array of wind turbines that are encircled with different colors indicating their model name, rated power and hub heights. Data Source: https://en.wind-turbine.com/tools/wkamap (Last Accessed on 08/06/2023). Inset shows a photograph of turbines in the wind farm.

### Predicted resonance frequencies of Enercon E70 wind turbine

We chose to evaluate the resonance frequencies of the ENERCON E-70 turbine which has a Lennartz 5-s broadband sensor installed at its base and the DAS fiber optic cable in close proximity. This helps us better understand the recorded signals. This WT with a nominal power of 2.3 MW, has a hub height of 113.5 m and is mounted over a hybrid precast concrete-steel tower (Fig. 3.16 (a)). Since there was no explicit measurement of the WT resonances in the field, we resort to eigenfrequency analysis using COMSOL, a commercial FEA package. Unlike the previous study, where the Micon M108 WT resonance was analytically determined with a reasonable accuracy, in the case of Enercon E70 WT, it is more complicated due to the hybrid nature of the tower. Thus, we have to use a finite-element model of the WT. The diameter of

the tubular tower varies from 9.3 m at the base and smoothly tapers to 2 m at the top. The lower two thirds of the tower is a precast concrete construction with 22 segments, each 3.8 m high with a 300 mm thick shell. The upper third of the tower is composed of two structural steel segments 3 and 25 m long, having a shell thickness of 40 and 25 mm, respectively. The tower is idealized as a vertical cantilever beam (neglecting the effects of damping) of multiple segments having a mean annular cross section with constant thickness. The rotor assembly, the nacelle and generator, which weigh around 104 tons in total (Source: http://www.darsunsolar.pl/wp-content/uploads/2015/08/Enercon-E70-E4-23MW.pdf), are modeled as a concentrated mass placed on top of the beam, whereas the bottom end of the tower is assigned a fixed boundary condition (neglecting soil-structure interaction). The tower is discretized with one-dimensional beam elements available with the COMSOL structural mechanics module. The elastic parameters of concrete and structural steel are obtained from the Euro codes 2 and 3 respectively (**??**). Table3.2 lists the natural tower frequencies for both the Euler-Bernoulli (slender beam) and Timoshenko (thick beam) formulations.

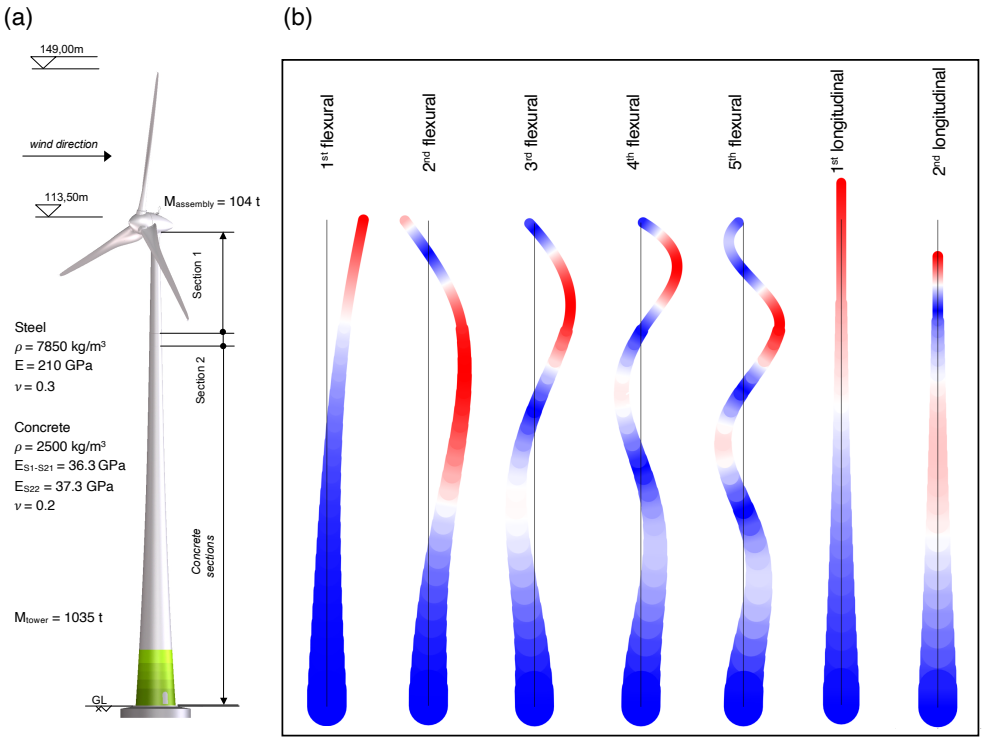


Figure 3.16: Modal representations of the 112.3 m high ENERCON E70 wind turbine tower motion under flexural and compressional resonances. (a) Technical drawing of the wind turbine (© ENERCON GmbH). (b) Flexural and compressional oscillations of the tower. The concrete and steel segments are assigned a uniform annulus cross section with material properties shown in the left panel. Although 1D beam elements are used, the tubular representation of the tower is shown for better visualization. The color represents the normalized eigen displacement magnitude, blue and red indicating the respective minimum and maximum for each characteristic mode. The eigenvalues corresponding to the Euler-Bernoulli and Timoshenko beam formulations are shown in Table 1.

| | Flexural modes | | | | | Longitudinal modes | |
|---|---|---|---|---|---|---|---|
| Beam formulation | $f_1$ | $f_2$ | $f_3$ | $f_4$ | $f_5$ | $\overline{f_1}$ | $\overline{f_2}$ |
| Euler-Bernoulli | 0.42 | 1.46 | 3.84 | 6.75 | 10.36 | 10.58 | 20.60 |
| Timoshenko | 0.42 | 1.44 | 3.72 | 6.47 | 9.56 | 10.58 | 20.60 |

Table 3.2: Numerically obtained eigen values for the ENERCON E-70 wind turbine tower.

The foundation is coupled to the ground by a micropile or monopile system based on the soil properties. This is done to ensure that the turbine does not lose traction and also improves the shear strength of the soil. In the vicinity of the turbine the soil is prepared artificially by compaction, to ensure that the foundation loads are safely transferred. The exact type of foundation system used in Nauen is unknown. We thus model a fixed base to give a perfect clamping to the WT base, but in the field there is a role played by the interaction between the WT structure and the subsurface soil. In this section, we have looked at only one kind of WT resonator. This single WT cannot be considered to be representative of the entire wind farm. We expect a heterogeneous distribution of resonances inside the wind farm that can still be interesting and could potentially lead to wider frequency bandgaps.

### 3.4.2 Array deployment

Of the various instruments that were deployed in the field, the dense nodal array is particularly prominent and spans 2.5 km and 1.5 km in the N-S and E-W directions, respectively (see Fig. 3.17(a)). It is composed of 400 geophones with an equal number of 1C and 3C sensors, deployed with a 100m grid spacing. The 1C geophones have a 4.5 Hz cut-off while the 3C geophone have a 5.0 Hz cut-off which are connected to Reftek digitizers (shown in the foreground of Fig. 3.18(a)). In addition to this dense grid, we also deployed eight Trillium Compact 120-s broadband senors along a radial line running in the N-S direction cutting across the wind farm. These serve as a reference for comparing the response within the wind farm. In the S-E sector of the wind farm we also have eight Lennartz 5-s three-component instruments, seven iXblue blueSeis-3A rotational seismometers co-located with seven Trillium compact 120-s seismometers and with a Paroscientific pressure sensor on six of these stations. Finally, we deployed a 1 km linear fiber optic cable traversing an L shape, trenching a shallow 10 cm of the top layer of the soil. The backfill is well compacted by walking back and forth, in order to have good ground coupling. The DAS cable is co-located with the broadband sensors and the rotational sensors (a zoomed-in view is shown in Fig. 3.17 (b)). The starting point is where the cable is connected to an OptoDAS interrogator unit, which is seen in a photo taken in the field (see Fig. 3.18(d)). Along the length of the linear fiber optic cable we have similar turbines belonging to the manufacturer Enercon GmbH at 350m (PR05), 600m (PR06), and 850m (PR07). In particular, one turbine (PR06) is selected to closely monitor the signals in the near-field by installing various sensors - a Lennartz 5-s 3C sensor over the foundation slab, seven 3C geophones in a circular fashion around the foundation, and a DAS cable that is running in close proximity. Additional experiment details are provided in Pilz et al. [2024]. In the next section, we focus on DAS data acquisition after

briefly introducing its measurement principle.

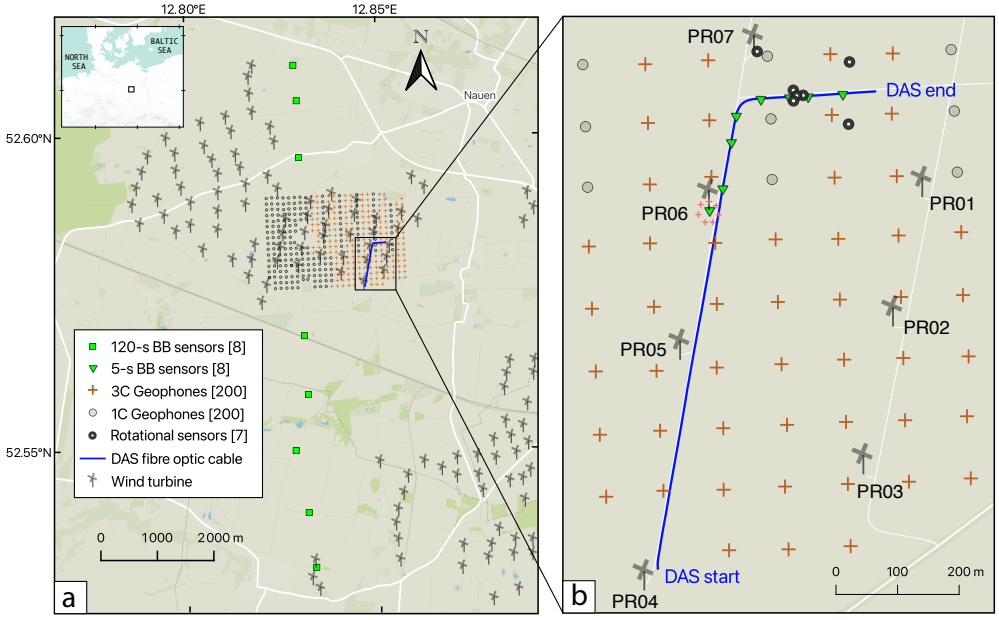


Figure 3.17: Experimental configuration in the wind farm near Nauen (Bradenburg region, Germany shown in the inset). [Panel a] The 2D array of 400 geophones is composed of an equal number of 4.5-Hz one-component geophones and 5-Hz three-component geophones positioned on a 100-m grid. The radial line array of Trillium Compact 120-s broadband instruments extends north-south. [Panel b] In the south-eastern sector, the grid was densified by Lennartz 5-s short period sensors, iXblue blueSeis-3A rotational seismometers co-located with Trillium compact 120-s seismometers and pressure sensors (not shown here for clarity). The blue line represents the position of the DAS fiber optic cable.

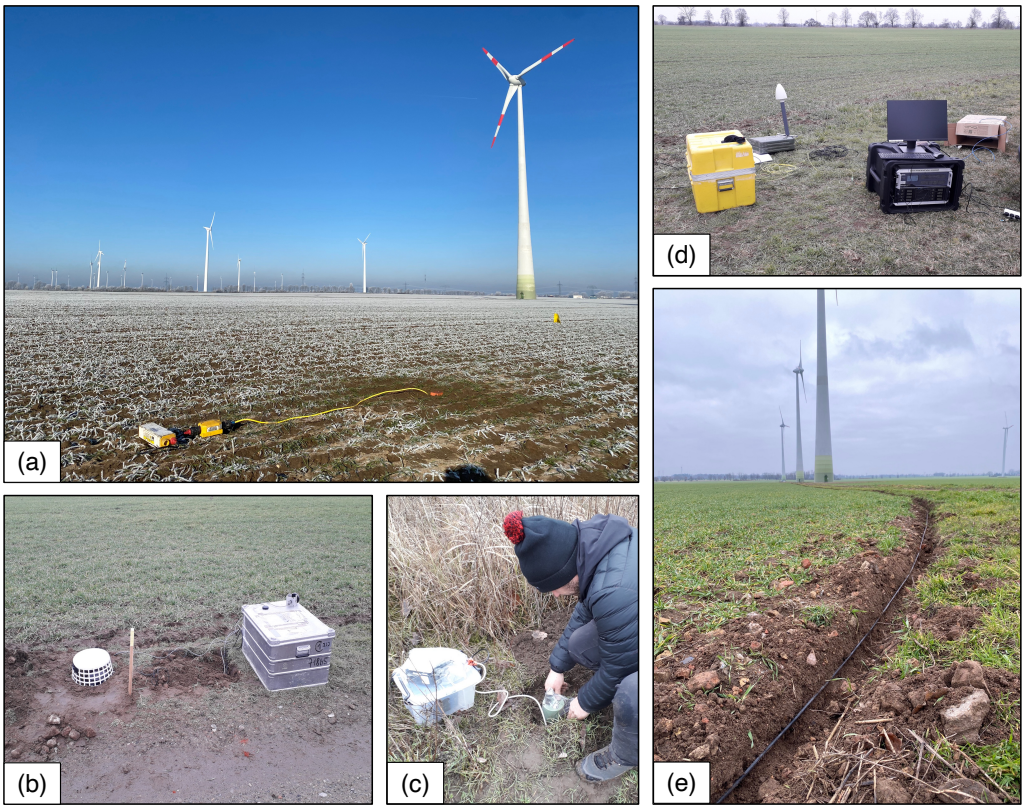


Figure 3.18: Deployment of various geophysical instrumentation in the wind farm. (a) A GS-One 3C geophone connected to a Reftek digitizer is seen installed in the foreground and an Enercon E-70 turbine standing 113m high in the background. (b) A rotational 6C station installed inside the wind farm, (c) 3C Broadband seismometer installation along the radial array, south of the wind farm, (d) An Alcatel Submarine Networks 'OptoDAS' interrogator at the start point of the cable, and (e) A 1km long DAS cable - Universal cable 8x50/125, OM2 fiber being deployed inside the wind turbine field.

### 3.4.3 DAS acquisition

#### Measurement Principle

Fiber-optic Distributed acoustic sensing (DAS) has developed across multiple industries and offered new possibilities in geophysics and especially in seismology. A DAS system essentially measures the strain along the fiber optic cable by turning them into a dense array of strain sensors - typically spaced between 1 to 10 m over several kilometers (Zhan [2020], Lindsey and Martin [2021]). The principle of strain measurement is based on the optical phase changes detected in Rayleigh backscattered light at one end, when laser pulses are repeatedly sent through the cable. These continuous laser pulses are sent out by an optoelectronic instrument, called an interrogator unit (IU), which also measures the subtle phase shifts in Rayleigh scattered light along different points of the fiber (Fig. 3.19). The spatial resolution along the fiber is fixed, called the gauge length (usually between 1 and 40 m). Any disturbance in the medium, for example, a seismic wave impinging on the fiber, slightly alters the fiber mechanical strain. The phases of the backscattered laser are proportional to the change in length of the path over this gauge length, i.e. the

signal phase is linearly related to the gauge strain and directly proportional to the dynamic mechanical strain of the fiber. This forms the basis of DAS measurement. The virtual nodes (or channels) at which the DAS data are reported are often a subset of the gauge length. While DAS units generally have a lower signal-to-noise ratio and a stronger angular sensitivity than standard seismometers (discussed in detail later), this drawback will be compensated by having an ultra-dense series of highly-resistant seismic sensors. Another advantage of DAS recordings is that it can capture dynamic deformations in a broad range of frequencies $f = 0.001 - 1000Hz$ (Lindsey and Martin [2021]).

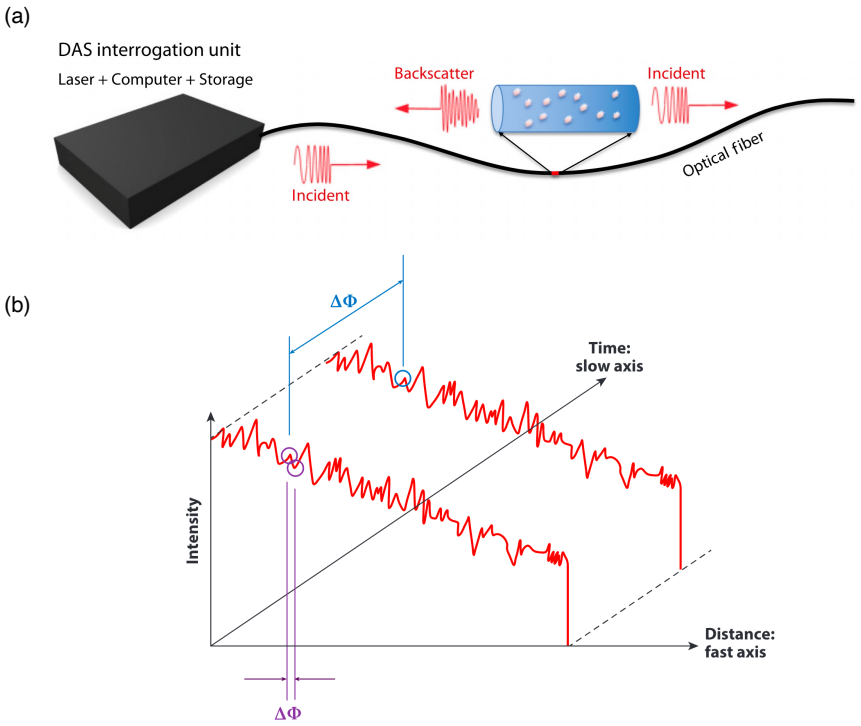


Figure 3.19: DAS measurement principle. (a) A DAS unit attaches to one end of a long optical fiber cable, sends laser pulses (harmonic or chirp) to the fiber, and interrogates the Rayleigh backscattered light from intrinsic fiber defects. The data processing and storage occur in real time within the DAS unit (adapted from Zhan [2020]). (b) Intensity versus time and distance of two pulses demonstrates how the optical phase information for a gauge length can be computed as the phase change across a gauge measured using a single pulse along the fast axis or as the rate of phase change across a gauge between repeat pulses along the slow axis. (adapted from Lindsey and Martin [2021])

### Ambient noise inside the wind farm

The DAS data were acquired for short periods on February 14, 16, and 23 with the OptoDAS interrogator. Here, in this chapter, we analyze the data only from the 16-Feb-2023 which is 2-hour long recording with the highest wind speed and has the most stable noise amplitude among the three recording periods. The native (optical) sampling frequency is 5 kHz (i.e. $20\mu s$ sampling period), but for convenience, we downsample the data to 500 Hz, which is quite sufficient for our analysis. The

gauge length selected for the acquisition was 10m. We chose a channel spacing of 4m, since this provides the best compromise between self-noise and the spatial resolution. This dense spatial sampling is important for near-field analysis, which is otherwise difficult to capture with a sparse array of traditional seismometers (with the METAFORET experiment being an exception). The lowpass filtered (below 10 Hz) strain-rate data is shown in Fig.3.20. The signals at distances close to the WTs PR05 and PR06, i.e., at $\sim 350m$ and $\sim 610m$ are the strongest as expected. Of the two turbines, PR06 is positioned slightly closer to the cable compared to PR05, thus higher in amplitude.

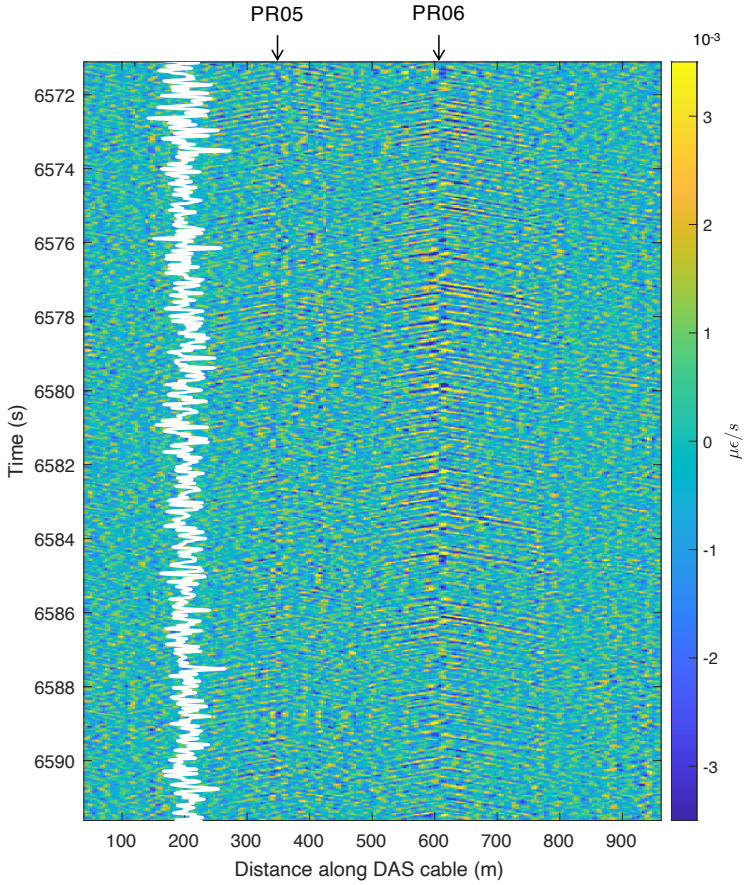


Figure 3.20: DAS linear cable profile showing the strain-rate amplitude of seismic noise along the fibre-optic cable for a few seconds. The waveforms are lowpass filtered below 10 Hz. The vertical axis denotes the time in seconds after the start time of the recording, whereas the horizontal axis is the linear fiber length in meters with a resolution of 4m. The high amplitudes in the beginning and the end of the cable due to interfering signals of the power supply of the interrogator are not shown. The radiation from the wind turbines PR05 and PR06 can be observed at $\sim 350m$ and $\sim 610m$ of the cable, respectively (marked by an arrow to guide the readers eye). The latter being located more closer to the cable shows stronger amplitudes. The wiggles at 200m is the noise time series for illustration.

### 3.4.4 Spectral Analyses

In this section, we look at the spectral properties of the ambient noise recorded by a short segment of the DAS fiber optic cable in the vicinity (20m on either side of the turbine) of the WT PR06. We choose the same dataset from 16th Feb 2023 for consistency. The whole time series of 2 hours is divided in to half-overlapping consecutive windows of 10-s and the average spectrogram is plotted in Fig 3.21(a). We observe a number of stationary peaks that are explicitly identified from the spectral amplitudes in Fig. 3.21(c). These peaks correspond to the WT resonances, and are similarly observed in the literature. We also plot the wind speed during the same period to show the amplitude dependency on the wind speed. The direction of wind does not vary much during the recording ($240° - 260°$). The turbine should be active during the whole period since the wind speed is always above the threshold cut-in wind speed. Indeed, the noise seems to be elevated during windows of high wind, similar to what has been observed in other studies related to WT seismic noise.

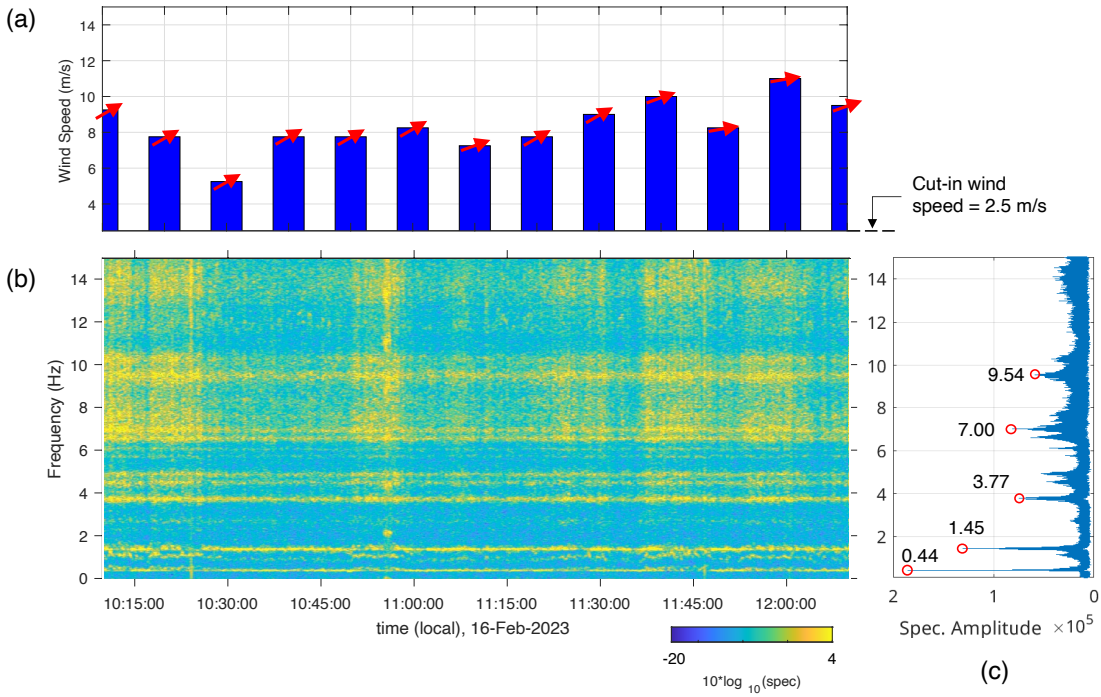


Figure 3.21: (b) Strain-rate spectrogram of the ∼2 hr DAS recording on 16-Feb-2023 from 10:09:29 to 12:10:09 (CET) for the channels 20m on either side of the Enercon E-70 wind turbine (designated PR06 in the Fig. 3.17). Each column of the spectrogram results from the average of spectral estimates obtained over 10-s-long windows with 5-s overlap. (a) The wind speed measured at the hub height with a resolution of 10 min is plotted for the same duration of the recording. The red arrows indicate the direction of the wind, which is mostly constant throughout the period. (c) In the spectral amplitude plot, the stationary peaks encircled in red are at the discrete frequencies that correspond to the resonances of the wind turbine structure. The other peaks are either WT blade rotation or sub-harmonics of current grid frequency.

We now compare the peaks observed from the DAS data with those of the 5-s broadband sensor installed on the foundation of the same WT under the operating conditions (gray dotted curve in Fig. 3.22(b)). We see almost identical values of the peaks from the DAS and BB sensors. In addition to this, over the whole frequency range, the numerically obtained eigenvalues are in good agreement with the observations, and small deviations can only be seen for higher modes. The fixed base model predicts the natural frequency of the WT with reasonable accuracy. Although our model does not take into account the flexibility of the foundation due to the soil coupling, the numerical results obtained are evidence that the foundation is almost clamped due to the type of foundation system that has been used.Apart from the unknown foundation clamping, slight deviations might also be caused by the eccentricity of the head mass with respect to the center of gravity of the tower

cross-section. This causes the resonance frequencies to widen (seen in Fig. 3.22) when the WT is operational with respect to when it is non-operational and the higher modes shift. However, since Rayleigh waves have an elliptical polarization, which implies both horizontal and vertical displacements, a straightforward coupling of both the flexural and the compressional resonances of the WT towers with the seismic wavefield is also possible. Secondly, most of the resonances here are caused by flexural modes. This might be due to the fact that flexural resonances of slender structures such as WTs are excited more easily than compressional ones. This is different from the METAFORET experiment in which no efficient coupling between the horizontal components of the Rayleigh waves with the flexural resonances of the trees was observed, which might be due to different material properties. Although from a theoretical point of view we do not see an overlap between the flexural and compressional resonance frequency ranges, we cannot exclude the possibility of interaction between the two. Finally, the other peaks that are not related to the resonances of the turbine correspond to the blade-passing frequency and its harmonics. The blade passing frequency for the Enercon E-70 model can vary between 0.1 – 0.34 Hz (also measured in the field), thus the 3P frequency can vary between. 0.3 – 1 Hz.

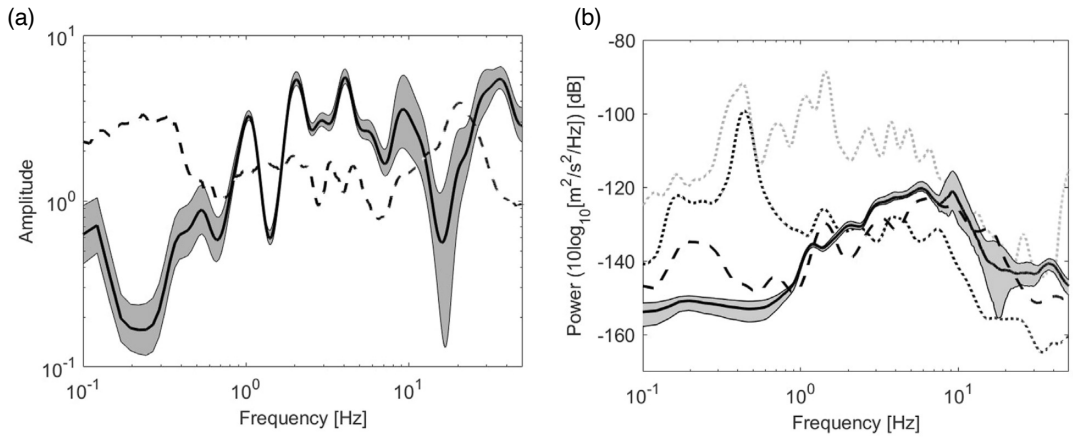


Figure 3.22: (a) Spectral ratios (vertical component) between the 400 array nodes and the three most distant broadband stations outside the wind farm (adapted from Pilz et al. [2024]). The solid line is the mean and the shaded area is ± one standard deviation. The dashed line corresponds to the horizontal-to-vertical spectral ratio for the southernmost broadband station. (b) Power spectral densities of the 400 array nodes (solid line) and the broadband stations (dashed line). The dotted lines show the geometrical mean of the two horizontal components of the 5-s sensor installed on the foundation of a single wind turbine during operation (gray) and at standstill (black).

Since the DAS cable was only deployed inside the wind farm, we cannot compare the ratio of the spectra inside and outside with a spectral ratio analysis. However, spectral analyses of the nodal array and the radial BB array under no-wind conditions have been discussed in the attached article. For the method of computation of the spectral ratio, we refer the reader to Pilz et al. [2024]. The results suggest drops in the spectral ratio (Fig. 3.22(a)) in several frequency bands. For exam-

ple, the width of the first drop spans the subhertz frequency spectrum between 0.1-0.5 Hz, where one would except the individual WTs to oscillate in the fundamental flexural mode. It is interesting to note that similar to what we observed in the METAFORET experiment around the tree longitudinal resonance, the drop in spectral ratio is caused by a spectral peak outside the wind farm. This means less energy penetrates through the ground inside the wind farm, even though the WTs are resonating at these frequencies - implying propagation of evanescent waves, as one would expect for a metasurface. The drop after 10 Hz has to be linked to the longitudinal resonances of the WTs. The interpretation of the bandgap after 10 Hz should be done carefully as the the wind farm and the BB stations outside are separated by a large distance. The sources of these high-frequency surface waves can be of different origin as they attenuate (intrinsic attenuation) much strongly as compared to low-frequency surface waves.

### 3.4.5 Source radiation for different WT modes

We take advantage of the dense sampling offered by the DAS measurements, to verify the radiation pattern from each of the WT modes. Fig. 3.23 shows the profiles for different peaks observed in the spectra that correspond to the WT resonances from different time windows of the recording. We observe two distinct features of the signals in the frequency bands we chose:

1. The dipolar source radiation is observed for all the modes i.e., an anti-symmetric motion about the WT due to the bending moment at the foundation induced by tower flexure, and

2. The amplitudes for the lower frequencies drop off in a much shorter distance from the WT source, which is counter-intuitive, since higher frequencies typically attenuate more rapidly.

For the latter, we have found that this effect is seen for both the WTs at 350 and 600 m along the cable. In contrast, signals of high frequency can be seen spreading hundreds of meters, with tower resonance frequencies experiencing significant attenuation. Peculiarly, the drop in the attenuation factor coincides well with the resonance frequencies of the WT (Pilz et al. [2024] ). Such an unusual attenuation of surface waves, which are mainly emitted by WTs, cannot be explained by near-field effects. Among the hypotheses, this effect could be due to the destructive interferences of surface waves from neighboring WTs, meaning that if the WT were to be isolated we would not have observed this strong attenuation. This can be verified by running time-domain simulations with an isolated WT with the inverted velocity model in the following section.

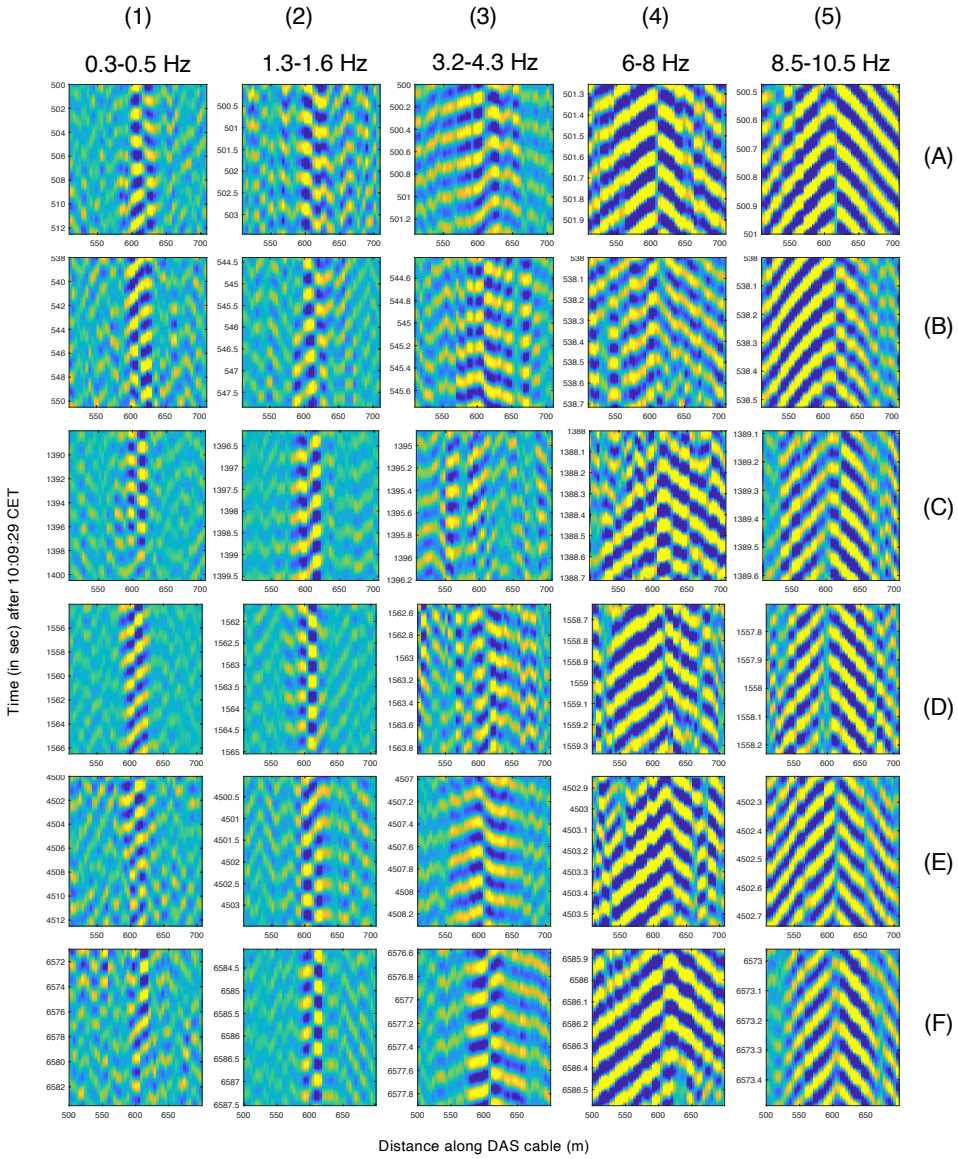


Figure 3.23: DAS profiles of a 200m segment of the cable for several time windows [rows A through F] with the wind turbine PR06 roughly centered on the horizontal axis. The columns (1) through (5) correspond to the WT resonance modes. The color represents the normalized strain-rate data after filtering around each of the spectral peaks indicated. All the modes show a dipolar radiation pattern. Note the different y-axes for each row, as only five cycles of oscillation are plotted for each frequency.

### Simulation of coupled WT-soil system

In order to gain insight into the seismic wavefield emitted from a WT and the associated radiation patterns, we run simulations in the time-domain with realistic modeling of the WT tower and a realistic ground model. We run P-SV time-domain simulations using the solid-beam coupling module available in COMSOL Mutiphysics. The turbines PR05, PR06 and PR07 are all Enercon E-70 models with hybrid towers. The tower is modeled as a Timoshenko beam and the turbine assembly as a concentrated mass at the top end, similar to the model used in the

simulations in the section 3.4.1. However, instead of clamping the base, we now rigidly couple it to a tapering concrete foundation base slab anchored in the top layer of the soil. For the velocity model, we used the four-layer S-wave velocity (Fig. 3.24(a)), obtained from the inversion of field data from the META-WT nodal array (Pilz et al. [2024]). We neglect here the effects of damping for the tower as well as the soil. The low reflecting boundary (LRB) condition is assigned to the bottom and side boundaries, whereas the top boundary is traction free. In this section, we are mainly interested in understanding the radiation pattern when the WT oscillates in both bending and compression modes. As stated before, the exact type of foundation system used in Nauen is unknown, but this should not drastically effect the radiation patterns. However, a result of the unknown soil clamping is that we obtain slightly lower resonance frequencies than those observed.

We choose to first excite the turbine with a horizontal force using a flat chirp from 0 to 10 Hz, at the free end of the turbine for a duration of $20s$ (see Fig. 3.24 (b,c)). We apply a Tukey window to gradually taper both sides of the signal. In the WT response, we observe two flexure modes to dominate. As we would expect, we see an inverse polarization of the vertical displacement on either side of the tower (shown in Fig. 3.24 (d,e)) for every oscillation of the WT as we observed in the data (Fig. 3.23). The total duration of the applied force is 20s, but the total simulation time is $\sim 33s$, which means the WT continues to resonate freely in the first two modes even after the force is removed. In real situations, the tower excitation, for example due to wind acting horizontally along the tower height, is more complex than a chirp and the force spectrum is low frequency dominated. The radiation of the first two flexural modes in the near-field is nevertheless similar as we see that from the DAS profiles (see Fig. 3.23).

In the second simulation, we excite the top of the WT with the same chirp in the vertical direction. As expected, we see a monopolar radiation for the longitudinal excitation of the turbine that is caused by a purely up and down motion of the foundation (Fig. 3.24 (f,g)). In contrast to the flexural excitation, the turbine stops resonating immediately after the force is removed. This is explained by the fact that the compressional resonance exhibits a low Q-factor, indicating that the WT rapidly re-emits the energy that is injected to it by the external force. On the other hand, flexural resonances demonstrate high Q-factors, implying that the WT flexural vibrations persist for an extended duration before dissipating the energy fully into the ground. This was also confirmed by Lott and Roux [2019b] in the case of resonances of the rods attached to a plate. Thus, when the WT is not forced by the wind, it will mainly resonate in the various flexural modes emitting a dipolar radiation. In addition to the Q-factor, the strong impedance mismatch at the foundation-soil interface will not permit an efficient exchange of energy between the turbine and the ground.

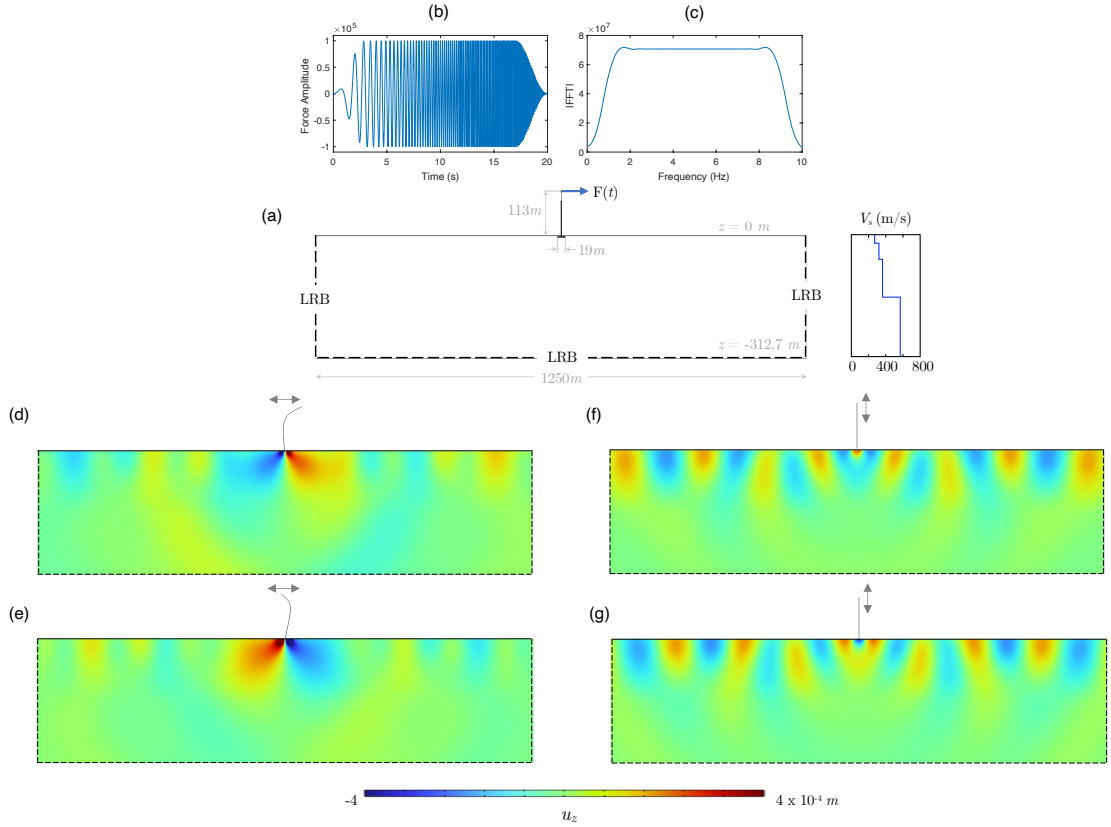


Figure 3.24: P-SV simulations in time-domain for a single WT coupled to the ground. (a) Simulation box with the WT modeled as beam elements, whereas the foundation slab and the soil layers are solid elements. The free end of the WT is excited by a vertical and horizontal force separately using a 20-s chirp signal going from 0 to 10 Hz (b,c). Snapshots of the vertical displacement field $u_z$ for two consecutive cycles of WT tower oscillation for horizontal forcing (d,e) and vertical forcing (f,g) a few seconds after the zero time of the applied force. We see a dipole like source that continuously alternates when the WT is oscillating in flexure, and a classical monopolar radiation for the longitudinal excitation of the turbine. The symmetric rainbow color map goes from blue (downward motion) to red (upward motion).

### 3.4.6 Surface wave dispersion and scattering

An immediate question arises from the unusual drops observed in the spectral ratio: *Does this phenomenon in the wavefield intensity also manifest in the effective phase properties of surface waves in the wind farm?* To answer this question, the surface wave phase velocity and scattering inside the wind farm can be extracted from noise correlations, similar to the approach taken in the study of ambient noise in the San Gorgonio wind farm (Section 3.3.4). However, in this case, we use DAS data, which offer much denser spatial and temporal sampling as compared to the geophones. The META-WT nodal array has a grid spacing of 100m, which allows analysis up to 2 Hz (beyond which we have aliasing $\lambda = 200m$). Consequently, the frequency range for DAS array processing is less constrained with a much denser (4m) channel spacing. A distinctive feature of DAS is that it offers an effective means of capturing wavefield

data for analysis using array processing tools (Lindsey et al. [2017], van den Ende and Ampuero [2021]).

### Correlations of axial strain measurements

DAS measures average axial strain rate along the fiber. The only difference compared to a geophone array is that we are now dealing with a tensor field (strain rate) instead of a vector field (particle velocity). Various studies have been able to successfully separate coherent signals from background noise using DAS-based interferometry. The noise correlation functions were formed using strain-rate sensor data captured by collinear channels from several surface DAS arrays set up in various configurations (Martin* et al. [2015], Martin et al. [2016], Dou et al. [2017], Zeng et al. [2017], Lindsey [2019]). In a theoretical study of interferometry based on DAS measurements, Martin et al. [2021] concluded that cross-correlation of DAS sensor data leads to important radiation pattern sensitivity depending on the wave type, orientation of the cable and azimuth between the sensors. The rigorous equations are derived for the plane wave incidence i.e, source is in the far-field. In our case, however, the seismic energy radiated from WTs is in the near-field. That means if the energy propagates with wavelengths higher than the gauge length (here $L_g = 10m$), then this effect should be less pronounced. We anyways plot in Fig. 3.25, the sensitivity of the DAS measurements to plane waves arriving from different azimuths using the expression derived in Martin et al. [2021] (only the amplitude terms ignoring the oscillatory terms and exponentially decaying depth-dependent Rayleigh wave terms). As already shown in their study, we see that the axial strain measurement over a gauge length is most sensitive to Rayleigh waves such that $\phi - \theta = 0, \pi$, where $\phi$ is the angle of plane wave incidence and $\theta$ is the orientation of the DAS cable itself. This holds good for wavelengths that are a few times higher than the gauge length. As the wavelength approaches the gauge length ($\lambda \sim l_g$), the sensitivity lobes start to flatten along the cable direction and eventually when the wavelength and the gauge length become equal, the Rayleigh waves incident along the cable direction cannot be detected as the strain is not measured (in our case this happens around f = 27 Hz). For even smaller wavelengths, the pattern changes to four-lobed instead of two-lobed, with a maximum sensitivity again in the direction of the cable.

Similarly, Rayleigh wave radial-radial correlations between DAS channels exhibit a dipole sensitivity, peaking in the in-line direction similar to the directly incident plane RW sensitivity, but forms additional lobes at higher frequencies (Fig. 3.26). If we limit our analysis to frequencies up to 15 Hz (For $C \approx 300m/s$ at $f = 15Hz; \lambda = 20m$), where $\lambda \sim 2l_g$, then sensitivity is always maximum along the DAS cable. This means, for a fiber-optic cable where the channels are aligned in a linear fashion, the 2-point correlation functions are primarily interpreted as approximations of Rayleigh wave 2D Green's functions.

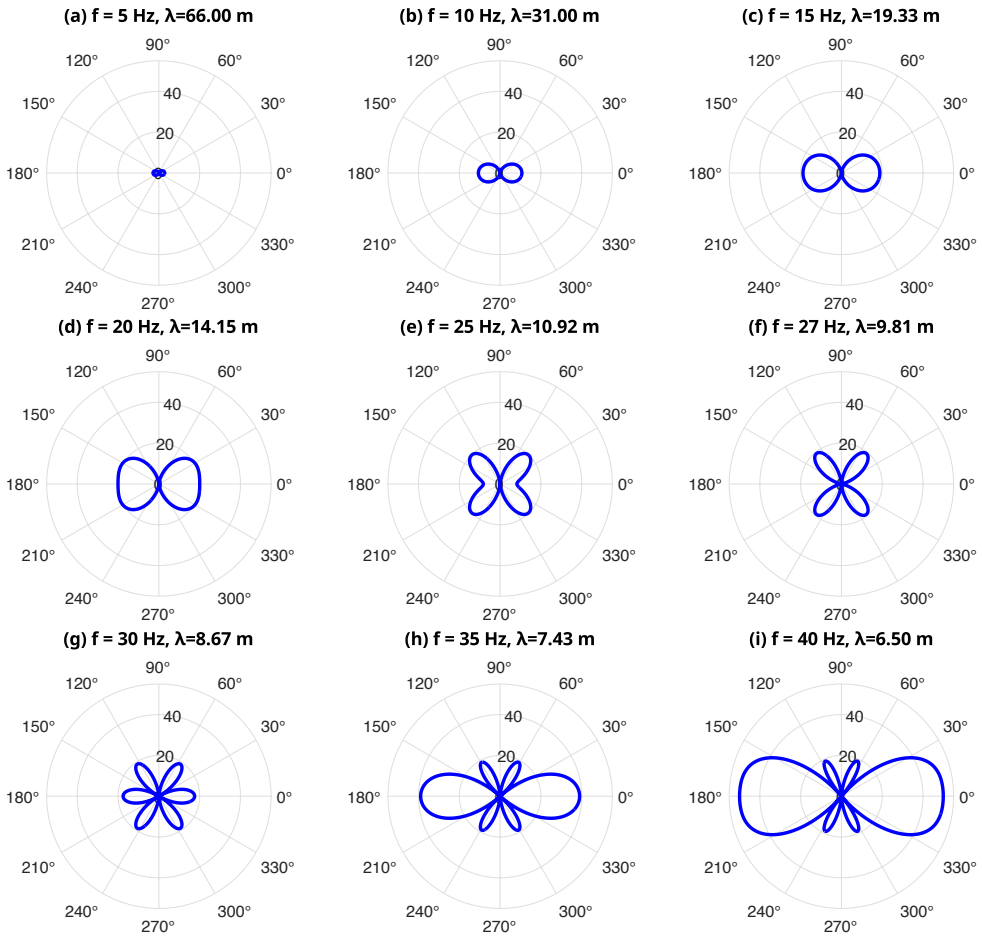


Figure 3.25: Amplitude sensitivity of DAS measurements to planar surface waves of varying azimuth and wavelength. Each polar plot represents the sensitivity of DAS measurements (cable oriented along $0° - 180°$) with a 10m gauge length to a range of wavelengths for the META-WT velocity model. The expression is taken from Martin et al. [2021] keeping only the amplitude terms and ignoring the oscillatory terms and exponentially decaying depth-dependent Rayleigh wave terms, which is given as $\frac{2ck}{L_g} cos(\phi - \theta) sin(\frac{kL_g cos(\phi - \theta)}{2})$.

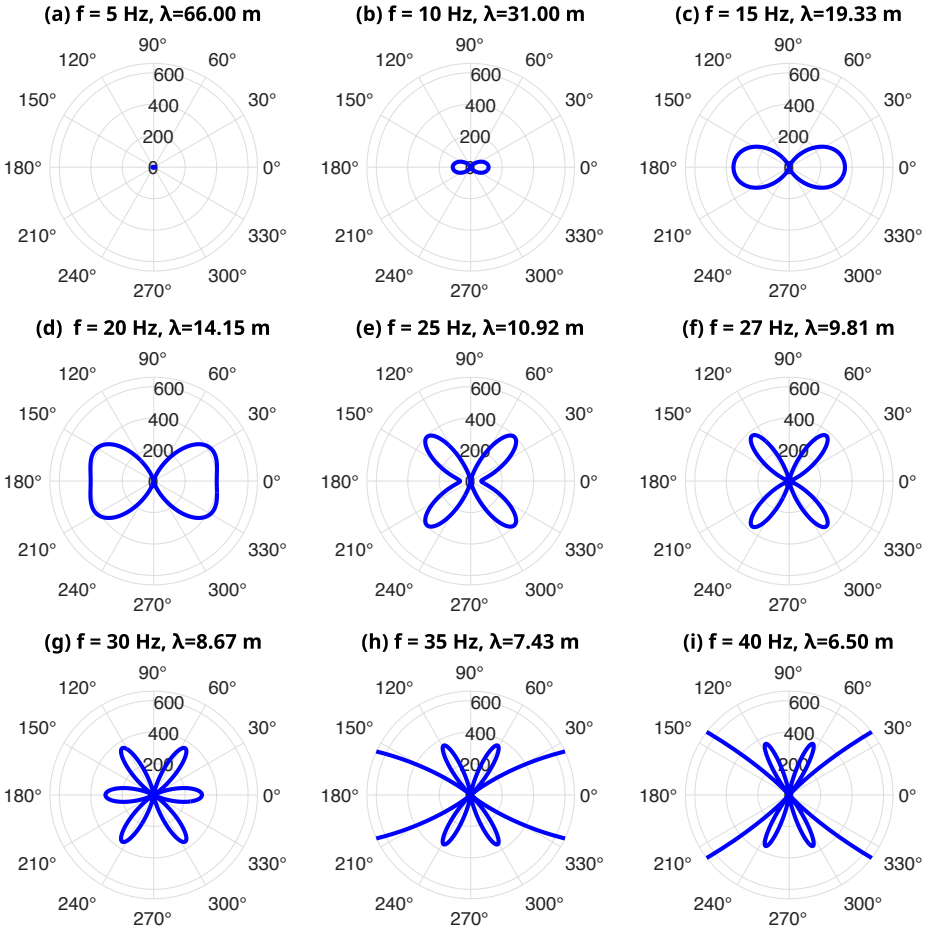


Figure 3.26: Same as Fig. 3.25 but for amplitude sensitivity of radial-radial cross-correlations of DAS measurements (cable oriented along $0° - 180°$) at two sensors simultaneously recording the same (Rayleigh) plane wave of varying azimuth and wavelength. The expression is extracted from Martin et al. [2021], which are simply the square of the amplitudes plotted in the 3.25, and given as $\frac{4c^2k^2}{L_g^2} cos^2(\phi - \theta) sin^2(\frac{kL_g cos(\phi-\theta)}{2})$.

### Cross Spectral Density Matrix (CSDM)

We recall the steps involved in computing a CSDM, which was already discussed in the previous chapter in Section 2.4.1 in the context of the dense array of the METAFORET experiment. In this case, we process the noise data for each DAS channel and populate the CSDM for every channel pair $(i, j)$, $\mathbf{K}_{ij}(f) = \left\langle \mathbf{d}_i(f)\, \mathbf{d}_j^*(f) \right\rangle$. We compute $\mathbf{K}$ for each frequency by averaging estimates from individual time windows. As $\mathbf{K}$ is a function of both frequency $f$ and time $t$, we take a time interval $\Delta t$ that varies with frequency bands, i.e. $\Delta t$ varies from 10 s to 2 s in the 0.25-15 Hz frequency band. By taking an ensemble average, we eliminate the coupling of the sources inside each time window (here the WT signals are the dominant source). We use the full 2 hour recording to maximize the number of time windows $M$, such that $M \gg N$ usually $M \approx 3N$, where $N$ is the number of DAS channels; thus giving a full-rank CSDM. The results for the time-averaged CSDM for a few selected frequencies are shown in Fig. 3.27.

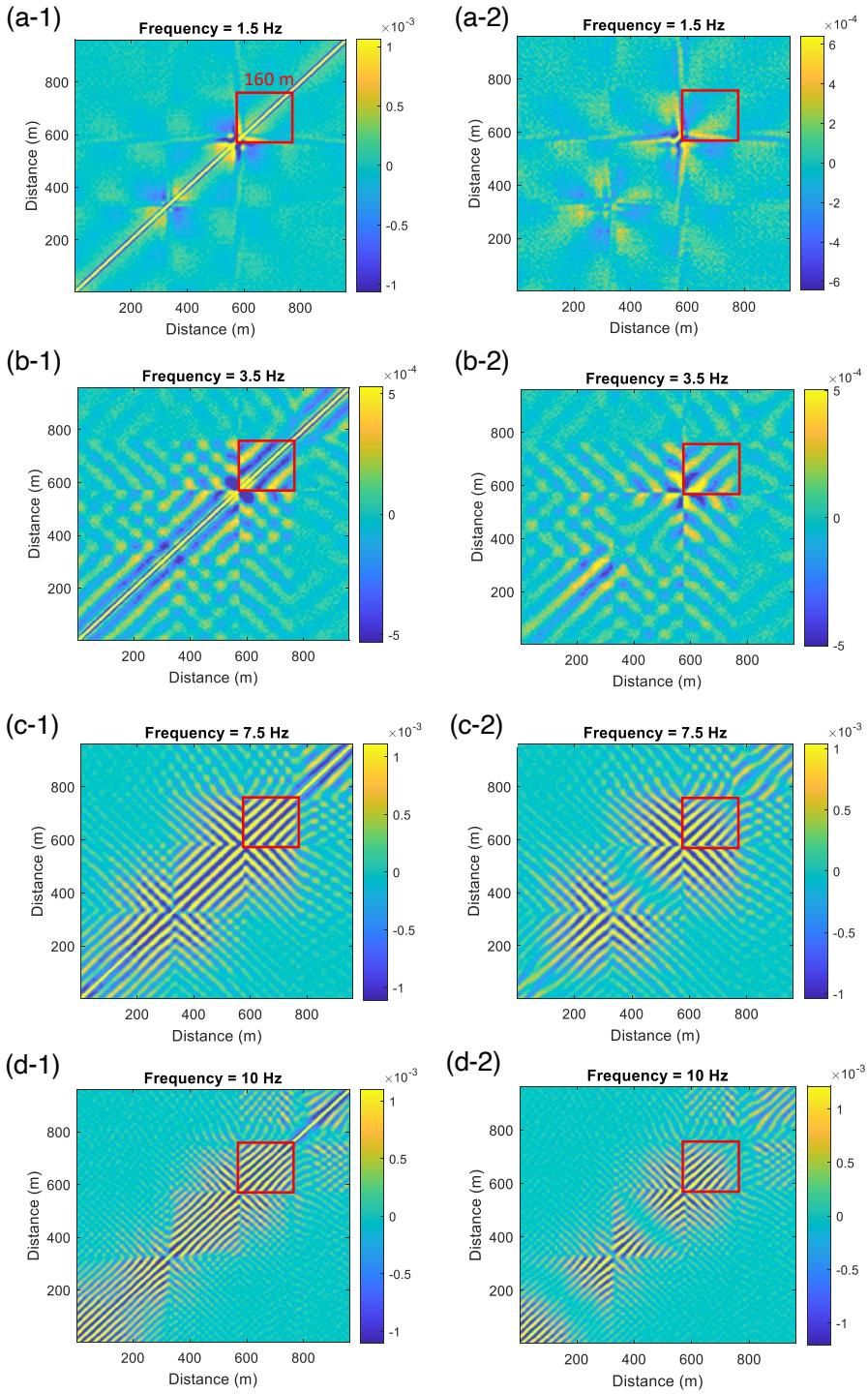


Figure 3.27: Real (a-1 through d-1) and imaginary (a-2 through d-2) parts of the cross-spectral density matrix along the optical fiber for frequencies of 1.5 Hz, 3.5 Hz, 7.5 Hz and 10 Hz. The red box marks the channels which are used for the two-point correlation analysis.

The initial observation drawn from the CSDM plots for various frequencies reveals a coherent wave propagation around the closest WTs to the cable i.e, PR05 and PR06, but also from the turbines to the south and north (PR04 and PR07) - see Fig. 3.17. According to the correlation theorem, we except that in a medium having

random spatial distribution of the noise sources considering long time series, the average cross-correlation should give a non-zero real part, and an imaginary part that goes to zero. But here, we have both the real part and an imaginary part that are nonzero. The latter, however, is in fact the only part of the complex cross-spectra that reflects true nonzero-lagged interactions, meaning that this observed effect does not have a time-lag with respect to the source activity of the WTs.

At 1.5 Hz the cross-spectral density amplitude drops rapidly around the WTs, meaning that the scattering intensity is significant at this frequency. The coherent signal is strongly attenuated with respect to the diffusive wavefield, also evident from the DAS profiles. For the other frequencies at 3.5 Hz, 7.5 Hz and 10 Hz the cross-spectral density amplitude remains high over a much longer distance range and a coherent signal can be detected over several hundred meters. Similar observations apply for both the real and imaginary parts of the cross-spectral density. A peculiar feature of the CSDM is that around the channels near the WT sources, there is 180°phase flip, i.e. $x = 320m$ for PR05 at $x = 576m$ for PR06. This phase shift comes from the dipolar source of the WT, which if it were a monopole, the phase would have been continuous (recall the simulations in the previous section). Tracing the strain-rate measurements in the near-field of the turbine makes this effect clear (Fig. 3.23). Another benefit of dense wavefield sampling is the ability to locate precisely the point along the cable where this shift in phase polarity occurs, which seems to also vary with frequency. This, for example, was not observed in the case for the San Gorgonio wind farm, where the stations were relatively sparse (80-110 m) compared to the WT spacing (40 m) and it was not possible to see any abrupt phase shift in the frequency range of our interest.

### Average two-point correlation of DAS channels

We now perform the two-point correlation on the DAS channels. The theory and background related to the two-point correlation technique have already been discussed in Section 3.3.4 in the context of previous experimental investigations on seismic metamaterials and also in this thesis for the San Gorgonio wind farm array. We choose channels starting from the position of the PR06 turbine up to a distance of 160 m north of it (enclosed in a red box marked in the CSDM plots of Fig. 3.27). This is necessary, because if we consider the CSDM that includes channels on either side of the WT, then we end up with meaningless correlation functions. Therefore, we simply stay on one side of the dipolar source, with the inflection point on the DAS cable acting as the reference point. Then, we average the correlation functions over 4m bins at each frequency and plot them as a function of distance for the same frequencies as the CSDM in Fig. 3.28. In both the real and imaginary part of the correlation function, we see the oscillations for the higher frequencies, meaning that surface waves can propagate in these bands. However, there is weak propagation at f=3.5 Hz, but purely evanescent propagation at f=1.5 Hz. The imaginary part of the correlation function cannot be neglected due to the dipolar source. The imaginary part below 2 Hz is mostly flat, but becomes more clear as we move higher in frequency. We now collect the correlation functions at different frequencies and normalize them for each frequency to plot the frequency-vs-distance representation of the 2-point correlation function $C(\omega, dr)$ in Fig. 3.29.

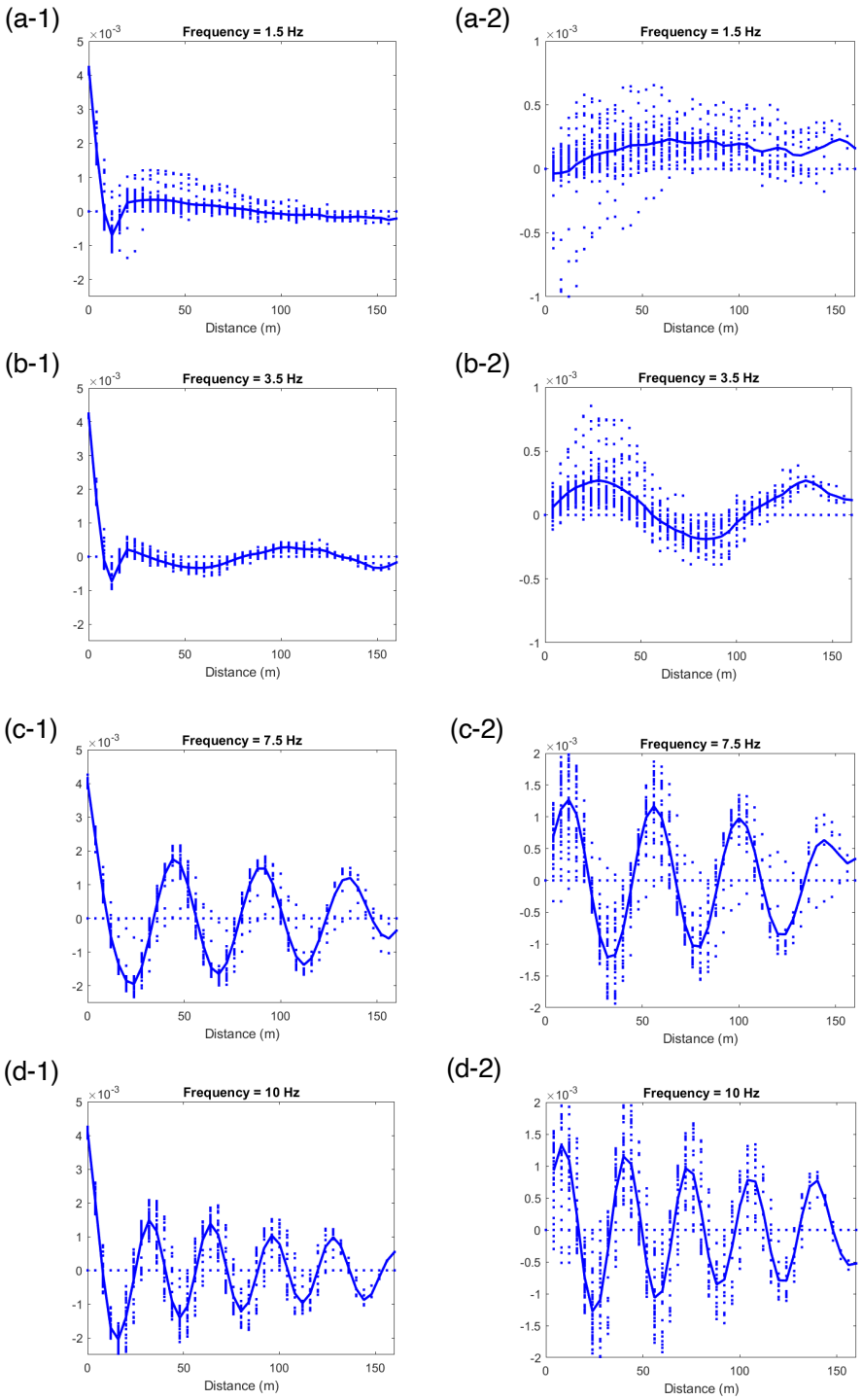


Figure 3.28: Averaging of the real (a-1 through d-1) and imaginary (a-2 through d-2) parts of the two-point correlation function for various frequencies for DAS channel pairs in the interval $x = 576m$ to $x = 736m$ along the fiber-optic cable (marked with a red box in Fig. 3.27).

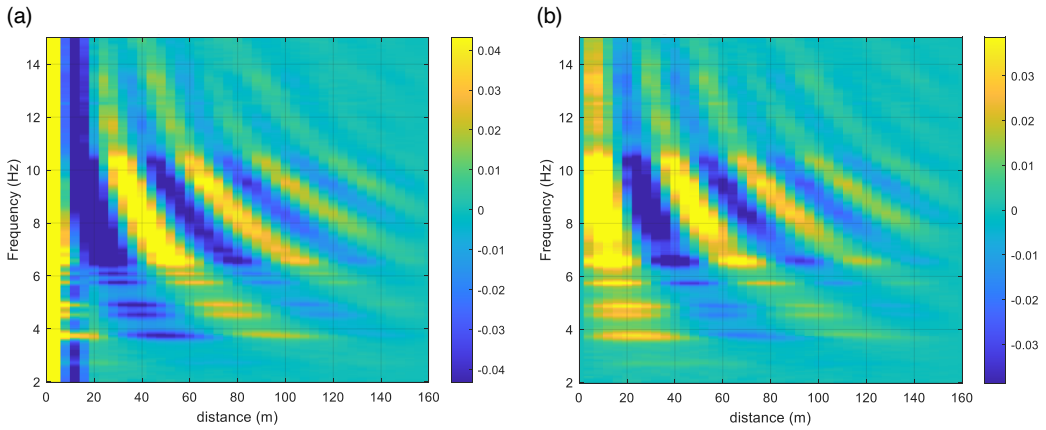


Figure 3.29: Frequency normalized real (a) and imaginary (b) parts of the averaged two-point correlation function $C(\omega, dr)$ inside the wind farm for the DAS channel pairs in the interval $x = 576m$ to $x = 736m$ along the fiber-optic cable (marked with a red box in Fig. 3.27).

From the frequency-vs-distance plots of both the real and imaginary parts of the correlation function, we see propagation in the frequency band of 7-10 Hz and at discrete frequencies between 3.5-7 Hz that correspond to the spectral amplitude peaks (Fig. 3.21). Around 11 Hz, there is suddenly an increase in surface wave attenuation, where we had interestingly also seen the start of the drop in spectral ratio from the nodal array. The low-frequency band below 2 Hz is omitted as we see a uniform phase for all the channels in the CSDM. We can better interpret the potential metamaterial effect by fitting a model 2D Green's function to the average two-point correlation at each frequency. This can then give us the phase velocity and the attenuation length in the wind farm.

### Monopolar and Dipolar source models

For the estimation of the phase velocity and attenuation length inside the wind farm, the correlation function needs to be modeled using a suitable 2D Green's function for Rayleigh waves. Although we are considering the correlations for the channels locally around one WT, this does not mean that the WT is isolated, but rather is among a set of other WTs which are also contributing to the surface wavefield. However, we assume that the PR06 turbine is the dominant source for the segment of the DAS cable considered for all the frequencies. We search for a model that can represent the contributions of the WT in both the near-field and the far-field. It has to be noted that in the case of a half-space, a near-field formulation does not exist because Rayleigh waves are a combination of both P and S waves. Thus, one way is to start from the formulation for the 2D Green's function of Lamb waves (bending waves) in an infinite plate (Ljunggren [1983]) that includes both the propagative and evanescent terms. Thus, we conveniently use the same form of 2D Green's function that was also used by Lott and Roux [2019a] for a plate with contributions from (1) a propagative part - a Hankel function of the second kind and zero-order $H_0^{(2)}(kr)$ and (2) an evanescent part - a hyperbolic Bessel function $K_0(kr)$. We plot these individual constituent functions in Fig. 3.30 for a wavelength $\lambda = 40m$ as an example.

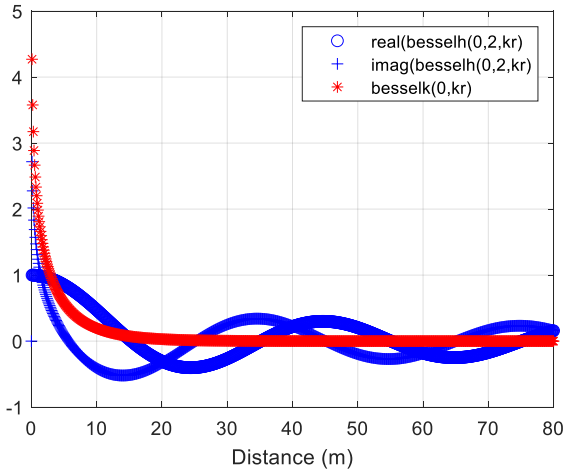


Figure 3.30: Constituent functions of the model 2D Green function for a wavelength $\lambda = 40m$ or $k = 0.157\ m^{-1}$. The real and imaginary part of the oscillating zero-order Hankel function of the second kind are shown in blue circles and '+' symbols respectively. The hyperbolic Bessel function $K_0$ which decays rapidly with distance, represents the evanescent part and is shown with red asterisks.

The WT can ideally behave as both a dipolar and a monopolar source depending on the forces exciting it and the frequency in consideration. A schematic for the WT source and the DAS receivers configuration is shown in Fig. 3.31, assuming that the axis of the dipole is parallel to the DAS fiber-optic cable. For a monopole, it should simply be the 2D Green's function excited by a force $F_z^{\odot}$. On the other hand, for expressing a dipole source, we need to have two point sources or 'monopoles' that are of equal magnitude but opposite polarity (out of phase by $\pi$), i.e. $F_z^{\oplus}$ and $F_z^{\ominus} = -F_z^{\oplus}$. These two sources are co-located around the WT separated by a finite distance that we assume should depend on the source frequency, as discussed in Section 3.23.

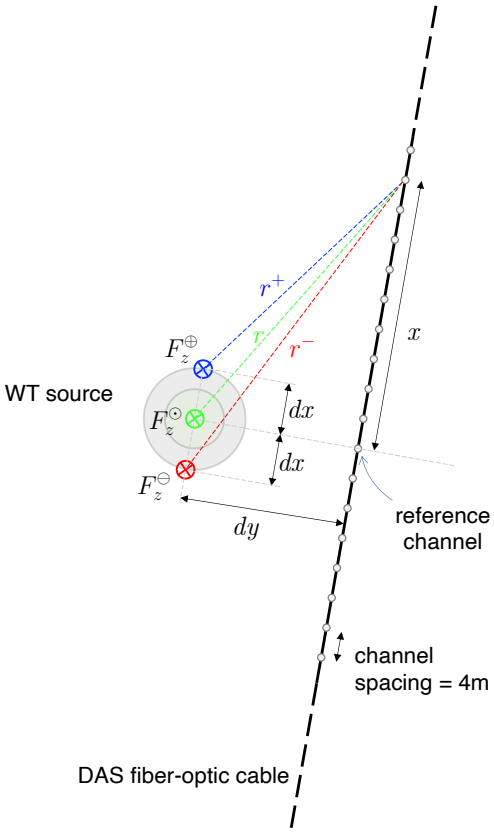


Figure 3.31: Schematic for the formulation of the WT source model representing the monopolar $F_z^{\odot}$ and the dipolar sources $F_z^{\oplus}$ and $F_z^{\ominus}$.

We can write the proposed 2D Green's function due to a normal force $F_z$ and measured at any given distance $r$ on the surface of the half-space, for both the monopolar and dipolar sources respectively as below,

Monoplar source :

$$V_z^{\odot}(\omega, r) = A^{\odot}\left[H_0^{(2)}(kr) - i\frac{2}{\pi}K_0(kr)\right]$$

Dipolar source :

$$V_z^{\oplus}(\omega, r^+) = A^{\oplus\ominus}\left[H_0^{(2)}(kr^+) - i\frac{2}{\pi}K_0(kr^+)\right]$$
$$V_z^{\ominus}(\omega, r^-) = A^{\oplus\ominus}\left[H_0^{(2)}(kr^-) - i\frac{2}{\pi}K_0(kr^-)\right]$$

The amplitude of the function $A = \tilde{A}e^{\frac{-dr}{2l_s}}$ depends on the attenuation distance, and here $k$ is the effective wavenumber. We now fit the real and imaginary parts of the average two-point correlation function frequency-by-frequency with a trial approximation that is a linear combination of the real and imaginary parts of the monopole and dipole 2D Green's functions as below:

$$\Re(C(r)) \approx \Re(V_z^{\odot}) + \Im(V_z^{\oplus} - V_z^{\ominus}) \tag{3.4}$$
$$\Im(C(r)) \approx \Im(V_z^{\odot}) + \Re(V_z^{\oplus} - V_z^{\ominus}) \tag{3.5}$$

There is a weight for the monopolar and the dipolar sources in the both the real and imaginary part of the two-point correlation. All the four right-hand terms in equations 3.4 and 3.5, are on the same order. Thus, neglecting the off-diagonal/imaginary terms degrades the quality of the fit. With such a model we will need to fit for a total of 7 parameters assuming the data reference point does not shift, and 8 parameters when the data shifts along the x-axis by $\Delta x$. This shift parameter is basically required because the dipole inflection point on the DAS cable can lie between any two channels and not necessarily at the channel position. Thus,

Neglecting the reference shift

$$A^{\odot} = \tilde{A}^{\odot} e^{\frac{-x}{2l_s^{\odot}}}$$
$$A^{\oplus\ominus} = \tilde{A}^{\oplus\ominus} e^{\frac{-x}{2l_s^{\oplus\ominus}}}$$
$$k = \frac{2\pi}{\lambda}$$
$$r = \sqrt{x^2 + dy^2}$$
$$r^{+} = \sqrt{(x - dx)^2 + dy^2}$$
$$r^{-} = \sqrt{(x + dx)^2 + dy^2}$$

Considering the reference shift

$$A^{\odot} = \tilde{A}^{\odot} e^{\frac{-(x-\Delta x)}{2l_s^{\odot}}}$$
$$A^{\oplus\ominus} = \tilde{A}^{\oplus\ominus} e^{\frac{-(x-\Delta x)}{2l_s^{\oplus\ominus}}}$$
$$k = \frac{2\pi}{\lambda}$$
$$r = \sqrt{(x - \Delta x)^2 + dy^2}$$
$$r^{+} = \sqrt{(x - dx - \Delta x)^2 + dy^2}$$
$$r^{-} = \sqrt{(x + dx - \Delta x)^2 + dy^2}$$

Fit parameters at any frequency $\omega$

$\{\lambda,\ \tilde{A}^{\odot}, \tilde{A}^{\oplus\ominus}, l_s^{\odot}, l_s^{\oplus\ominus}, dx, dy\}$

$\{\lambda,\ \tilde{A}^{\odot}, \tilde{A}^{\oplus\ominus}, l_s^{\odot}, l_s^{\oplus\ominus}, dx, dy, \Delta x\}$

Having a single phase velocity i.e, a single wavelength value $\lambda$ for the fit at a given frequency $\omega$, is more rational as it is a property of the half-space medium and should not be different for the monopolar or dipolar sources (even though the values are not very different with two separate fits). However, the justification that scattering attenuation $l_s$ is allowed to have two different values for the monopole and dipole comes from the observation in the plate-and-rods experiment (Lott and Roux [2019b]), where the monopole and dipole had very different attenuation in the vicinity of the source. The monopole energy was evanescent while the dipole energy was able to propagate. This is brought up in more detail within the Discussion section.

We first try to fit the real and imaginary parts of the correlation function with the model without considering the shift of the data from the original reference point. Then by including the shift of the reference, we manage to obtain a slightly better fitting model. We show here one example of a fit at frequency f=7.5 Hz in Fig. 3.32. For some discrete frequencies below 6 Hz, we do not have a good fit in the short range of 20m of the cable segment. This is irrespective of whether the shift in the reference

channel is considered or not, which could be due to the long wavelengths and near-field effects that the model is not fully able to replicate. We assume reasonable limits for the parameters including the distances $dx$ and $dy$ whose absolute values are both free to vary between 2m to 100m. However, they are more meaningful when normalized with the wavelength, as their absolute values do not really matter in the diffraction physics we are in. Even when the absolute values $dx$ and $dy$ are better constrained, there seems to be a trade-off between these spatial features and the quality of the fit in different frequency regimes.

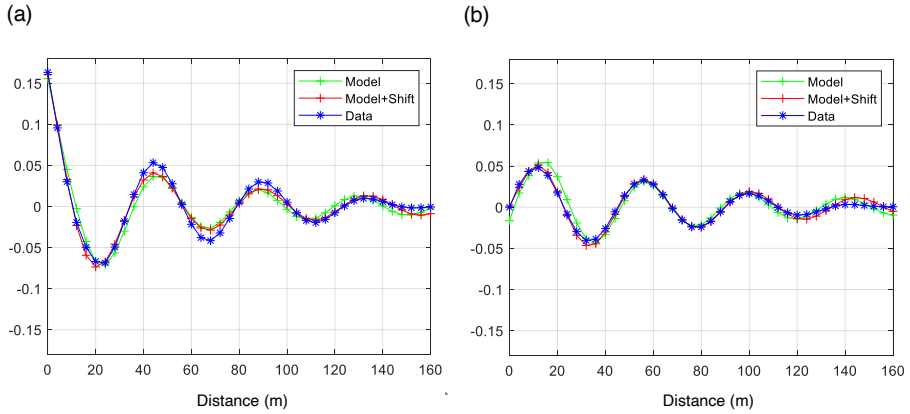


Figure 3.32: Fit of the 2D Green's function model approximation with the (a) real and (b) imaginary parts of the average two-point correlation function at frequency f=7.5 Hz. There is a better agreement between the model considered with shift of reference for the real and imaginary parts of the experimental two-point correlation function $C(r)$.

The phase velocity and the attenuation due to scattering are extracted from the best fit at each frequency. However, we do not report this here as the parameter values from the best fit change abruptly below f=6Hz. A better way to relate the 8 fit parameters and understand their relative robustness is necessary, which could be achieved, for example, by a genetic algorithm. After understating the correlation between the multiple parameters, the model needs to be better constrained and re-fitted with an improved physical interpretation of these parameters, including the observations from the numerical simulations. Our current effort is to try to develop a model with fewer and more accurate parameters to understand how surface waves propagate inside the wind farm.

### 3.4.7 Discussion

The overall results of the META-WT experiment are encouraging from the perspective that the surface wavefield interacts strongly with tall structures on the urban scale. Despite observing a notable impact of the wind farm on the seismic wave field across a wide frequency spectrum, the relatively soft soil conditions result in shorter wavelengths above 2 Hz, relative to the spacing of the WTs, which is around a few hundred meters. This means that only the first two modes are really sub-wavelength ($\lambda/8$ and $\lambda/2$ for the first and second flexural mode). From the two-point correlation analysis of the DAS data we found that,

1. The bands where the surface waves propagate for larger distances are associated with the spectral amplitude peaks observed in the near-field (Fig. 3.21). This means that the wavefield emitted by WT flexural resonances propagates inside the wind farm, even though the frequencies in their vicinity are strongly damped. This behavior resembles the observation in the frequency bandgap regime, that was made for bending waves in a plate excited by flexural resonances of rods attached to it (Lott and Roux [2019b]).

2. The frequency bands in which we observe strong damping is similar to the observation made in the literature for (a) the plate-and-rods metamaterial where the average two-point correlation function shows a strong damping of $A_0$ Lamb waves in the stopbands (Lott and Roux [2019a]); and (b) in the forest of trees where we see a strong damping near longitudinal resonance of the trees (Lott et al. [2020a]). The correlation function was shown for both these cases in the Fig. 3.12 panels A and B, respectively.

3. The potential "stopbands" do not exactly coincide with the global spectral ratio drops in Fig. 3.22 (a), which is expected as the DAS array is local to one sector of the wind farm while the spectral ratio was calculated for the global node array. The strong damping immediately after 11 Hz, however, coincides with the start of the bandgap which seems to originate due to the longitudinal resonances of the WTs.

4. The monopolar and dipolar source models considered together, fit well both the evanescent and the oscillating parts of the correlation function with a few exceptions at discrete frequencies. However, without the extraction of the phase velocity and scattering attenuation, no conclusion can be made from the two-point correlation analysis on the behavior of the wind farm as a metamaterial.

5. There is a need to verify the time-dependent behavior of the two-point correlation functions within the recordings and also between different days of recordings that have different wind conditions. The recording of 23rd Feb which has a switch-off condition of the turbine PR06, will further help establish the robustness of the metamaterial-like behavior of the wind farm.

**Remark on analogy with plate-and-rods metamaterial**

We try to draw an analogy between the wind farm and the laboratory experiment of the plate-and-rod metamaterial, which although are on extremely different spatial scales, could have interesting analogies. As demonstrated by Lott and Roux [2019b], around the flexural resonance frequency of the rods, when a source was placed within the plate metamaterial, energy could escape from the metamaterial (region where rods are attached to the plate), even in the bandgap regime. The wavefield in the region near the source exhibited a dipole-like behavior, consistent with the flexural deformation of the rods (see Fig. 3.33 (b)). The behavior of a monopolar radiation from a source inside the same metamaterial, on the other hand, is well restricted within the small spatial region around the source. Interestingly, even in the case of a wind farm, we see at discrete frequencies where the surface waves are propagative, coincide with the flexural resonances of the WTs (Fig. 3.29). This means

the energy emitted by a cluster of beams resonating in flexure, be it either in a plate or a half-space can propagate more effectively. The physics of wave propagation in plates differs from a half-space, mainly in the dispersion characteristics. Linking the plate-and-rods case with a WTs on a half-space is not straightforward because of two reasons: (a) we also have body waves in a half-space, and (b) the impedance contrast between the resonator and the substrate is very different in the two cases. Nonetheless, such analogy can offer potential insights into the interpretation of evanescent waves around WT flexural resonances to some extent. We also predict that the numerical simulations of the WT coupled to a half-space, shown earlier in Section 3.4.5, can better explain the observations of the near-field radiation and propagation of surface waves. That said, we believe it is not necessary to invoke metamaterial physics to interpret the observations across the broadband frequency range. In certain regimes, there could potentially be other source effects itself that dictate the radiation (or inhibition) of surface waves.

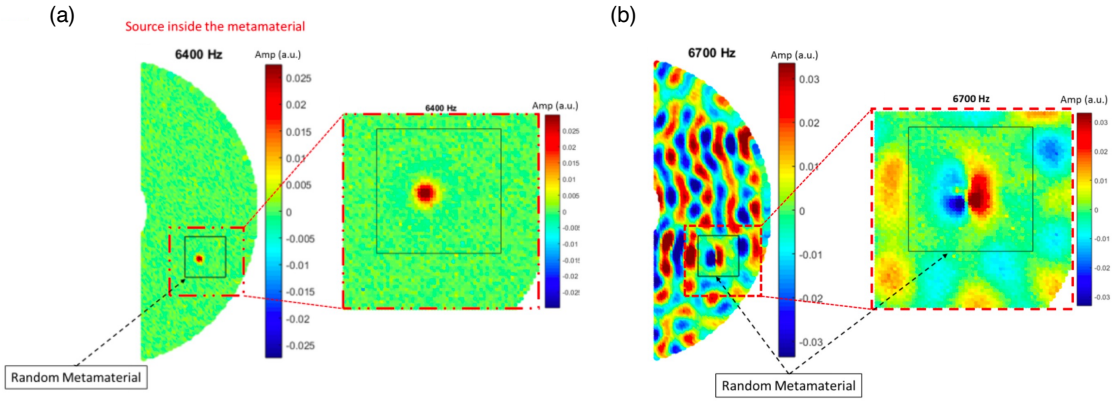


Figure 3.33: Analogy of the wind turbines to rods attached to a plate, adapted from Lott and Roux [2019b]. Spatial representation of the Fourier transform (real part) of the wavefield at (a) f = 6400 Hz and (b) f = 6700 Hz. In both the cases the source is located inside the metamaterial region (shown by the black box). In the case of monopolar excitation, energy being restricted within the metamaterial, whereas for the dipolar excitation the wavefield pattern shows that there is energy leakage in a stopband through one flexural resonance. In the case of a wind farm, we observe energy transmission for the spectral peaks associated with the flexural resonances of the wind turbines.

## 3.5 Concluding remarks

The META-WT experiment is the very first field test of metamaterial physics applied to a larger spatial scale in seismology after the successful recording of meter scale field experiments with a borehole array in 2012 (Brûlé et al. [2014]) and the tree forest METAFORET project in 2016 (Roux et al. [2018]). We have demonstrated the idea that a set of wind turbines on the ground can show effective metamaterial-like properties to some extent. The dynamic strain data measured by DAS fiber-optic cable deployed inside the wind farm gives interesting insight into the Rayleigh waves radiated by the turbines. The transmission bands and stopbands observed

from the two-point correlation allow us to link the characteristics of the wavefield inside the wind farm to the wind turbine flexural resonances. Although the complex wind turbine source is better idealized with the help of numerical simulations, the extraction of phase velocity and scattering requires a more rigorous approach. In addition, the time-dependent behavior of these effective properties of surface wave will have to be verified.

frontiers | Frontiers in Earth Science

TYPE Original Research
PUBLISHED 05 February 2024
DOI 10.3389/feart.2024.1352027



OPEN ACCESS

EDITED BY
Chong Xu,
Ministry of Emergency Management (China), China

REVIEWED BY
Keith Attenborough,
The Open University, United Kingdom
Lei Gao,
Hohai University, China

*CORRESPONDENCE
Marco Pilz,
pilz@gfz-potsdam.de

RECEIVED 07 December 2023
ACCEPTED 22 January 2024
PUBLISHED 05 February 2024

CITATION
Pilz M, Roux P, Mohammed SA, Garcia RF, Steinmann R, Aubert C, Bernauer F, Guéguen P, Ohrnberger M and Cotton F (2024), Wind turbines as a metamaterial-like urban layer: an experimental investigation using a dense seismic array and complementary sensing technologies. *Front. Earth Sci.* 12:1352027. doi: 10.3389/feart.2024.1352027



# Wind turbines as a metamaterial-like urban layer: an experimental investigation using a dense seismic array and complementary sensing technologies

Marco Pilz[1]*, Philippe Roux[2], Shoaib Ayjaz Mohammed[2], Raphael F. Garcia[3], Rene Steinmann[1], Coralie Aubert[2], Felix Bernauer[4], Philippe Guéguen[2], Matthias Ohrnberger[5] and Fabrice Cotton[1,5]

[1]Helmholtz Center Potsdam–GFZ, German Research Center for Geosciences, Potsdam, Germany, [2]CNRS, IRD, IFSTTAR, University Grenoble Alpes, University Savoie Mont Blanc, Grenoble, France, [3]Institut Supérieur de l'Aéronautique et de l'Espace–ISAE-SUPAERO, Toulouse, France, [4]Geophysical Observatory Fürstenfeldbruck, Ludwig Maximilian University of Munich, Munich, Germany, [5]Institute of Geosciences, University of Potsdam, Potsdam, Germany

The deflection and the control of the effects of the complex urban seismic wavefield on the built environment is a major challenge in earthquake engineering. The interactions between the soil and the structures and between the structures strongly modify the lateral variability of ground motion seen in connection to earthquake damage. Here we investigate the idea that flexural and compressional resonances of tall turbines in a wind farm strongly influence the propagation of the seismic wavefield. A large-scale geophysical experiment demonstrates that surface waves are strongly damped in several distinct frequency bands when interacting at the resonances of a set of wind turbines. The ground-anchored arrangement of these turbines produces unusual amplitude and phase patterns in the observed seismic wavefield, in the intensity ratio between stations inside and outside the wind farm and in surface wave polarization while there is no metamaterial-like complete extinction of the wavefield. This demonstration is done by setting up a dense grid of 400 geophones and another set of radial broadband stations outside the wind farm to study the properties of the seismic wavefield propagating through the wind farm. Additional geophysical equipment (e.g., an optical fiber, rotational and barometric sensors) was used to provide essential explanatory and complementary measurements. A numerical model of the turbine also confirms the mechanical resonances that are responsible for the strong coupling between the wind turbines and the seismic wavefield observed in certain frequency ranges of engineering interest.

KEYWORDS

**soil structure interaction, seismic metamaterials, local resonance, wind turbines, bandgaps**

# 1 Introduction

The interactions between the soil and urban structures above it can strongly modify seismic ground motion, as first outlined by Jennings and Kuroiwa (1968) and Luco and Contesse (1973). Following the 1985 Michoacán (Mexico) earthquake, due to the difficulties of traditional computational approaches in matching seismic records, Wirgin and Bard (1996) proposed that some of the seismic energy transmitted to the buildings is redistributed in their surroundings through numerous structure-soil-structure interactions. This phenomenon was called "site-city interaction" or "city effect". Following this study, a number of authors have investigated the possible feedback of the soil-structure interaction on the free-field ground motion with a special focus on densely urbanized areas. These studies involved either numerical simulations based on more or less detailed soil properties and/or structural characteristics (e.g., Guéguen et al., 2002; Tsogka and Wirgin, 2003; Kham et al., 2006; Schwan et al., 2016) as well as laboratory experiments at a reduced scale based on shaking tables or acoustic devices (e.g., Mason et al., 2013; Tian et al., 2023). The majority of them yield consistent results showing the possibility of observable effects on seismic ground motion with an overall decrease in the average level of ground motion at specific frequency ranges with greater spatial variability.

In this sense, the emergence of the so-called metamaterial-like concept in the urban fabric is a promising prospect to be developed. Typically, a metamaterial is based either on the periodic arrangement or on the resonant properties of elements with their dimension being much smaller than the wavelength considered (typically $\lambda/2$ to $\lambda/10$). As a result, these materials acquire effective properties not observed in constituent materials. Metamaterials have expanded the variety of options for influencing and directing wave propagation including ultrasound, acoustic, thermodynamic, electromagnetic and elastic waves (reviews provided by Simovski, 2009; Kadic et al., 2013; 2019; Turpin et al., 2014; Kumar et al., 2022; Qahtan et al., 2022 among others). Although these mentioned topics deal with different kinds of waves, analogies between them can still be drawn.

For applications in seismology, the innovative work of Liu et al. (2000) on locally resonant crystals with structural periodicity two orders of magnitude smaller than the respective sonic wavelength and exhibiting clear bandgaps clears the way for the damping of Rayleigh waves within the sub-wavelength regime. Following on from this study, experiments ranging from optical wave manipulation to acoustic testing have been used to study the underlying nature and resilience of metamaterial physics. Common vibration mitigation measures that have been proposed include the use of rows of piles (Avilés and Sánchez-Sesma, 1988; Gao et al., 2006; Dijckmans et al., 2016), open or infill trenches (Dasgupta et al., 1990; Laghfiri and Lamdouar, 2022) and wave impeding barrier. Regarding the first issue, Brule et al. (2014) explored the impact of a periodic arrangement of pile foundations in soft soils as a seismic barrier as if it was a giant crystal. The authors have demonstrated that boreholes with meter-long spacing can attenuate seismic surface waves in the Bragg scattering regime, achieving vibration isolation and absorption control at frequencies around 50 Hz at the geoengineering scale. For isolating vibrations at even lower frequencies, Miniaci et al. (2016) investigated the attenuation behaviour of different periodic structures for bulk and surface waves indicating that only unit cells with decameter size may attain bandgaps for frequencies less than 10 Hz. In addition, the Bragg scattering mechanism has also been used to attenuate traffic-induced ground vibrations using periodic inclusions (Huang et al., 2017; Castanheira Pinto et al., 2018; Pu and Shi, 2018; Albino et al., 2019) and trenches (Pu and Shi, 2020). For example, Pu and Shi (2020) explored surface wave attenuation by periodic trenches, which may give a wide bandgap starting at roughly 30 Hz when the lattice constant and trench depth are meter-size.

Based on the research on negative refraction caused by perfect lenses as metamaterials (Guenneau and Ramakrishna, 2009), a slightly different concept was explored by Colombi et al. (2016a) who numerically demonstrated that natural forests act as local resonators, opening the bandgaps for Rayleigh waves around 30 and 100 Hz corresponding to the longitudinal resonances of the trees. These complex wave propagation phenomena were then experimentally demonstrated by the deployment of a large number of receivers in a forest in south-western France (METAFORET experiment, Colquitt et al., 2017; Roux et al., 2018; Lott et al., 2020a), illustrating that metamaterial physics–classically being observed at small scales in acoustics and optics at frequencies from kHz to MHz–does also exist at larger spatial scales in geophysics. The results of this experiment conclusively describe how trees in a forest, acting as locally resonant structures, strongly modify the propagation of surface waves. These experiments have confirmed the scalability in spatial dimension and frequency that underlies such behaviour (Wegener, 2013), i.e., the frequency range in which a strong modification of the wavefield occurs is positively correlated with the natural frequency of the resonators. This in turn means that, on the geoengineering scale, long and heavy masses are required to modify and dampen the wavefield at even lower frequencies.

As far as earthquake ground motion in urban areas is concerned, which is also the motivation for this study, the target frequency band is one to two orders lower (~0.5–25 Hz). However, there are only a few investigations on metamaterial-like behaviour at the earthquake engineering scale (e.g., Brule et al., 2014; Guéguen et al., 2019; Ungureanu et al., 2019; Joshi and Narayan, 2022), pushing forward a different approach of structuring the urban environment. In fact, a key point is that this shifts the standard passive-approach, where the building should adapt to the imposed seismic input, to a method where a group of structured buildings capable of reacting together at the district scale are considered together. We therefore turn our attention to wind turbines, which are man-made structures that are relatively tall, heavy, and well-coupled to the ground.

Taking advantage of the METAFORET results, here we experimentally explore how interactions between locally resonant structures, in this case a large number of wind turbines, degenerate low-frequency seismic surface (Rayleigh) waves. We analyse the effects of such large number of wind turbines on the surface wavefield and separate this from other effects like soil layering. The wind turbines are not studied as single elements with their own characteristics but as an interacting set of above-ground resonators at the size of a city district. After a description of the experimental setup, we analyse the recorded seismic noise wavefield in terms of

spectral ratios, polarization, dispersion and attenuation properties through advanced array processing methods. For reaching the full potential, measurements are complemented by additional seismic sensors outside the wind farm, pressure sensors and distributed acoustic sensing (DAS) using a fiber-optic cable to measure strain through the wind farm, i.e., to use the strain data as a seismic array with which we overcome small-scale spatial limitations. The experimental results are finally compared with numerical modeling results.

## 2 Natural setting and experimental configuration

The site of the experiment is located south of the town of Nauen in north-eastern Germany about 40 km west of Berlin. The area can be characterized as a low plateau rising on average 15 m above the surrounding landscape, flanking glacial valleys. The geology of the area consists of Quaternary unconsolidated sediments, i.e., sandy-gravelly silts with a thickness of several tens up to 80 m overlying homogeneous Tertiary strata (Stackebrandt and Manhenke, 2010; Gau and Gau, 2011).

In February 2023, a dense acquisition grid of 200 vertical-component 4.5-Hz geophones and 200 three-component 5.0-Hz geophones spaced regularly with an interstation distance of 100 m was deployed covering an area of 1.5 x 2.5 km (Figure 1). While the entire wind farm is composed of more than 70 wind turbines, the area of the dense grid covers around 30 of them which are placed along slightly angled lines with a distance of 200–250 m in the north-south direction and around 400 m in the east-west direction between the individual wind turbines. The installation was complemented by nine Trillium Compact 120-s broadband instruments forming a radial line outside the wind farm. After deployment, the instruments were recording seismic noise continuously for around 2 weeks. In the south-eastern sector of the array, eight Lennartz 5-s three-component instruments, seven iXblue blueSeis-3A rotational seismometers co-located with seven Trillium compact 120-s seismometers and with a Paroscientific pressure sensor on six of these stations as well as an optical fiber with a length of 1,000 m connected to an OptoDAS interrogator were installed for a shorter period of time between 14 and 21 February 2023. The deployment of the optical fiber forms an L-shape and passes four wind turbines at different distances from ten to around 60 m (details of which will be discussed below). One of the 5-s sensors, one of the rotational sensors and one of the pressure sensors were installed at the same location near the optical fiber and another one of the 5-s sensors was located directly on the foundation of one of the wind turbines.

The wind turbines are mainly identically constructed turbines of the types Wind World WW 750 with a hub height of 73.9 m and NEG Micon M1500-750 with a hub height of 73.8 m, both of them having rated output power of 750 kW. In the south-eastern sector of the seismic array, seven wind turbines are of the type ENERCON E-70 with hub heights of 113 and 114.5 m. In the transition area between these two areas there are still four wind turbines NEG Micon NM82/1500 with a hub height of 93.6 m. All types are variable-speed wind turbines, i.e., their blade rotational speed varies with incident wind speed although they all begin to operate only if the wind speed exceeds a threshold value of approximately 3 m/s.

## 3 Data analysis and interpretation

### 3.1 Spectral ratios

As a first examination of the role of the field of wind turbine towers on the seismic wavefield we calculate the ratio between the Fourier spectra (vertical component) measured separately for all sensors in the wind farm and for the three southern-most broadband station which are located far enough outside the wind farm so that it can be assumed that their recordings are not directly affected by the wind turbines. For each station, we take a 1-h signal starting at midnight on 16 February 2023 when there was almost no wind (less than 2 m/s average wind speed at the top of the wind turbines, most likely no rotation of the wind turbine blades). We divide the 1-h window into 120-s long windows, each of which is tapered with a 5-per cent cosine function. The corresponding Fourier spectra are then averaged for stations inside and outside the wind farm and the corresponding mean spectral ratio with a confidence interval as the standard deviation of all averaging processes shown in Figure 2A. As a side note, we have assured that the spectra are reliable for frequencies lower than 1 Hz since we have set the pre-amplifier gain to 8 and since the input level of noise is significantly higher than the minimum new low-noise model of Peterson (1993) in this frequency range. For comparison, Figure 2A also shows the horizontal-to-vertical spectral ratio (HVSR) for the southernmost station of the radial array. The latter (Nogoshi and Igarashi, 1970; 1971; Bard, 1999) is a passive technique that can be used to estimate a resonance frequency and a lower-bound level of amplification of the soft soil layers above the main impedance contrast.

Three strong minima for the inside-to-outside spectral ratio can be identified at around 0.25, 1.4 and 13 Hz. At these frequencies, the spectral amplitude in the wind farm is smaller by a factor of more than 5 compared to the neighbouring frequencies. Other smaller minima can be seen between 3 and 4 Hz and around 8 Hz. The occurrence of these spectral minima is well constrained, in particular for intermediate frequencies, and larger standard deviations only occur for the first minimum and for frequencies higher than ~ 7 Hz. Looking at the HVSR and comparing it with the data in the frequency domain represented by the power spectral densities (PSDs) for stations inside and outside the wind farm (Figure 2B), it can be concluded that these troughs cannot be related to soil resonance effects at the stations outside the wind farm, meaning that the spectral pattern reveals a strong attenuation of the wavefield between the individual wind turbines. In these frequency bands, the spectral amplitude inside the wind farm is reduced relative to the spectral amplitude outside and significantly less energy penetrates through the ground. The only exception to this is the peak at 0.25 Hz in Figure 2A which might be amplified due to an increased amplitude of the vertical spectra of the outside station. This could either be caused by soil resonance effects or due to secondary microseisms which the geophones were not able to record sufficiently well.

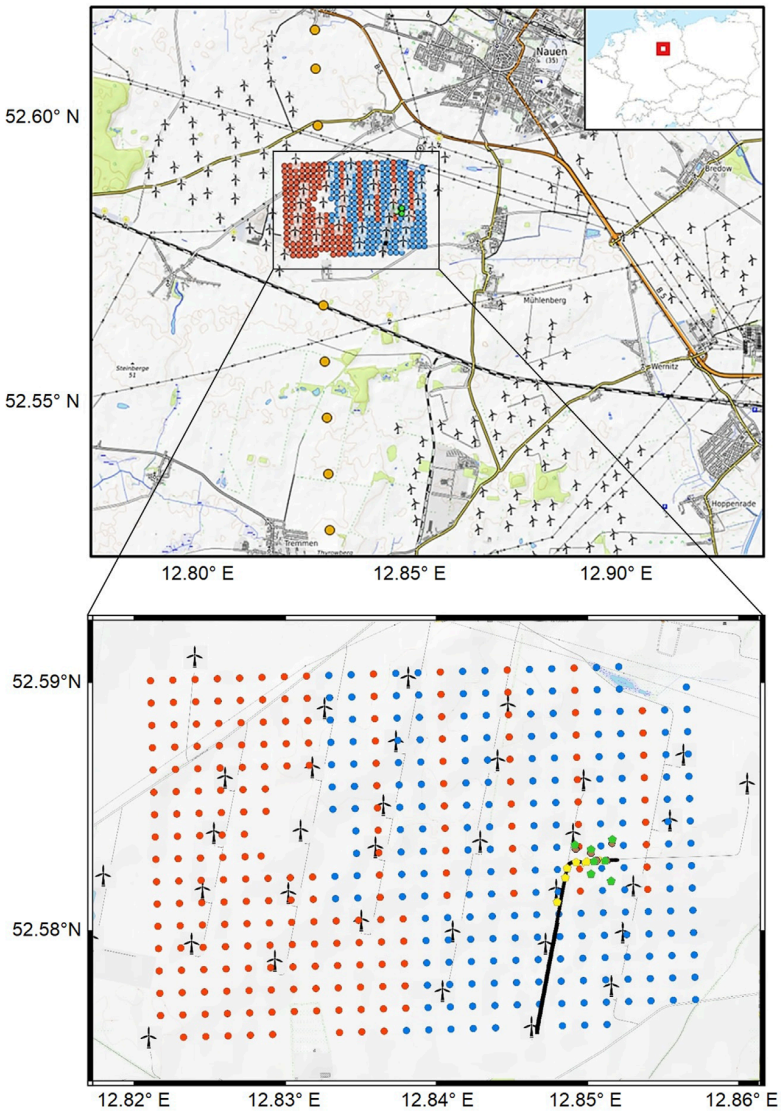


FIGURE 1
Geometry of the experiment in the wind farm near Nauen (north-eastern Germany). The 2D array is composed of 200 4.5-Hz one-component geophones (red circles) and 200 5.0-Hz three-component sensors (blue circles) positioned on a 100-m grid. In the south-eastern sector, the grid was densified by Lennartz 5-s short period sensors (yellow circles), iXblue blueSeis-3A rotational seismometers co-located with Trillium compact 120-s seismometers (green circles) and pressure sensors (brown circles). The black line represents the position of the optical fiber. The radial line array extending north-south with Trillium Compact 120-s broadband instruments is represented by orange circles.

## 3.2 Rayleigh wave dispersion curve

If less energy is propagating through the wind farm in certain frequency ranges, this effect may also be observed in other space-frequency patterns. To estimate the dispersion curve of Rayleigh waves, we consider two different methodologies, the Extended Spatial AutoCorrelation (ESAC, Ohori et al., 2002 based on Aki, 1957) and the slant stack method, described by Thorson and Claerbout (1985). The former is based on the calculation of the spatial correlation coefficients between pairs of stations which are then fitted to Bessel functions for a range of frequencies. In this way, for each frequency, the average phase velocity can be obtained. The slant stack method translates seismogram amplitudes relative to distance and time to amplitudes relative to the ray parameter (the inverse of the apparent velocity) and an intercept time. This in turn gives a power spectral density function, which is a representation of signal strength as a function of frequency and apparent phase velocity. While the ESAC method provides reliable dispersion curves over a broader frequency range, especially toward lower frequencies, the slant stack method can determine the frequency ranges where higher surface wave modes dominate.

Here we take a total of 120 non-overlapping vertical component signal windows from all geophones, each window being 120 s long, again starting at midnight on 16 February 2023 when almost no

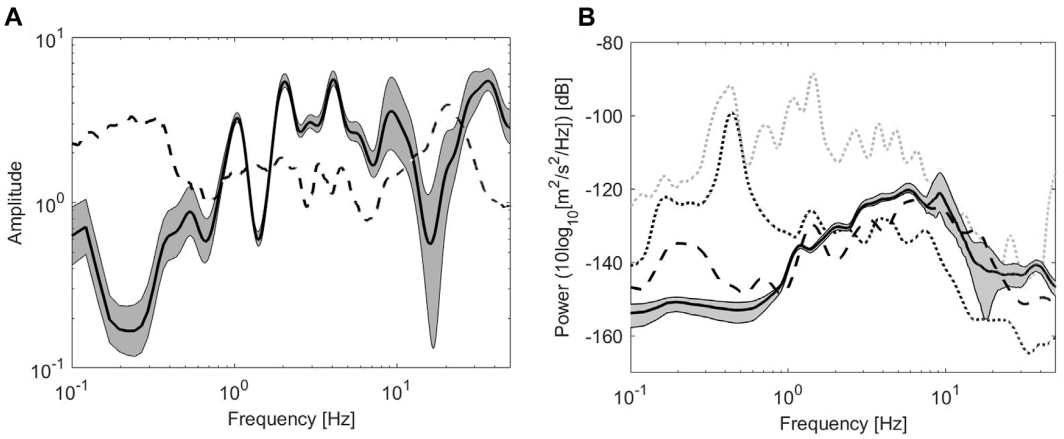


FIGURE 2
**(A)** Spectral ratios (vertical component) between the 400 array nodes and the three most distant broadband stations outside the wind farm (solid line plus/minus one standard deviation). The dashed line corresponds to the horizontal-to-vertical spectral ratio for the southernmost broadband station. **(B)** Power spectral densities of the 400 array nodes (solid line) and the broadband stations (dashed line). The dotted lines show the geometrical mean of the two horizontal components of the 5-s sensor installed on the foundation of a single wind turbine during operation (gray) and at standstill (black).

wind prevailed and the blades of the wind turbine were not expected to have rotated. As shown in Figure 3, the two approaches provide equivalent average dispersion curves spanning a range from 0.4 to 4 Hz with phase velocities ranging from 900 to 350 m/s and corresponding wavelengths ranging from 90 m to over 2 km. As usual, the slant stack approach shows decreasing resolution for lower frequencies and cannot be used for frequencies much lower than 1 Hz. Although the dimension of the entire array should allow a determination of phase velocities at even lower frequencies, incoherent noise prevents the use of the ESAC analysis in long wavelength range (Cho and Iwata, 2021). A representation of the covariance matrix, discussed below (cf. Figure 5B), will confirm this hypothesis.

Between 1 and 2 Hz, the dispersion curves from both methods are characterized by a flat shape–there is even a slight through around 1.4 Hz. As we can assume from the slant stack image, only a single mode is present. In order to check that there is no mode interference of different propagation modes that would either cross or overlap in the time-frequency space (commonly referred to as mode kissing or osculation phenomenon, Forbriger, 2003), we determine a one-dimensional S wave velocity profile by a joint inversion of Rayleigh wave dispersion curve (as shown in Figure 3) and the HVSR from the three-component sensors inside the wind farm based on Parolai et al. (2005). Herein, the dispersion curve is considered to be an apparent one (Tokimatsu et al., 1992). This approach has the advantage to properly account for all modal contributions which means that an explicit mode-number identification is not required (O'Neill and Matsuoka, 2005). As we do not observe strong lateral variations in the shape of the HVSR within the wind farm, the inversion is performed out under the assumption that the structure below the site is nearly 1D for the studied frequency range. During the inversion analysis, the S wave velocity and the thickness of the individual layers were allowed to vary within pre-defined but large ranges while the density of the soil and its P wave velocity were constrained based on geological information and the results provided of Kitsunezaki, (1990).

As shown in Figure 3, inside the wind farm, the sedimentary layers uniformly extend for several tens of meters with S wave velocities increasing steadily and ranging from 400 to just over 800 m/s. No significant impedance contrasts are mapped down to a depth of more than 300 m. This is expected as also the HVSR curves (as shown in Figure 2 for a station near the wind farm) are characterized by low amplitude levels. The narrow distribution of models with a misfit of 10% of the best-fit model around this best-fit model itself (red curves in Figure 3B) is another indication that the S wave velocity profile is well constrained. As we do not observe any large velocity contrasts and/or velocity inversions, it is reasonable to assume that the dispersion curve is representative of the fundamental mode only. The dispersion curve, however, does not show any anomalous behaviour with frequency ranges at which strong bending occurs.

## 3.3 Influence of infrasound signals on the seismic records

As we are dealing with data recorded in a wind farm, one has to be aware that a seismological footprint of atmospheric pressure perturbations on the recorded signals might also exist. This means that for a proper interpretation of the seismic data, in particular the spectral troughs in Figure 2A, it is necessary to investigate whether the ground motion signals might actually be caused by the pressure fluctuations or by ground vibrations. Such disturbances can also induce ground motion through the ground's elastic response to pressure forcing. These compliance effects include both pressure disturbances arising from atmospheric dynamics and horizontally propagating infrasound waves. They were first described by the plane wave approximation by Sorrells et al. (1971) for a homogeneous half-space and by Kenda et al. (2017) for a layered soil structure.

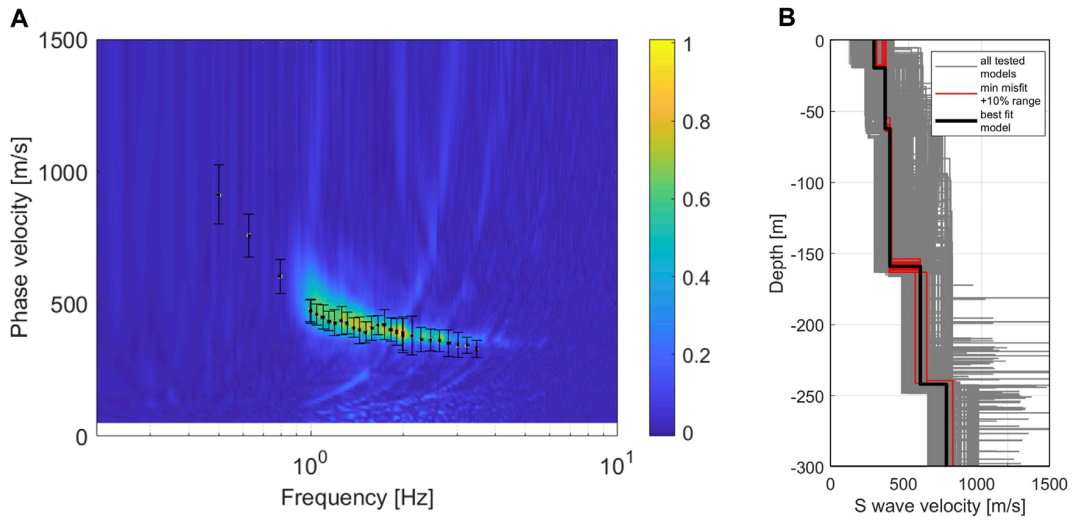


FIGURE 3
**(A)** ESAC (black dots) and slant stack (colour scale) Rayleigh wave dispersion curves. For the latter the colouring indicates the calculated wavefield power normalized relative to the maximum at each processing frequency. **(B)** S wave velocity profile showing all tested models (gray lines), the minimum cost model (black line) and all models within the minimum cost ±10% range (red lines).

The inertial effects are much stronger for infrasound signals than for pressure perturbations moving at wind speed. The pressure forcing creates ground displacement in the horizontal and vertical directions with the horizontal motion being in phase with the pressure, whereas vertical ground motion is phase shifted by 90° relative to the pressure. Garcia et al. (2021) perform an extensive search of the seismic and pressure data for pressure infrasound signals that produce ground signals through compliance effects.

To study the compliance effects, we focus on two time periods during 14 February 2023: the early day around 06:00 UTC that present infrasound signals due to the slamming of the door of a truck deployed in the field, and the late night between 22:00 and 23:00 UTC when the wind was not blowing at the ground level but it was at the top of the wind turbine. This second time period is interesting because the noise on the pressure sensors induced by the wind is minimum whereas the blades of the wind turbines are rotating. In a first step, we process the door slam events in order to estimate the compliance from these events. The 90° phase shift between the pressure vertical velocity during such events is clearly visible in Figures 4A, B. The compliance estimate is done through envelope ratios by using narrow-band pass filtered data. Figures 4C, 4D presents the compliance values estimated in the frequency range between 0.2 and 3 Hz. The compliance values increase above 1 Hz due to a higher sensitivity to soft layers near the surface.

We then use the data from the second time period to estimate how much of the signal from the seismic sensors could be attributed to compliance effects. During this period, the blades of the wind turbines are rotating and several peaks in the pressure Amplitude Spectral Density (ASD) are observed in the 0.4–3 Hz range (Figure 4E). Some of these signals can be attributed to infrasound generated by the wind turbines. Multiplying the pressure ASD by the estimated compliance values provides an estimate of the compliance effects (red curve in Figure 4F) which can be compared to the measured ASD of vertical ground motions by the co-located broadband seismometer (blue curve in Figure 4F). This comparison clearly indicates that the two main peaks around 0.43 and around 1.4 Hz are not due to compliance effects whereas the peaks in spectra of the broadband seismometer between 2.13 and 2.3 Hz are mainly driven by compliance effects. The source of these infrasound waves is probably external to the wind farm. The comparison of the ASD suggests that compliance effects are over-estimated for frequencies higher than 2.6 Hz, probably because the door slamming events have a poor signal-to-noise ratio above 2.6 Hz, thus generating a larger error in the compliance estimates in this frequency range. In contrast, the two main peaks at 0.43 and 1.4 Hz are due to causes other than pressure interference and infrasound waves.

## 3.4 Time-dependence of resonance effects

Of course, when studying wind turbines, an obvious question might arise to what extent the wind and the prevailing wind speed will contribute to the observed effects. A general correlation between meteorological parameters, the operation of a single or only a limited number of wind turbines and the corresponding seismic signals has already been studied by several authors (Withers et al., 1996; Zieger and Ritter, 2018; Neuffer et al., 2019; Limberger et al., 2022 among others), indicating that narrow spectral amplitude peaks can develop with increasing wind speed. From the PSDs for the station installed on the foundation of a single ENERCON E–70 wind turbine (Figure 2B), spectral peaks around 0.43, 1.4, 4 and 8 Hz can be observed both during operation at high wind speed and at standstill due to maintenance operations on 23 February between 11:00 and 12:55 UTC. This indicates that the observed peak frequencies represent tower resonance effects while additional

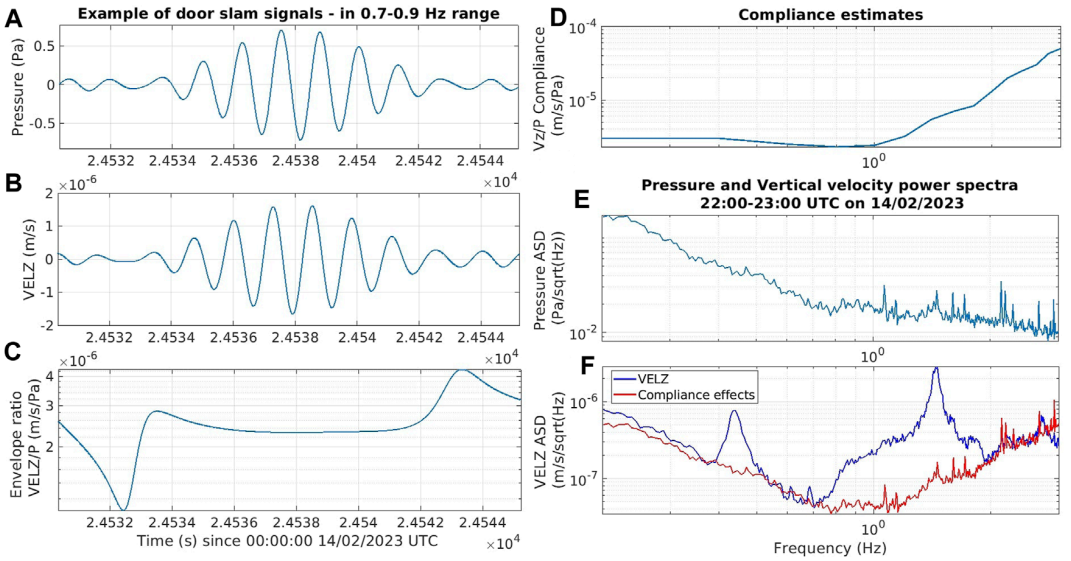


FIGURE 4
Pressure **(A)**, vertical velocity **(B)** and energy envelope ratios of vertical velocity to pressure **(C)** filtered in the frequency range between 0.7 and 0.9 Hz range during a door slam event on 14 February 2023. On the right, compliance estimates in the frequency range between 0.2 and 3 Hz range **(D)** and Amplitude Spectral Density (ASD) of pressure **(E)** and ground velocity records **(F)** during the time range 22:00–23:00 UTC on 14 February. The red curve in **(F)** is an estimate of the vertical ground velocity variations induced by compliance effects (the product of the curves in panels **(D, E)**.

spectral peaks during operation are expected to represent wind turbine excitation frequencies (e.g., turbine rotation, rotor blade passing) and multiples thereof.

To quantify the temporal stability of these effects over the 2-week period of the experiment, Figure 5A shows the spectrogram from continuous seismic time series. The spectrograms are calculated from the measured spectral ratios (vertical component, 120-s long windows) between the 400 stations inside and the three southernmost stations outside the wind farm. Over the entire period, the spectral shape is very stable and the spectral signatures of the wind farm dominate over much of the array, particularly at times of moderate-to-high wind speeds. As can already be seen from Figure 2, for intermediate frequencies between 1 and 10 Hz, peak amplitudes are slightly higher for increased wind speeds though the differences are less than a factor 3.

Besides building the spectral ratio, we also calculate the spectral width of the covariance matrix of the time series (vertical component) of 16 geophones inside the wind farm in the south-eastern sector (Figures 5B, C). The spectral width is a measurement for the eigenvalue distribution of the covariance matrix and reflects the spatial coherence of the seismic wavefield. A high spectral width indicates a diffusive wavefield with a low spatial coherence while a low spectral width indicates a high spatial coherence. This measurement has been introduced to identify coherent seismo-volcanic tremor signals (Seydoux et al., 2016) and has been applied to identify flexural resonances in an elastic metamaterial (Lott et al., 2020b). Due to the eigenmodes and seismic signals generated by the wind farm one might expect a rather coherent wavefield. Interestingly, the covariance matrix spectral width shows similar patterns as for the spectral ratio. There are temporarily relative stable values for the minima of the spectral width between 1 and 10 Hz, indicating a coherent wave field due to the tower resonances displayed by the greenish colors. On the other hand, as expected, a low spatial coherence can be observed for microseisms, i.e., for frequencies less than 1 Hz (e.g., Correig and Urquizú, 2002).

We further would like to point out that the large values in the spectrogram and the contemporaneous small values for the spectral width towards the end of 15 and 21 February, to a lesser extent also on 23 February, are interpreted as disturbing signals due to the rotation of the nacelle due to changing wind incidence direction as well as due to the permanent starting and stopping of the rotation of the blades. During these periods, the wavefield shows a more uncorrelated behaviour and these minima become less prominent. However, the minima at 1.4, 4 Hz and around 8 Hz appear to be more stable than the other minima (e.g., towards the end of 15 February).

This means that external factors like wind speed or blade rotation frequency will cause a variation in the amplitudes of the certain spectral peaks while the resonance frequencies of the tower eigenmodes remain stable in time. More importantly and also clearly visible in Figure 5, the spectral troughs around 1.4 and 13 Hz, to a lesser degree also at 8 Hz, at which significantly less energy is transmitted to the ground, are also temporarily stable with their amplitude being smaller than 1 for most of the time (pale and blueish horizontal lines in Figure 5A, most visible between 17 and 22 February and after 24 February). This holds both for small and high wind speeds Figure 5D and seems to confirm that the inside-to-outside spectral minima described in section 3.1 are caused by the strong interaction due to local resonances of the large number of wind turbine towers in the wind farm. As already mentioned above, the trough at 0.25 Hz might not be caused by resonance effects but this trough is likely due to the fact that the amplitude of the second

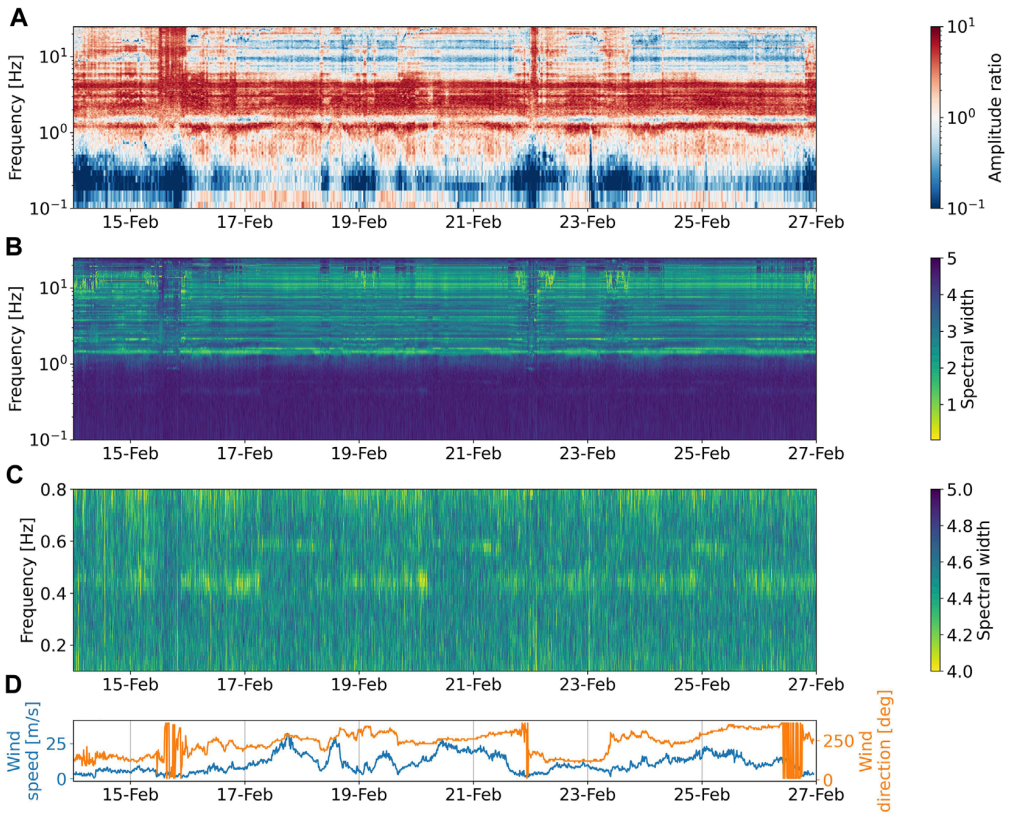


FIGURE 5
**(A)** Spectrogram for the spectral ratio between the array nodes and the most distant broadband stations to the south of the wind farm. **(B)** Spectral width of the covariance matrix of a subarray of 16 vertical component time series within the large nodal array estimating the spatial coherence of the seismic wavefield. **(C)** A zoom on **(B)** with an adapted color-scale highlighting the spectral width minimum around 0.43 Hz. **(D)** Wind speed and wind direction measured at the top of a wind turbine with 10-min sampling interval.

microseism cannot be measured correctly due to the self-noise of the geophones in the low-frequency range while it can be assessed correctly at the broadband stations outside the wind farm.

## 3.5 Phase differences and signal amplitude

As there is a strong interaction between the soil and the structures, the horizontal and vertical components of the Rayleigh waves will excite the resonances of the large number of individual wind turbines around their resonance frequencies (both flexural and compressional resonances). This behaviour will induce a phase shift of π on the incoming waves, i.e., a reflection of the wavefield around the resonant frequencies of the wind turbines. When in anti-resonance, the attachment point between the earth surface and the wind turbine is at rest (Ewins, 2000; Williams et al., 2015), achieving the desired reduction of the incoming wavefield energy. Due to the sub-wavelength arrangement of the wind turbines, there is a less strong wavefield power within the wind farm between resonance and anti-resonance (smaller amplitude, i.e., greenish color in the slant stack image around 1.4 Hz, see Figure 3A) when considering the cumulative effect of the array of wind turbines.

To study the influence of possible phase differences on the amplitude decay, we calculate the phase differences between signals measured at the foundation of one wind turbine and at a single short-period station in the south-eastern sector of the seismic array. The investigated station (yellow circles in Figure 1) is located at a distance of around 50 m from the wind turbine, i.e., at the sub-wavelength scale (the wavelength for Rayleigh waves is ~ 500 m at 1 Hz). For calculating possible phase differences, we refer to the cross-correlation analysis with a moving window with a length of 5 s and a total length of 1 hour (again starting from 16 February 2023 at midnight). The signals are filtered in narrow frequency bands around the observed minima and maxima of the inside-to-outside spectral ratio shown in Figure 2. Exemplarily, in Figure 6 we show the phase differences for frequency ranges between 0.7 and 1.1 Hz where a well-constrained peak can be seen and between 1.3 and 1.6 Hz in which the inside-to-outside spectral ratio is characterized by a strong trough. In the former case, the wind turbine and the soil are oscillating in phase as there is almost no phase difference between the signal at the foundation of the wind turbine and a station a few tens of meters away. Similar effects, although less clear, can be observed for the other frequency ranges where the inside-to-outside spectral ratio shows a trough (not shown). On the contrary,

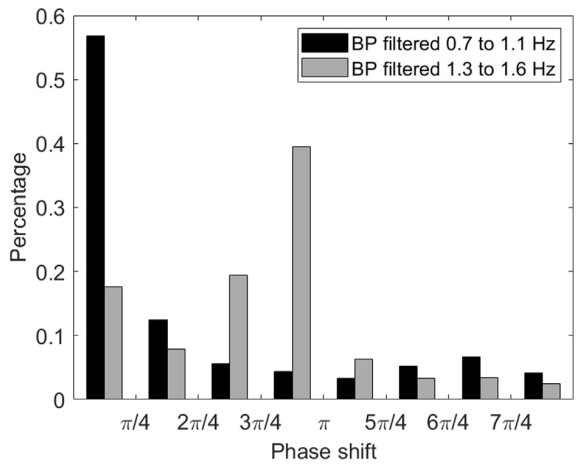


FIGURE 6
Phase shift between bandpass filtered signals at the foundation of the wind turbine with respect to recordings at a short-period station at a distance of 50 m.

around 1.4 Hz, we observe a phase shift that is mainly limited to the range between π/2 and π, meaning that the oscillating wind turbine is mostly moving in an opposite direction at the sub-wavelength scale compared to the soil, thus decreasing its motion. This out-of-phase motion is, however, confined to the surface resonators, i.e., the wind turbines, meaning that such behaviour would not be observed for arbitrary pairs of stations in the seismic array nor when the distances between the resonators and the station approaches the wavelength of the surface waves but only on the sub-wavelength scale.

In the high-frequency range, which is not affected by resonance effects, the phase differences between source signals appear rather randomly and no clear phase shift can be detected (already discussed by Saccorotti et al., 2011; Limberger et al., 2021). The scattered wavefields of the individual wind turbines lead to apparently random constructive and destructive interferences, making the interference condition very sensitive to any phase difference which can lead to strong spatial and temporal changes in the wavefield amplitude along the optical fiber (Figure 7B). In this plot, wind turbines are located at meter points 0, 350, 600 and 850 along the fiber. The respective wind turbines are located around 50, 16, 10 and 60 m away from the fiber and the blades of all wind turbines were rotating at apparently identical rotation rates at moderate wind speeds. The highest amplitude values are found for the two closest wind turbines but the corresponding amplitude pattern is not stable in time.

On the contrary, a temporally stable amplitude pattern is observed in a frequency range between 1.3 and 1.6 Hz (Figure 7A). Here we see an extremely rapid drop in signal amplitude around the wind turbine resonances. Only the signals from the third wind turbine closest to the fiber at meter point 600 can be detected while for the second wind turbine at meter point 350 the signal can only be approximated (the signals from the first wind turbine are strongly disturbed by the power supply of the interrogator). After further 10–15 m, signals of the wind turbine are already barely discernible although all signals are in phase, revealing a strong damping of the wavefield inside the wind farm at the resonance frequencies of the wind turbine towers.

At first glance, it might look strange that lower frequencies of surface waves are more strongly damped. To this regard, we obtain complementary information on the attenuation by the PSD along the fiber. The PSD allows the frequency-dependent wave propagation characteristics to be revealed. After anti-alias filtering and downsampling to 100 Hz, we calculate strain-rate PSDs. We follow the procedure described by McNamara and Buland (2004) although PSDs are classically calculated for ground-motion accelerations; the relationship between ground-motion and strain-rate is not straightforward though. The PSDs calculated for each fiber channel at 16 February 2023 between 11:00 and 13:00 UTC are shown in Figure 8. PSD amplitudes strongly vary along the fiber. Signals from wind turbines at meter points 350 and 600 can clearly be identified in the high-frequency range while signals from wind turbines at meter points 0 and 850, which are around 50 and 60 m away from the fiber, are barely visible. For frequencies lower than a few Hz, only signals from the wind turbine closest to the fiber are seen. Counter-intuitively, these low-frequency signals attenuate very quickly and this effect is identical for all four wind turbines near the fiber. As wind turbines mainly emit surface waves (Styles et al., 2011 among others), intuitively one would expect stronger attenuation for higher but not for low frequencies. However, the high-frequency signals can be detected over distances of several hundred meters and it is the tower resonance frequencies that are strongly attenuated. Notably, the attenuation pattern for frequencies between 5 and 10 Hz is rather similar, already reported by Gortsas et al. (2017), with the exception that signals around 8 Hz attenuate very rapidly.

## 3.6 Attenuation factor and attenuation length

The basic premise is that the PSD amplitude decay follows a power law, meaning that there should be a linear relationship between the logarithm of the amplitude and the logarithm of the distance. The slope of a linear fit of the decay can then be used to calculate an attenuation factor, first proposed by Stammler and Ceranna (2016) and by Flores-Estrella et al. (2017). The results in Figure 9 show peak values between 2.5 and 3 in frequency ranges around 0.43, 1.4, 4, 9 and 13 Hz. Most of these values coincide with the resonance frequencies of the wind turbine tower shown in Figure 2B. For frequencies in-between, the attenuation takes values between 1 and 2. For high frequencies above 20 Hz, there is a systematic decrease down to values between 0.5 and 1. By multiplying PSD amplitudes by a factor of 0.5, the corresponding attenuation values for time signals can be estimated as they are proportional to the square of time domain amplitudes. Note, however, that we are discussing strain-rate PSD, not ground-motion values. Nevertheless, after multiplication by 0.5, attenuation values significantly greater than 1 occur in the five distinct frequency ranges which have already been discussed earlier, indicating an attenuation even stronger than that of classical body waves, meaning that this behaviour cannot be explained by near-field effects.

Another way to identify the existence of frequency ranges where attenuation effects occur is to examine the correlation between different channels along the optical fiber. This involved processing

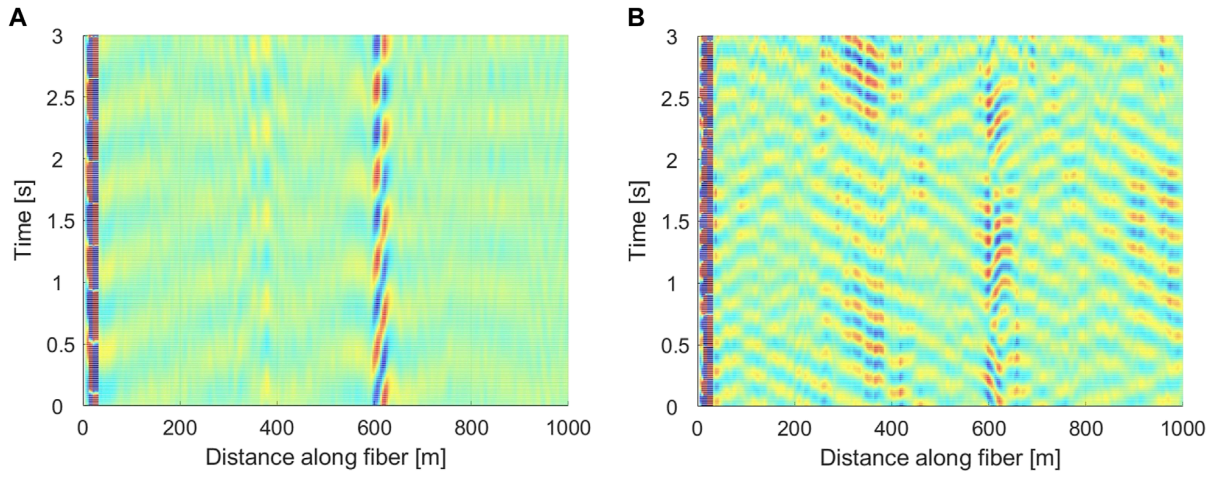


FIGURE 7
3-s normalized strain amplitude of seismic noise along the optical fiber filtered in frequency ranges between 1.3 and 1.6 Hz **(A)** and 3–4 Hz **(B)**. Measurements were taken at 16 February 2023 at 11:15 UTC. The high amplitude at very small distances is due to interfering signals due to the power supply of the interrogator.

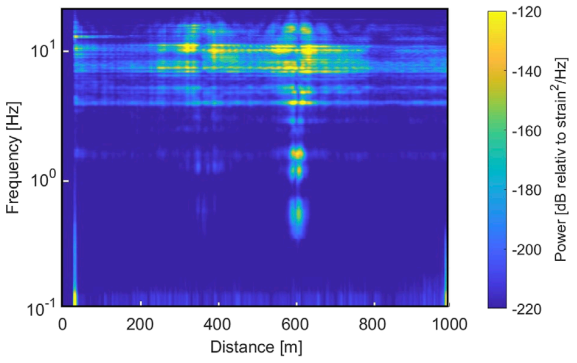


FIGURE 8
Two-hour PSDs (16 February 2023, 11:00 to 13:00 UTC) as a function of frequency and distance along the optical fiber. For a range of distances between 0 and 30 m, the signal power has been set to zero to eliminate the power supply signals from the interrogator.

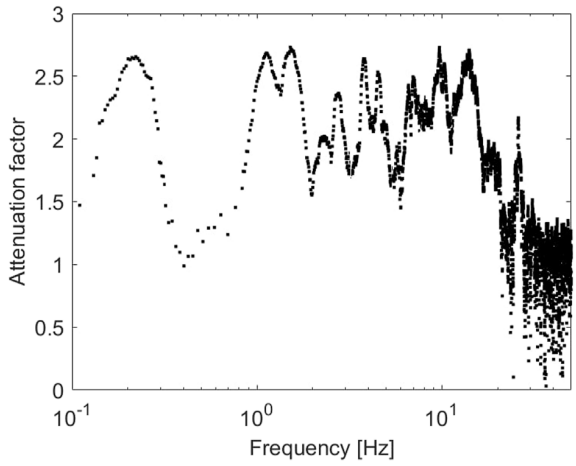


FIGURE 9
Frequency-dependent attenuation factor determined from the double-logarithmic representation of PSD amplitude decay (16 February 2023, 11:00 to 13:00 UTC).

of the noise data for each channel $i$ to accumulate a coherent phase signal in the form of a cross-spectral density matrix which is the spatial covariance matrix of the data in the Fourier domain (e.g., Gerstoft and Tanimoto, 2007; Roux, 2009)

$$S(\omega, i) = d(\omega, i)d^{*}(\omega, i) \quad (1)$$

In Eq. 1, $d$ is the Fourier transform of the data and the asterisk represents the Hermitian transpose. $\mathbf{S}$ is a symmetric matrix with the autocorrelations of all stations on the diagonal elements and the cross-correlations on the off-diagonal elements. As $\mathbf{S}$ is a function of both angular frequency $\omega$ and time $t$, we take a time interval of 5 s for each channel of the fiber and compute $\mathbf{S}$ for each angular frequency and individual time window. The results for the time-averaged cross-spectral density matrix are shown in Figure 10.

At 1.5 Hz the cross-spectral density amplitude drops very rapidly around the wind turbines, meaning that the scattering intensity is significant at this frequency. The coherent signal is strongly attenuated with respect to the diffusive wavefield. At 7.5 Hz the cross-spectral density amplitude remains high over a much longer distance range and a coherent signal can be detected over several hundred meters. Similar observations apply for both the real and the imaginary parts of the cross-spectral density. The latter, however, is in fact the only part of the complex cross-spectra that reflects true non-zero-lagged interactions, meaning that this observed effect does not have a time-lag with respect to the source activity of

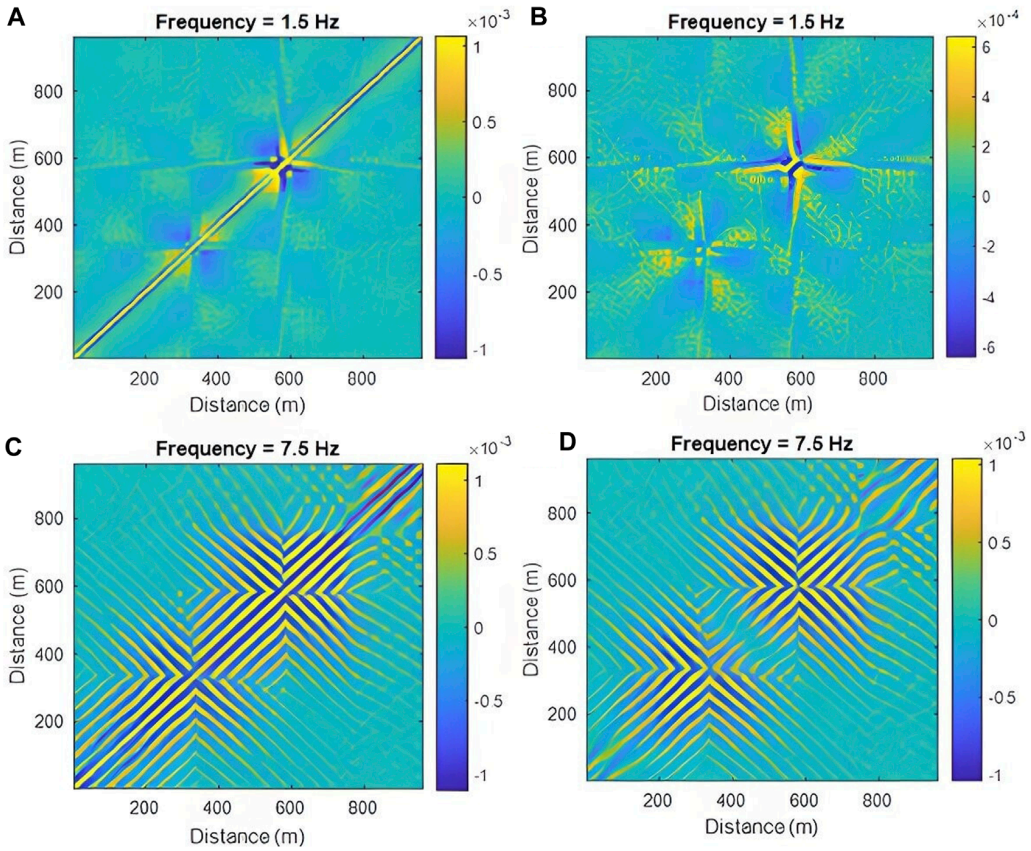


FIGURE 10
Real **(A, C)** and imaginary **(B, D)** parts of the cross-spectral density matrix along the optical fiber for frequencies of 1.5 Hz (top) and 7.5 Hz (bottom).

the wind turbines. A significant damping attenuation of the wave field around 1.5 Hz is also evident here while this effect cannot be observed for 7.5 Hz.

## 3.7 Polarization of seismic noise

In the penultimate section we discussed the phase shift of the incident waves which causes a reflection of the wavefield around the resonance frequencies of the wind turbines. Such a phase shift also exists between coupled P and SV waves, i.e., for the classical Rayleigh waves. Here the coupling between the SV waves on the vertical component and the P waves on the horizontal component is only possible if both components are shifted in phase by ±90°. Since the particle motion of the different seismic wave types is different, the key parameter for the proper identification is their polarization. The analysis is based on Vidale's (1986) complex particle motion polarization analysis approach. A three-component ground motion recording of seismic noise is used to calculate the coherency matrix or complex covariance matrix. Kulesh et al. (2007) adapted the conventional covariance approach (e.g., Kanasewich, 1981) and utilized it to estimate time-frequency dependent polarization. In this process, time-averaging is not required explicitly. Prior to applying polarization analysis to the complex wavelet amplitude for each time-frequency pair, we first decompose the signal using a continuous wavelet transform (CWT). The ellipse, which is often inclined in 3D Euclidian space, then describes the particle motion at each time and frequency. The frequency-dependent particle motion is finally fitted to an ellipse which is characterized by its ellipticity ratio, i.e., the ratio between the minor and the major axis of the ellipse (Greenhalgh et al., 2018). The ratio takes a value of zero for a fully linearly polarized waves and a value of one for a circularly polarized arrival.

The average ellipticity ratio, i.e., the ratio of the minor to the major axis, for the seven 5-s three-component instruments inside the wind farm and the three southernmost stations outside the wind farm for 60 signal windows with a length of 120 s again starting at 16 February 2023 at midnight is shown in Figure 11. While for the latter the ellipticity ratio does not show any significant variation over the entire frequency range, for stations inside the wind farm the shape of the ellipse is frequency-dependent. For frequencies between 0.3 and 0.4 Hz, around 1.5 Hz, between 2 and 2.5 Hz and around 13 Hz there is a significant decrease towards a more linearized polarization (although the particle motion still has to be considered elliptical). These results of polarization analyses are stable in time. While, as discussed above, the trough between 2 and 2.5 Hz is likely to be caused by compliance effects (see peaks in the red curve in Figure 4F), a possible explanation for the low values in the

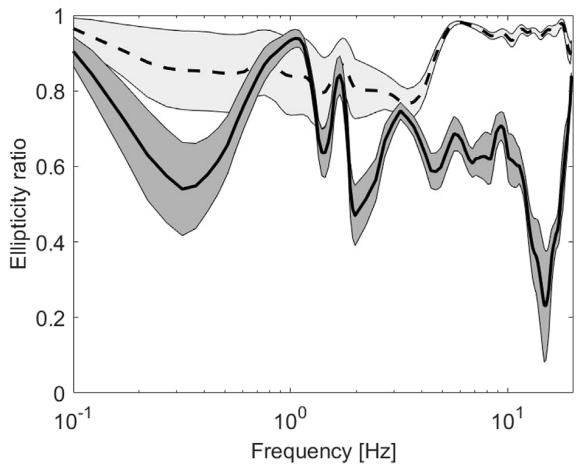


FIGURE 11
Ellipticity ratio of the reconstructed particle motion through the continuous wavelet transform for 5-s short-period stations inside (solid line) and the broadband stations outside (dashed line) the wind farm.

other frequency ranges could be that the local resonances (partially) cause an energy conversion. Herein, Rayleigh waves are (partially) converted into nearly linearly polarized S waves (or more linearly polarized Rayleigh waves) at the resonance frequencies of the wind turbines in the wind farm. In the context of surface resonators over a homogeneous semi-infinite elastic medium, such conversion of the Rayleigh waves has already been predicted theoretically and observed numerically (Colombi et al., 2016a; 2017; Colquitt et al., 2017). The abrupt shift in particle motion observed in the wind farm provides a further indication of the influence of the wind turbines on the propagation of surface waves as these effects are not observed for stations outside the wind farm.

## 4 Numerical modeling of the wind turbine and discussion

Understanding the surface wave dynamics observed in this experiment also requires a good understanding of the dynamic characteristics of the wind turbine resonators present in the field. On the experimental side, there is a high degree of consistency with respect to the frequency ranges in which strong damping effects occur and some of these observations cannot be interpreted as the behaviour of individual wind turbines but only as the interaction of a large number of wind turbines. The peaks that we observe in the spectra can originate from flexural and compressional oscillations of the tower, blade rotation or power grid frequency including harmonics and subharmonics. For a numerical evaluation of mechanical resonance effects, the eigenvalues for one of the turbines in the wind farm are obtained using COMSOL Multiphysics® , a finite element analysis program. We specifically choose to evaluate the resonances of the wind turbine from type ENERCON E-70 which has a Lennartz 5-s broadband sensor installed at its base and the DAS fiber optic cable in close proximity. This will help us better understand the recorded signals. This wind turbine with nominal power of 2.3 MW has a hub height of 113.5 m and is mounted over a prestressed concrete-steel hybrid tower (Figure 12, left panel). The diameter of the tubular tower varies from 9.3 m at the base and smoothly tapers to 2 m diameter at the very top. The bottom two-thirds of the tower is a precast concrete construction with 22 segments, each 3.8 m high with a 300 mm thick shell. The top one-third of the tower is composed of 2 structural steel segments 3 and 25 m long, having a shell thickness of 40 and 25 mm respectively. The tower is idealised as a vertical cantilever beam of multiple segments having a mean annular cross section with constant thickness. The rotor assembly, the nacelle and generator which weigh around 104 tons in total, are modeled as a concentrated mass placed on top of the beam, whereas the bottom end of the tower is assigned a fixed boundary condition. The tower is discretised with one-dimensional beam elements available with the Structural Mechanics module of COMSOL. The elastic parameters of concrete and structural steel, as seen in Figure 12, are obtained from the Euro code 2 and 3 respectively (British Standard Institution, 2004; John Wiley and Sons, 2005).

Table 1 lists the natural frequencies of the tower for both the Euler-Bernoulli (slender beam) and Timoshenko beam (thick beam) formulations. As can be seen from the table, the fixed-base model predicts the natural frequency of the wind turbine with reasonable accuracy. The slightly lower eigen values for the fundamental mode may be due to neglecting the steel reinforcement of the concrete sections as well as the pre-stress that would further stiffen the tower. Although our model does not take into account the flexibility of the foundation due to the soil coupling, the numerical results obtained are evidence that the foundation is almost clamped due to the type of foundation system that has been used. We do not have information on the foundation system. For soft soil sites like that in Nauen, deep foundations are usually used with micro-piles for resisting traction but it is very difficult to imagine the size, the number and the length of such piles, if any.

The numerical modelling allows two observations to be made. First, over the whole frequency range, the eigenvalues are in good agreement with the observations and small deviations can only be seen for higher modes. Apart from the unknown foundation clamping, such deviations might also be caused by the eccentricity of the head mass with respect to the centre of gravity of the tower cross-section. This causes the resonance frequencies to widen (seen in Figure 2B when the wind turbine is operational with respect to when it is non-operational and higher modes to shift. However, since Rayleigh waves have an elliptical polarization, which implies both horizontal and vertical displacements, a straightforward coupling of both the flexural and the compressional resonances of the wind turbine towers with the seismic wavefield is also possible.

Secondly, most of the resonances here are caused by flexural modes. This might be due to the fact that flexural resonances of slender structures like wind turbines are excited more easily than compressional ones. This is different from the METAFORET experiment in which no efficient coupling between the horizontal components of the Rayleigh waves with the flexural resonances of the trees was observed which might be due to different material properties. A few theoretical studies have focused on flexural resonances and its interaction with the seismic wavefield indicating that these flexural resonances can play an important role in certain

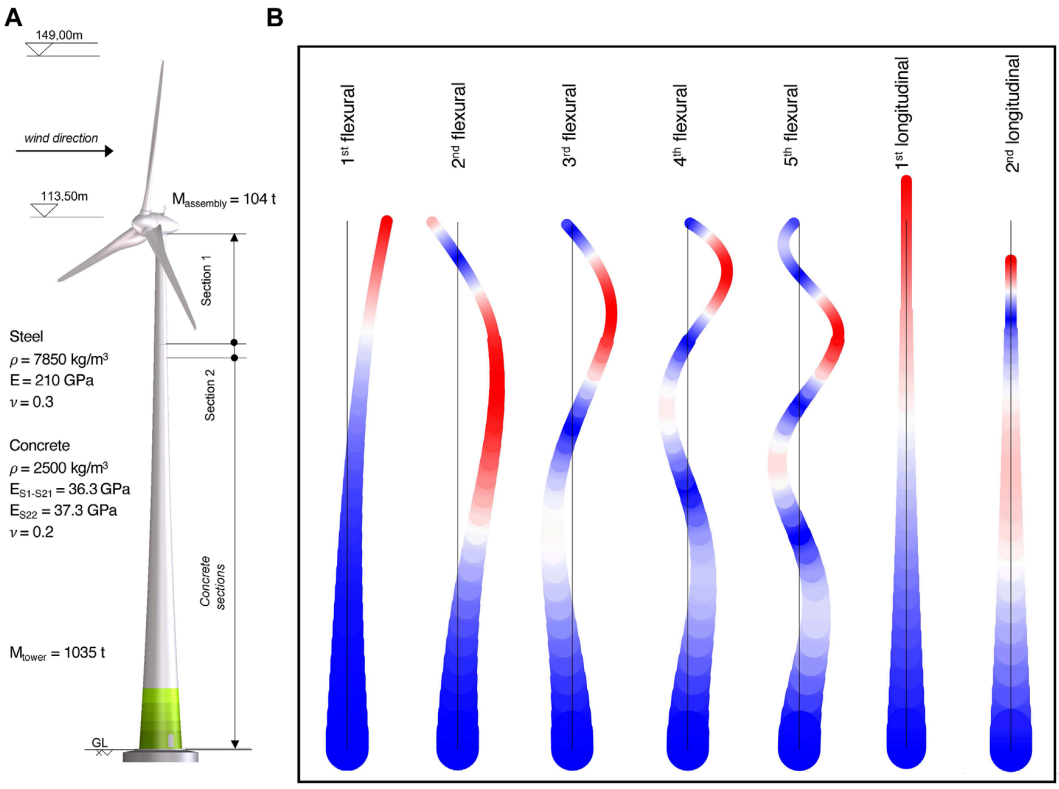


FIGURE 12
Modal representations of the 112.3 m high ENERCON E–70 wind turbine tower motion under flexural and compressional resonances. **(A)** Technical drawing of the wind turbine (© ENERCON GmbH). **(B)** Flexural and compressional oscillations of the tower. The concrete and steel segments are assigned a uniform annulus cross section with material properties shown in the left panel. Although 1D beam elements are used, the tubular representation of the tower is shown for better visualisation. The color represents the normalized eigen displacement magnitude, blue and red indicating the respective minimum and maximum for each characteristic mode. The eigenvalues corresponding to the Euler-Bernoulli and Timoshenko beam formulations are shown in Table 1.

material regimes (Xiao et al., 2012; Colquitt et al., 2017; Lott and Roux, 2019; Wootton et al., 2019; Marigo et al., 2020). In particular, flexural resonances become more important for less rigid substrates (i.e., softer and more flexible soils) but that is exactly what we see in our experiment.

Although from a theoretical point of view we do not see an overlap between the flexural and compressional resonance frequency ranges, we cannot exclude the possibility of interaction between the two. However, it seems clear that for the first compressional resonance around 13 Hz, its effect on the seismic wavefield is stronger. This can be seen from the lowest troughs in Figures 2, 11 and the highest peak in Figure 9 caused by the compressional resonances of the wind turbine. Consistent with the findings of Roux et al. (2018) and Lott et al. (2020a), this may be due to the surface waves being more strongly slowed down and damped around the compressional resonance of the resonators.

While it seems clear that the set of wind turbines in the wind farm does have an impact on surface waves propagation in distinct frequency ranges, the results also indicate that there is no complete extinction of the surface wavefield as observed in classical metamaterials but only a metamaterial-approximate behaviour. Several possible factors are at play here.

(1) The frequency ranges of flexural resonances overlap with the passband of compressional waves, i.e., no compressional resonances are found below 10 Hz. Longitudinal (Rayleigh) waves can still propagate throughout the wind farm in the frequency ranges of the flexural resonances as can also be seen in Figure 11, meaning that there is no full elimination of (Rayleigh) surface waves. Similar observations have already been made by Ma et al. (2016).
(2) As we do not have a single height for all wind turbines, the damping effects associated with different heights overlap, i.e., we are mapping effective material properties. This, in turn, will cause a weakening of the overall damping but a broadening of the frequency ranges in which the damping occurs (similar to what has been described by Colombi et al., 2016b; Li and Li, 2020).
(3) Although the arrangement of the wind turbines in the north-south direction is periodic, in 3D the chosen wind farm is not sufficiently periodic for “seismic crystal” effects to become dominant as described by Colombi et al. (2016c) and by Qahtan et al. (2022).
(4) For the dispersion curve (Figure 3), we do not observe a clear slowdown of surface wave velocities around 1.5 Hz as predicted

TABLE 1 Numerically obtained eigenvalues of the ENERCON E-70 wind turbine tower and comparison with the experimental results with values taken from the 5-s sensor installed on the foundation of the single wind turbine (black dotted line in Figure 2B).

| Mode | Eigenvalue [hz] | | Experimental value [hz] peak values in Figure 2B |
|---|---|---|---|
| | Euler-Bernoulli | Timoshenko | |
| 1st flexural | 0.42 | 0.42 | 0.43 |
| 2nd flexural | 1.46 | 1.44 | 1.39 |
| 3rd flexural | 3.84 | 3.72 | 3.85 |
| 4th flexural | 6.75 | 6.47 | 7.61 |
| 5th flexural | 10.36 | 9.56 | 10.2 (only partially visible) |
| 1st compressional | 10.58 | 10.58 | 12.8 |
| 2nd compressional | 20.60 | 20.60 | not observed |

theoretically in previous studies (e.g., Colombi et al., 2016b; Colombi et al., 2017) but we only observe a flattening of the dispersion curve. This could be due to the interaction of the surface waves with body waves in the frequency range of the flexural resonances of the wind turbines.

(5) Although we see a significant influence of the wind farm on the seismic wave field in a broad frequency range, given the rather soft soil conditions (Figure 3) and a spacing between the wind turbines in the order of a few hundred meters, the wavelengths are rather short. This means that only the first two modes are really sub-wavelength ($\lambda/8$ for the first, $\lambda/2$ for the second flexural mode).

(6) In addition, the degree of coupling of Rayleigh waves and hybrid Rayleigh waves at the soil-resonator interface is sensitive to the mass of the resonator. Such heavy masses–here we are discussing masses in the order of much more than 1,000 tonnes–do not cause a smooth bending of the dispersion curve for frequencies smaller than the resonance frequencies but a very sharp deviation of the dispersion curve towards low velocities just before this frequency (Boechler et al., 2013; Palermo et al., 2016).

(7) The heavy masses are associated with a strong impedance contrast at the soil-resonator interface. Assuming values for $\rho_{soil} \approx 1800$ kg/m$^3$, $\rho_{steel/concrete} \approx 8{,}000$ kg/m$^3$, $v_{Ssoil} \approx 500$ m/s, $v_{Ssteel/concrete} \approx 3{,}200$ m/s results in an impedance contrast in the order of 30. While we generally observe an increase in the width of the damping frequency ranges for decreasing impedance contrasts, for strong impedance contrasts–as seen here–the corresponding damping frequency ranges tend to become smaller due to a weakened coupling between the ground and the resonators (Colombi et al., 2014; Joshi and Narayan, 2022).

(8) While previous reference studies have generally been performed for a homogeneous halfspace, a multi-layered soil will result in a more complex wavefield. The coupling of the wavefield with the resonators will then depend more strongly on the variation of the soil properties with depth (Chen et al., 2019) although a leakage to higher-mode surface waves which cannot be resolved with our experimental configuration (Lott et al., 2020a) as well as an interplay between flexural and compressional resonance resonances (as described, for example, by Marigo et al., 2020) might also be possible.

While so far we only have focused on Rayleigh waves, layered soils will practically also allow the study of anti-plane waves, i.e., Love waves requiring horizontal resonators (Palermo and Marzani, 2018). Although the overall results are consistent, there are a number of experimental peculiarities which can be excluded in theoretical studies but which are unavoidable in the real-world experiments. Such peculiarities can only be resolved by dense spatial sampling of the seismic wavefield.

## 5 Conclusion

We have demonstrated for the first time that tall structures at the city-district scale can interact with each other, with the seismic wavefield and with the atmospheric pressure field. The spatially dense installation of extended resonators can produce strong structural damping of Rayleigh waves in the frequency range of engineering interest (a few Hz). A dense grid of seismic geophones and complementary instrumentation allows the physical interpretation of the observed wavefield properties to be validated. Around the flexural and compressional resonance frequencies of the wind turbine towers, the coupling between the resonators and surface waves in the wind farm is demonstrated taking into account amplitude and phase patterns, attenuation length, spectral ratio and surface wave polarization. The damping effect in these frequency ranges is further clearly observed in the strain amplitude along the optical fiber. The spectral ratio between stations inside and outside the wind farm reveals that this attenuation results from the incoherent scattering linked to the interaction of surface waves with the wind turbines, meaning that these effects cannot be observed outside the wind farm and can only be explained by the interaction of a large number of wind turbines. The shift in particle motion ellipticity at frequencies near to the resonance of the wind turbines is another indicator of the resonance impact of the resonant structures on the propagation of Rayleigh waves which is supposed to be stronger for compressional resonances with respect to the flexural ones. With respect to metamaterial-like effects, although both types of resonances (flexural and compressional) certainly have an impact on the wavefield of seismic surface waves, we do not see evidence of a classical metamaterial with a strict bandgap in the sense of one or several frequency range(s) where the propagation of seismic surface waves is completely inhibited. The results still pave the way to potential future applications in terms of urban seismic hazard mitigation and/or earthquake engineering in urban environments. In a first step, for example, arrays of buildings could be studied with a focus on building component resonances like large concrete floors or an emphasis on designs of buildings

with resonances in the frequency range of earthquake engineering. One could then ask to what extent the real urban organization with a highly heterogeneous building stock can contribute to the emergence of frequency ranges in which the seismic energy is strongly reduced.

## Data availability statement

The datasets presented in this study can be found in online repositories. The names of the repository/repositories and accession number(s) can be found below: https://fdsn.org/networks/detail/XF_2023/.

## Author contributions

MP: Conceptualization, Data curation, Formal Analysis, Investigation, Writing–original draft. PR: Conceptualization, Data curation, Formal Analysis, Investigation, Writing–review and editing. SM: Formal Analysis, Investigation, Software, Writing–review and editing. RG: Data curation, Formal Analysis, Investigation, Writing–review and editing. RS: Formal Analysis, Investigation, Writing–review and editing. CA: Conceptualization, Data curation, Writing–review and editing. FB: Conceptualization, Data curation, Writing–review and editing. PG: Investigation, Writing–review and editing. MO: Conceptualization, Formal Analysis, Investigation, Writing–review and editing. FC: Supervision, Writing–review and editing.

## Funding

The author(s) declare financial support was received for the research, authorship, and/or publication of this article. The authors declare that financial support by the GeoForschungsZentrum Potsdam (GFZ) was received for the research, authorship, and/or publication of this article.

## Acknowledgments

We are very grateful to the private land owners and the community of Nauen for hosting our instruments. We also thank our colleagues who came on the field for station deployment and maintenance (Andreas Brotzer, Andrés Olivar Castaño, Alex Dombrowsky, Reza Esfahani, Fandy Adji Fachtony, Annabel Haendel, Sebastian Heimann, Axel Jung, Frank Krueger, Lukas Lehmann, Henning Lilienkamp, Chen-Ray Lin, Karina Loviknes, Malte Metz, Sebastián Nuñez Jara, Laurens Oostwegel, Elif Tuerker, Nele Vesely, Daniel Vollmer, Ming-Suan Yen). Instruments were provided by the Geophysical Instrumental Pool Potsdam (GIPP), by the University of Potsdam, by the Ludwig Maximilian University of Munich and by ISAE-SUPAERO Toulouse. SM received funding from the URBASIS project (H2020-MSCA-ITN-2018, grant number 813137). We would also like to warmly thank Martin Drews, ENERCON GmbH for providing the information on the wind turbines. Map data copyrighted OpenStreetMap contributors and available from https://www.openstreetmap.org. The two reviewers and the associate editor Chong Xu are also thanked for their constructive comments which helped to improve the manuscript.

## Conflict of interest

The authors declare that the research was conducted in the absence of any commercial or financial relationships that could be construed as a potential conflict of interest.

## Publisher's note



## References

Aki, K. (1957). Space and time spectra of stationary stochastic waves, with special reference to microtremors. *Bull. Earthq. Res. Inst.* 35, 415–456.

Albino, C., Godinho, L., Amado-Mendes, P., Alves-Costa, P., Dias-da-Costa, D., and Soares, D., Jr (2019). 3D FEM analysis of the effect of buried phononic crystal barriers on vibration mitigation. *Eng. Struct.* 196, 109340. doi:10.1016/j.engstruct.2019.109340

Avilés, J., and Sánchez-Sesma, F. J. (1988). Foundation isolation from vibrations using piles as barriers. *J. Eng. Mech.* 114 (11), 1854–1870. doi:10.1061/(asce)0733-9399(1988)114:11(1854)

Bard, P. Y. (1999). Microtremor measurements: a tool for site effect estimation. *Eff. Surf. Geol. seismic motion* 3, 1251–1279.

Boechler, N., Eliason, J. K., Kumar, A., Maznev, A. A., Nelson, K. A., and Fang, N. (2013). Interaction of a contact resonance of microspheres with surface acoustic waves. *Phys. Rev. Lett.* 111 (3), 036103. doi:10.1103/physrevlett.111.036103

British Standard Institution (2004). *Eurocode 2: design of concrete structures - Part 1-1: general rules and rules for buildings*. EN 1992-1-1 (2004), 668. London: British Standard Institution, 659–668.

Brûlé, S., Javelaud, E. H., Enoch, S., and Guenneau, S. (2014). Experiments on seismic metamaterials: molding surface waves. *Phys. Rev. Lett.* 112 (13), 133901. doi:10.1103/physrevlett.112.133901

Castanheira-Pinto, A., Alves-Costa, P., Godinho, L., and Amado-Mendes, P. (2018). On the application of continuous buried periodic inclusions on the filtering of traffic vibrations: a numerical study. *Soil Dyn. Earthq. Eng.* 113, 391–405. doi:10.1016/j.soildyn.2018.06.020

Chen, Y., Qian, F., Scarpa, F., Zuo, L., and Zhuang, X. (2019). Harnessing multi-layered soil to design seismic metamaterials with ultralow frequency band gaps. *Mater. Des.* 175, 107813. doi:10.1016/j.matdes.2019.107813

Cho, I., and Iwata, T. (2021). Limits and benefits of the spatial autocorrelation microtremor array method due to the incoherent noise, with special reference to the analysis of long wavelength ranges. *J. Geophys. Res. Solid Earth* 126 (2). doi:10.1029/2020JB019850

Code, P. (2005). *Eurocode 2: design of concrete structures-part 1–1: general rules and rules for buildings*. London: British Standard Institution, 659–668.

Colombi, A., Ageeva, V., Smith, R. J., Clare, A., Patel, R., Clark, M., et al. (2017). Enhanced sensing and conversion of ultrasonic Rayleigh waves by elastic metasurfaces. *Sci. Rep.* 7 (1), 6750. doi:10.1038/s41598-017-07151-6

Colombi, A., Colquitt, D., Roux, P., Guenneau, S., and Craster, R. V. (2016a). A seismic metamaterial: the resonant metawedge. *Sci. Rep.* 6 (1), 27717. doi:10.1038/srep27717

Colombi, A., Guenneau, S., Roux, P., and Craster, R. V. (2016c). Transformation seismology: composite soil lenses for steering surface elastic Rayleigh waves. *Sci. Rep.* 6 (1), 25320. doi:10.1038/srep25320

Colombi, A., Roux, P., Guenneau, S., Guéguen, P., and Craster, R. V. (2016b). Forests as a natural seismic metamaterial: Rayleigh wave bandgaps induced by local resonances. *Sci. Rep.* 6 (1), 19238. doi:10.1038/srep19238

Colombi, A., Roux, P., and Rupin, M. (2014). Sub-wavelength energy trapping of elastic waves in a metamaterial. *J. Acoust. Soc. Am.* 136 (2), 192–198. doi:10.1121/1.4890942

Colquitt, D. J., Colombi, A., Craster, R. V., Roux, P., and Guenneau, S. R. L. (2017). Seismic metasurfaces: sub-wavelength resonators and Rayleigh wave interaction. *J. Mech. Phys. Solids* 99, 379–393. doi:10.1016/j.jmps.2016.12.004

COMSOL AB (2023). COMSOL Multiphysics® v. 6.0. www.comsol.com.

Correig, A. M., and Urquizú, M. (2002). Some dynamical characteristics of microseism time-series. *Geophys. J. Int.* 149 (3), 589–598. doi:10.1046/j.1365-246x.2002.01602.x

Dasgupta, B., Beskos, D. E., and Vardoulakis, I. G. (1990). Vibration isolation using open or filled trenches Part 2: 3-D homogeneous soil. *Comput. Mech.* 6 (2), 129–142. doi:10.1007/bf00350518

Dijckmans, A., Ekblad, A., Smekal, A., Degrande, G., and Lombaert, G. (2016). Efficacy of a sheet pile wall as a wave barrier for railway induced ground vibration. *Soil Dyn. Earthq. Eng.* 84, 55–69. doi:10.1016/j.soildyn.2016.02.001

Ewins, D. J. (2000). *Modal testing: theory, practice and application*. New York, USA: Wiley, 562.

Flores-Estrella, H., Korn, M., and Alberts, K. (2017). Analysis of the influence of wind turbine noise on seismic recordings at two wind parks in Germany. *J. Geoscience Environ. Prot.* 5 (5), 76–91. doi:10.4236/gep.2017.55006

Forbriger, T. (2003). Inversion of shallow-seismic wavefields: I. Wavefield transformation. *Geophys. J. Int.* 153 (3), 719–734. doi:10.1046/j.1365-246x.2003.01929.x

Gao, G. Y., Li, Z. Y., Qiu, C., and Yue, Z. Q. (2006). Three-dimensional analysis of rows of piles as passive barriers for ground vibration isolation. *Soil Dyn. Earthq. Eng.* 26 (11), 1015–1027. doi:10.1016/j.soildyn.2006.02.005

Garcia, R. F., Murdoch, N., Lorenz, R., Spiga, A., Bowman, D. C., Lognonné, P., et al. (2021). Search for infrasound signals in InSight data using coupled pressure/ground deformation methods. *Bull. Seismol. Soc. Am.* 111 (6), 3055–3064. doi:10.1785/0120210079

Gau, C., and Gau, C. (2011). *Geologie des Arbeitsgebietes Berlin. Geostatistik in der Baugrundmodellierung: die Bedeutung des Anwenders im Modellierungsprozess*, 7–17. (in German).

Gerstoft, P., and Tanimoto, T. (2007). A year of microseisms in southern California. *Geophys. Res. Lett.* 34 (20). doi:10.1029/2007gl031091

Gortsas, T. V., Triantafyllidis, T., Chrisopoulos, S., and Polyzos, D. (2017). Numerical modelling of micro-seismic and infrasound noise radiated by a wind turbine. *Soil Dyn. Earthq. Eng.* 99, 108–123. doi:10.1016/j.soildyn.2017.05.001

Greenhalgh, S., Sollberger, D., Schmelzbach, C., and Rutty, M. (2018). Single-station polarization analysis applied to seismic wavefields: a tutorial. *Adv. Geophys.* 59, 123–170. doi:10.1016/bs.agph.2018.09.002

Guéguen, P., Bard, P. Y., and Chávez-García, F. J. (2002). Site-city seismic interaction in Mexico city–like environments: an analytical study. *Bull. Seismol. Soc. Am.* 92 (2), 794–811. doi:10.1785/0120000306

Guéguen, P., Mercerat, E. D., Singaucho, J. C., Aubert, C., Barros, J. G., Bonilla, L. F., et al. (2019). METACity-quito: a semi-dense urban seismic network deployed to analyze the concept of metamaterial for the future design of seismic-proof cities. *Seismol. Res. Lett.* 90 (6), 2318–2326. doi:10.1785/0220190044

Guenneau, S., and Ramakrishna, S. A. (2009). Negative refractive index, perfect lenses and checkerboards: trapping and imaging effects in folded optical spaces. *Comptes Rendus Phys.* 10 (5), 352–378. doi:10.1016/j.crhy.2009.04.002

Huang, J., Liu, W., and Shi, Z. (2017). Surface-wave attenuation zone of layered periodic structures and feasible application in ground vibration reduction. *Constr. Build. Mater.* 141, 1–11. doi:10.1016/j.conbuildmat.2017.02.153

Jennings, P. C., and Kuroiwa, J. H. (1968). Vibration and soil-structure interaction tests of a nine-story reinforced concrete building. *Bull. Seismol. Soc. Am.* 58 (3), 891–916. doi:10.1785/bssa0580030891

John Wiley and Sons (2005). *Eurocode 3: design of steel structures - Part 1-1: general rules and rules for buildings*. EN 1993-1-1 (2005). Hoboken, NJ, USA: John Wiley and Sons.

Joshi, L., and Narayan, J. P. (2022). Quantification of the effects of an urban layer on Rayleigh wave characteristics and development of a meta-city. *Pure Appl. Geophys.* 179 (9), 3253–3277. doi:10.1007/s00024-022-03111-y

Kadic, M., Bückmann, T., Schittny, R., and Wegener, M. (2013). Metamaterials beyond electromagnetism. *Rep. Prog. Phys.* 76 (12), 126501. doi:10.1088/0034-4885/76/12/126501

Kadic, M., Milton, G. W., van Hecke, M., and Wegener, M. (2019). 3D metamaterials. *Nat. Rev. Phys.* 1 (3), 198–210. doi:10.1038/s42254-018-0018-y

Kanasewich, E. R. (1981). *Time sequence analysis in geophysics*. Canada: University of Alberta, 480.

Kenda, B., Lognonné, P., Spiga, A., Kawamura, T., Kedar, S., Banerdt, W. B., et al. (2017). Modeling of ground deformation and shallow surface waves generated by Martian dust devils and perspectives for near-surface structure inversion. *Space Sci. Rev.* 211, 501–524. doi:10.1007/s11214-017-0378-0

Kham, M., Semblat, J. F., Bard, P. Y., and Dangla, P. (2006). Seismic site–city interaction: main governing phenomena through simplified numerical models. *Bull. Seismol. Soc. Am.* 96 (5), 1934–1951. doi:10.1785/0120050143

Kitsunezaki, C. (1990). Estimation of P-and S-wave velocity in deep soil deposits for evaluating ground vibrations in earthquake. *J. Jpn. Soc. Nat. Disaster Sci.* 9, 1–17.

Kulesh, M., Diallo, M. S., Holschneider, M., Kurennaya, K., Krüger, F., Ohrnberger, M., et al. (2007). Polarization analysis in the wavelet domain based on the adaptive covariance method. *Geophys. J. Int.* 170 (2), 667–678. doi:10.1111/j.1365-246x.2007.03417.x

Kumar, R., Kumar, M., Chohan, J. S., and Kumar, S. (2022). Overview on metamaterial: history, types and applications. *Mater. Today Proc.* 56, 3016–3024. doi:10.1016/j.matpr.2021.11.423

Laghfiri, H., and Lamdouar, N. (2021). "The screening efficiency of open and infill trenches: a review," in International Conference on Advanced Technologies for Humanity, Rabat, Morocco, November, 2021, 346–351.

Li, Y., and Li, H. (2020). Bandgap merging and widening of elastic metamaterial with heterogeneous resonator. *J. Phys. D Appl. Phys.* 53 (47), 475302. doi:10.1088/1361-6463/abab2b

Limberger, F., Lindenfeld, M., Deckert, H., and Rümpker, G. (2021). Seismic radiation from wind turbines: observations and analytical modeling of frequency-dependent amplitude decays. *Solid earth.*, 12 (8), 1851–1864. doi:10.5194/se-12-1851-2021

Limberger, F., Rümpker, G., Lindenfeld, M., and Deckert, H. (2022). Development of a numerical modelling method to predict the seismic signals generated by wind farms. *Sci. Rep.* 12 (1), 15516. doi:10.1038/s41598-022-19799-w

Liu, Z., Zhang, X., Mao, Y., Zhu, Y. Y., Yang, Z., Chan, C. T., et al. (2000). Locally resonant sonic materials. *science* 289 (5485), 1734–1736. doi:10.1126/science.289.5485.1734

Lott, M., and Roux, P. (2019). Locally resonant metamaterials for plate waves: the respective role of compressional versus flexural resonances of a dense forest of vertical rods. *Fundam. Appl. Acoust. Metamaterials Seismic Radio Freq.* 1, 25–45.

Lott, M., Roux, P., Garambois, S., Guéguen, P., and Colombi, A. (2020a). Evidence of metamaterial physics at the geophysics scale: the METAFORET experiment. *Geophys. J. Int.* 220 (2), 1330–1339. doi:10.1093/gji/ggz528

Lott, M., Roux, P., Seydoux, L., Tallon, B., Pelat, A., Skipetrov, S., et al. (2020b). Localized modes on a metasurface through multiwave interactions. *Phys. Rev. Mater.* 4 (6), 065203. doi:10.1103/physrevmaterials.4.065203

Luco, J. E., and Contesse, L. (1973). Dynamic structure-soil-structure interaction. *Bull. Seismol. Soc. Am.* 63 (4), 1289–1303. doi:10.1785/bssa0630041289

Ma, G., Fu, C., Wang, G., Del Hougne, P., Christensen, J., Lai, Y., et al. (2016). Polarization bandgaps and fluid-like elasticity in fully solid elastic metamaterials. *Nat. Commun.* 7 (1), 13536–13538. doi:10.1038/ncomms13536

Marigo, J. J., Pham, K., Maurel, A., and Guenneau, S. (2020). Surface waves from flexural and compressional resonances of beams. https://arxiv.org/abs/2001.06304.

Mason, H. B., Trombetta, N. W., Chen, Z., Bray, J. D., Hutchinson, T. C., and Kutter, B. L. (2013). Seismic soil–foundation–structure interaction observed in geotechnical centrifuge experiments. *Soil Dyn. Earthq. Eng.* 48, 162–174. doi:10.1016/j.soildyn.2013.01.014

McNamara, D. E., and Buland, R. P. (2004). Ambient noise levels in the continental United States. *Bull. Seismol. Soc. Am.* 94 (4), 1517–1527. doi:10.1785/012003001

Miniaci, M., Krushynska, A., Bosia, F., and Pugno, N. M. (2016). Large scale mechanical metamaterials as seismic shields. *New J. Phys.* 18 (8), 083041. doi:10.1088/1367-2630/18/8/083041

Neuffer, T., Kremers, S., and Fritschen, R. (2019). Characterization of seismic signals induced by the operation of wind turbines in North Rhine-Westphalia (NRW), Germany. *J. Seismol.* 23, 1161–1177. doi:10.1007/s10950-019-09866-7

Nogoshi, M., and Igarashi, T. (1970). On the propagation characteristics of microtremor. *J. Seism. Soc. Jpn.* 23, 264–280. doi:10.4294/zisin1948.23.4_264

Nogoshi, M., and Igarashi, T. (1971). On the amplitude characteristics of microtremor (Part 2). *J. Seism. Soc. Jpn.* 24, 26–40. doi:10.4294/zisin1948.24.1_26

Ohori, M., Nobata, A., and Wakamatsu, K. (2002). A comparison of ESAC and FK methods of estimating phase velocity using arbitrarily shaped microtremor arrays. *Bull. Seismol. Soc. Am.* 92 (6), 2323–2332. doi:10.1785/0119980109

O'Neill, A., and Matsuoka, T. (2005). Dominant higher surface-wave modes and possible inversion pitfalls. *J. Environ. Eng. Geophys.* 10 (2), 185–201. doi:10.2113/jeeg10.2.185

Palermo, A., Krödel, S., Marzani, A., and Daraio, C. (2016). Engineered metabarrier as shield from seismic surface waves. *Sci. Rep.* 6 (1), 39356. doi:10.1038/srep39356

Palermo, A., and Marzani, A. (2018). Control of Love waves by resonant metasurfaces. *Sci. Rep.* 8 (1), 7234–7238. doi:10.1038/s41598-018-25503-8

Parolai, S., Picozzi, M., Richwalski, S. M., and Milkereit, C. (2005). Joint inversion of phase velocity dispersion and H/V ratio curves from seismic noise recordings using a genetic algorithm, considering higher modes. *Geophys. Res. Lett.* 32 (1). doi:10.1029/2004gl021115

Peterson, J. (1993). *Observations and modeling of seismic background noise*. Reston, VA, USA: USGS Technical Report, 1–95.

Pu, X., and Shi, Z. (2018). Surface-wave attenuation by periodic pile barriers in layered soils. *Constr. Build. Mater.* 180, 177–187. doi:10.1016/j.conbuildmat.2018.05.264

Pu, X., and Shi, Z. (2020). Broadband surface wave attenuation in periodic trench barriers. *J. Sound Vib.* 468, 115130. doi:10.1016/j.jsv.2019.115130

Qahtan, A. S., Huang, J., Amran, M., Qader, D. N., Fediuk, R., and Wael, A. D. (2022). Seismic composite metamaterial: a review. *J. Compos. Sci.* 6 (11), 348. doi:10.3390/jcs6110348

Roux, P. (2009). Passive seismic imaging with directive ambient noise: application to surface waves and the San Andreas Fault in Parkfield, CA. *Geophys. J. Int.* 179 (1), 367–373. doi:10.1111/j.1365-246x.2009.04282.x

Roux, P., Bindi, D., Boxberger, T., Colombi, A., Cotton, F., Douste-Bacque, I., et al. (2018). Toward seismic metamaterials: the METAFORET project. *Seismol. Res. Lett.* 89 (2A), 582–593. doi:10.1785/0220170196

Saccorotti, G., Piccinini, D., Cauchie, L., and Fiori, I. (2011). Seismic noise by wind farms: a case study from the Virgo Gravitational Wave Observatory, Italy. *Bull. Seismol. Soc. Am.* 101 (2), 568–578. doi:10.1785/0120100203

Schwan, L., Boutin, C., Padrón, L. A., Dietz, M. S., Bard, P. Y., and Taylor, C. (2016). Site-city interaction: theoretical, numerical and experimental crossed-analysis. *Geophys. J. Int.* 205 (2), 1006–1031. doi:10.1093/gji/ggw049

Seydoux, L., Shapiro, N. M., de Rosny, J., Brenguier, F., and Landès, M. (2016). Detecting seismic activity with a covariance matrix analysis of data recorded on seismic arrays. *Geophys. J. Int.* 204 (3), 1430–1442. doi:10.1093/gji/ggv531

Simovski, C. R. (2009). Material parameters of metamaterials (a review). *Opt. Spectrosc.* 107, 726–753. doi:10.1134/s0030400x09110101

Sorrells, G. G., McDonald, J. A., Der, Z. A., and Herrin, E. (1971). Earth motion caused by local atmospheric pressure changes. *Geophys. J. Int.* 26 (1-4), 83–98. doi:10.1111/j.1365-246x.1971.tb03384.x

Stackebrandt, W., and Manhenke, V. (2010). *Atlas zur Geologie von Brandenburg, Landesamt für Bergbau*. Cottbus, Germany: Geologie und Rohstoffe Brandenburg. (in German).

Stammler, K., and Ceranna, L. (2016). Influence of wind turbines on seismic records of the Gräfenberg array. *Seismol. Res. Lett.* 87 (5), 1075–1081. doi:10.1785/0220160049

Styles, P., Westwood, R. F., Toon, S. M., Buckingham, M. P., Marmo, B., and Carruthers, B. (2011). "Monitoring and mitigation of low frequency noise from wind turbines to protect comprehensive test ban seismic monitoring stations," in Fourth international Meeting on wind turbine noise, Rome, Italy, April, 2011, 1–13.

Thorson, J. R., and Claerbout, J. F. (1985). Velocity-stack and slant-stack stochastic inversion. *Geophysics* 50 (12), 2727–2741. doi:10.1190/1.1441893

Tian, Y., Chen, S., Liu, S., and Lu, X. (2023). Influence of tall buildings on city-scale seismic response analysis: a case study of Shanghai CBD. *Soil Dyn. Earthq. Eng.* 173, 108063. doi:10.1016/j.soildyn.2023.108063

Tokimatsu, K., Tamura, S., and Kojima, H. (1992). Effects of multiple modes on Rayleigh wave dispersion characteristics. *J. geotechnical Eng.* 118 (10), 1529–1543. doi:10.1061/(asce)0733-9410(1992)118:10(1529)

Tsogka, C., and Wirgin, A. (2003). Simulation of seismic response in an idealized city. *Soil Dyn. Earthq. Eng.* 23 (5), 391–402. doi:10.1016/s0267-7261(03)00017-4

Turpin, J. P., Bossard, J. A., Morgan, K. L., Werner, D. H., and Werner, P. L. (2014). Reconfigurable and tunable metamaterials: a review of the theory and applications. *Int. J. Antennas Propag.* 2014, 1–18. doi:10.1155/2014/429837

Ungureanu, B., Guenneau, S., Achaoui, Y., Diatta, A., Farhat, M., Hutridurga, H., et al. (2019). The influence of building interactions on seismic and elastic body waves. *EPJ Appl. Metamat.*, 6–18.

Vidale, J. E. (1986). Complex polarization analysis of particle motion. *Bull. Seismol. Soc. Am.* 76 (5), 1393–1405.

Weemstra, C., Snieder, R., and Boschi, L. (2015). On the estimation of attenuation from the ambient seismic field: inferences from distributions of isotropic point scatterers. *Geophys. J. Int.* 203 (2), 1054–1071. doi:10.1093/gji/ggv311

Wegener, M. (2013). Metamaterials beyond optics. *Science* 342 (6161), 939–940. doi:10.1126/science.1246545

Williams, E. G., Roux, P., Rupin, M., and Kuperman, W. A. (2015). Theory of multiresonant metamaterials for A0 lamb waves. *Phys. Rev. B* 91 (10), 104307. doi:10.1103/physrevb.91.104307

Wirgin, A., and Bard, P. Y. (1996). Effects of buildings on the duration and amplitude of ground motion in Mexico City. *Bull. Seismol. Soc. Am.* 86 (3), 914–920. doi:10.1785/bssa0860030914

Withers, M. M., Aster, R. C., Young, C. J., and Chael, E. P. (1996). High-frequency analysis of seismic background noise as a function of wind speed and shallow depth. *Bull. Seismol. Soc. Am.* 86 (5), 1507–1515. doi:10.1785/bssa0860051507

Wootton, P. T., Kaplunov, J., and Colquitt, D. J. (2019). An asymptotic hyperbolic–elliptic model for flexural-seismic metasurfaces. *Proc. R. Soc. A* 475 (2227), 20190079. doi:10.1098/rspa.2019.0079

Xiao, Y., Wen, J., and Wen, X. (2012). Flexural wave band gaps in locally resonant thin plates with periodically attached spring–mass resonators. *J. Phys. D Appl. Phys.* 45 (19), 195401. doi:10.1088/0022-3727/45/19/195401

Zieger, T., and Ritter, J. R. (2018). Influence of wind turbines on seismic stations in the Upper Rhine Graben, SW Germany. *J. Seismol.* 22, 105–122. doi:10.1007/s10950-017-9694-9

# Chapter 4

# Experimental evaluation of Soil-Structure Interaction

The description of the data obtained from the experiment and the preliminary results were published in Anna Maria Skłodowska, Chiara Amendola, Shoaib Ayjaz Mohammed, Srihari Sangaraju, Carla Barnaba, Dimitris Pitilakis, Philippe Roux, Alessio Compagno, Bojana Petrovic, Valentin Schindelholz, Stefano Maffione, Fabio Meneghini, David Zuliani, Stefano Parolai; EuroMASS Soil-Structure Interaction Experiment: A Semi-Dense Array for the Analysis of Wave Propagation from a Single-Degree-of-Freedom Structure to Its Surroundings. *Seismological Research Letters* 2024; https://doi.org/10.1785/0220240018

**Summary**

We study the dynamic coupling of a resonator with the ground, often termed as 'soil-structure interaction' in the engineering context. We perform a field experiment that attempts to characterize the response of a ground coupled 'single degree-of-freedom' isolated structure. We design and deploy a set of arrays that are specific to the different phases of the experiment. Both active and passive data are acquired. We only present here the preliminary results obtained from ambient noise data; however, conclusive SSI effects remain undemonstrated, prompting consideration for future studies with active data.

## 4.1 Background

In theory, in certain frequency regimes, the joint response of the soil-structure system can be different from (a) the 'free-field' response of the soil (neglecting the structure) and on the other hand, the (b) 'rigid-base' response of the structure (neglecting the soil). This collective dynamic behavior is classically termed the 'Soil-structure interaction' (SSI) phenomenon, and in the context of multiple resonators as 'Structure-soil-structure interaction' (SSSI) or in terms of the city scale as 'Site-city interaction' (SCI). For a compilation of observations, specific experiments, and numerical computations related to these phenomena in the context of urban seismology, see Guéguen et al. [2022] and the references therein.

### 4.1.1 Motivation for this study

In this thesis, we have seen that the resonator dynamics in each of the three cases of seismic metamaterials considered, whether it is a clamped pile or a tree or a wind turbine, can interact differently with the subsurface dynamics. It is well proven in the literature that the unusual scattering of the surface wavefield observed in locally-resonant metamaterials is driven by the mechanical coupling (impedance contrast) between the resonators and the substrate. Scattering inside locally resonant media is different from the multiple-scattering phenomenon that occurs at relatively shorter wavelengths. Resonant scattering inside a metasurface causes the wave to slow down, forcing it to additionally travel up and down the resonators. This kind of scattering by modifying the wave path depends on the effective impedance of the metasurface. If the wave is traveling through resonant media having impedance similar to that of the substrate, there is a decent coupling that leads to stronger attenuation by the metasurface. The perturbations of the wavefield in the case of the multiply scattered waves is higher when the impedance contrast between the soil and the heterogeneities is high. In contrast, in the scenario of resonant scattering, a lower impedance contrast leads to higher scattering around the resonance frequencies of the resonators.

Let us now examine the impedance contrast of the resonators and the substrate media in light of the previous experiments concerning elastic metamaterials. On a laboratory-scale, aluminum rods attached to the plate (Lott and Roux [2019a]), the same material was chosen for the plate and rods, which allowed efficient energy exchange. In the case of trees in a forest, Colombi et al. [2016c] used the same acoustic impedance for the longitudinal velocity in trees and the ground which resulted in a strong attenuation of the surface field inside the bandgap. However, they found the bandgaps to persist only if the impedance ratio between the trees and the ground was in the range of 0.5 to 2, and for any stronger impedance mismatch, the bandgaps gradually disappear thus limiting the energy trapped by the trees. Now, consider the wind turbine resonators from the previous chapter where heavy masses are associated with a strong impedance contrast at the soil-resonator interface. Assuming values $\rho_{soil} \approx 1800$ kg/m$^3$, $\rho_{concrete} \approx 7800$ kg/m$^3$, $V_{s,soil} \approx 500$ m/s, $V_{s,concrete} \approx 3200$ m/s results in an impedance contrast on the order of 30 (Pilz et al. [2024]). For strong impedance contrasts like this, the corresponding bandgap frequency ranges tend to become smaller due to a weak coupling between the ground and the resonators. For buildings, as in the case of wind turbines, the foundation is usually more rigid than the underlying soil. While studying SSI effects in the case of buildings, Petrovic et al. [2018] found that the proportion of the wave field observed to be radiated back from the building to the soil decreases as the impedance contrast increases. In a numerical study considering a cluster of buildings, Joshi and Narayan [2022] concluded that both the insulation capacity and the meta-capacity of a city increase with the decrease in impedance contrast between structures and the soil. Each of these studies emphasizes how crucial the coupling between the ground and resonators is for the metamaterial effect to manifest.

Given that the wind turbine tower in the META-WT experiment was itself not instrumented, it eliminates the possibility to analyze the SSI effects and the energy radiated back to the soil by the turbines alone. Nonetheless, using state-of-the-art numerical simulations, one could study such an effect. Our aim with this study is to

design a new experiment that can evaluate the coupling of a simple resonator to the surrounding soil in a relatively controlled environment. This is done by installing sensors not only on the ground, but also instrumenting the foundation and structure itself. This can potentially help us identify, reconstruct and characterize the surface wave field radiated from a vibrating structure, and estimate the amount of energy associated with it (Skłodowska et al. [2023]).

### Contribution to the collaborative study

This experiment is a collaborative effort within the framework of the WP3 work package of the URBASIS-EU project. A significant portion of the initial results comes from the analyses performed by colleagues from OGS Trieste and the AU Thessaloniki. The article associated with this chapter describes the various aspects of the deployment, array configurations, and the comprehensive first results of the EuroMASS SSI experiment. The attached version of the article is from two cycles of peer review. Our primary contributions to this study include:

- planning, design and implementation of various optimized seismic array configurations, and
- active participation in a seismic experimental campaign

Although only a preliminary analysis of passive data has been performed in this study, we anticipate interesting results from the analysis of active source signals, which are yet to be analyzed. Through this effort, we generated a quality data set in a controlled environment for future investigation of soil-structure interaction.

Data Mine

# EuroMASS Soil-Structure Interaction Experiment: A Semi-Dense Array for the Analysis of Wave Propagation from a Single-Degree-of-Freedom Structure to Its Surroundings

Anna Maria Skłodowska[*1,2], Chiara Amendola[3], Shoaib Ayjaz Mohammed[4], Srihari Sangaraju[5], Carla Barnaba[1], Dimitris Pitilakis[3], Philippe Roux[4], Alessio Compagno[1], Bojana Petrovic[1,6], Valentin Schindelholz[4], Stefano Maffione[1], Fabio Meneghini[1], David Zuliani[1], and Stefano Parolai[7]

## Abstract

**For years, soil-structure interaction (SSI) has been a subject of interdisciplinary studies, although full-scale SSI experiments and the use of real data are rare. To study SSI in a well-known and controlled environment, a full-scale experiment, EuroMASS, was conducted at the Piana di Toppo test site in Northeast Italy. For the needs of the experiment, a simple structure consisting of a lumped mass overtopping a steel column on a concrete base was designed and assembled at the test site. In April 2022, a three-component instrumentation network was installed to record the seismic noise, weak earthquake motions, and active source signals to study the structure, the foundation, and the soil seismic responses. The experiment was designed to collect data that can be used for accurate dynamic characterization of the structure and analysis of wave propagation in the soil-structure system.**

**Cite this article as** Skłodowska, A. M., C. Amendola, S. A. Mohammed, S. Sangaraju, C. Barnaba, D. Pitilakis, P. Roux, A. Compagno, B. Petrovic, V. Schindelholz, *et al.* (2024). EuroMASS Soil-Structure Interaction Experiment: A Semi-Dense Array for the Analysis of Wave Propagation from a Single-Degree-of-Freedom Structure to Its Surroundings, *Seismol. Res. Lett.* **XX**, 1–13, doi: 10.1785/0220240018.

## Introduction

The seismic excitation of structures exposed to earthquake shaking is a combination of effects related to (1) the earthquake source, (2) the travel path, (3) local site effects, and (4) soil-structure interaction (SSI; Stewart *et al.*, 1999). The first three compose the "free-field" ground motion. However, the seismic response of structures to free-field motion is affected by dynamic interaction with the underlying soil (e.g., Gazetas, 1983; Mylonakis and Gazetas, 2000; Todorovska, 2009; Kausel, 2010), also known as SSI. As a result of kinematic interaction, the actual base-slab motions deviate from free-field motions (Kausel, 2010). These deviations arise due to effects such as base-slab averaging, wave scattering, and embedment effects (Kramer, 1996).

When the foundation supporting soil is compliant, flexural, axial, and shear deformations of structural foundation elements occur as a result of the inertial response and displacements applied by the superstructure and the soil medium (National Institute of Standards and Technology [NIST], 2012). Because of inertial interaction, the fundamental frequency of the soil-structure system decreases. Furthermore, additional energy is dissipated by downward wave radiation from the structure, on top of the soil hysteretic behavior (Richart *et al.*, 1970). In the case of structures founded on stiff soil, the decrease in the resonant frequency might be related to changes in the dynamic

1. National Institute of Oceanography and Applied Geophysics, OGS, Sgonico, Italy, https://orcid.org/0000-0002-4931-8664 (AMS); https://orcid.org/0000-0003-3863-8969 (CB); https://orcid.org/0000-0002-8390-6259 (AC); https://orcid.org/0000-0003-3985-2959 (BP); https://orcid.org/0000-0002-9269-3259 (SM); https://orcid.org/0000-0002-4752-2928 (FM); https://orcid.org/0000-0002-8359-040X (DZ); 2. Now at Federal Institute for Materials Research and Testing, Bundesanstalt für Materialforschung und -prüfung (BAM), Berlin, Germany; 3. Department of Civil Engineering, Aristotle University of Thessaloniki, Thessaloniki, Greece, https://orcid.org/0000-0001-8149-6391 (CA); https://orcid.org/0000-0001-7363-3667 (DP); 4. ISTerre, Université Grenoble Alpes, Grenoble, France, https://orcid.org/0000-0003-4353-2173 (SAM); https://orcid.org/0000-0002-5639-8869 (PR); https://orcid.org/0009-0000-1111-2751 (VS); 5. Department of Civil and Environmental Engineering, Politecnico di Milano, Milan, Italy, https://orcid.org/0000-0001-6232-8288 (SS); 6. Now at Helmholtz Centre Potsdam, GFZ German Research Centre for Geosciences, Potsdam, Germany; 7. Department of Mathematics and Geosciences, University of Trieste, Trieste, Italy, https://orcid.org/0000-0002-9084-7488 (SP)

*Corresponding author: anna.maria.sklodowska@gmail.com

behavior of the structure and not necessarily to SSI effects (e.g., Astorga *et al.*, 2018; Skłodowska *et al.*, 2021).

The influence of SSI on the dynamic behavior of existing structures has been identified from the analysis of their response to seismic noise (Luco *et al.*, 1988; Luco and de Barros, 2005; Pitilakis *et al.*, 2018) and weak-to-strong earthquakes (Gueguen and Bard, 2005; Brunelli *et al.*, 2021). Nevertheless, the analysis of existing buildings prone to SSI phenomena can be a challenging task. The introduction of properties for the definition of complete models is often problematic because the geometry of foundations is usually unknown and properties of the underlying soil are, on average, not fully documented.

In this context, field experiments can provide valuable insights because they may help in the development of improved models and design guidelines for seismic-resistant structures. Previously published onsite investigations provide results over a limited frequency range (e.g., Tileylioglu *et al.*, 2011; Amendola *et al.*, 2021) or for specific structures, such as a nuclear reactor (Luco and de Barros, 2005). In all cases, (1) the limited resolution of the data acquisition system introduced significant noise, leading to spurious results and (2) the shear-wave velocity profile was measured in the so-called "free-field" conditions, neglecting the stress increment exerted by the structural weight. Therefore, it is difficult to identify the most suitable experimental layout for SSI problems and the dynamic structure–foundation–soil system from recorded data.

SSI describes not only the influence of the soil on the response of the structure but also, as many studies have shown, the effect that the buildings have on the response of the soil (e.g., Jennings, 1970; Wirgin and Bard, 1996; Cardenas *et al.*, 2000; Chávez-García and Cárdenas-Soto, 2002; Guéguen *et al.*, 2002; Petrovic and Parolai, 2016; Petrovic *et al.*, 2018; Chandra and Guéguen, 2019; Skłodowska *et al.*, 2023). Based on the example of the destructive effects of the 1985 Michoacan earthquake on Mexico City, Wirgin and Bard (1996) showed that in densely urbanized areas, the so-called "free-field" strong-motion recordings include the possible effects of the nearby located buildings. The significance of the contamination of the "free-field" motion by the wavefield radiated from a vibrating structure into the ground was also underlined by Gueguen and Bard (2005) and recently by Petrovic and Parolai (2016) and Skłodowska *et al.* (2023).

In this framework, full-scale field tests were conducted in April 2022 at the instrumented facility of Piana di Toppo (PITOP, latitude 46.20°, longitude 12.82°) in Northeast Italy. The experimental campaign included seismic noise measurements and active source tests throughout wide frequency and amplitude ranges. In addition, due to the long acquisition time, several weak earthquakes were recorded. A dense three-component instrumentation network was arranged to record the structure, foundation, and soil responses. The main objective of the tests was to study the SSI phenomenon on both the dynamic behavior of a simple structure and its surroundings, in a well-known and controlled environment. The experiment was coordinated by the National Institute of Oceanography and Applied Geophysics (OGS, Italy) in collaboration with Aristotle University of Thessaloniki (Greece), the Institute of Earth Sciences (ISTerre) of Université Grenoble Alpes (France), and Politecnico di Milano (Italy) as a part of the URBASIS-EU ITN project (see Data and Resources).

TABLE 1
**Average Shear-Wave Velocities of the Soil Layers at the Piana di Toppo Test Site (Dreossi and Parolai, 2022)**

| Layer Number | Depth (m) | *S*-Wave Velocity (m/s) |
|---|---|---|
| 1 | 0–11.1 | 551.4 |
| 2 | 11.1–33.2 | 741.6 |
| 3 | Below 33.2 | 1011.8 |

## Instrument Deployment and Details

### Test site description

The Piana di Toppo test site is located in the Friuli Venezia Giulia region of northeastern Italy, about 70 km from Udine in the intermountain plain on the external thrust belt of the eastern Southern Alps (Fig. 1a). The test site is 80 m long and 50 m wide (Fig. 1b), located in a seismically active area (Slejko *et al.*, 1999) with relatively low levels of seismic noise originating from the urban environment. To the south of the test site is a railway line on which a train runs during the summer (not in operation during this experiment). About 100 m north of the test site runs a provincial road (SP32). Otherwise, the test site is far from any other infrastructure.

The geology of the test site consists of Quaternary alluvial sediments (loose coarse gravels) overlying Miocene conglomerates (the Morello formation; Poletto *et al.*, 2011; Dreossi and Parolai, 2022). The *S*-wave velocity profile for the Piana di Toppo test site was calculated from seismic noise data using a modified version of the extended spatial autocorrelation approach by Dreossi and Parolai (2022) and is presented in Table 1.

### Design of the structure

The EuroMASS prototype structure was specifically designed for full-scale tests for the assessment of SSI effects. The structure consists of a square concrete shallow foundation (2 m × 2 m × 0.3 m) with a quadratic hollow steel column (QHS profiles 250 mm × 250 mm × 10 mm) overtopped by a similar concrete slab (2 m × 2 m × 0.5 m, Fig. 2). It was constructed in the northwestern part of the test site (Fig. 1b). The total height of the structure was 2.5 m and the width was 2 m × 2 m. The symmetry ensures the same bending stiffness in both plane directions. The higher mass

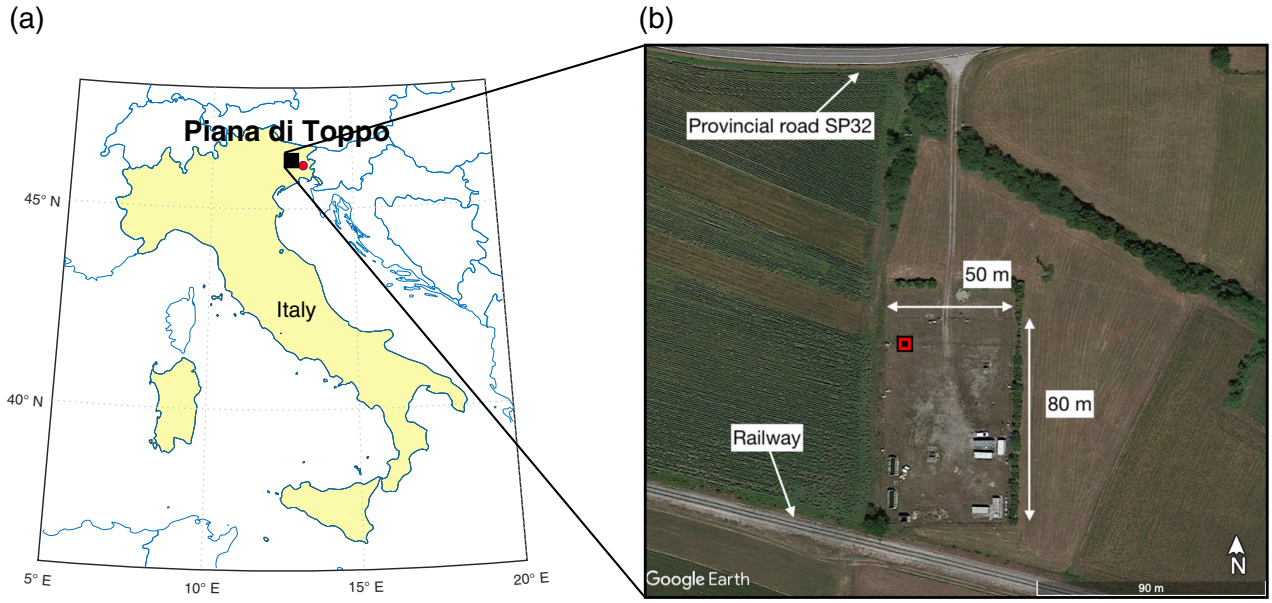


**Figure 1.** (a) Map of Italy with the location of the Piana di Toppo test site indicated with the black square. Udine, around 70 km from the test site, is indicated with a red circle. (b) Satellite view zoom on the Piana di Toppo test site. The location of the center of the assembled EuroMASS structure is marked with a red square. The color version of this figure is available only in the electronic edition.

of the top slab (~5 tonne) with respect to the bottom (~3 tonne) shifts the center of gravity of the system closer to the top, making the structural configuration similar to an single-degree-of-freedom system. The fixed-base fundamental frequency of 5.0 Hz was estimated using SAP2000 software (see Data and Resources, Fig. 2b). In the numerical model, the column was modeled as an elastic beam element with a QHS steel section ($\gamma_S = 78$ kN/m$^3$) characterized by Young's modulus equal to $2.10 \times 10^8$ kN/m$^2$. The foundation and top slabs were modeled as shell elements made of concrete material ($\gamma_C = 25$ kN/m$^3$). In the model, the column was fully fixed to the slabs using linear link element constraints. The constructed structure with a part of the installed instruments is presented in Figure 2c.

## Instrumentation and experimental setups

**Instrumentation.** During the experiment, seismic data were recorded by 15 three-component Lennartz sensors connected to 12 RefTek130 digitizers (nine with three channels and three with six channels, Table 2, Fig. 3a). There were nine LE-3D/1s (Fig. 3b) connected to three-channel digitizers and three LE-3D/1s and LE-3D/5s Lennartz sensors pairs connected to the three digitizers with six channels. Global Positioning System (GPS) antennas were used for the time synchronization of the instruments. The digitizers' power supply was provided by external batteries, which were replaced every few days. The sampling frequency of the digitizers was set to 250 Hz. An example of the components of the instrumentation installed at the test site is presented in Figure 3c.

All the sensors, installed both in the field and on the EuroMASS structure, were aligned with the primary axes of the assembled structure, which is approximately true north (rotated about 5° toward the east). For the field sensors, a shallow hole was dug in the ground, the bottom was leveled with sand, and the sensor was then covered with soil. This was done to ensure good coupling of sensors with the ground, to decrease the negative impact of adverse weather conditions on the recordings, and to avoid potential damage to the instruments.

The sensors installed on the structure were leveled and aligned with the main axes of the structure. Because all the digitizers were placed on the ground, the cables were secured to the concrete slab to prevent the sensors installed on the top of the structure from being displaced by the movement of the cables (e.g., caused by wind). After installation of the sensors, digitizers along with the batteries were placed on the styrofoam and covered with the boxes. To ensure proper time synchronization of the recordings, the GPS antennas were placed on top of the secured digitizers.

Hereafter, the digitizer–sensor combinations will be referred to as "stations." The 1s Lennartz sensors (LE-3D/1s) will be identified by the subscript "E" (corresponding to the digitizer channels used to connect those sensors—e.g., 921D$_E$ or 931D_E) and 5s Lennartz sensors (LE-3D/5s) will be identified by the subscript "H" next to the station ID (e.g., 931C$_H$ or 931C_H).

**Experimental setups.** During the Piana di Toppo experiment, the 15 instruments were used in the following three different spatial configurations:

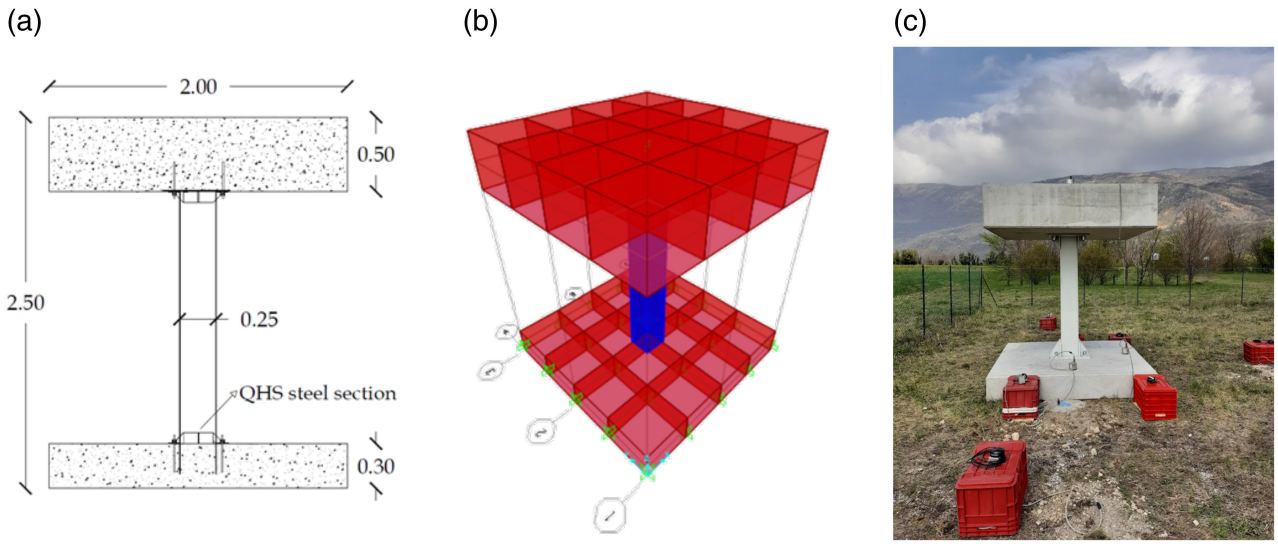


**Figure 2.** (a) Schematic drawing of the designed structure (dimensions in meters), QHS, quadratic hollow steel column, (b) 3D numerical model of the structure from SAP2000, and (c) assembled EuroMASS structure with a part of the installed instrumentation located in the northwest part of the Piana di Toppo test site. The color version of this figure is available only in the electronic edition.

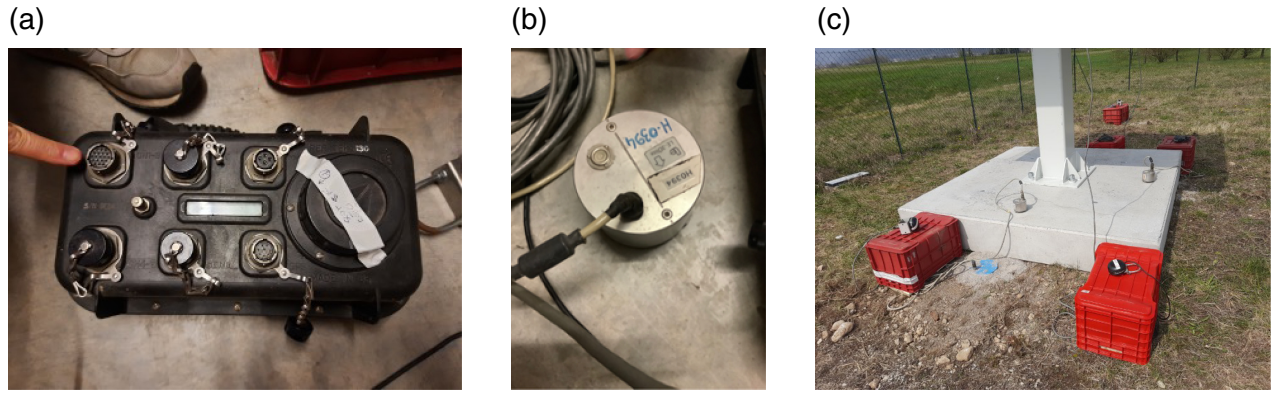


**Figure 3.** (a) RefTek130 digitizer used in the study, (b) 1s Lennartz sensor LE-3D/1s, and (c) installed instrumentation at the test site. The color version of this figure is available only in the electronic edition.

- setup 1 (S1): Before installation of the structure, only on the field (Fig. 4a);
- setup 2 (S2): After installation of the structure, with a dense sensor array on the top and bottom slabs (Fig. 4b); and
- setup 3 (S3): After installation of the structure, with sensors installed both on the top and bottom slabs of the structure and on the field (Fig. 4c).

In the first setup S1, all available sensors were installed on the field in two perpendicular linear arrays aligned with the north–south and east–west axes of the future structure (Fig. 4a). The two arms of the L-shape array had an interstation spacing that loosely followed the Fibonacci sequence with the sensor spacing increasing away from the structure. Such an array shape was chosen because it provides the best data analysis quality in L-shape arrays for an additional passive-seismic study (Napa Seismic, 2023). In this setup, 5s sensors were installed right next to the 1s sensors connected to the same digitizer to have a direct comparison of the recordings from two different sensor types. Approximately 20 hr of seismic noise was recorded in this setup.

For the installation of the EuroMASS structure, all the sensors were removed from their positions to avoid potential damage from the heavy construction machinery that was used for

TABLE 2
**List of Acquisition Systems Deployed for the Piana di Toppo Experiment**

| Acquisition Station Name | Sensor | Channel | Location Setup 1 | Setup 2 | Setup 3 |
|---|---|---|---|---|---|
| 921B | LE-3Dlite 1s | EHE, EHN, EHZ | Field | Bottom slab | Bottom slab |
| 962F | LE-3Dlite 1s | EHE, EHN, EHZ | Field | Top slab | Field |
| 921E | LE-3Dlite 1s | EHE, EHN, EHZ | Field | Bottom slab | Field |
| | LE-3Dlite 5s | HHE, HHN, HHZ | Field | Bottom slab | Field |
| A928 | LE-3Dlite 1s | EHE, EHN, EHZ | Field | Top slab | Field |
| 9EAA | LE-3Dlite 1s | EHE, EHN, EHZ | Field | Top slab | Field |
| 921A | LE-3Dlite 1s | EHE, EHN, EHZ | Field | Bottom slab | Field |
| | LE-3Dlite 5s | HHE, HHN, HHZ | Field | Bottom slab | Field |
| A894 | LE-3Dlite 1s | EHE, EHN, EHZ | Field | Top slab | Field |
| 921C | LE-3Dlite 1s | EHE, EHN, EHZ | Field | Top slab | Top slab |
| 931D | LE-3Dlite 1s | EHE, EHN, EHZ | Field | Top slab | Field |
| 931C | LE-3Dlite 1s | EHE, EHN, EHZ | Field | Bottom slab | Bottom slab |
| | LE-3Dlite 5s | HHE, HHN, HHZ | Field | Field | Field |
| 921D | LE-3Dlite 1s | EHE, EHN, EHZ | Field | Top slab | Top slab |
| 9EDA | LE-3Dlite 1s | EHE, EHN, EHZ | Field | Field | Field |

the structure assembly. After the structure was assembled, in setup S2 (Fig. 4b), most of the sensors were installed on the top and bottom slabs of the assembled structure. On the top slab of the structure, a total of seven sensors were installed in four corners and on three sides, to enable the use of the active source (seismic vibrator) in the middle of the slab. Such placement of the active source was chosen due to the relatively small available area on the top slab for such a type of excitation (2 m × 2 m). On the bottom slab, there were six sensors in total: one in each corner of the foundation and two on the sides facing the north–south and east–west legs of the field array. Two remaining sensors were installed on the soil to the south of the structure: one right next to the bottom slab (the 5s $931C_H$) and the second 2 m away (9EDA). This setup was installed for approximately 19 hr.

In the last setup S3, all but four of the sensors were installed in the field (Fig. 4c). Of the four sensors on the structure, two each were installed on the top and bottom slabs. At the top slab, sensor 912C was left in its original position from setup S2 (on the south edge), and sensor 921D was moved from the corner of the slab to the east edge to be aligned in the east–west field array. The two sensors installed on the foundation slab were located on the south and east sides of the slab. The sensors installed on the structure were positioned to be aligned with the field arrays. The field sensors were placed in the L-shape array in similar positions as in setup S1. This setup was installed until the end of the experiment, for around 20 days.

The setup layouts were chosen to enable a comparison of the dynamic characteristics obtained from the recordings collected before and after the installation of the structure, to assess possible changes in the soil-structure system. Therefore, in the S3 setup, the location of the field instruments was the same as before and after the installation of the structure.

## Overall Quality

During the Piana di Toppo experiment, seismic data were recorded from 6 April to the end of 27 April 2022. All the data with the poles and zeros files for instrument response removal are available in MiniSEED format (see Data and Resources). Data continuity is described in Figure 5 for the east component of all stations used during the experiment. The recordings of the north–south and vertical components are of the same duration as the presented east–west component. From 6 April to the end of 14 April, the continuity of the recordings is very good for almost all of the sensors. Because of battery limitations, there are no recordings from 15 to 16 April for all the sensors.

Because of the malfunction of the GPS antenna, the recordings of the 9EDA station are not synchronized with the other instrumentation and therefore not shown in the following figures. In addition, the vertical component of sensor A928 in setup S1 did not record properly. However, in setups S2 and S3, the sensor started to function and record seismic data properly again.

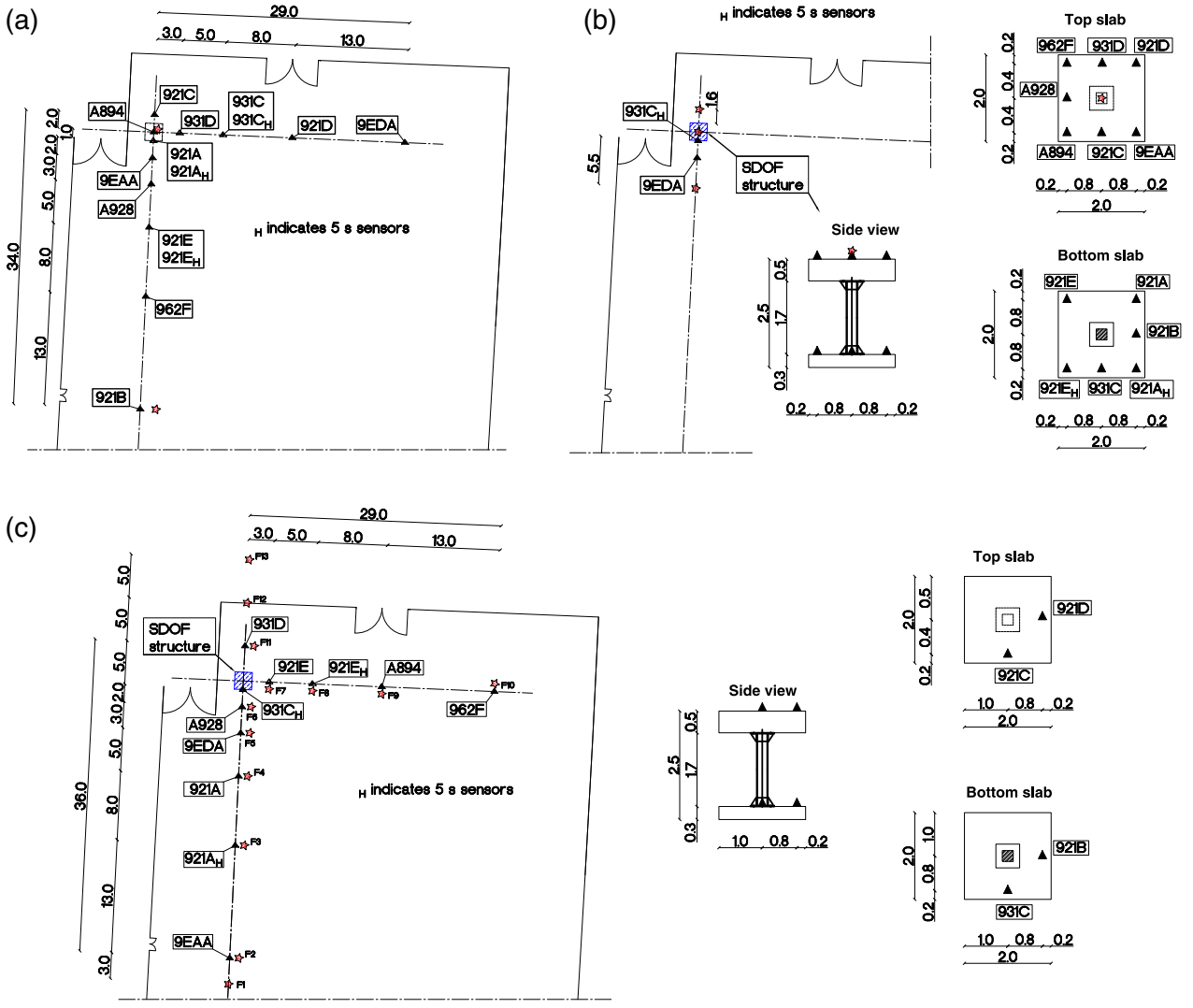


**Figure 4.** (a) Setup S1, (b) setup S2, and (c) setup S3. Triangles represent sensors, red stars indicate active source locations, and the blue square is the location of the structure. H next to the sensor name indicates 5s Lennartz sensors. No subscript next to the sensor name indicates 1s Lennartz sensors. (c) Numbers from F1 to F13 next to the red stars refer to the active source position. Dimensions are in meters. The color version of this figure is available only in the electronic edition.

## Seismic noise

During the Piana di Toppo experiment, seismic noise was recorded on 23 consecutive days using the three described setups.

An example of the unfiltered seismic noise recordings of 10-minute-long time windows for all sensors for all three instrumental setups is presented in Figure 6. The mean, trend, and instrumental response are removed from the presented data.

The initial evaluation of the seismic noise recordings shows that, as expected, the signals recorded at the top of the structure were amplified compared with the motion recorded at the foundation slab and on the ground due to the vibration of the structure.

## Active source

In addition to the seismic noise recordings, active source measurements were performed using an Elvis VII-type seismic vibrator source (see Data and Resources). To maximize coupling, ensure stability, and prevent the vibrator from moving or vibrating inconsistently during the test, we loaded weight on the shaker (an operator sitting on the robust suitcase on the upper part of the device). The vibrator generated a *P*-wave upsweep of 30 s with a theoretical frequency range from 10 to 200 Hz and force amplitude equal to 1 kN. Three to four sweeps for each source position were made (red stars in Fig. 4).

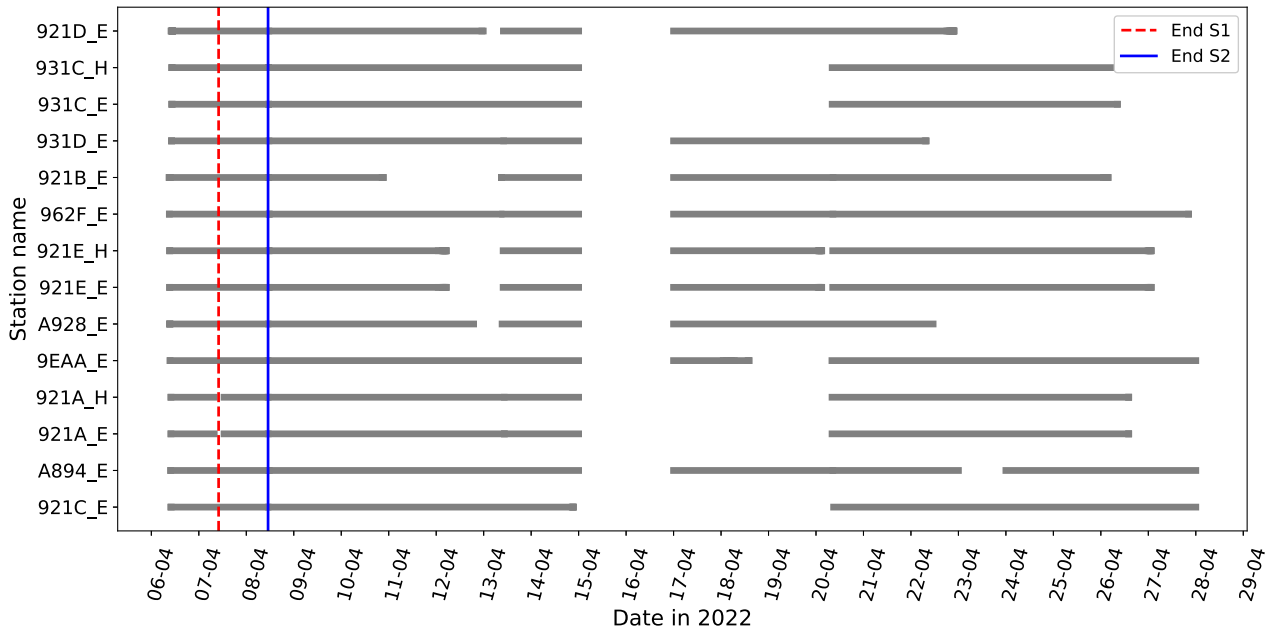


**Figure 5.** Data availability of Piana di Toppo experiment. Data were recorded between 6 and 28 April 2022 in three different instrument setups. The vertical lines indicate the change in the instrumental setups: a dashed red line, from setup S1 to S2; a solid blue line, from setup S2 to S3. The time axis corresponds to the dates in April 2022. Station names with the tag "_E" indicate 1s sensors and "_H" denotes 5s sensors. The color version of this figure is available only in the electronic edition.

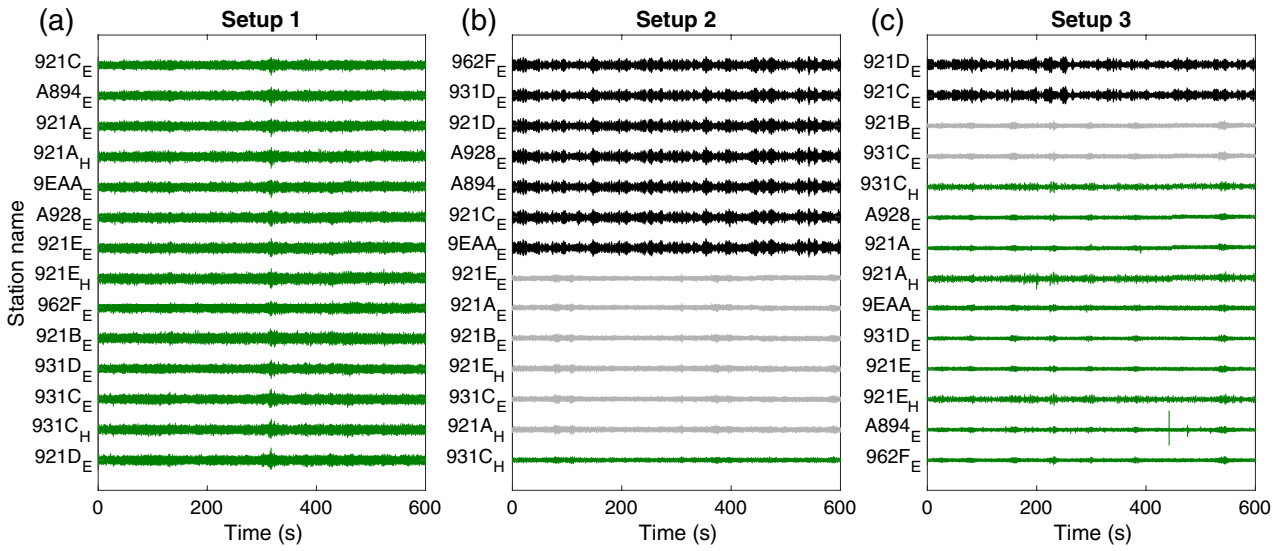


**Figure 6.** The 10 min-long east–west-component seismic noise data examples from (a) setup S1, (b) setup S2, and (c) setup S3. Green traces, on the field; black traces, on the top slab of the structure; and gray traces, on the bottom slab of the structure. Subscript "E" refers to 1s sensors and "H" refers to 5s sensors. Because of the lack of recording synchronization, data from sensor 9EDA are not shown. The scale on each plot is normalized with the maximum amplitude recorded in each setup. The color version of this figure is available only in the electronic edition.

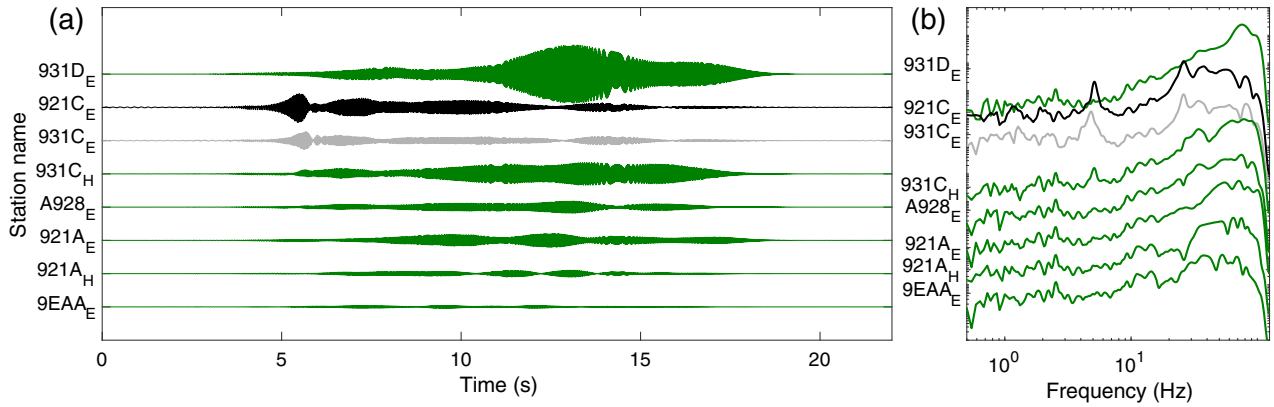


**Figure 7.** (a) Example of the vertical-component recordings of the active source in the north–south instrument's lines from setup S3. The source was located 13 m north of the structure (F13 in Fig. 4c). The black lines show the recordings of sensors installed on the top slab of the structure and gray lines represent the recordings of sensors located at the bottom slab. Green lines represent sensors installed on the field. (b) Corresponding Fourier amplitude spectra smoothed with the Konno–Ohmachi smoothing function (Konno and Ohmachi, 1998). Subscript "E" refers to 1s sensors and "H" refers to 5s sensors. The color version of this figure is available only in the electronic edition.

In setup S1, the vibrator was placed in two positions: (1) next to the 921B station in the north–south line of the array and (2) next to the A894 station installed in the center of the planned location of the structure. In setup S2, three active source positions were considered: one directly on the top of the structure in the center of the slab and two on the ground—one 5.5 m and another 1.6 m from the southern and the northern edge of the foundation, respectively. In setup S3, 13 vibrator positions (F1–F13), all on the ground, were used (Fig. 4). The vibrator was placed next to each of the field sensors, apart from the one next to the bottom slab—931C$_H$ (shots F2–F11) and in three additional locations in the north–south line of the sensors (shots F1, F12, and F13).

An example of recordings of one sweep source (F13) recorded by sensors from the north–south array line of setup S3 and the corresponding Fourier amplitude spectra smoothed with Konno–Ohmachi smoothing function (smoothing coefficient $b$ = 80, Konno and Ohmachi, 1998) is shown in Figure 7 for the vertical component. The data are filtered with a high-pass filter at 1 Hz and the mean, trend, and instrument response are removed from the presented data.

# Initial Observations

## Dynamic characterization of the soil

To estimate the fundamental frequency of the soil in the location of the future structure, we performed horizontal-to-vertical spectral ratio (HVSR, e.g., Nakamura, 1989). We used 2 hr (0:00 a.m. to 2:00 a.m. on 7 April 2022) of seismic noise recordings from sensor A894 from setup S1, located in the center of the future EuroMASS structure (Fig. 4). The analysis was performed using the HVSR Python package by Vantassel (2021). The data were filtered between 0.5 and 30 Hz and divided into 60 s long windows. The obtained HVSR curve is presented in Figure 8.

From the obtained HVSR curve in the location of the EuroMASS structure, the resonance frequency of the soil corresponding to the highest peak is estimated at around 10 Hz. Some additional peaks are also visible at around 2.1, 2.9, and 6.4 Hz.

## Dynamic behavior of the structure

Figure 9 shows the average Fourier amplitude spectra of 1 hr of seismic noise (unfiltered) recorded by all the stations in setup S1 (Fig. 9a), setup S2 (Fig. 9b), and setup S3 (Fig. 9c). The peaks in the Fourier amplitude spectra of all seismic noise recordings are between 1 and 30 Hz.

The spectra of the recordings of the sensors from the three setups show peaks related either only to the soil (setup S1) or to both (setups S2 and S3). The presence of peaks at 1.6, 2.3, 2.6,

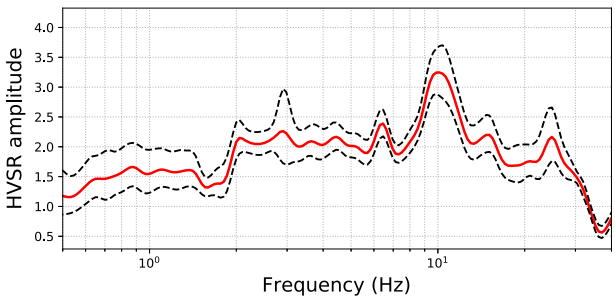


**Figure 8.** Horizontal-to-vertical spectral ratio (HVSR) of the 2 hr (0:00 a.m. to 2:00 a.m., 7 April 2022) of seismic noise recordings from sensor A894 in setup S1. The thick red line indicates the HVSR curve, and the dashed black lines are ± 1 standard deviation. The color version of this figure is available only in the electronic edition.

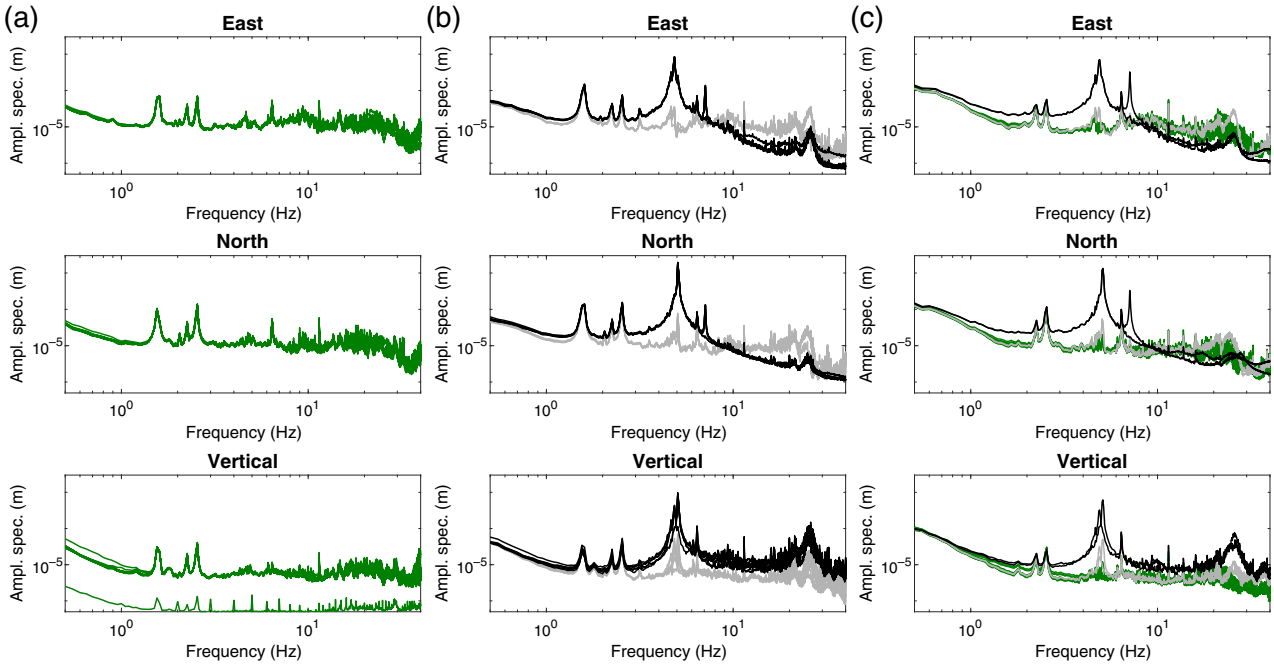


**Figure 9.** Fourier amplitude spectra of all sensors installed in (a) setup S1 (before installation of the EuroMASS structure), (b) setup S2 (most of the sensors installed on the structure), and (c) setup S3 (sensors both on the structure and the field). Green lines correspond to the sensors installed on the ground, gray lines correspond to those installed on the bottom slab of the EuroMASS structure, and black lines correspond to those installed on the top of the structure. The color version of this figure is available only in the electronic edition.

and 6.4 Hz in setup S1 (i.e., before the installation of the structure) implies that they are unrelated to the dynamic behavior of the structure, even though they are also visible in the spectra of the sensors installed on the slabs.

The spectra of the recordings collected by sensors installed in setup S2 (Fig. 9b) show clear dominant peaks, around 4.9 Hz for the east–west component and 5.1 Hz for the north–south component, related to the structure. The peaks are visible both in the spectra of the recordings of the sensors installed on the top slab of the structure (black lines) and, with lower amplitudes, in those related to the recordings of the sensors installed on the foundation slab (gray lines). The spectra of the vertical component of motion show a double peak at 4.9 and 5.1 Hz.

The spectra of the recordings collected by the stations installed on the structure in setup S3 (Fig. 9c) show clear peaks at the same frequencies as those identified using setup S2, that is, 4.9 Hz for the east–west component, 5.1 Hz for the north–south component, and a double peak at 4.9 and 5.1 Hz for the vertical component. The peaks at 4.9 and 5.1 Hz are related to the bending modes in the east–west and north–south directions, respectively. The peak at 7.1 Hz, which is present in all spectra of the horizontal components of sensors installed on the top of the structure, is most likely related to the torsional mode of the structure.

The numerical model of the EuroMASS structure designed for the Piana di Toppo experiment showed the existence of three modes: two bending modes in two orthogonal directions at 5.0 Hz and a torsional mode at 5.9 Hz. The frequencies observed in the Fourier amplitude spectra are in good agreement for the two bending modes with the modes obtained from the numerical model. However, the difference between the numerical model and recorded data is observed for the third torsional mode.

In both setups, S2 and S3, the amplitudes of the spectral peaks are around 20–30 times bigger in the recordings of the sensors installed on the top slab with respect to those collected by the sensors installed on the foundation slab.

## Earthquake recordings

Because the stations installed in the setup S3 configuration were used for recording seismic signals for almost three weeks, weak motions from moderate-magnitude regional events and small-magnitude local events were also recorded during the acquisition time. Figure 10 shows an example of the time history of velocity (filtered using a band-pass Butterworth filter between 0.1 and 35 Hz) and the corresponding Fourier amplitude spectra of the east–west component of the $M_w$ 5.5 earthquake that occurred on 22 April at

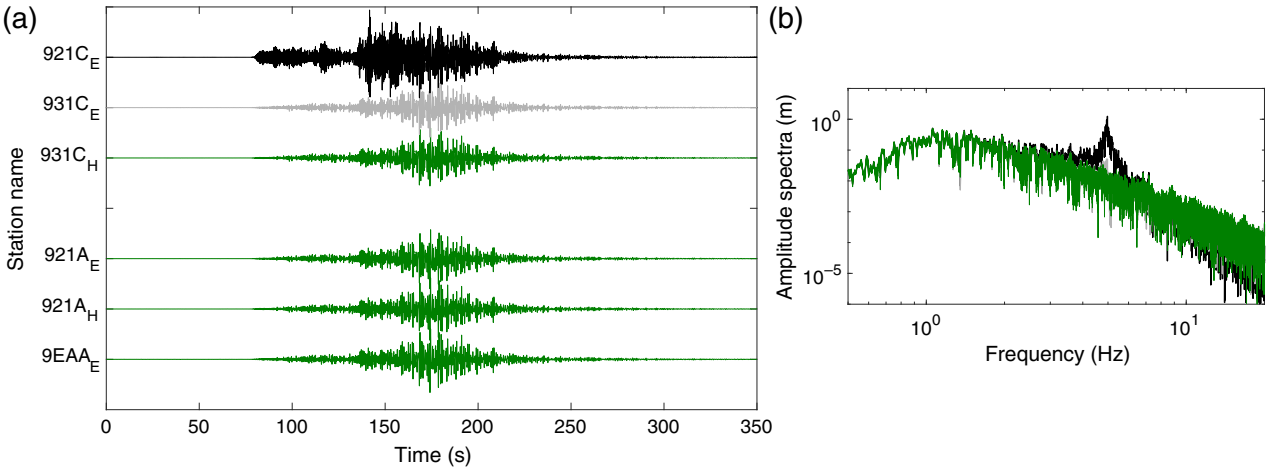


**Figure 10.** (a) An example of the time history of the east–west component recordings of the $M_w$ 5.5 earthquake occurred on 22 April at 21:07:49.1 (UTC) near Stolac in Bosnia and Herzegovina (~550 km from the test site), registered by the north–south line from setup S3. The black trace depicts the time series registered by the sensor installed on the top slab of the structure, the gray trace registered by a sensor at the bottom slab, and the green trace collected by the sensors installed on the field. (b) Corresponding Fourier amplitude spectra. The color version of this figure is available only in the electronic edition.

21:07:49.1 (UTC) near Stolac in Bosnia and Herzegovina (~550 km from the test site) recorded by the north–south line of the array. The mean, trend, and instrument response are removed from the presented data.

Similar to the seismic noise recordings, the amplitudes of the signal recorded by the sensor installed on the top slab of the structure are larger with respect to those of the recordings collected by the sensors located on the bottom slab and the surroundings (Fig. 10a).

The fundamental mode peak at 5 Hz can be seen in the spectra of the recorded shaking of the sensors installed at the top (black lines) and the bottom (gray lines) of the structure (Fig. 10b).

From the previous results and the comparison of the amplification functions, which were calculated as the spectral ratio between the top structure and the free-field motion and the top of the structure and the foundation (Appendix), it can be seen that the predominant frequency slightly decreases, confirming the effects of SSI.

## Summary

The EuroMASS structure was designed to study complex SSI phenomena in a controlled well-understood environment. The first results show that the peaks in the Fourier amplitude spectra correspond to the first three modes—the two bending modes in the two orthogonal directions of the structure and the torsional one. In addition, the analysis of the dynamic behavior of the structure from the recorded data is in agreement with the numerical model, especially for the two first bending modes. Because the EuroMASS structure is symmetric, the vibration frequencies of the first two bending modes are very close for both the east and north components. However, the differences between the numerical model and the observed data are most likely because the stiffness of the structure is in reality slightly unequally distributed in the two orthogonal directions.

Even though we notice a small disparity between the resonant frequencies of the numerical model and the EuroMASS structure, the model is a good representation of the assembled structure and can be used for supportive analyses. In addition, the different instrumental setups during the experiment, the sufficiently long recording time, and the availability of the numerical model make the experimental data ideal for studying in detail the dynamic behavior of the built structure.

The key outcome of the performed tests was the identification of the most suitable experimental layout for the experimental characterization of the dynamic response of similar prototypes and, more generally, existing buildings.

## Data and Resources

The raw velocity data collected during the experiment, separated for each day of the recording, along with the detailed description are available at https://opendata.ogs.it/SSI_EuroMASS_April2022/ and doi: 10.13120/zzeg-j721. The EuroMASS structure is available for further experiments at the Oceanography and Applied Geophysics (OGS) test site Piana di Toppo (https://www.ogs.it/en). The URBASIS-EU ITN project is available at https://urbasis-eu.osug.fr. The SAP2000 software is available at www.csiamerica.com/products/sap2000. The Elvis VII seismic vibrator information is available at GEOSYM website (https://www.geosym.de/en/systems/). All websites were last accessed in December 2023. The supplementary files include (1) technical drawings of the three setups with the indicated location of the sensors, (2) coordinates of the sensors, (3) poles and zeros (PAZ) files for instrument response removal, and (4) information about the active source used during the experiment.

## Declaration of Competing Interests

The authors acknowledge that there are no conflicts of interest recorded.

## Acknowledgments

The authors would like to thank Elvio del Negro for his great help with the organization and logistics of the experiment. A. M. S., C. A., S. A. M., and S. S. have received funding from the ITN-Marie Sklodowska-Curie project "New challenges for Urban Engineering Seismology (URBASIS-EU)" (GA 813137). B. P. was supported by a research fellowship from the German Research Foundation (Deutsche Forschungsgemeinschaft, DFG, PE 2891/1-1, Projektnummer 428372009). ISTerre is a part of Labex OSUG@2020. Finally, the authors would like to thank Jonathan Ford for kindly proofreading the article before submission.

## References

Amendola, C., F. De Silva, A. Vratsikidis, D. Pitilakis, A. Anastasiadis, and F. Silvestri (2021). Foundation impedance functions from full-scale soil-structure interaction tests, *Soil Dynam. Earthq. Eng.* **141,** 106523.

Astorga, A., P. Guéguen, and T. Kashima (2018). Nonlinear elasticity observed in buildings during a long sequence of earthquakes, *Bull. Seismol. Soc. Am.* **108,** no. 3, 1185–1198.

Brunelli, A., F. De Silva, A. Piro, F. Parisi, S. Sica, F. Silvestri, and S. Cattari (2021). Numerical simulation of the seismic response and soil-structure interaction for a monitored masonry school building damaged by the 2016 central Italy earthquake, *Bull. Earthq. Eng.* **19,** no. 2, 1181–1211.

Cardenas, M., P.-Y. Bard, P. Guéguen, and F. J. Chavez-Garcia (2000). Soil-structure interaction in Mexico city. Wave field radiated away from Jalapa building: Data and modelling, *Proc. of the 12th World Conf. on Earthquake Engineering, 12 WCEE 2000*, Auckland, New Zealand, Paper No. 385.

Chandra, J., and P. Guéguen (2019). Nonlinear response of soil–structure systems using dynamic centrifuge experiments, *J. Earthq. Eng.* **23,** no. 10, 1719–1741.

Chávez-García, F. J., and M. Cárdenas-Soto (2002). The contribution of the built environment to the 'free-field' ground motion in Mexico City, *Soil Dynam. Earthq. Eng.* **22,** nos. 9/12, 773–780.

Dreossi, I., and S. Parolai (2022). Robust estimation of 1D shear-wave quality factor profiles for site response analysis using seismic noise, *Soil Dynam. Earthq. Eng.* **161,** 107387.

Gazetas, G. (1983). Analysis of machine foundation vibrations: State of the art, *Int. J. Soil Dynam. Earthq. Eng.* **2,** no. 1, 2–42.

Gueguen, P., and P.-Y. Bard (2005). Soil-structure and soil-structure-soil interaction: Experimental evidence at the Volvi test site, *J. Earthq. Eng.* **9,** no. 5, 657–693.

Guéguen, P., P.-Y. Bard, and F. J. Chavez-Garcia (2002). Site-city seismic interaction in Mexico city–like environments: An analytical study, *Bull. Seismol. Soc. Am.* **92,** no. 2, 794–811.

Jennings, P. C. (1970). Distant motions from a building vibration test, *Bull. Seismol. Soc. Am.* **60,** no. 6, 2037–2043.

Kausel, E. (2010). Early history of soil–structure interaction, *Soil Dynam. Earthq. Eng.* **30,** no. 9, 822–832.

Konno, K., and T. Ohmachi (1998). Ground-motion characteristics estimated from spectral ratio between horizontal and vertical components of microtremor, *Bull. Seismol. Soc. Am.* **88,** no. 1, 228–241.

Kramer, S. (1996). *Geotechnical Earthquake Engineering*, Prentice Hall, Inc., Upper Saddle River, New Jersey.

Luco, J., M. Trifunac, and H. Wong (1988). Isolation of soil-structure interaction effects by full-scale forced vibration tests, *Earthq. Eng. Struct. Dynam.* **16,** no. 1, 1–21.

Luco, J. E., and F. C. de Barros (2005). Identification of structural and soil properties from vibration tests of the Hualien containment model, *Earthq. Eng. Struct. Dynam.* **34,** no. 1, 21–48.

Mylonakis, G., and G. Gazetas (2000). Seismic soil-structure interaction: Beneficial or detrimental? *J. Earthq. Eng.* **4,** no. 3, 277–301.

Nakamura, Y. (1989).A method for dynamic characteristics estimation of surface using microtremor on the ground surface, *Quarterly Reports*, Vol. 30, Railway Technical Research Institute, 25–33, available at https://trid.trb.org/View/294184 (last accessed December 2023).

Napa Seismic (2023). Survey geometries for passive seismic, available at https://www.napaseismic.org/education/survey-geometries/ (last accessed December 2023).

National Institute of Standards and Technology (NIST) (2012). Soil-structure interaction for building structures, *National Institute of Standards and Technology (NEHRP)*, available at https://www.nist.gov/publications/soil-structure-interaction-building-structures (last accessed December 2023).

Petrovic, B., and S. Parolai (2016). Joint deconvolution of building and downhole strong-motion recordings: Evidence for the seismic wavefield being radiated back into the shallow geological layers, *Bull. Seismol. Soc. Am.* **106,** no. 4, 1720–1732.

Petrovic, B., S. Parolai, G. Pianese, S. U. Dikmen, B. Moldobekov, S. Orunbaev, and R. Paolucci (2018). Joint deconvolution of building and downhole seismic recordings: An application to three test cases, *Bull. Earthq. Eng.* **16,** no. 2, 613–641.

Pitilakis, D., E. Rovithis, A. Anastasiadis, A. Vratsikidis, and M. Manakou (2018). Field evidence of SSI from full-scale structure testing, *Soil Dynam. Earthq. Eng.* **112,** 89–106.

Poletto, F., L. Petronio, B. Farina, and A. Schleifer (2011). Seismic interferometry experiment in a shallow cased borehole using a seismic vibrator source, *Geophys. Prospect.* **59,** no. 3, 464–476.

Richart, F. E., J. R. Hall, and R. D. Woods (1970). *Vibrations of Soils and Foundations*, Prentice-Hall. Inc., Englewood Cliffs, New Jersey.

Rovithis, E., K. Pitilakis, and G. Mylonakis (2009). Seismic analysis of coupled soil-pile-structure systems leading to the definition of a pseudo-natural SSI frequency, *Soil Dynam. Earthq. Eng.* **29,** no. 6, 1005–1015.

Rovithis, E., K. Pitilakis, and G. Mylonakis (2011). A note on a pseudo-natural SSI frequency for coupled soil–pile–structure systems, *Soil Dynam. Earthq. Eng.* **31,** no. 7, 873–878.

Skłodowska, A. M., C. Holden, P. Guéguen, J. P. Finnegan, and G. Sidwell (2021). Structural change detection applying long-term seismic interferometry by deconvolution method to a modern civil engineering structure (New Zealand), *Bull. Earthq. Eng.* **19,** 3551–3569.

Skłodowska, A. M., S. Parolai, B. Petrovic, and F. Romanelli (2023). Soil-structure interaction assessment combining deconvolution of building and field recordings with polarization analysis: Application to the Matera (Italy) experiment, *Bull. Earthq. Eng.* **21,** no. 13, 5867–5891.

Slejko, D., G. Neri, I. Orozova, G. Renner, and M. Wyss (1999). Stress field in Friuli (NE Italy) from fault plane solutions of activity following the 1976 main shock, *Bull. Seismol. Soc. Am.* **89,** no. 4, 1037–1052.

Stewart, J. P., G. L. Fenves, and R. B. Seed (1999). Seismic soil-structure interaction in buildings. I: Analytical methods, *J. Geotech. Geoenviron. Eng.* **125,** no. 1, 26–37.

Tileylioglu, S., J. P. Stewart, and R. L. Nigbor (2011). Dynamic stiffness and damping of a shallow foundation from forced vibration of a field test structure, *J. Geotech. Geoenviron. Eng.* **137,** no. 4, 344–353.

Todorovska, M. I. (2009). Seismic interferometry of a soil-structure interaction model with coupled horizontal and rocking response, *Bull. Seismol. Soc. Am.* **99,** no. 2A, 611–625.

Vantassel, J. (2021). jpvantassel/hvsrpy: v1.0.0, doi: 10.5281/zenodo.5563211.

Wirgin, A., and P.-Y. Bard (1996). Effects of buildings on the duration and amplitude of ground motion in Mexico City, *Bull. Seismol. Soc. Am.* **86,** no. 3, 914–920.

## Appendix

Figure A1 shows spectral ratio of the magnitude 5.5 earthquake (see Fig. 10) and Figure A2 depicts spectral ratio of a small local earthquake with an epicentral distance of around 20 km from the test site.

Although we do not anticipate significant soil-structure interaction (SSI) effects due to the medium-stiff soil, the comparison of the amplification functions calculated as the spectral ratio between the top structure and the free

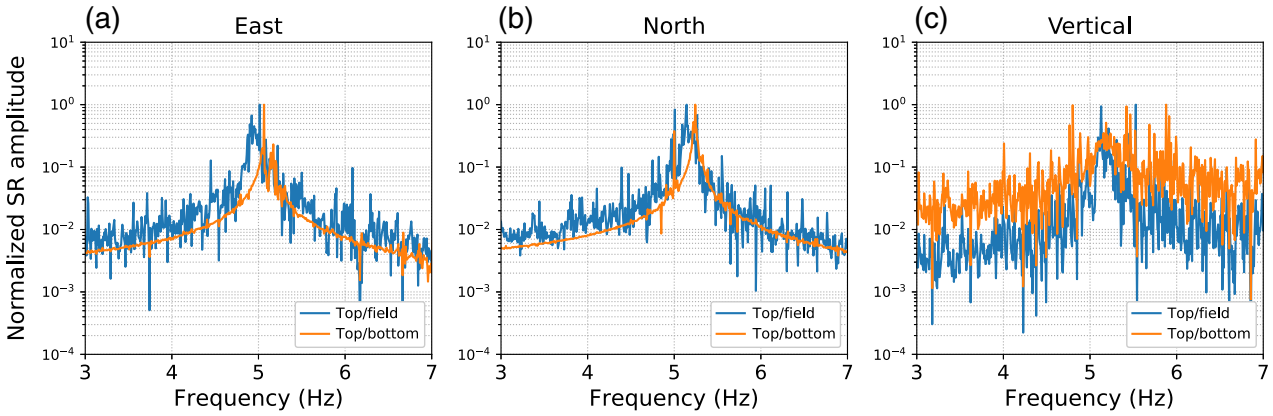


**Figure A1.** Comparison of normalized spectral ratios of the $M_w$ 5.5 earthquake (see Fig. 10) for (a) east, (b) north, and (c) vertical components. The blue line indicates the spectral ratio between recordings from the top of the structure and the furthest away sensor installed in the field. Orange lines indicate the spectral ratio between recordings from the top and the bottom of the structure. The color version of this figure is available only in the electronic edition.

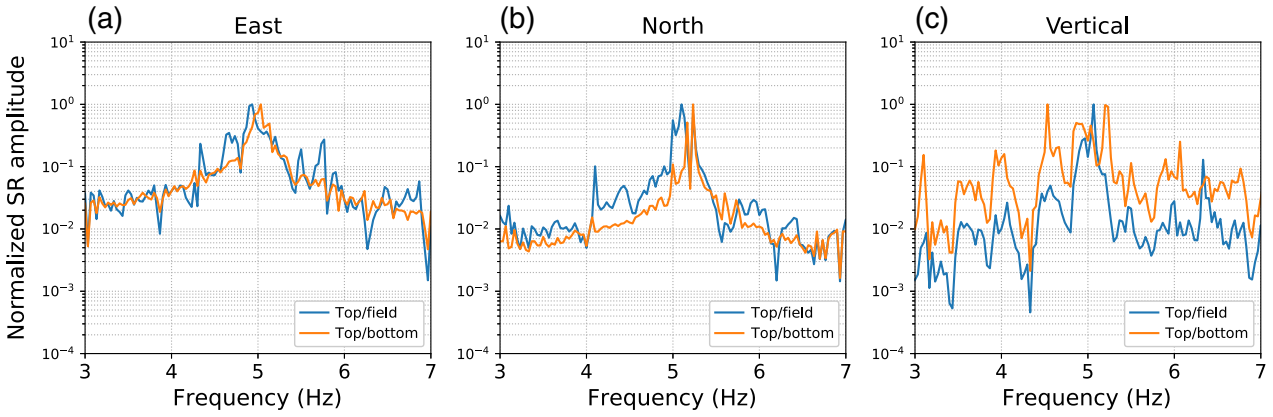


**Figure A2.** Comparison of normalized spectral ratios of small local earthquake recordings for (a) east, (b) north, and (c) vertical components. The blue line indicates the spectral ratio between recordings from the top of the structure and the furthest away sensor installed in the field. Orange lines indicate the spectral ratio between recordings from the top and the bottom of the structure. The color version of this figure is available only in the electronic edition.

field (blue lines in Figs. A1, A2) and between the top structure and the foundation (orange lines in Figs. A1, A2) shows a slight decrease in the peak frequency, highlighting the presence of SSI effects. These plots do not directly compare the resonant frequencies of the soil-structure system and the fixed-base structure, as it is typically done, because the fixed-base frequency for this structure is not directly measured. In contrast, the plots in Figures A1 and A2 show a comparison between the soil-structure system frequency and a pseudonatural soil-structure system frequency, as defined in Rovithis *et al.* (2009, 2011). From Figures A1 and A2, a slight decrease in the resonant system frequency is witnessed because of SSI.

**Manuscript received 10 January 2024**
**Published online 13 September 2024**

# Conclusion

Metamaterial physics presents a novel perspective of anomalous seismic wave propagation arising due to the local resonance properties of the medium constituents. This thesis encompasses various investigations that contribute to the understanding of the physics governing complex surface wave propagation within locally-resonant media, across scales spanning from a few meters to a few kilometers. Expanding upon previous research in elastic wave manipulation, each of the four main chapters discusses a different scale and setting. Moreover, we validate the physics observed at smaller scales, now extending its relevance to geophysical and seismological contexts.

In summary, we have shown evidence of the following:

- Time-average cross-correlations of seismic noise from dense arrays can be an effective way to study metamaterial physics. Apparently, a few hours of ambient seismic wavefield is sufficient to evaluate the coupling between the ground and the resonators.
- At the scale of a city, surface wave propagation is modified by a set of wind turbines inside a wind farm in a broad frequency band of 0.25-15 Hz, both in terms of amplitude and phase properties. Particularly, a spatially dense configuration of resonators can produce strong damping of Rayleigh waves in the frequency range of engineering interest (a few Hz).
- Longitudinal resonances of elongated structures couple well with Rayleigh waves, resulting in wider frequency bandgaps as compared to the flexural resonances. Densely arranged trees inside a forest and wind turbines in a wind farm emitting evanescent waves at their longitudinal resonances are a case in point.
- Azimuthal anisotropy of the near-surface structure can be evaluated using a dense nodal array through cross-correlation based plane wave beamforming of ambient noise.
- Distributed Acoustic Sensing (DAS) is an optimal way to obtain dense sampling, not only for studying the near-field properties of a resonator, but also necessary for measuring the dispersion of surface waves for a potential metasurface.
- It is possible to preferentially excite surface wave modes, in a layered halfspace by using a combination of time reversal and a phased source array. This can be used to study the sensitivity of modes in a scattering medium.

- Clamping a buried pile column to a stiffer half-space leads to a resonant scattering of the dominant fundamental mode of Rayleigh waves in the Mie-scattering regime. This is in contrast to the rigid scattering behavior when the pile is not clamped. Therefore, a group of clamped piles could potentially behave as a locally-resonant metamaterial.
- Impedance contrast between the resonator and the substrate is indeed the most important driving factor for the soil-structure coupling and thus for the local resonance bandgaps to manifest.

# Perspectives

Going forward, there are more questions than answers, which provide opportunities to expand this research in many directions. To conclude this dissertation, in the following sections I present some key questions that remain unanswered, followed by suggestions and possible directions for future studies.

### Outstanding questions from Chapter 1

Keeping in view the limitations of the mode-selective focusing methodology and the scattering study (already discussed in Section 1.4), I ask the following questions:

- Can we come up with an empirical relation between the optimal number of sources/receivers for the symmetric arrays ($N \geq N^*$) and the medium parameters ($H, \rho, V_p, V_s$), such that the Rayleigh wave modes in a layer over half-space medium are satisfactorily excited?
- To what extent is the bandgap (if any) induced by local-resonances for a clamped-pile-metamaterial related to the zero-frequency stopband proposed in the literature?
- How do the (a) contact conditions at the pile-soil interface, and (b) the pile-soil stiffness contrast affect the resonant behavior of the pile and thus the Rayleigh wave scattering?
- How different (both qualitatively and quantitatively) would be the forward scattering of Rayleigh wave for single and multiple-piles in a realistic 3D domain as compared to a P-SV domain?
- Is it possible to define thumb rules, as a function of soil type, for optimal pile arrangement, with the aim of reducing the ground motion? How can this interact with the site response features at the urban scale?

An additional practical question for the civil engineering community relates to the realization of the pile clamping effect in the field. Since the pile tip needs to be well anchored in the bedrock or a stiffer half-space, how deep would the pile need to be drilled to achieve the desired clamping, and how is this effected by the different soil parameters? Questions related to the effect of the pile-soil interface and clamping depth could perhaps be answered through numerical simulations using engineering-oriented FEA packages, for example Real-ESSI (Jeremic, B. et al. [1989-2024]), that has capabilities for realistic modeling of soils, structures and their interaction.

### Scattering of P-SV modes in a granular medium

The methodology devised for the Rayleigh wave mode separation and phased array excitation in Chapter 1 was discussed for the simplest case of a layer over half-space considering two dominant modes. More realistic earth models however, can have a complex velocity model, for example, unconsolidated granular materials having a power-law elastic profile that originates from their gravitational compaction. During this thesis, our collaborators at ETH Zürich performed a lab scale experiment with the aim of evaluating the scattering due to buried pile-like heterogenities in a granular medium (Fig. 4.1). Although in theory, there exist an infinite number of P-SV modes that arise from the dispersion relation, only the two dominant lowest-order modes are observed. The same methodology demonstrated using numerical data in Section 1.2.3, can be applied to this acquisition to preferentially excite the two dominant P-SV modes. Two different configurations of 3D printed pile-like heterogenities were buried in the top few centimeters of the sand that can scatterer these surface modes. The eventual goal would be to study the scattering sensitivity of the modes to such pile arrangements. The proposed scattering matrix approach can be used to quantify the scattering coefficients in each case.

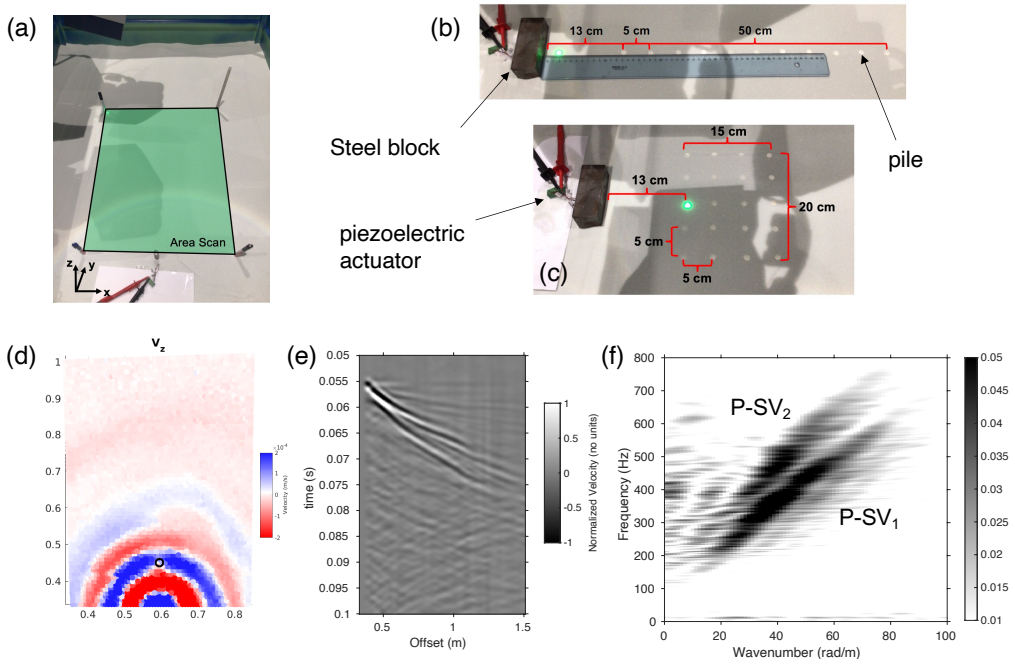


Figure 4.1: Surface waves in granular media. (a) Photograph of the experimental setup of the sand box used in the lab-scale experiment at the IBK structure laboratory at ETH Zürich. Buried scatterers arranged in two different configurations of (b) 11 piles, and (c) 5x4 grid, that are excited by a piezoelectric actuator fixed to a steel block (Credits: Henrik Thomsen). (d) Snapshot of the wavefield excited by a vertical Riker source centered at 420 Hz. (e) Seismogram of a Ricker pulse along the symmetry axis of the sandbox without the scatterers. (f) Frequency-wavenumber spectrum representing the experimental dispersion shows two dominant P-SV modes propagating in the pristine granular medium. These modes can be preferentially excited using the proposed methodology in Section 1.2.3 in order to study the sensitivity of each mode to the scatterers.

**Outstanding questions from Chapter 2**

The overall conclusion we reach from the study of the surface wave azimuthal anisotropy is that the trees in the forest themselves may not be contributing to any anisotropy observed. However, the total anisotropy we observe could be either due to: (1) intrinsic anisotropy of the shallow soil layer, (2) near-surface heterogeneities introduced by the root structure, and (3) preferential fracturing of the layers, or a combination of these factors. Given this uncertainty, I am interested in the following questions:

- What is the underlying cause of the prominent RW azimuthal anisotropy with a consistent fast axis observed over a broad frequency range?
- Can we reproduce the observed anisotropy with numerical simulations considering both the tree-root arrangement, and a subsurface that is more accurate than a simple 1D velocity model?
- Can we invert the noise data and the observed azimuthal anisotropy to get the approximate velocity model using a HTI medium for the top layer overlying other homogeneous layers?
- How does the azimuthal phase velocity extracted from the beamforming approach compare to those evaluated by following an eikonal strategy or by fitting a Rayleigh wave 2D Green's function to noise correlations?

**Outstanding questions from Chapter 3**

Since this an ongoing study, there are several questions that are being addressed by our current work. Several additional investigations should be performed to confirm (or eliminate) the "meta-effect" interpretation. A couple of important ones that should be considered by a separate study are listed here:

- How does the wavefield produced by the torsional mode or hybrid flexural-torsional mode (usually corresponding to the third peak) of the neighboring wind turbines interact?
- Is there any correlation of the "meta"-effect with meteorological conditions like wind speed (and thus, with the WT blade rotation)?
- To what extent does a real urban organization with an array of buildings in a sub-wavelength configuration behave as a metamaterial?

For the torsional modes, shear forces from torsion produce Love waves, which can exist in a layered medium. This can also be studied using data recorded by the 6C rotational sensors that were deployed during the META-WT experiment. I expect that 3D numerical simulations will improve the prediction of the seismic wavefield attenuation and thus provide a quantitative prediction of both the near-field and far-field effects of the WTs in the real data. This can be achieved with COMSOL, by using the beam-solid coupling module (as presented in the thesis for the 2D model), with the WT coupled to a solid circular foundation embedded in a 3D layered half-space. There are other open-source codes more popular among

the seismological community, for example SPECFEM3D, where the WT can be approximated as cylindrical beams, like trees were modeled in the METAFORET experiment simulations. However, I expect the COMSOL model to be more accurate in terms of reproducing the WT resonances. A newly implemented module (SPEED-SCI) in the high-performance code SPEED, developed by the URBASIS project partners, has the capability to couple physics-based ground motion with reduced models for both linear and non-linear structural response. This feature of SPEED-SCI also seems convenient to study the surface wave interaction with the (non-linear) response of a cluster of buildings in urbanized environments.

### Dense urban areas as a metamaterial

This dissertation had begun with a motivation to better explain the spatial variability of ground motion in urban areas. Several studies have explored the potential impact of SSI on the "free-field" ground motion, particularly in dense urban areas. Nevertheless, these studies have either relied on theoretical analysis, or numerical simulations. Even if experimental investigations were made, these were scaled-down laboratory experiments employing centrifuges and shaking tables. In this thesis, we have experimentally studied more realistic full-scale proxies of an urban setting, like a dense forest and wind farm. These observations have provided a first order understanding on what effects can be expected in an urban setting with tall buildings. We have come to a conclusion that surface waves, which can be a major part of the seismic wavefield, are strongly modified due to the presence of building-like resonators. The modification of the surface wavefield can therefore result in a reduction or increase in site response and therefore might have implications for seismic hazard in urban areas.

To further develop the idea of metamaterials on the geophysics scale, one can work with the existing dataset from an urban area in Quito city (Guéguen et al. [2019]), where a semi-dense array was deployed for a few hours (Fig. 4.2 (a-1)). This could be a good starting point towards understanding the meta-city effect. There is however also the Long-beach "Large-N" array that had a total of 7800 nodes with an inter-sensor spacing of 120m and was deployed for 9 months (Fig. 4.2(a-2)). The Long beach downtown has a few high-rise buildings which can resonate with frequencies below 1-2 Hz that can potentially modify the surface wavefield in the frequency range of engineering interest.

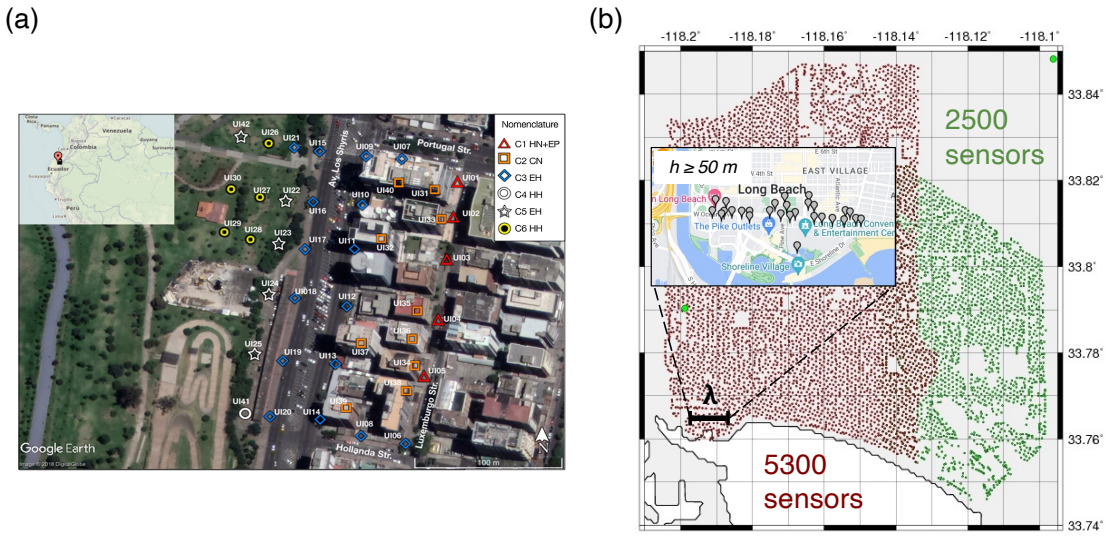


Figure 4.2: Examples of dense seismic arrays deployed in urban areas. (a-1) METACity-Quito experiment in Quito City, Ecuador where a temporary array was installed in 2018 specifically designed to analyze the coupling between soil and structures at short wavelengths. (b) Dense Long beach urban seismic arrays (LB3D and ELB) with 5300 and 2500 sensors respectively and an average spacing of 100 m (Image Source: https://web.gps.caltech.edu/člay/LB3D/Survey.html). The wavelength $\lambda \approx 1$ km is denoted for a typical tall building resonance frequency of 0.6 Hz. The inset demarcates the buildings that are 50m or taller in the Long Beach downtown area.

In the future, I envision research on seismic metamaterials leading towards even large scale features, for example, modern cities hosting tall buildings of heights more than 100-150m which resonate at even longer periods ($> 2s$ or $f < 0.5Hz$). A quite recent and interesting observation by Bard, P. Y. et al. [2024] is the reduction in site response which is strongly affected by surface waves in the downtown area of Tokyo in the low frequency regime of 0.2-1 Hz. This drop is calculated over a 20 year period which has seen the construction of tall buildings whose fundamental resonance frequencies falls in the same frequency band. A possible explanation of this observation could be the "meta-city" effect due to the long-period Rayleigh waves generated by the basin edge being dampened inside the downtown. Interestingly, this agrees with the larger attenuation coefficient of earthquake motions that Yamabe and Kanai [1988] found in the urbanized areas of Tokyo.

Another example similar to the Tokyo downtown is the New York City downtown which has skyscrapers that are densely spaced in a relatively small area (Fig. 4.3). As we know, ground motion in urban areas exhibits a high spatial variability, which makes it difficult to accurately quantify unless we have an extremely dense spatial sampling of the wavefield. This dense spatial sampling is also necessary for the computation of the dispersion inside the urban area. One way to achieve this sampling is to use existing underground telecommunication infrastructure (so-called 'dark fiber') as DAS arrays. This is an appealing alternative to geophone arrays due to their durability, the requirement for just one power source for hundreds to thousands of virtual sensors at meter-scale spacing but also it's cost effectiveness. In the coming years, such an experiment can be performed to confirm the meta-city

effect.

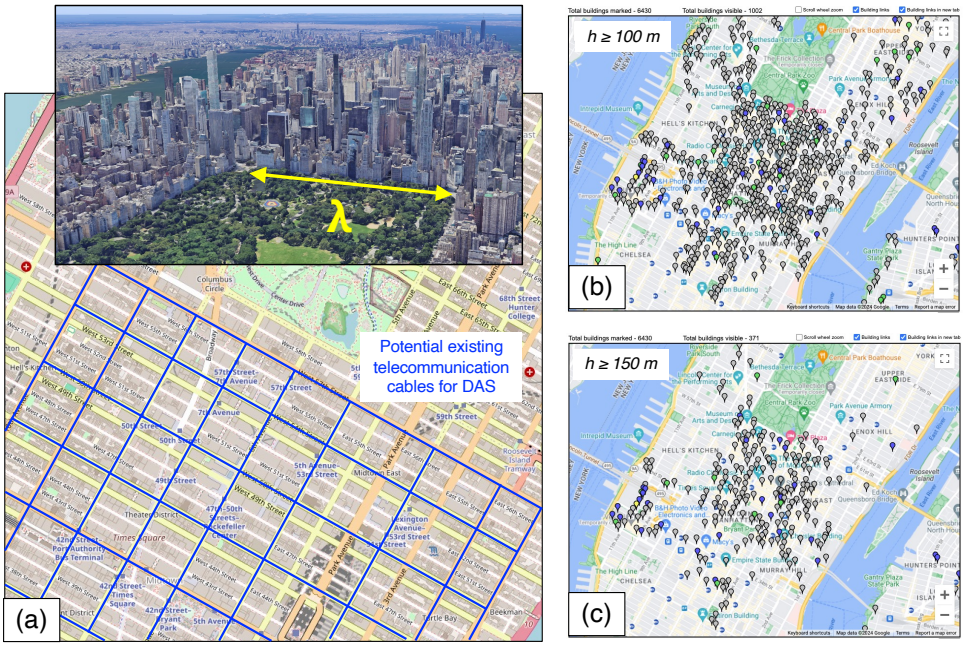


Figure 4.3: Example of a potential Meta-City: (a) The map shows the New York City downtown area with blue lines indicating potential telecommunication cables that can form an ultra-dense urban DAS array in a grid-like configuration (Source: Open Street maps). Whereas the inset shows a bird's eye view of the NYC skyline over the Central Park (Image: Google Earth). The right panels (b,c) display a wider zone, demarcating the high-rise buildings of heights greater than 100m and 150m respectively (Data source: https://skyscraperpage.com/)

A case-by-case study of dense city layouts is essential to evaluate local energy trapping in certain building configurations or to evaluate which buildings might undergo more shaking in earthquake scenarios. This can help to better constrain urban planning for new cities or in the expansion of current cities. Accurate ground motion prediction at a site is crucial for the estimation of seismic hazard, and therefore for the optimal design of robust civil engineering structures. The idea of seismic metamaterials can potentially be transformative to the field of urban seismology. Our understanding, however, is still rudimentary, and further full-scale experimental studies are needed for a better understanding of the complex physics.

# Bibliography


VIBRATION OF SYSTEMS HAVING DISTRIBUTED MASS AND ELASTICITY. In Thomas L. Paez, editor, *Harris' Shock and Vibration Handbook*. McGraw-Hill Education, 6th edition edition, 2010. ISBN 978-0-07-150819-3. URL https://www.accessengineeringlibrary.com/content/book/9780071508193/chapter/chapter7.

Y Achaoui, T Antonakakis, S Brûlé, R V Craster, S Enoch, and S Guenneau. Clamped seismic metamaterials: ultra-low frequency stop bands. *New Journal of Physics*, 19(6):063022, June 2017. ISSN 1367-2630. doi: 10.1088/1367-2630/aa6e21. URL https://iopscience.iop.org/article/10.1088/1367-2630/aa6e21.

Younes Achaoui, Abdelkrim Khelif, Sarah Benchabane, Laurent Robert, and Vincent Laude. Experimental observation of locally-resonant and Bragg band gaps for surface guided waves in a phononic crystal of pillars. *Physical Review B*, 83(10):104201, March 2011. doi: 10.1103/PhysRevB.83.104201. URL https://link.aps.org/doi/10.1103/PhysRevB.83.104201. Publisher: American Physical Society.

Rasheed Ajala, Patricia Persaud, Joann M. Stock, Gary S. Fuis, John A. Hole, Mark Goldman, and Daniel Scheirer. Three-Dimensional Basin and Fault Structure From a Detailed Seismic Velocity Model of Coachella Valley, Southern California. *Journal of Geophysical Research: Solid Earth*, 124 (5):4728–4750, 2019. ISSN 2169-9356. doi: 10.1029/2018JB016260. URL http://onlinelibrary.wiley.com/doi/abs/10.1029/2018JB016260. _eprint: https://agupubs.onlinelibrary.wiley.com/doi/pdf/10.1029/2018JB016260.

Kanamori Aki. Aki: Space and time spectra of stationary stochastic... - Google Scholar, 1957. URL https://scholar-google-com.sid2nomade-1.grenet.fr/scholar_lookup?title=Space%20and%20time%20spectra%20of%20stationary%20stochastic%20waves%20with%20special%20reference%20to%20microtremors&author=K.%20Aki&publication_year=1957&pages=415-456.

Celso Alvizuri and Toshiro Tanimoto. Azimuthal anisotropy from array analysis of Rayleigh waves in Southern California. *Geophysical Journal International*, 186 (3):1135–1151, September 2011. ISSN 0956-540X. doi: 10.1111/j.1365-246X.2011.05093.x. URL https://doi.org/10.1111/j.1365-246X.2011.05093.x.

T. Antonakakis, R. V. Craster, and S. Guenneau. High-frequency homogenization of zero-frequency stop band photonic and phononic crystals. *New Journal of*

*Physics*, 15(10):103014, October 2013. ISSN 1367-2630. doi: 10.1088/1367-2630/15/10/103014. URL https://dx.doi.org/10.1088/1367-2630/15/10/103014. Publisher: IOP Publishing.

T. Antonakakis, R. V. Craster, and S. Guenneau. Homogenisation for elastic photonic crystals and dynamic anisotropy. *Journal of the Mechanics and Physics of Solids*, 71:84–96, November 2014a. ISSN 0022-5096. doi: 10.1016/j.jmps.2014.06.006. URL https://www.sciencedirect.com/science/article/pii/S0022509614001252.

T. Antonakakis, R. V. Craster, and S. Guenneau. Moulding and shielding flexural waves in elastic plates. *Europhysics Letters*, 105(5):54004, March 2014b. ISSN 0295-5075. doi: 10.1209/0295-5075/105/54004. URL https://dx.doi.org/10.1209/0295-5075/105/54004. Publisher: EDP Sciences, IOP Publishing and Società Italiana di Fisica.

Tryfon Antonakakis, Richard CRASTER, Younes Achaoui, Stefan ENOCH, Sebastien Guenneau, and Stephane Brule. Seismic defence structures, May 2023. URL https://patents.google.com/patent/US11655610B2/en.

J.-F. Aubry, M. Tanter, J. Gerber, J.-L. Thomas, and M. Fink. Optimal focusing by spatio-temporal inverse filter. II. Experiments. Application to focusing through absorbing and reverberating media. *The Journal of the Acoustical Society of America*, 110(1):48–58, July 2001. ISSN 0001-4966. doi: 10.1121/1.1377052. URL http://asa.scitation.org/doi/10.1121/1.1377052.

J. L. Auriault and C. Boutin. Long wavelength inner-resonance cut-off frequencies in elastic composite materials. *International Journal of Solids and Structures*, 49(23):3269–3281, November 2012. ISSN 0020-7683. doi: 10.1016/j.ijsolstr.2012.07.002. URL https://www.sciencedirect.com/science/article/pii/S0020768312002867.

Jean-Louis Auriault and Guy Bonnet. Dynamique des composites élastiques périodiques. *Archives of Mechanics*, 37:269–284, January 1985.

J Avilés and F Sánchez-Sesma. Piles as Barriers for Elastic Waves. page 14, September 1983.

Javier Avilés and Francisco J. Sánchez-Sesma. Foundation Isolation from Vibrations Using Piles as Barriers. *Journal of Engineering Mechanics*, 114(11):1854–1870, November 1988. ISSN 0733-9399, 1943-7889. doi: 10.1061/(ASCE)0733-9399(1988)114:11(1854). URL http://ascelibrary.org/doi/10.1061/%28ASCE%290733-9399%281988%29114%3A11%281854%29.

A. B. Baggeroer, W. A. Kuperman, and Henrik Schmidt. Matched field processing: Source localization in correlated noise as an optimum parameter estimation problem. *The Journal of the Acoustical Society of America*, 83(2):571–587, February 1988. ISSN 0001-4966. doi: 10.1121/1.396151. URL https://doi.org/10.1121/1.396151.

M. R. Bakker, L. Augusto, and D. L. Achat. Fine root distribution of trees and understory in mature stands of maritime pine (Pinus pinaster) on dry and humid sites. *Plant and Soil*, 286(1):37–51, August 2006. ISSN 1573-5036. doi: 10.1007/s11104-006-9024-4. URL https://doi.org/10.1007/s11104-006-9024-4.

Bard, P. Y., K. Nakano, E. Ito, J. Sun, Z. Wang, and H. Kawase. From site response to site-city interaction: a case study in the Tokyo area. *Proceedings of the 18th World Conference on Earthqauke Engineering*, July 2024.

Émilie Blanc, Dimitri Komatitsch, Emmanuel Chaljub, Bruno Lombard, and Zhinan Xie. Highly accurate stability-preserving optimization of the Zener viscoelastic model, with application to wave propagation in the presence of strong attenuation. *Geophysical Journal International*, 205(1):427–439, April 2016. ISSN 0956-540X. doi: 10.1093/gji/ggw024. URL https://doi.org/10.1093/gji/ggw024.

Jacopo Boaga, Giulio Vignoli, Rita Deiana, and Giorgio Cassiani. The Influence of Subsoil Structure and Acquisition Parameters in MASW Mode Mis-identification. *Journal of Environmental and Engineering Geophysics*, 19(2):87–99, June 2014. ISSN 1083-1363. doi: 10.2113/JEEG19.2.87. URL https://doi.org/10.2113/JEEG19.2.87.

M. G. Bostock. Surface wave scattering from 3-D obstacles. *Geophysical Journal International*, 104(2):351–370, February 1991. ISSN 0956-540X. doi: 10.1111/j.1365-246X.1991.tb02516.x. URL https://doi.org/10.1111/j.1365-246X.1991.tb02516.x.

C. Boutin and J. L. Auriault. Rayleigh scattering in elastic composite materials. *International Journal of Engineering Science*, 31(12):1669–1689, December 1993. ISSN 0020-7225. doi: 10.1016/0020-7225(93)90082-6. URL https://www.sciencedirect.com/science/article/pii/0020722593900826.

Claude Boutin and Jean Soubestre. Generalized inner bending continua for linear fiber reinforced materials. *International Journal of Solids and Structures*, 48(3):517–534, February 2011. ISSN 0020-7683. doi: 10.1016/j.ijsolstr.2010.10.017. URL https://www.sciencedirect.com/science/article/pii/S0020768310003719.

Claude Boutin, Jean Soubestre, Matt S. Dietz, and Colin Taylor. Experimental evidence of the high-gradient behaviour of fiber reinforced materials. *European Journal of Mechanics - A/Solids*, 42:280–298, November 2013. ISSN 0997-7538. doi: 10.1016/j.euromechsol.2013.06.003. URL https://www.sciencedirect.com/science/article/pii/S0997753813000685.

Daniel C. Bowden and Victor C. Tsai. Earthquake ground motion amplification for surface waves. *Geophysical Research Letters*, 44(1):121–127, 2017. ISSN 1944-8007. doi: 10.1002/2016GL071885. URL https://onlinelibrary.wiley.com/doi/abs/10.1002/2016GL071885. _eprint: https://onlinelibrary.wiley.com/doi/pdf/10.1002/2016GL071885.

F. Brenguier, P. Boué, Y. Ben-Zion, F. Vernon, C.w. Johnson, A. Mordret, O. Coutant, P.-E. Share, E. Beaucé, D. Hollis, and T. Lecocq.

Train Traffic as a Powerful Noise Source for Monitoring Active Faults With Seismic Interferometry. *Geophysical Research Letters*, 46(16):9529–9536, 2019. ISSN 1944-8007. doi: 10.1029/2019GL083438. URL https://onlinelibrary.wiley.com/doi/abs/10.1029/2019GL083438. _eprint: https://onlinelibrary.wiley.com/doi/pdf/10.1029/2019GL083438.

Stephane Brule and Gillian Erbeja. Proposition d'analyse complémentaire de vibration pour les sources à impacts. Le cas du compactage dynamique. In *11èmes journées nationales de géotechnique et de géologie de l'ingénieur*, Lyon, France, June 2022. Institut National des Sciences Appliquées de Lyon [INSA Lyon], CFMS, CFMR, CFGI. URL https://hal.science/hal-03720130.

S. Brûlé, E.H. Javelaud, S. Enoch, and S. Guenneau. Experiments on Seismic Metamaterials: Molding Surface Waves. *Physical Review Letters*, 112(13):133901, March 2014. doi: 10.1103/PhysRevLett.112.133901. URL https://link.aps.org/doi/10.1103/PhysRevLett.112.133901. Publisher: American Physical Society.

S. Brûlé, B. Ungureanu, Y. Achaoui, A. Diatta, Ronald Aznavourian, T. Antonakakis, R. Craster, S. Enoch, and S. Guenneau. Metamaterial-like transformed urbanism. *Innovative Infrastructure Solutions*, 2:1–11, 2017a. doi: 10.1007/s41062-017-0063-x. URL https://www.semanticscholar.org/paper/707362fc8ef8be94e84c6186419792865847ac11.

Stéphane Brûlé, Stefan Enoch, and Sébastien Guenneau. Sols structurés sous sollicitation dynamique : des métamatériaux en géotechnique. *Revue Française de Géotechnique*, (151):4, 2017b. ISSN 0181-0529, 2493-8653. doi: 10.1051/geotech/2017010. URL https://www.geotechnique-journal.org/articles/geotech/abs/2017/02/geotech160015/geotech160015.html. Number: 151 Publisher: EDP Sciences.

Michel Campillo and Anne Paul. Long-Range Correlations in the Diffuse Seismic Coda. *Science*, 299(5606):547–549, January 2003. doi: 10.1126/science.1078551. URL https://www.science.org/doi/full/10.1126/science.1078551. Publisher: American Association for the Advancement of Science.

Michel Campillo and Philippe Roux. Seismic imaging and monitoring with ambient noise correlations. 1:256–271, January 2015.

A. Colombi, R. Zaccherini, and A. Palermo. Mitigation of seismic waves: Metabarriers and metafoundations bench tested. *Journal of Sound and Vibration*, 485:115537, 2019. doi: 10.1016/J.JSV.2020.115537. URL https://www.semanticscholar.org/paper/9f8ac3405305071afbf24f8ec9c462494a13d033.

Andrea Colombi, Philippe Roux, and Matthieu Rupin. Sub-wavelength energy trapping of elastic waves in a metamaterial. *The Journal of the Acoustical Society of America*, 136(2):EL192–EL198, August 2014. ISSN 0001-4966. doi: 10.1121/1.4890942. URL http://asa.scitation.org/doi/10.1121/1.4890942. Publisher: Acoustical Society of America.

Andrea Colombi, Philippe Roux, Sebastien Guenneau, and Matthieu Rupin. Directional cloaking of flexural waves in a plate with a locally resonant metamaterial. *The Journal of the Acoustical Society of America*, 137(4):1783–1789, April 2015. ISSN 0001-4966. doi: 10.1121/1.4915004. URL http://asa.scitation.org/doi/10.1121/1.4915004. Publisher: Acoustical Society of America.

Andrea Colombi, Daniel Colquitt, Philippe Roux, Sebastien Guenneau, and Richard V. Craster. A seismic metamaterial: The resonant metawedge. *Scientific Reports*, 6(1):27717, June 2016a. ISSN 2045-2322. doi: 10.1038/srep27717. URL http://www.nature.com/articles/srep27717. Number: 1 Publisher: Nature Publishing Group.

Andrea Colombi, Sebastien Guenneau, Philippe Roux, and Richard V. Craster. Transformation seismology: composite soil lenses for steering surface elastic Rayleigh waves. *Scientific Reports*, 6(1):25320, April 2016b. ISSN 2045-2322. doi: 10.1038/srep25320. URL http://www.nature.com/articles/srep25320. Number: 1 Publisher: Nature Publishing Group.

Andrea Colombi, Philippe Roux, Sebastien Guenneau, Philippe Gueguen, and Richard V. Craster. Forests as a natural seismic metamaterial: Rayleigh wave bandgaps induced by local resonances. *Scientific Reports*, 6(1):19238, January 2016c. ISSN 2045-2322. doi: 10.1038/srep19238. URL http://www.nature.com/articles/srep19238. Number: 1 Publisher: Nature Publishing Group.

Andrea Colombi, Victoria Ageeva, Richard J. Smith, Adam Clare, Rikesh Patel, Matt Clark, Daniel Colquitt, Philippe Roux, Sebastien Guenneau, and Richard V. Craster. Enhanced sensing and conversion of ultrasonic Rayleigh waves by elastic metasurfaces. *Scientific Reports*, 7(1):6750, July 2017a. ISSN 2045-2322. doi: 10.1038/s41598-017-07151-6. URL http://www.nature.com/articles/s41598-017-07151-6. Number: 1 Publisher: Nature Publishing Group.

Andrea Colombi, Richard V. Craster, Daniel Colquitt, Younes Achaoui, Sebastien Guenneau, Philippe Roux, and Matthieu Rupin. Elastic Wave Control Beyond Band-Gaps: Shaping the Flow of Waves in Plates and Half-Spaces with Subwavelength Resonant Rods. *Frontiers in Mechanical Engineering*, 3, 2017b. ISSN 2297-3079. URL https://www.frontiersin.org/article/10.3389/fmech.2017.00010.

D. J. Colquitt, R. V. Craster, T. Antonakakis, and S. Guenneau. Rayleigh–Bloch waves along elastic diffraction gratings. *Proceedings of the Royal Society A: Mathematical, Physical and Engineering Sciences*, 471(2173):20140465, January 2015. doi: 10.1098/rspa.2014.0465. URL https://royalsocietypublishing.org/doi/10.1098/rspa.2014.0465. Publisher: Royal Society.

D. J. Colquitt, A. Colombi, R. V. Craster, P. Roux, and S. R. L. Guenneau. Seismic metasurfaces: Sub-wavelength resonators and Rayleigh wave interaction. *Journal of the Mechanics and Physics of Solids*, 99:379–393, February 2017. ISSN 0022-5096. doi: 10.1016/j.jmps.2016.12.004. URL https://www.sciencedirect.com/science/article/pii/S002250961630549X.

F. Danjon, D. Bert, C. Godin, and P. Trichet. Structural root architecture of 5-year-old Pinus pinaster measured by 3D digitising and analysed with AMAPmod. *Plant and Soil*, 217(1):49–63, December 1999a. ISSN 1573-5036. doi: 10.1023/A:1004686119796. URL https://doi.org/10.1023/A:1004686119796.

F. Danjon, H. Sinoquet, C. Godin, F. Colin, and M. Drexhage. Characterisation of structural tree root architecture using 3D digitising and AMAPmod software. *Plant and Soil*, 211(2):241–258, April 1999b. ISSN 1573-5036. doi: 10.1023/A:1004680824612. URL https://doi.org/10.1023/A:1004680824612.

Frédéric Danjon, Thierry Fourcaud, and Didier Bert. Root architecture and wind-firmness of mature Pinus pinaster. *New Phytologist*, 168(2):387–400, 2005. ISSN 1469-8137. doi: 10.1111/j.1469-8137.2005.01497.x. URL https://onlinelibrary.wiley.com/doi/abs/10.1111/j.1469-8137.2005.01497.x. _eprint: https://onlinelibrary.wiley.com/doi/pdf/10.1111/j.1469-8137.2005.01497.x.

Raffaele De Risi, Subhamoy Bhattacharya, and Katsuichiro Goda. Seismic performance assessment of monopile-supported offshore wind turbines using unscaled natural earthquake records. *Soil Dynamics and Earthquake Engineering*, 109:154–172, June 2018. ISSN 0267-7261. doi: 10.1016/j.soildyn.2018.03.015. URL https://www.sciencedirect.com/science/article/pii/S0267726117309454.

Arnaud Derode, Arnaud Tourin, and Mathias Fink. Random multiple scattering of ultrasound. I. Coherent and ballistic waves. *Physical Review E*, 64(3):036605, August 2001. ISSN 1063-651X, 1095-3787. doi: 10.1103/PhysRevE.64.036605. URL https://link.aps.org/doi/10.1103/PhysRevE.64.036605.

A. Diatta, Y. Achaoui, St'ephane Brul'e, S. Enoch, and S. Guenneau. Control of Rayleigh-like waves in thick plate Willis metamaterials. *AIP Advances*, 6:121707, 2016. doi: 10.1063/1.4972280. URL https://www.semanticscholar.org/paper/02e98e1297e4ce2df81169a0a42e38a7d6e36171.

Hao Ding, Lei Xue, Hongyan Liu, Longfei Li, Haoyu Wang, and Mengyang Zhai. Influence of Root Volume, Plant Spacing, and Planting Pattern of Tap-like Tree Root System on Slope Protection Effect. *Forests*, 13(11):1925, November 2022. ISSN 1999-4907. doi: 10.3390/f13111925. URL https://www.mdpi.com/1999-4907/13/11/1925. Number: 11 Publisher: Multidisciplinary Digital Publishing Institute.

Shan Dou, Nate Lindsey, Anna M. Wagner, Thomas M. Daley, Barry Freifeld, Michelle Robertson, John Peterson, Craig Ulrich, Eileen R. Martin, and Jonathan B. Ajo-Franklin. Distributed Acoustic Sensing for Seismic Monitoring of The Near Surface: A Traffic-Noise Interferometry Case Study. *Scientific Reports*, 7(1):11620, September 2017. ISSN 2045-2322. doi: 10.1038/s41598-017-11986-4. URL https://www.nature.com/articles/s41598-017-11986-4. Publisher: Nature Publishing Group.

C. Esmersoy, V.F. Cormier, and M. N. Toksoz. Three-component array processing. The VELA Program. A Twenty-Five Year Review of Basic Research, edited by A. U. Kerr, xviii, 964 p. 1985. URL https://apps.dtic.mil/sti/citations/ADA222289.

Hortencia Flores Estrella, Michael Korn, and Kilian Alberts. Analysis of the Influence of Wind Turbine Noise on Seismic Recordings at Two Wind Parks in Germany. *Journal of Geoscience and Environment Protection*, 5(5):76–91, May 2017. doi: 10.4236/gep.2017.55006. URL https://www.scirp.org/journal/paperinformation.aspx?paperid=76324. Number: 5 Publisher: Scientific Research Publishing.

Mathias Fink. Time Reversed Acoustics. *Physics Today*, 50(3):34–40, March 1997. ISSN 0031-9228. doi: 10.1063/1.881692. URL https://doi.org/10.1063/1.881692.

Thomas Forbriger, Lingli Gao, Peter Malischewsky, Matthias Ohrnberger, and Yudi Pan. A single Rayleigh mode may exist with multiple values of phase-velocity at one frequency. *Geophysical Journal International*, 222(1):582–594, July 2020. ISSN 0956-540X. doi: 10.1093/gji/ggaa123. URL https://doi.org/10.1093/gji/ggaa123.

Laura Gaßner, Marie A. Gärtner, and Joachim Ritter. Simulation of ground motion emissions from wind turbines in low mountain ranges: implications for amplitude decay prediction. *Journal of Seismology*, 27(6):933–952, December 2023. ISSN 1573-157X. doi: 10.1007/s10950-023-10172-6. URL https://doi.org/10.1007/s10950-023-10172-6.

Peter Gerstoft and Toshiro Tanimoto. A year of microseisms in southern California. *Geophysical Research Letters*, 34(20), 2007. ISSN 1944-8007. doi: 10.1029/2007GL031091. URL https://onlinelibrary.wiley.com/doi/abs/10.1029/2007GL031091. _eprint: https://onlinelibrary.wiley.com/doi/pdf/10.1029/2007GL031091.

Peter Gerstoft, Karim G. Sabra, Philippe Roux, W. A. Kuperman, and Michael C. Fehler. Green's functions extraction and surface-wave tomography from microseisms in southern California. *GEOPHYSICS*, 71(4):SI23–SI31, July 2006. ISSN 0016-8033. doi: 10.1190/1.2210607. URL https://library.seg.org/doi/full/10.1190/1.2210607. Publisher: Society of Exploration Geophysicists.

Theodore V. Gortsas, Theodoros Triantafyllidis, Stylianos Chrisopoulos, and Demosthenes Polyzos. Numerical modelling of micro-seismic and infrasound noise radiated by a wind turbine. *Soil Dynamics and Earthquake Engineering*, 99:108–123, August 2017. ISSN 0267-7261. doi: 10.1016/j.soildyn.2017.05.001. URL https://www.sciencedirect.com/science/article/pii/S026772611730297X.

Philippe Gueguen, Pierre-Yves Bard, and Carlos S. Oliveira. Experimental and Numerical Analysis of Soil Motions Caused by Free Vibrations of a Building Model. *Bulletin of the Seismological Society of America*, 90(6):1464–1479, December 2000. ISSN 0037-1106. doi: 10.1785/0119990072. URL https://doi.org/10.1785/0119990072.

PHILIPPE GUÉGUEN and PIERRE-YVES BARD. Soil-Structure and Soil-Structure-Soil Interaction: Experimental Evidence at the Volvi Test Site. *Journal of Earthquake Engineering*, 9(5):657–693, September 2005. ISSN 1363-2469. doi: 10.1080/13632460509350561. URL https://doi.

org/10.1080/13632460509350561. Publisher: Taylor & Francis _eprint: https://doi.org/10.1080/13632460509350561.

Philippe Guéguen, Pierre-Yves Bard, and Francisco J. Chávez-García. Site-City Seismic Interaction in Mexico City–Like Environments: An Analytical Study. *Bulletin of the Seismological Society of America*, 92(2):794–811, March 2002. ISSN 0037-1106. doi: 10.1785/0120000306. URL https://doi.org/10.1785/0120000306.

Philippe Guéguen, E. Diego Mercerat, Juan Carlos Singaucho, Coralie Aubert, Juan Gabriel Barros, L. Fabian Bonilla, Mutiara Cripstyani, Isabelle Douste-Bacqué, Philippe Langlaude, Stéphane Mercier, Daniel Pacheco, Michel Pernoud, Mathieu Perrault, Ildut Pondaven, and David Wolyniec. METACity-Quito: A Semi-Dense Urban Seismic Network Deployed to Analyze the Concept of Metamaterial for the Future Design of Seismic-Proof Cities. *Seismological Research Letters*, 90(6):2318–2326, September 2019. ISSN 0895-0695. doi: 10.1785/0220190044. URL https://doi.org/10.1785/0220190044.

Philippe Guéguen, Philippe Roux, and Andrea Colombi. Urban Seismology: Experimental Approach to Soil–Structure Interaction Towards the Concept of Meta-city. In *Deterministic Numerical Modeling of Soil–Structure Interaction*, pages 181–209. John Wiley & Sons, Ltd, 2022. ISBN 978-1-119-88769-0. doi: 10.1002/9781119887690.ch5. URL http://onlinelibrary.wiley.com/doi/abs/10.1002/9781119887690.ch5. Section: 5 _eprint: https://onlinelibrary.wiley.com/doi/pdf/10.1002/9781119887690.ch5.

Liang Han, John A. Hole, Joann M. Stock, Gary S. Fuis, Annie Kell, Neal W. Driscoll, Graham M. Kent, Alistair J. Harding, Michael J. Rymer, Antonio González-Fernández, and Octavio Lázaro-Mancilla. Continental rupture and the creation of new crust in the Salton Trough rift, Southern California and northern Mexico: Results from the Salton Seismic Imaging Project. *Journal of Geophysical Research: Solid Earth*, 121(10):7469–7489, 2016. ISSN 2169-9356. doi: 10.1002/2016JB013139. URL https://agupubs.onlinelibrary.wiley.com/doi/abs/10.1002/2016JB013139. _eprint: https://agupubs.onlinelibrary.wiley.com/doi/pdf/10.1002/2016JB013139.

R. B. Herrmann. Computer Programs in Seismology: An Evolving Tool for Instruction and Research. *Seismological Research Letters*, 84(6):1081–1088, November 2013. ISSN 0895-0695, 1938-2057. doi: 10.1785/0220110096. URL https://pubs.geoscienceworld.org/srl/article/84/6/1081-1088/315307.

Gregor Hillers, Michel Campillo, Y.-Y. Lin, K.F. Ma, and Philippe Roux. Anatomy of the high-frequency ambient seismic wave field at the TCDP borehole. *Journal of Geophysical Research*, VOL. 117:19 PP., June 2012. doi: 10.1029/2011JB008999. URL https://hal.archives-ouvertes.fr/hal-00706923. Publisher: American Geophysical Union.

Ben Hoen, James E Diffendorfer, Joseph Rand, Louisa A. Kramer, Christopher P Garrity, Aaron D. Roper, and Hannah Hunt. United States Wind Turbine Database, 2018. URL https://www.sciencebase.gov/catalog/item/57bdfd8fe4b03fd6b7df5ff9.

Weifei Hu, Rebecca J. Barthelmie, Frederick Letson, and Sara C. Pryor. Seismic Noise Induced by Wind Turbine Operation and Wind Gusts. *Seismological Research Letters*, 91(1):427–437, October 2019. ISSN 0895-0695. doi: 10.1785/0220190095. URL https://doi.org/10.1785/0220190095.

Asaf Inbal, Tudor Cristea-Platon, Jean-Paul Ampuero, Gregor Hillers, Duncan Agnew, and Susan E. Hough. Sources of Long-Range Anthropogenic Noise in Southern California and Implications for Tectonic Tremor Detection. *Bulletin of the Seismological Society of America*, 108(6):3511–3527, October 2018. ISSN 0037-1106. doi: 10.1785/0120180130. URL https://doi.org/10.1785/0120180130.

IRENA. (2022) Renewable Technology Innovation Indicators: Mapping progress in costs, patents and standards, March 2022. URL https://www.irena.org/publications/2022/Mar/Renewable-Technology-Innovation-Indicators.

Paul C. Jennings. Distant motions from a building vibration test. *Bulletin of the Seismological Society of America*, 60(6):2037–2043, December 1970. ISSN 0037-1106. doi: 10.1785/BSSA0600062037. URL https://doi.org/10.1785/BSSA0600062037.

Finn B. Jensen, William A. Kuperman, Michael B. Porter, and Henrik Schmidt. *Computational Ocean Acoustics*. Modern Acoustics and Signal Processing. Springer, New York, NY, 2011. ISBN 978-1-4419-8677-1 978-1-4419-8678-8. doi: 10.1007/978-1-4419-8678-8. URL https://link.springer.com/10.1007/978-1-4419-8678-8.

Jeremic, B., G. Jie, Z. Cheng, N. Tafazzoli, P. Tasiopoulou, F. Pisanò, J. A. Abell, K. Watanabe, Y. Feng, S. K. Sinha, F. Behbehani, H. Yang, and H. Wang. The Real ESSI / MS ESSI Simulator System, 1989-2024. URL http://real-essi.us/.

John Hole. Seismic imaging of new transitional crust in the salton trough oblique rift, 2011. URL https://www.fdsn.org/networks/detail/YG_2011/.

Lav Joshi and J. P. Narayan. Quantification of the Effects of an Urban Layer on Rayleigh Wave Characteristics and Development of a Meta-City. *Pure and Applied Geophysics*, July 2022. ISSN 1420-9136. doi: 10.1007/s00024-022-03111-y. URL https://doi.org/10.1007/s00024-022-03111-y.

C. Juretzek and C. Hadziioannou. Where do ocean microseisms come from? A study of Love-to-Rayleigh wave ratios. *Journal of Geophysical Research: Solid Earth*, 121(9):6741–6756, 2016. ISSN 2169-9356. doi: 10.1002/2016JB013017. URL https://onlinelibrary.wiley.com/doi/abs/10.1002/2016JB013017. _eprint: https://onlinelibrary.wiley.com/doi/pdf/10.1002/2016JB013017.

Nadège Kaina, Mathias Fink, and Geoffroy Lerosey. Composite media mixing Bragg and local resonances for highly attenuating and broad bandgaps. *Scientific Reports*, 3(1):3240, November 2013a. ISSN 2045-2322. doi: 10.1038/srep03240. URL https://www.nature.com/articles/srep03240. Number: 1 Publisher: Nature Publishing Group.

Nadège Kaina, Fabrice Lemoult, Mathias Fink, and Geoffroy Lerosey. Ultra small mode volume defect cavities in spatially ordered and disordered metamaterials. *Applied Physics Letters*, 102(14):144104, April 2013b. ISSN 0003-6951. doi: 10.1063/1.4801308. URL https://doi.org/10.1063/1.4801308.

Hiroo Kanamori, Jim Mori, Don L. Anderson, and Thomas H. Heaton. Seismic excitation by the space shuttle Columbia. *Nature*, 349(6312):781–782, February 1991. ISSN 1476-4687. doi: 10.1038/349781a0. URL https://www.nature.com/articles/349781a0. Publisher: Nature Publishing Group.

Eduardo Kausel. Early history of soil–structure interaction. *Soil Dynamics and Earthquake Engineering*, 30(9):822–832, September 2010. ISSN 0267-7261. doi: 10.1016/j.soildyn.2009.11.001. URL https://www.sciencedirect.com/science/article/pii/S0267726109001754.

Marc Kham, Jean-François Semblat, Pierre-Yves Bard, and Patrick Dangla. Seismic Site–City Interaction: Main Governing Phenomena through Simplified Numerical Models. *Bulletin of the Seismological Society of America*, 96(5):1934–1951, October 2006. ISSN 0037-1106. doi: 10.1785/0120050143. URL https://doi.org/10.1785/0120050143.

Abdelkrim Khelif, Younes Achaoui, Sarah Benchabane, Vincent Laude, and Boujamaa Aoubiza. Locally resonant surface acoustic wave band gaps in a two-dimensional phononic crystal of pillars on a surface. *Physical Review B*, 81(21):214303, June 2010. doi: 10.1103/PhysRevB.81.214303. URL https://link.aps.org/doi/10.1103/PhysRevB.81.214303. Publisher: American Physical Society.

Dimitri Komatitsch and Jeroen Tromp. Introduction to the spectral element method for three-dimensional seismic wave propagation. *Geophysical Journal International*, 139(3):806–822, December 1999. ISSN 0956-540X. doi: 10.1046/j.1365-246x.1999.00967.x. URL https://doi.org/10.1046/j.1365-246x.1999.00967.x.

Victoria Korchagova, Matvey Kraposhin, and Sergei Strijhak. *Computational Aeroacoustics Methods with OpenFOAM v. 4.1*. July 2017. doi: 10.13140/RG.2.2.32022.24641.

A. O. Krushynska, M. Miniaci, F. Bosia, and N. M. Pugno. Coupling local resonance with Bragg band gaps in single-phase mechanical metamaterials. *Extreme Mechanics Letters*, 12:30–36, April 2017. ISSN 2352-4316. doi: 10.1016/j.eml.2016.10.004. URL https://www.sciencedirect.com/science/article/pii/S2352431616300542.

Éric Larose. Mesoscopics of ultrasound and seismic waves: application to passive imaging. *Annales de Physique*, 31(3):1–126, 2006. URL https://hal.archives-ouvertes.fr/hal-00276840. Publisher: EDP Sciences.

Giovanna Laurenzano, Enrico Priolo, Maria Rosaria Gallipoli, Marco Mucciarelli, and Felice C. Ponzo. Effect of Vibrating Buildings on Free-Field Motion and on Adjacent Structures: The Bonefro (Italy) Case History. *Bulletin of the Seismological Society of America*, 100(2):802–818, April 2010. ISSN 0037-1106. doi: 10.1785/0120080312. URL https://doi.org/10.1785/0120080312.

François Lavoué, Olivier Coutant, Pierre Boué, Laura Pinzon-Rincon, Florent Brenguier, Romain Brossier, Philippe Dales, Meysam Rezaeifar, and Christopher J. Bean. Understanding Seismic Waves Generated by Train Traffic via Modeling: Implications for Seismic Imaging and Monitoring. *Seismological Research Letters*, 92(1):287–300, October 2020. ISSN 0895-0695. doi: 10.1785/0220200133. URL https://doi.org/10.1785/0220200133.

Fabrice Lemoult, Mathias Fink, and Geoffroy Lerosey. Dispersion in media containing resonant inclusions: where does it come from? In *Conference on Lasers and Electro-Optics 2012 (2012), paper QF3H.8*, page QF3H.8. Optica Publishing Group, May 2012. doi: 10.1364/QELS.2012.QF3H.8. URL https://opg.optica.org/abstract.cfm?uri=QELS-2012-QF3H.8.

Nikolaus Lerbs, Toni Zieger, Joachim Ritter, and Michael Korn. Wind turbine induced seismic signals: the large-scale SMARTIE1 experiment and a concept to define protection radii for recording stations. *Near Surface Geophysics*, 18(5):467–482, 2020. ISSN 1873-0604. doi: 10.1002/nsg.12109. URL https://onlinelibrary.wiley.com/doi/abs/10.1002/nsg.12109. _eprint: https://onlinelibrary.wiley.com/doi/pdf/10.1002/nsg.12109.

Fabian Limberger, Michael Lindenfeld, Hagen Deckert, and Georg Rümpker. Seismic radiation from wind turbines: observations and analytical modeling of frequency-dependent amplitude decays. *Solid Earth*, 12(8):1851–1864, August 2021. ISSN 1869-9529. doi: 10.5194/se-12-1851-2021. URL https://se.copernicus.org/articles/12/1851/2021/.

Fabian Limberger, Georg Rümpker, Michael Lindenfeld, and Hagen Deckert. Development of a numerical modelling method to predict the seismic signals generated by wind farms. *Scientific Reports*, 12(1):15516, September 2022. ISSN 2045-2322. doi: 10.1038/s41598-022-19799-w. URL https://www.nature.com/articles/s41598-022-19799-w. Publisher: Nature Publishing Group.

Fabian Limberger, Georg Rümpker, Michael Lindenfeld, and Hagen Deckert. The impact of seismic noise produced by wind turbines on seismic borehole measurements. *Solid Earth*, 14(8):859–869, August 2023. ISSN 1869-9510. doi: 10.5194/se-14-859-2023. URL https://se.copernicus.org/articles/14/859/2023/. Publisher: Copernicus GmbH.

Nathaniel J. Lindsey. *Fiber-optic Seismology in Theory and Practice*. PhD thesis, UC Berkeley, 2019. URL https://escholarship.org/uc/item/1fs925tc.

Nathaniel J. Lindsey and Eileen R. Martin. Fiber-Optic Seismology. *Annual Review of Earth and Planetary Sciences*, 49(Volume 49, 2021):309–336, May 2021. ISSN 0084-6597, 1545-4495. doi: 10.1146/annurev-earth-072420-065213. URL https://www.annualreviews.org/content/journals/10.1146/annurev-earth-072420-065213. Publisher: Annual Reviews.

Nathaniel J. Lindsey, Eileen R. Martin, Douglas S. Dreger, Barry Freifeld, Stephen Cole, Stephanie R. James, Biondo L. Biondi, and Jonathan B. Ajo-Franklin. Fiber-Optic Network Observations of Earthquake Wavefields: FIBER-OPTIC

EARTHQUAKE OBSERVATIONS. *Geophysical Research Letters*, 44(23):11,792–11,799, December 2017. ISSN 00948276. doi: 10.1002/2017GL075722. URL http://doi.wiley.com/10.1002/2017GL075722.

S. Ljunggren. Generation of waves in an elastic plate by a vertical force and by a moment in the vertical plane. *Journal of Sound and Vibration*, 90(4):559–584, October 1983. ISSN 0022-460X. doi: 10.1016/0022-460X(83)90811-8. URL https://www.sciencedirect.com/science/article/pii/0022460X83908118.

Patrícia Lopes, P. Alves Costa, M. Ferraz, R. Calçada, and A. Silva Cardoso. Numerical modeling of vibrations induced by railway traffic in tunnels: From the source to the nearby buildings. *Soil Dynamics and Earthquake Engineering*, 61-62:269–285, June 2014. ISSN 0267-7261. doi: 10.1016/j.soildyn.2014.02.013. URL https://www.sciencedirect.com/science/article/pii/S0267726114000530.

Friederike F. Lott, Joachim R. R. Ritter, Mahmoud Al-Qaryouti, and Ulrich Corsmeier. On the Analysis of Wind-Induced Noise in Seismological Recordings. *Pure and Applied Geophysics*, 174(3):1453–1470, March 2017. ISSN 1420-9136. doi: 10.1007/s00024-017-1477-2. URL https://doi.org/10.1007/s00024-017-1477-2.

M. Lott and P. Roux. Effective impedance of a locally resonant metasurface. *Physical Review Materials*, 3(6):065202, June 2019a. doi: 10.1103/PhysRevMaterials.3.065202. URL https://link.aps.org/doi/10.1103/PhysRevMaterials.3.065202. Publisher: American Physical Society.

Martin Lott and Philippe Roux. Locally Resonant Metamaterials for Plate Waves: the Respective Role of Compressional Versus Flexural Resonances of a Dense Forest of Vertical Rods. pages 25–45. August 2019b. ISBN 978-1-78630-336-3. doi: 10.1002/9781119649182.ch2.

Martin Lott and Philippe Roux. Random versus regular square lattice experimental comparison for a subwavelength resonant metasurface. *The Journal of the Acoustical Society of America*, 149(5):3645–3653, May 2021. ISSN 0001-4966. doi: 10.1121/10.0005060. URL http://asa.scitation.org/doi/10.1121/10.0005060. Publisher: Acoustical Society of America.

Martin Lott, Philippe Roux, Stéphane Garambois, Philippe Guéguen, and Andrea Colombi. Evidence of metamaterial physics at the geophysics scale: the METAFORET experiment. *Geophysical Journal International*, 220(2):1330–1339, February 2020a. ISSN 0956-540X. doi: 10.1093/gji/ggz528. URL https://doi.org/10.1093/gji/ggz528.

Martin Lott, Philippe Roux, Léonard Seydoux, Benoit Tallon, Adrien Pelat, Sergey Skipetrov, and Andrea Colombi. Localized modes on a metasurface through multiwave interactions. *Physical Review Materials*, 4(6):065203, June 2020b. ISSN 2475-9953. doi: 10.1103/PhysRevMaterials.4.065203. URL https://link.aps.org/doi/10.1103/PhysRevMaterials.4.065203.

D. López-Mendoza, A. Romero, D. P. Connolly, and P. Galvín. Scoping assessment of building vibration induced by railway traffic. *Soil Dynamics and Earthquake*

*Engineering*, 93:147–161, February 2017. ISSN 0267-7261. doi: 10.1016/j.soildyn.2016.12.008. URL https://www.sciencedirect.com/science/article/pii/S0267726116306418.

Katrin Löer, Nima Riahi, and Erik H Saenger. Three-component ambient noise beamforming in the Parkfield area. *Geophysical Journal International*, 213(3):1478–1491, June 2018. ISSN 0956-540X, 1365-246X. doi: 10.1093/gji/ggy058. URL https://academic.oup.com/gji/article/213/3/1478/4858389.

Peter G. Malischewsky, Thomas Forbriger, and Cinna Lomnitz. Unusual, equivocal Rayleigh-dispersion curves for simple models taking into account the special propagation conditions in the valley of Mexico City (CDMX) – Preliminary results. *Geofísica internacional*, 56(1):7–12, March 2017. ISSN 0016-7169. doi: 10.19155/geofint.2017.056.1.1. URL http://www.scielo.org.mx/scielo.php?script=sci_abstract&pid=S0016-71692017000100007&lng=es&nrm=iso&tlng=en.

Jean-Jacques Marigo, Agnès Maurel, Kim Pham, and Amine Sbitti. Effective Dynamic Properties of a Row of Elastic Inclusions: The Case of Scalar Shear Waves. *Journal of Elasticity*, 128(2):265–289, August 2017. ISSN 1573-2681. doi: 10.1007/s10659-017-9627-4. URL https://doi.org/10.1007/s10659-017-9627-4.

Eileen Martin, Nathaniel Lindsey, Shan Dou, Jonathan Ajo-Franklin, Thomas Daley, Barry Freifeld, Michelle Robertson, Craig Ulrich, Anna Wagner, and Kevin Bjella. Interferometry of a roadside DAS array in Fairbanks, AK. In *SEG Technical Program Expanded Abstracts 2016*, SEG Technical Program Expanded Abstracts, pages 2725–2729. Society of Exploration Geophysicists, September 2016. doi: 10.1190/segam2016-13963708.1. URL https://library.seg.org/doi/abs/10.1190/segam2016-13963708.1.

Eileen Martin, Nathaniel J. Lindsey, Jonathan Ajo-Franklin, and Biondo L. Biondi. Introduction to Interferometry of Fiber-Optic Strain Measurements. In *Geophysical Monograph Series*. Wiley Online Library, 2021. URL https://agupubs.onlinelibrary.wiley.com/doi/abs/10.1002/9781119521808.ch9.

E.r. Martin*, J. Ajo-Franklin, S. Dou, N. Lindsey, T.m. Daley, B. Freifeld, M. Robertson, A. Wagner, and C. Ulrich. Interferometry of ambient noise from a trenched distributed acoustic sensing array. In *SEG Technical Program Expanded Abstracts 2015*, SEG Technical Program Expanded Abstracts, pages 2445–2450. Society of Exploration Geophysicists, August 2015. doi: 10.1190/segam2015-5902207.1. URL https://library.seg.org/doi/abs/10.1190/segam2015-5902207.1.

Roland Martin and Dimitri Komatitsch. An unsplit convolutional perfectly matched layer technique improved at grazing incidence for the viscoelastic wave equation. *Geophysical Journal International*, 179(1):333–344, October 2009. ISSN 0956-540X. doi: 10.1111/j.1365-246X.2009.04278.x. URL https://doi.org/10.1111/j.1365-246X.2009.04278.x.

Agnès Maurel, Jean-Jacques Marigo, Kim Pham, and Sébastien Guenneau. Conversion of Love waves in a forest of trees. *Physical Review B*, 98(13):134311, October 2018. doi: 10.1103/PhysRevB.98.134311. URL https://link.aps.org/doi/10.1103/PhysRevB.98.134311. Publisher: American Physical Society.

A. A. Maznev and A. G. Every. Existence of backward propagating acoustic waves in supported layers. *Wave Motion*, 48(5):401–407, July 2011. ISSN 0165-2125. doi: 10.1016/j.wavemoti.2011.02.002. URL https://www.sciencedirect.com/science/article/pii/S0165212511000205.

F. Meseguer, M. Holgado, D. Caballero, N. Benaches, J. Sánchez-Dehesa, C. López, and J. Llinares. Rayleigh-wave attenuation by a semi-infinite two-dimensional elastic-band-gap crystal. *Physical Review B*, 59(19):12169–12172, May 1999. doi: 10.1103/PhysRevB.59.12169. URL https://link.aps.org/doi/10.1103/PhysRevB.59.12169. Publisher: American Physical Society.

M. Miniaci, A. Krushynska, F. Bosia, and N. Pugno. Large scale mechanical metamaterials as seismic shields. *New Journal of Physics*, 18:null, 2016. doi: 10.1088/1367-2630/18/8/083041. URL https://www.semanticscholar.org/paper/3f0fbf591e1f2953606673e342318740eb8c21f3.

Shoaib Ayjaz Mohammed and S. N. Somala. Seismic Metamaterials: Rayleigh Wave Control in an Elastic Half-Space. Master's thesis, Indian Institute of Technology Hyderabad, 2019. URL http://raiith.iith.ac.in/7282/.

Jean-Paul Montagner and Don L. Anderson. Petrological constraints on seismic anisotropy. *Physics of the Earth and Planetary Interiors*, 54(1):82–105, April 1989. ISSN 0031-9201. doi: 10.1016/0031-9201(89)90189-1. URL https://www.sciencedirect.com/science/article/pii/0031920189901891.

Jean-Paul Montagner and Henri-Claude Nataf. A simple method for inverting the azimuthal anisotropy of surface waves. *Journal of Geophysical Research: Solid Earth*, 91(B1):511–520, 1986. ISSN 2156-2202. doi: 10.1029/JB091iB01p00511. URL http://onlinelibrary.wiley.com/doi/abs/10.1029/JB091iB01p00511. _eprint: https://agupubs.onlinelibrary.wiley.com/doi/pdf/10.1029/JB091iB01p00511.

Pierric Mora, Mathieu Chekroun, and Vincent Tournat. Seismic Metashielding by a Line of Resonators Over a Granular Layer. *Physical Review Applied*, 16(4):044002, October 2021. ISSN 2331-7019. doi: 10.1103/PhysRevApplied.16.044002. URL https://link.aps.org/doi/10.1103/PhysRevApplied.16.044002.

Nicolas Mordant, Claire Prada, and Mathias Fink. Highly resolved detection and selective focusing in a waveguide using the D.O.R.T. method. *The Journal of the Acoustical Society of America*, 105(5):2634–2642, May 1999. ISSN 0001-4966. doi: 10.1121/1.426879. URL http://asa.scitation.org/doi/10.1121/1.426879.

Tobias Neuffer and Simon Kremers. How wind turbines affect the performance of seismic monitoring stations and networks. *Geophysical Journal International*, 211 (3):1319–1327, December 2017. ISSN 0956-540X. doi: 10.1093/gji/ggx370. URL https://doi.org/10.1093/gji/ggx370.

Tobias Neuffer, Simon Kremers, and Ralf Fritschen. Characterization of seismic signals induced by the operation of wind turbines in North Rhine-Westphalia (NRW), Germany. *Journal of Seismology*, 23(5):1161–1177, September 2019. ISSN 1383-4649, 1573-157X. doi: 10.1007/s10950-019-09866-7. URL http://link.springer.com/10.1007/s10950-019-09866-7.

Tobias Neuffer, Simon Kremers, Philipp Meckbach, and Michael Mistler. Characterization of the seismic wave field radiated by a wind turbine. *Journal of Seismology*, 25(3):825–844, June 2021. ISSN 1383-4649, 1573-157X. doi: 10.1007/s10950-021-10003-6. URL https://link.springer.com/10.1007/s10950-021-10003-6.

H. Nyquist. Certain Topics in Telegraph Transmission Theory. *Transactions of the American Institute of Electrical Engineers*, 47(2):617–644, April 1928. ISSN 2330-9431. doi: 10.1109/T-AIEE.1928.5055024. URL https://ieeexplore.ieee.org/document/5055024. Conference Name: Transactions of the American Institute of Electrical Engineers.

Antonio Palermo, Sebastian Krödel, Alessandro Marzani, and Chiara Daraio. Engineered metabarrier as shield from seismic surface waves. *Scientific Reports*, 6(1):39356, December 2016. ISSN 2045-2322. doi: 10.1038/srep39356. URL http://www.nature.com/articles/srep39356. Number: 1 Publisher: Nature Publishing Group.

Antonio Palermo, Sebastian Krödel, Kathryn H. Matlack, Rachele Zaccherini, Vasilis K. Dertimanis, Eleni N. Chatzi, Alessandro Marzani, and Chiara Daraio. Hybridization of Guided Surface Acoustic Modes in Unconsolidated Granular Media by a Resonant Metasurface. *Physical Review Applied*, 9(5):054026, May 2018. doi: 10.1103/PhysRevApplied.9.054026. URL https://link.aps.org/doi/10.1103/PhysRevApplied.9.054026. Publisher: American Physical Society.

J.B. Pendry, A.J. Holden, D.J. Robbins, and W.J. Stewart. Magnetism from conductors and enhanced nonlinear phenomena. *IEEE Transactions on Microwave Theory and Techniques*, 47(11):2075–2084, November 1999. ISSN 1557-9670. doi: 10.1109/22.798002. URL https://ieeexplore-ieee-org.sid2nomade-2.grenet.fr/abstract/document/798002. Conference Name: IEEE Transactions on Microwave Theory and Techniques.

Bojana Petrovic, Stefano Parolai, Giovanna Pianese, S. Umit Dikmen, Bolot Moldobekov, Sagynbek Orunbaev, and Roberto Paolucci. Joint deconvolution of building and downhole seismic recordings: an application to three test cases. *Bulletin of Earthquake Engineering*, 16(2):613–641, February 2018. ISSN 1573-1456. doi: 10.1007/s10518-017-0215-6. URL https://doi.org/10.1007/s10518-017-0215-6.

Kim Pham, Agnès Maurel, and Jean-Jacques Marigo. Two scale homogenization of a row of locally resonant inclusions - the case of anti-plane shear waves. *Journal of the Mechanics and Physics of Solids*, 106:80–94, September 2017. ISSN 0022-5096. doi: 10.1016/j.jmps.2017.05.001. URL https://www.sciencedirect.com/science/article/pii/S002250961630672X.

Marco Pilz, Stefano Parolai, Bojana Petrovic, Natalya Silacheva, Tanatkan Abakanov, Sagynbek Orunbaev, and Bolot Moldobekov. Basin-edge generated Rayleigh waves in the Almaty basin and corresponding consequences for ground motion amplification. *Geophysical Journal International*, 213(1):301–316, April 2018. ISSN 0956-540X. doi: 10.1093/gji/ggx555. URL https://doi.org/10.1093/gji/ggx555.

Marco Pilz, Philippe Roux, Shoaib Ayjaz Mohammed, Raphael F. Garcia, Rene Steinmann, Coralie Aubert, Felix Bernauer, Philippe Guéguen, Matthias Ohrnberger, and Fabrice Cotton. Wind turbines as a metamaterial-like urban layer: an experimental investigation using a dense seismic array and complementary sensing technologies. *Frontiers in Earth Science*, 12, February 2024. ISSN 2296-6463. doi: 10.3389/feart.2024.1352027. URL https://www.frontiersin.org/articles/10.3389/feart.2024.1352027. Publisher: Frontiers.

Valerio Poggi and Donat Fäh. Estimating Rayleigh wave particle motion from three-component array analysis of ambient vibrations. *Geophysical Journal International*, 180(1):251–267, January 2010. ISSN 0956-540X. doi: 10.1111/j.1365-246X.2009.04402.x. URL https://doi.org/10.1111/j.1365-246X.2009.04402.x.

R. Porter and D. V. Evans. Rayleigh–Bloch surface waves along periodic gratings and their connection with trapped modes in waveguides. *Journal of Fluid Mechanics*, 386:233–258, May 1999. ISSN 1469-7645, 0022-1120. doi: 10.1017/S0022112099004425. URL https://www.cambridge.org/core/journals/journal-of-fluid-mechanics/article/rayleighbloch-surface-waves-along-periodic-gratings-and-their-connection-with-tra2874E86006EB2658BA7A69A2AD4149CD. Publisher: Cambridge University Press.

Claire Prada, Sébastien Manneville, Dimitri Spoliansky, and Mathias Fink. Decomposition of the time reversal operator: Detection and selective focusing on two scatterers. *The Journal of the Acoustical Society of America*, 99(4):2067–2076, April 1996. ISSN 0001-4966. doi: 10.1121/1.415393. URL http://asa.scitation.org/doi/10.1121/1.415393.

Joseph T. Rand, Louisa A. Kramer, Christopher P. Garrity, Ben D. Hoen, Jay E. Diffendorfer, Hannah E. Hunt, and Michael Spears. A continuously updated, geospatially rectified database of utility-scale wind turbines in the United States. *Scientific Data*, 7(1):15, January 2020. ISSN 2052-4463. doi: 10.1038/s41597-020-0353-6. URL https://www.nature.com/articles/s41597-020-0353-6.

Nima Riahi and Erik H. Saenger. Rayleigh and Love wave anisotropy in Southern California using seismic noise. *Geophysical Research Letters*, 41(2):363–369, 2014. ISSN 1944-8007. doi: 10.1002/2013GL058518. URL https://onlinelibrary.wiley.com/doi/abs/10.1002/2013GL058518. _eprint: https://onlinelibrary.wiley.com/doi/pdf/10.1002/2013GL058518.

Nima Riahi, Götz Bokelmann, Paola Sala, and Erik H. Saenger. Time-lapse analysis of ambient surface wave anisotropy: A three-component array study above an underground gas storage. *Journal of Geophysical Research: Solid Earth*, 118(10):5339–5351, 2013. ISSN 2169-9356. doi: 10.1002/jgrb.50375. URL https://onlinelibrary.wiley.com/doi/abs/10.1002/jgrb.50375. _eprint: https://onlinelibrary.wiley.com/doi/pdf/10.1002/jgrb.50375.

A. T. Ringler, R. E. Anthony, M. S. Karplus, A. A. Holland, and D. C. Wilson. Laboratory Tests of Three Z-Land Fairfield Nodal 5-Hz, Three-Component Sensors. *Seismological Research Letters*, 89(5):1601–1608, February 2018. ISSN 0895-0695. doi: 10.1785/0220170236. URL https://doi.org/10.1785/0220170236.

E.J. Rose, G.S. Fuis, J.M. Stock, J.A. Hole, A.M. Kell, G. Kent, N.W. Driscoll, S. Crum, M. Goldman, A.M. Reusch, L. Han, R.R. Sickler, R.D. Catchings, M.J. Rymer, C.J. Criley, D.S. Scheirer, S.M. Skinner, C.J. Slayday-Criley, J.M. Murphy, E.G. Jensen, R. McClearn, A.J. Ferguson, L.A. Butcher, M.A. Gardner, I. Emmons, C.L. Loughran, J.R. Svitek, P.C. Bastien, J.A. Cotton, D.S. Croker, A.J. Harding, J.M. Babcock, S.H. Harder, and C.M. Rosa. Borehole-explosion and air-gun data acquired in the 2011 Salton Seismic Imaging Project (SSIP), southern California—Description of the survey: U.S. Geological Survey Open-File Report 2013–1172, 84 p., 2013. URL http://dx.doi.org/10.3133/ofr20131172.

Sebastian Rost and Christine Thomas. Array Seismology: Methods and Applications. *Reviews of Geophysics*, 40(3):2–1–2–27, 2002. ISSN 1944-9208. doi: 10.1029/2000RG000100. URL https://onlinelibrary.wiley.com/doi/abs/10.1029/2000RG000100. _eprint: https://onlinelibrary.wiley.com/doi/pdf/10.1029/2000RG000100.

Philippe Roux. New Trends Towards Seismic Metamaterials.

Philippe Roux. Passive seismic imaging with directive ambient noise: application to surface waves and the San Andreas Fault in Parkfield, CA. *Geophysical Journal International*, 179(1):367, 2009. doi: 10.1111/j.1365-246X.2009.04282.x. URL https://insu.hal.science/insu-00447731.

Philippe Roux, Dino Bindi, Tobias Boxberger, Andrea Colombi, Fabrice Cotton, Isabelle Douste-Bacque, Stéphane Garambois, Philippe Gueguen, Gregor Hillers, Dan Hollis, Thomas Lecocq, and Ildut Pondaven. Toward Seismic Metamaterials: The METAFORET Project. *Seismological Research Letters*, 89(2A): 582–593, January 2018. ISSN 0895-0695. doi: 10.1785/0220170196. URL https://doi.org/10.1785/0220170196.

Elmer Ruigrok, Steven Gibbons, and Kees Wapenaar. Cross-correlation beamforming. *Journal of Seismology*, 21(3):495–508, May 2017. ISSN 1573-157X. doi: 10.1007/s10950-016-9612-6. URL https://doi.org/10.1007/s10950-016-9612-6.

Matthieu Rupin and Philippe Roux. A multi-wave elastic metamaterial based on degenerate local resonances. *The Journal of the Acoustical Society of America*, 142 (1):EL75–EL81, July 2017. ISSN 0001-4966. doi: 10.1121/1.4992098. URL http://asa.scitation.org/doi/10.1121/1.4992098. Publisher: Acoustical Society of America.

Matthieu Rupin, Fabrice Lemoult, Geoffroy Lerosey, and Philippe Roux. Experimental Demonstration of Ordered and Disordered Multiresonant Metamaterials for Lamb Waves. *Physical Review Letters*, 112(23):234301, June 2014. ISSN 0031-9007, 1079-7114. doi: 10.1103/PhysRevLett.112.234301. URL https://link.aps.org/doi/10.1103/PhysRevLett.112.234301.

Matthieu Rupin, Philippe Roux, Geoffroy Lerosey, and Fabrice Lemoult. Symmetry issues in the hybridization of multi-mode waves with resonators: an example with Lamb waves metamaterial. *Scientific Reports*, 5(1):13714, September 2015. ISSN 2045-2322. doi: 10.1038/srep13714. URL http://www.nature.com/articles/srep13714. Number: 1 Publisher: Nature Publishing Group.

G. Saccorotti, D. Piccinini, L. Cauchie, and I. Fiori. Seismic Noise by Wind Farms: A Case Study from the Virgo Gravitational Wave Observatory, Italy. *Bulletin of the Seismological Society of America*, 101(2):568–578, April 2011. ISSN 0037-1106. doi: 10.1785/0120100203. URL https://pubs.geoscienceworld.org/bssa/article/101/2/568-578/349448.

L. Seydoux, N. M. Shapiro, J. de Rosny, and M. Landès. Spatial coherence of the seismic wavefield continuously recorded by the USArray. *Geophysical Research Letters*, 43(18):9644–9652, 2016a. ISSN 1944-8007. doi: 10.1002/2016GL070320. URL https://onlinelibrary.wiley.com/doi/abs/10.1002/2016GL070320. _eprint: https://onlinelibrary.wiley.com/doi/pdf/10.1002/2016GL070320.

L. Seydoux, N.M. Shapiro, J. de Rosny, F. Brenguier, and M. Landès. Detecting seismic activity with a covariance matrix analysis of data recorded on seismic arrays. *Geophysical Journal International*, 204(3):1430–1442, March 2016b. ISSN 0956-540X. doi: 10.1093/gji/ggv531. URL https://doi.org/10.1093/gji/ggv531.

Léonard Seydoux, Julien de Rosny, and Nikolai M. Shapiro. Pre-processing ambient noise cross-correlations with equalizing the covariance matrix eigenspectrum. *Geophysical Journal International*, 210(3):1432–1449, September 2017. ISSN 0956-540X. doi: 10.1093/gji/ggx250. URL https://doi.org/10.1093/gji/ggx250.

C.E. Shannon. Communication in the Presence of Noise. *Proceedings of the IRE*, 37 (1):10–21, January 1949. ISSN 2162-6634. doi: 10.1109/JRPROC.1949.232969. URL https://ieeexplore.ieee.org/document/1697831. Conference Name: Proceedings of the IRE.

N. M. Shapiro and M. Campillo. Emergence of broadband Rayleigh waves from correlations of the ambient seismic noise. *Geophysical Research Letters*, 31(7), 2004. ISSN 1944-8007. doi: 10.1029/2004GL019491. URL https://onlinelibrary.wiley.com/doi/abs/10.1029/2004GL019491. _eprint: https://onlinelibrary.wiley.com/doi/pdf/10.1029/2004GL019491.

Anna Maria Skłodowska, Stefano Parolai, Bojana Petrovic, and Fabio Romanelli. Soil-structure interaction assessment combining deconvolution of building and field recordings with polarization analysis: application to the Matera (Italy) experiment. *Bulletin of Earthquake Engineering*, 21(13):5867–5891, October 2023. ISSN 1573-1456. doi: 10.1007/s10518-023-01750-7. URL https://doi.org/10.1007/s10518-023-01750-7.

D. R. Smith, Willie J. Padilla, D. C. Vier, S. C. Nemat-Nasser, and S. Schultz. Composite Medium with Simultaneously Negative Permeability and Permittivity. *Physical Review Letters*, 84(18):4184–4187, May 2000. doi: 10.1103/PhysRevLett.84.4184. URL https://link.aps.org/doi/10.1103/PhysRevLett.84.4184. Publisher: American Physical Society.

Martin L. Smith and F. A. Dahlen. The azimuthal dependence of Love and Rayleigh wave propagation in a slightly anisotropic medium. *Journal of Geophysical Research*, 78(17):3321–3333, June 1973. ISSN 01480227. doi: 10.1029/JB078i017p03321. URL http://doi.wiley.com/10.1029/JB078i017p03321.

Jean Soubestre and Claude Boutin. Non-local dynamic behavior of linear fiber reinforced materials. *Mechanics of Materials*, 55:16–32, December 2012. ISSN 0167-6636. doi: 10.1016/j.mechmat.2012.06.005. URL https://www.sciencedirect.com/science/article/pii/S016766361200138X.

Jean Soubestre, Nikolai M. Shapiro, Léonard Seydoux, Julien de Rosny, Dmitry V. Droznin, Svetlana Ya. Droznina, Sergey L. Senyukov, and Evgeniy I. Gordeev. Network-Based Detection and Classification of Seismovolcanic Tremors: Example From the Klyuchevskoy Volcanic Group in Kamchatka. *Journal of Geophysical Research: Solid Earth*, 123(1): 564–582, 2018. ISSN 2169-9356. doi: 10.1002/2017JB014726. URL https://onlinelibrary.wiley.com/doi/abs/10.1002/2017JB014726. _eprint: https://onlinelibrary.wiley.com/doi/pdf/10.1002/2017JB014726.

Klaus Stammler and Lars Ceranna. Influence of Wind Turbines on Seismic Records of the Gräfenberg Array. *Seismological Research Letters*, 87(5):1075–1081, July 2016. ISSN 0895-0695. doi: 10.1785/0220160049. URL https://doi.org/10.1785/0220160049.

Seth Stein and Michael Wysession. *An introduction to seismology, earthquakes, and earth structure*. John Wiley & Sons, 2009.

Le Tang, Heiner Igel, and Jean-Paul Montagner. Single-point dispersion measurement of surface waves combining translation, rotation and strain in weakly anisotropic media: theory. *Geophysical Journal International*, 235(1):24–47, October 2023. ISSN 0956-540X. doi: 10.1093/gji/ggad199. URL https://doi.org/10.1093/gji/ggad199.

Toshiro Tanimoto. The azimuthal dependence of surface wave polarization in a slightly anisotropic medium. *Geophysical Journal International*, 156(1):73–78, January 2004. ISSN 0956-540X. doi: 10.1111/j.1365-246X.2004.02130.x. URL https://doi.org/10.1111/j.1365-246X.2004.02130.x.

M. Tanter, J.-F. Aubry, J. Gerber, J.-L. Thomas, and M. Fink. Optimal focusing by spatio-temporal inverse filter. I. Basic principles. *The Journal of the Acoustical Society of America*, 110(1):37–47, July 2001. ISSN 0001-4966. doi: 10.1121/1.1377051. URL http://asa.scitation.org/doi/10.1121/1.1377051.

Mickaël Tanter, Jean-Louis Thomas, and Mathias Fink. Time reversal and the inverse filter. *The Journal of the Acoustical Society of America*, 108(1):223–234, July 2000. ISSN 0001-4966. doi: 10.1121/1.429459. URL http://asa.scitation.org/doi/10.1121/1.429459.

R. W. Thresher and W. E. Holley. Response sensitivity of wind turbines to atmospheric turbulence. Technical Report DOE/ET/23144-81/1, Oregon State Univ., Corvallis (USA). Dept. of Mechanical Engineering, May 1981. URL https://www.osti.gov/biblio/6811583.

Marie Touboul, Kim Pham, Agnès Maurel, Jean-Jacques Marigo, Bruno Lombard, and Cédric Bellis. Effective Resonant Model and Simulations in the Time-Domain

of Wave Scattering from a Periodic Row of Highly-Contrasted Inclusions. *Journal of Elasticity*, 142(1):53–82, November 2020. ISSN 1573-2681. doi: 10.1007/s10659-020-09789-2. URL https://doi.org/10.1007/s10659-020-09789-2.

Martijn P. A. van den Ende and Jean-Paul Ampuero. Evaluating seismic beamforming capabilities of distributed acoustic sensing arrays. *Solid Earth*, 12(4):915–934, April 2021. ISSN 1869-9510. doi: 10.5194/se-12-915-2021. URL https://se.copernicus.org/articles/12/915/2021/. Publisher: Copernicus GmbH.

J Van der Tempel and DP Molenaar. Soft-soft, not hard enough? In *Proceedings of the World Wind Energy Conference, Berlin*, 2002.

Viktor G. Veselago. THE ELECTRODYNAMICS OF SUBSTANCES WITH SIMULTANEOUSLY NEGATIVE VALUES OF AND . *Soviet Physics Uspekhi*, 10(4):509, April 1968. ISSN 0038-5670. doi: 10.1070/PU1968v010n04ABEH003699. URL https://iopscience.iop.org/article/10.1070/PU1968v010n04ABEH003699/meta. Publisher: IOP Publishing.

S. C. Walker, Philippe Roux, and W. A. Kuperman. Data-based mode extraction with a partial water column spanning array. *The Journal of the Acoustical Society of America*, 118(3):1518–1525, September 2005. ISSN 0001-4966. doi: 10.1121/1.1993149. URL http://asa.scitation.org/doi/10.1121/1.1993149.

Richard L. Weaver and Oleg I. Lobkis. Fluctuations in diffuse field–field correlations and the emergence of the Green's function in open systems. *The Journal of the Acoustical Society of America*, 117(6):3432–3439, May 2005. ISSN 0001-4966. doi: 10.1121/1.1898683. URL https://doi.org/10.1121/1.1898683.

Rachel F. Westwood and Peter Styles. Assessing the seismic wavefield of a wind turbine using polarization analysis. *Wind Energy*, 20(11):1841–1850, 2017. ISSN 1099-1824. doi: 10.1002/we.2124. URL https://onlinelibrary.wiley.com/doi/abs/10.1002/we.2124. _eprint: https://onlinelibrary.wiley.com/doi/pdf/10.1002/we.2124.

Rachel F. Westwood, Peter Styles, and Samuel M. Toon. Seismic monitoring and vibrational characterization of small wind turbines: A case study of the potential effects on the Eskdalemuir International Monitoring System Station in Scotland. *Near Surface Geophysics*, 13(2):115–126, April 2015. ISSN 1569-4445, 1873-0604. doi: 10.3997/1873-0604.2015001. URL https://onlinelibrary.wiley.com/doi/abs/10.3997/1873-0604.2015001.

Earl G. Williams, Philippe Roux, Matthieu Rupin, and W. A. Kuperman. Theory of multiresonant metamaterials for ${A}_{0}$ Lamb waves. *Physical Review B*, 91(10):104307, March 2015. doi: 10.1103/PhysRevB.91.104307. URL https://link.aps.org/doi/10.1103/PhysRevB.91.104307. Publisher: American Physical Society.

Ryan Wiser, Mark Bolinger, Ben Hoen, Dev Millstein, Joseph Rand, Galen Barbose, Naïm Darghouth, Will Gorman, Seongeun Jeong, and Ben Paulos. Land-Based Wind Market Report: 2022 Edition. Technical report, Lawrence Berkeley National

Lab. (LBNL), Berkeley, CA (United States), August 2022. URL https://www.osti.gov/biblio/1882594.

Richard D. Woods. Screening of Surface Wave in Soils. *Journal of the Soil Mechanics and Foundations Division*, 94(4):951–979, July 1968. doi: 10.1061/JSFEAQ.0001180. URL https://ascelibrary.org/doi/10.1061/JSFEAQ.0001180. Publisher: American Society of Civil Engineers.

Tang-dai Xia, Miao-miao Sun, Chen Chen, Wei-yun Chen, and Xu Ping. Analysis on multiple scattering by an arbitrary configuration of piles as barriers for vibration isolation. *Soil Dynamics and Earthquake Engineering*, 31(3):535–545, March 2011. ISSN 0267-7261. doi: 10.1016/j.soildyn.2010.10.008. URL https://www.sciencedirect.com/science/article/pii/S0267726110002447.

Katsuyoshi Yamabe and Kiyoshi Kanai. An empirical formula on the attenuation of the maximum acceleration of earthquake motions. In *of: Proceedings of Ninth World Conference on Earthquake Engineering*, volume 2, pages 337–342, 1988.

R. Zaccherini, A. Palermo, A. Marzani, A. Colombi, V. K. Dertimanis, and E. N. Chatzi. Attenuation of surface modes in granular media. *arXiv:2111.07199 [physics]*, November 2021. URL http://arxiv.org/abs/2111.07199. arXiv: 2111.07199.

Rachele Zaccherini, Antonio Palermo, Alessandro Marzani, Andrea Colombi, Vasilis Dertimanis, and Eleni Chatzi. Mitigation of Rayleigh-like waves in granular media via multi-layer resonant metabarriers. *Applied Physics Letters*, 117(25):254103, December 2020. ISSN 0003-6951, 1077-3118. doi: 10.1063/5.0031113. URL http://arxiv.org/abs/2109.12917. arXiv: 2109.12917.

Xiangfang Zeng, Chelsea Lancelle, Clifford Thurber, Dante Fratta, Herb Wang, Neal Lord, Athena Chalari, and Andy Clarke. Properties of Noise Cross-Correlation Functions Obtained from a Distributed Acoustic Sensing Array at Garner Valley, California. *Bulletin of the Seismological Society of America*, 107 (2):603–610, January 2017. ISSN 0037-1106. doi: 10.1785/0120160168. URL https://doi.org/10.1785/0120160168.

Zhongwen Zhan. Distributed Acoustic Sensing Turns Fiber-Optic Cables into Sensitive Seismic Antennas. *Seismological Research Letters*, 91(1): 1–15, January 2020. ISSN 0895-0695, 1938-2057. doi: 10.1785/0220190112. URL https://pubs.geoscienceworld.org/ssa/srl/article/91/1/1/579426/Distributed-Acoustic-Sensing-Turns-FiberOptic.

Jian Zhang, Peter Gerstoft, and Peter M. Shearer. High-frequency P-wave seismic noise driven by ocean winds. *Geophysical Research Letters*, 36(9), 2009. ISSN 1944-8007. doi: 10.1029/2009GL037761. URL https://onlinelibrary.wiley.com/doi/abs/10.1029/2009GL037761. _eprint: https://onlinelibrary.wiley.com/doi/pdf/10.1029/2009GL037761.

T. Zieger, S. Nagel, P. Lutzmann, I. Kaufmann, J. Ritter, T. Ummenhofer, P. Knödel, and P. Fischer. Simultaneous identification of wind turbine vibrations by using seismic data, elastic modeling and laser Doppler vibrometry.

*Wind Energy*, 23(4):1145–1153, 2020. ISSN 1099-1824. doi: 10.1002/we.2479. URL http://onlinelibrary.wiley.com/doi/abs/10.1002/we.2479. _eprint: https://onlinelibrary.wiley.com/doi/pdf/10.1002/we.2479.